Lipid Based Anti-Fibrotic Formulations and Their Impact on Extracellular Vesicles

Inaugural dissertation

of the Faculty of Science,

University of Bern

presented by

Cristina Zivko

from Lumino (TI) and Croatia

Supervisor of the doctoral thesis:

Prof. Dr. Paola Luciani

Department of Chemistry, Biochemistry and Pharmaceutical Sciences,

University of Bern

Lipid Based Anti-Fibrotic Formulations and Their Impact on Extracellular Vesicles

Inaugural dissertation

of the Faculty of Science,

University of Bern

presented by

Cristina Zivko

From Lumino (TI) and Croatia

Supervisor of the doctoral thesis:

Prof. Dr. Paola Luciani

Department of Chemistry, Biochemistry and Pharmaceutical Sciences, University of Bern

Accepted by the Faculty of Science.

Bern, March 29th, 2021

The Dean

Prof. Dr. Z. Balogh

To my family.

*"**All my life through, the new sights of Nature made me rejoice like a child.**"*

Marie Skłodowska Curie

Table of Contents

Chapter 1.
Background and Purpose

“The important thing is not to stop questioning.”
Albert Einstein

Parts of this chapter are published:
Zivko, C., Fuhrmann G., Luciani, P., Liver-derived extracellular vesicles: A cell by cell overview to isolation and characterization practices. Biochimica et Biophysica Acta (BBA) - General Subjects (2020), 129559

1.1. Liver fibrosis

The liver is a large and complex organ responsible for a variety of essential physiological tasks including protein synthesis, lipid storage regulation, xenobiotic detoxification, and offering support to both immunological activity and food digestion.[1] It is difficult to understate its importance. When organ function is compromised, hepatic diseases are directly responsible for as many as 2 million deaths per year: liver cirrhosis alone kills 1.16 million people every year, and hepatocellular carcinoma accounts for the death of 788'000 more, meaning that combined they cause 3.5% of all yearly deaths in the world.[2,3] The global health burden of liver associated conditions is not sufficiently addressed as of yet.[4]

Hepatic fibrosis is the necessary wound-healing response to organ insult.[5] It becomes medically dangerous when exacerbated by chronic diseases, steadily advancing to a cirrhotic state and culminating in organ failure.[6,7] The most common causes of liver cirrhosis are excessive alcohol consumption, non-alcoholic fatty liver disease (NAFLD) and hepatitis.[8,9]

From a cellular perspective, hepatic stellate cells (HSCs) play a major role in the process.[10,11] Under physiologically healthy conditions, HSCs reside in the space of Disse, between hepatocytes and endothelial cells (**Figure 1-1**), and are mainly responsible for storing vitamin A in cytoplasmic lipid droplets.[12,13] Upon liver injury, however, they undergo transdifferentiation into a myofibroblast-like state, i.e., they become activated, progressively lose their lipid droplets and start promoting fibrogenesis, most notably by deposition of excessive and collagen rich extracellular matrix.[14,15] HSC-transdifferentiation is triggered by inflammatory responses mediated by liver resident macrophages (Kupffer cells).[16–18] Since the liver is frequently in contact with exogenous material, suppressing "unwanted" immune responses is essential. Kupffer cells have been shown to provide anti-inflammatory signals that allow homeostatic immunological tolerance under healthy conditions. As part of the innate immune system, these macrophages phagocyte invading pathogens and play a critical role for the initiation of immunological responses when inflammation and recruitment of other cells is required by the triggered defense mechanisms. These include the release of reactive oxygen species (ROS) and pro-inflammatory mediators (e.g., cytokines such as interleukin-1, IL-1 and tumor necrosis factor-α, TNF-α) by neighboring cells. As the main collagen-producing cells, persistently activated HSCs cause the progressive change within the extracellular matrix (ECM) of the perisinusoidal space to what is essentially scar tissue.[10,19] During chronic pathologies, if the fibrosis is not resolved, the excessive deposition of collagen rich ECM eventually leads to stiffness and loss of organ function.

The liver's ability for self-regeneration,[15] however, makes it particularly interesting to investigate, since early stages of fibrosis are considered to be reversible if the underlying cause is removed.[20,21] Resolution will result in HSCs apoptosis or reversion to a quiescent status.[22] This pivotal role of HSCs in hepatic fibrosis makes these cells crucial therapeutic and diagnostic targets.[23,24]

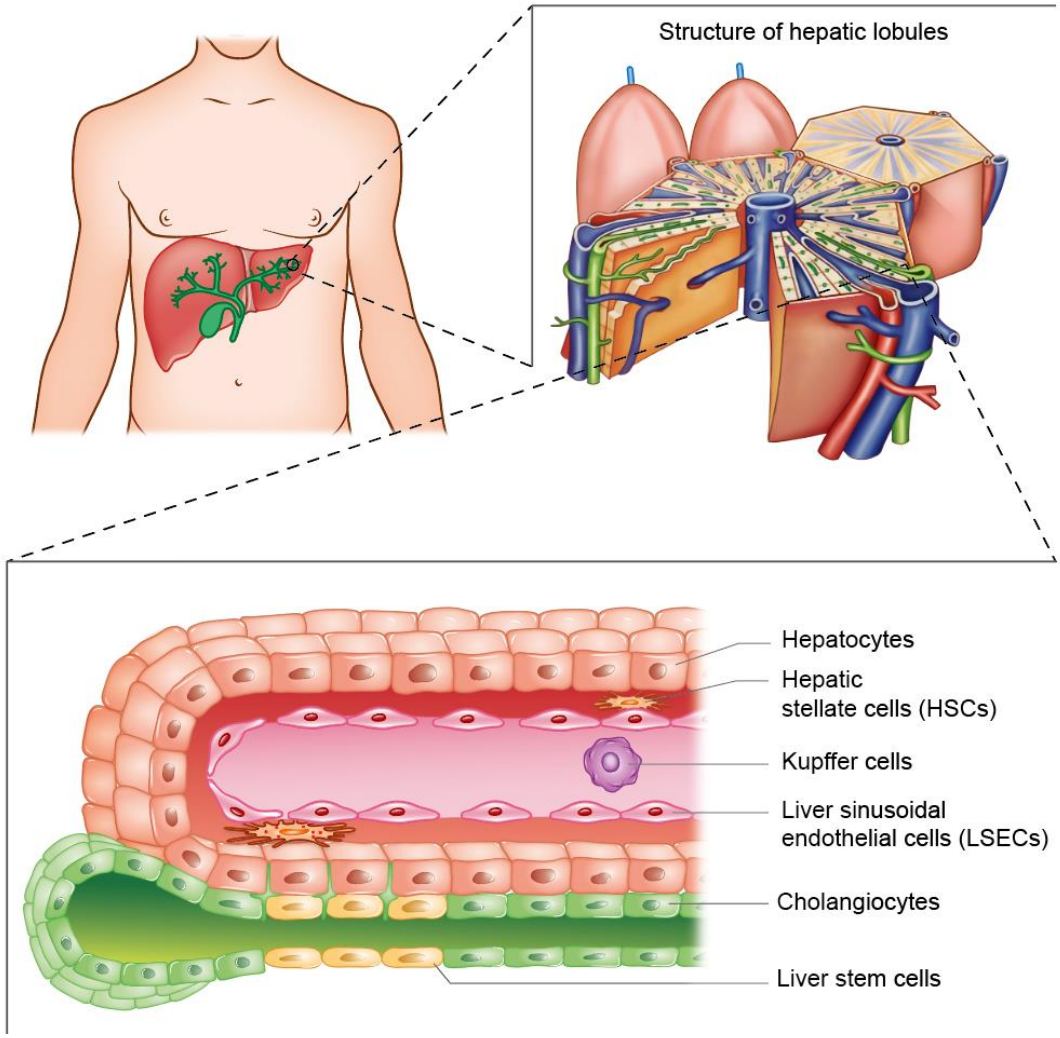

Figure 1-1: Liver location, structure of hepatic lobules (adapted with permission[25]) and their anatomy at the cellular level: hepatocytes (the most abundant cells in the liver and responsible for the most tasks), hepatic stellate cells (vitamin A storing cells), cholangiocytes (modifying the bile along the bile ducts), liver sinusoidal endothelial cells (lining the fenestrated layer of blood vessels), Kupffer cells (liver resident macrophages), liver stem cells (potentially playing a role in liver regeneration).

Currently, there is no treatment approved specifically for liver fibrosis, and the available options for the management of it are meant to address the underlying cause.[26,27] For example, viral hepatitis is treated with antiviral agents, such as entecavir,[21] and excessive hepatic inflammation in autoimmune hepatitis can be successfully managed with steroids.[28,29] When the fibrosis is linked to primary biliary cholangiatis (PBC), the use of ursodeoxycholic acid (UDCA) can help delaying the need for liver transplantation, although reports on its benefits are conflicting and the exploration of novel PBC treatments is underway.[30] Cenicriviroc has been emerging as a candidate drug for patients with NASH, due to its dual antagonism of the chemokine receptors CCR2 and CCR5 (involved in monocyte chemotactic recruitment).[31–33] Most recently, its application for non-alcoholic steatohepatitis (NASH) is being tested along with tropifexor, a

highly potent, non-bile acid, farnesoid X receptor (FXR) agonist (regulator of bile acid signaling).[32,34] Other drugs under investigation include obeticholic acid, a semi-synthetic bile acid analogue and FXR agonist, and elafibranor, a novel peroxisome proliferator-activated receptor α and δ (PPARα/δ) dual agonist.[35,36]

Essential phospholipids (EPLs, highly purified soybean extracts) have long been indicated as supportive therapy for fatty liver disease, due to their supposed anti-inflammatory effect.[37,38] EPLs are enriched in polyenylphosphatidylcholines (PPCs); the most abundant lipid is 1,2-dilinoleoylphosphatidylcholine (DLPC), which is also suggested to be the pharmaceutically active agent in PPCs.[39–41]

Many studies have been investigating EPLs' mode of action in chronic diseases of the liver,[42–44] including one where PPCs were shown to suppress collagen and α-SMA expression in human HSCs by reducing TGF-β1-induced ROS.[45] We have contributed to the field by investigating the anti-fibrotic role of PPC-based formulations in deactivating pro-fibrogenic HSCs in an in vitro model using the LX-2 human hepatic stellate cell line.[46] The optimized protocols could be successfully used for the screening of the impact of our own phospholipid-based formulations on activated HSCs by examining the accumulation of cytoplasmic lipid droplets and the absence of main fibrotic markers in the extracellular matrix (i.e., α-SMA, collagen). However, further efforts are required to elucidate their underlying mechanism of action.

The research into the treatment of hepatic fibrosis has not led to the approval of an effective drug yet; at the same time, its diagnosis is challenging as well. This is particularly problematic because of liver fibrosis's mostly asymptomatic progression in its early and crucial stages.[15,47] The current gold standard for the diagnosis of liver fibrosis is tissue biopsy, which is a highly invasive approach whereby liver tissue is provided for histopathological assessment.[24,48] These biopsies require multiple tissue sampling to increase the chances of detecting affected areas, which can still be missed given the size of the organ and the fact that liver fibrosis can develop across unconnected regions. Alternative methods, however imprecise, are considered and tried.[20,49] Those include ultrasonographic-based assessments such as transient elastography,[50–52] shear wave elastography (SWE)[53–56] and acoustic radiation force impulse (ARFI) imaging.[57–59] Another approach is magnetic resonance elastography, or relying on clinical parameters, which are minimally invasive since they are derived from routine biochemical panels (e.g., aspartate aminotransferase to platelet ratio index, APRI).[60]

The search for sensitive, precise and non-invasive tools for the evaluation of liver fibrosis and its progression is an open field of investigation.

1.2. EVs and their potential as diagnostic tools

Extracellular vesicles (EVs) is a collective term referring to a diverse group of small membrane vesicles virtually released by all cell types, and which are generally being categorized according to their biogenesis.[61,62] Apoptotic bodies are blebs of the dying cell membrane and have the broadest size range. Microvesicles, sometimes referred to as microparticles or ectosomes, stem from the outward budding of

the cellular membrane. Exosomes, which tend to be the smallest subpopulation, are released into the extracellular space after multivesicular bodies (MVB) fuse with the cell membrane (**Figure 1-2**). It is still not really possible to isolate one subpopulation from the others, and while it is believed that they may display biomolecules that are enriched to different extents, their overlapping composition, density and size, as well as the absence of subtype-specific markers still make for a considerable challenge.[63–65] Efforts in that direction are being attempted to different degrees of success: for example, Zhang et al. 2018 identified distinct EV subsets by asymmetric flow field flow fractionation (AF4), which they categorized according to their size rather than biogenesis.[66]

The relatively recent discovery of EVs' role in intercellular communication captivated the attention of a growing number of scientists anticipating the enormous potential of EVs in the fields of diagnostics and drug delivery.[67–69] For some pathological dispositions EVs can be applied as liquid biopsies, and that has sparked interest from a diagnostic perspective. EVs are enriched in selected biomolecules, they are intrinsically equipped to protect their cargo from degradation, and while their complexity offers many characterization opportunities (**Figure 1-2**), they are still simpler to analyze than total blood or serum samples.[70–72] The interest in EVs as drug delivery systems stems from their potential advantages over synthetic carriers: they are bioavailable, biocompatible, resistant to RNAases and proteases (high physicochemical stability), capable of long-distance communication and they are intrinsically able to interact with cells even across species.[73–75]

With its unique ensemble of diverse cells (**Figure 1-1**), the liver offers the opportunity to study intra- and inter-cellular communication. Elucidating the role of EV-mediated hepatic cellular crosstalk has gained the attention of many researchers, who have been able to review its critical role in both health and disease, pointing to differences in the set of EVs that are released, especially in the case of tumors.[76–80] In the context of liver pathologies, EVs would offer a valid alternative approach to diagnostic methods, which is why there has been extensive research delving into the diagnostic potential of EVs in the context of liver-associated conditions.[81–87]

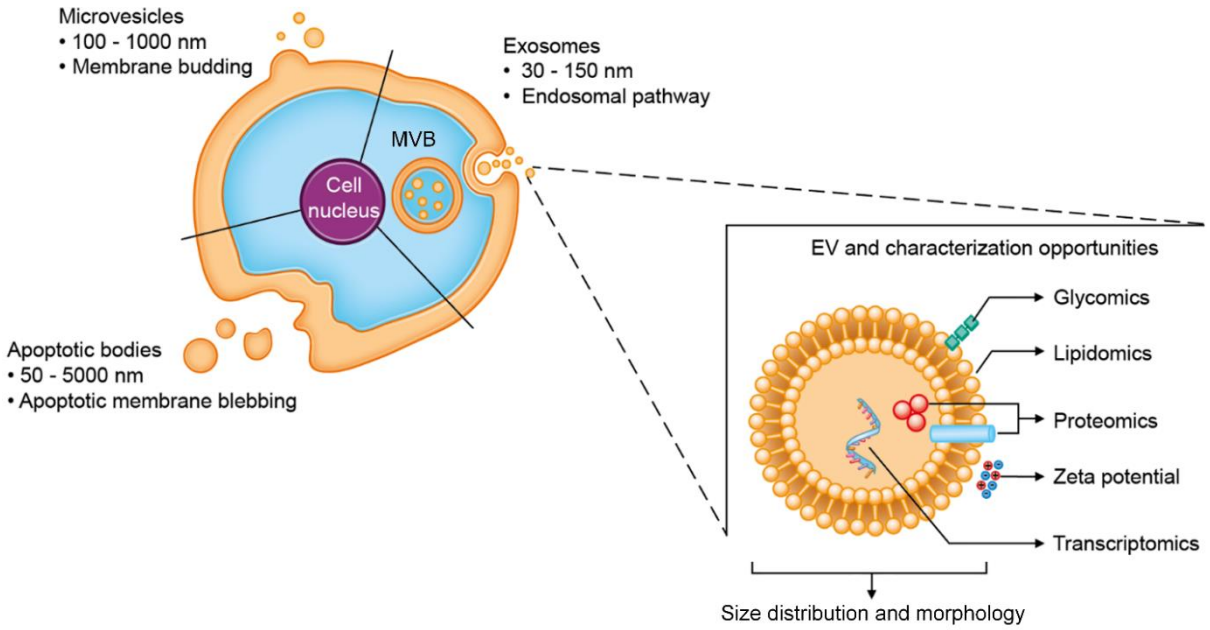

Figure 1-2: EV nomenclature according to biogenesis; zoomed insert shows a schematic representation of a single EV with characterization opportunities.

1.3. Liver-derived EVs

Liver-derived EVs have been gaining attention as a research topic, and there are already a few research papers addressing EVs from every liver resident cell type. Much work has already been published, but a rigorous standardization is needed. **Table 1-1** summarizes all such efforts.

Table 1-1: Overview of the methods for liver-derived EVs.

	EV origin	FBS handling	Isolation techniques	Yield determination	Storage	Analysis/ Characterization
[In vitro/Cell culture]						
h-hepatocytes	Hep3B,[88–96] HepG2,[88–94,97–111] PLC/PRF/5,[89,90,101,112] 97H,[96,113] LM3,[96,99,113,114] Huh6,[88] Huh7,[a)] Huh-7.5,[115,116] Bel-7402,[111] Q64-7703,[98] MH CC92-H,[98] LO2,[98,113] LSQT-2,[99] MHCC97L,[99] SMMO7721,[99] HKCI-C3,[117] HKCI-B [117]	UC-dep,[b)] ExoFree-FBS,[97,118] SSt (12, 24, 72 h)[c)]	dUc,[d)] filtration,[e)] ExoQuick™,[f)] Total Exosome Isolation™ (TEI),[104,114] density gradient UC,[g)] sucrose cushion UC[91,119]	protein content,[89,104,120,121] relative particle number,[h)] particle number per number of cells,[96,117] molar concentration[88]	at 4 °C for no longer than 48 h,[91] at -70 °C,[100] at -80 °C,[i)] dried EV-pellet at -80 °C[88]	TEM,[j)] immunogold TEM,[k)] flow cytometry,[l)] western blot,[m)] NTA,[n)] AFM,[88] DLS,[o)] BCA assay,[p)] Bradford assay,[94,104,117–119] RNA,[q)] proteomics,[93,96] custom colorimetric nanoplasmonic assay (molar concentration)[88]
r-hepatocytes	primary rat hepatocytes,[93,102,122] primary mouse hepatocytes,[123–127] Hca-F,[128] Hca-P,[128] H22,[129] IMH[130]	n/f	dUc, density gradient UC filtration	protein content, relative particle number, particle number per number of cells	n/f	TEM, DLS, zeta potential, western blot, fluorescence microscopy, qRT-PCR, proteomics, flow cytometry NTA
h-HSCs	LX-2[19,131–133]	SSt (16, 48 h),[19,132,133] ExoFree-FBS[131]	dUc,[19,133] ExoQuick™[131]	relative particle number[133]	n/f	NTA,[133] DLS,[19] zeta potential, [19] RNA, [131] TEM,[19,132,133] western blot[19,133]
r-HSCs	primary rat HSCs,[134] primary mouse HSCs,[19,135–137] rat HSC-derived PMF[138]	UC-dep,[136] SSt (16, 48 h)[134]	dUc,[r)] density gradient UC,[134,138] TEI[137]	relative particle number[135,136]	at 4 °C and used within 72 h[134]	TEM,[19,134–136,138] DLS,[19,138] zeta potential,[19] western blot,[19,135,137,138] fluorescence microscopy[136] qRT-PCR,[137]

						proteomics,[134,138,139] flow cytometry,[138] RNA[134]
h-Cholangiocytes	EGI1,[140] TFK-1,[140] H69[141]	UC-dep,[141] SSt (48 h)[140]	dUc, [140141] filtration[140]	relative particle number[140141]	at -80° C[140]	NTA, [140,141] TEM, [140,141] proteomics, [140] western blot[140]
r-Cholangiocytes	603B,[134] primary mice cholangiocytes[142]	UC-dep,[142] SSt (16 h)[134]	dUc[134] density gradient UC[134]	n/f	n/f	TEM, [134,142] RNA[134] Protein analysis[134] DLS,[142] RNA[142]
h-LSECs	TMNK-1[143]	n/f	ExoQuick, [143] dUc[144]	protein content [143,144]	n/f	flow cytometry, [143] TEM, [144] immunoblot, [144] Bradford assay, [144] BCA assay, [143] RNA[144]
r-LSECs	TSEC[145]	UC-dep then 20% FBS medium sterile filtration[145]	n/f	relative particle number, [145] protein content[145]	n/f	NTA, [145] western blot, [145] TEM,[145] Bradford assay[145]
h-Kupffer Cells	THP-1,[144,146,147] monocyte-derived macrophages[148]	ExoFree-FBS[148]	dUc,[134,135] filtration, [135] ExoQuick, TEI[148]	relative particle number, [135] protein content[134]	n/f	NTA, [135] EM,[134,148] western blot,[134,148] Bradford assay, [134] RNA[134]
r-Kupffer Cells	mice hepatic macrophages[97,126,127]	UC-dep[85]	dUc,[97,126,127] sucrose gradient[114,115]	relative particle number[114,115]	n/f	NTA[114,115] flow cytometry, [85] DLS, [85] TEM, [85] RNA[85]
h-Liver Stem Cells	HLSCs[149–158]	SSt (24 h)[149–158]	dUc,[149–158] custom charge-based precipitation method, [159] size exclusion chromatography[158]	relative particle number[149–158]	at -80° C with 5% (v/v) DMSO[149–158]	NTA, [149–158] TEM, [149–158] western blot, [149–158] RNA, [149–158] Raman spectroscopy,[158] flow cytometry[149–158]
r-Liver Stem Cells	Thp1+ cells[160]	n/f	dUc[160]	Spectrophotometry[160]	n/f	Spectrophotometry[160]

[ex vivo/Clinic]						
human	blood (circulation), [161–220] blood (liver), [221] bile[222] intraoperatively[223]	n/f	dUc[s)] ExoQuick or TEI[t)]	protein content, relative particle number	at -80°C	NTA, TEM, MS, western blot
rodent	blood (circulation)[215–251]	n/f	ExoQuick	relative particle number	at -80°C	TEM, RNA Protein analysis, DLS

Footnotes

a) [88,95,108,114,118,124,130,241,249,266–268]
b) [88–90,93,98,99,101,113,114,117,118,124,130,267,269]
c) [106,109,110,112,125,266,270,271]
d) [88–94,96–99,101–103,106,107,109,112,117–119,124,125,130,228,249,266,267,272]
e) [91–94,112,115,117,228]
f) [100,105,106,111,115,116,270,271,273]
g) [102,103,106,117,249]
h) [99,106,107,124,125,130]
i) [89,90,92,98,101,111,112,114,124,130,267,274]
j) [89,90,94,96,98–101,108–111,114,121,130,249,269]
k) [91,92,102,107,113,117,119,241,275]
l) [89,101,102,108–110,115,274,276]
m) [88,94,100,101,106,107,114,117–120,130,277,278]
n) [93,96,98,99,106,107,112,121,124,125,130,228,240,268,279]
o) [97,102,104,109,114,118]
p) [88,91,92,100–102,109,111,114,115,120,121]
q) [89,95,97,112,118,240,268,273,277,279]
r) [19,134,136,138,139,280]
s) [93,97–99,123,124,144,281]
t) [131,137,147,270,282]

Abbreviations

h: human
r: rodent (either mouse or rat)
UC: ultracentrifugation
dUc: differential centrifugation including UC
SSt: serum starvation
UC-dep: depleted of EVs by UC
n/f: not found (either non-applicable or not disclosed)

AFM: atomic force microscopy
BCA: bicinchoninic acid
DLS: dynamic light scattering
MS: mass spectrometry
NTA: nanoparticle tracking analysis
TEM: transmission electron microscopy
qRT-PCR: quantitative real-time polymerase chain reaction

From a diagnostic perspective, ex vivo EV samples mostly involve circulating vesicles isolated from the blood of human patients and healthy volunteers.[161–220] However, liver-derived EVs have also been recovered in and ex vivo from liver blood directly,[221] bile[216] and even from cancer cells that were extracted intraoperatively.[223]

When looking at the isolation of vesicles, the techniques used for EVs from human patients mirror protocols first developed for cell culture systems. Differential centrifugation (including ultracentrifugation, UC)[93,97,98,123,124,140,144] is the most frequently used method, and it is also considered the gold standard in EV research, even in spite of its relatively high inter-user variability.[283] Following UC, methods based on polymer precipitation of EVs (ExoQuick and Total Exomes Isolation, TEI)[137,256,282,284,285] are the second most prevalent approaches. Much like in viral research, polymeric precipitation strategies can be successfully employed to pellet nano-sized particles.[286] However, unless coupled to a further purification step, these methods are notoriously prone to the co-isolation of contaminants when used for EVs.[287] Given that their composition is proprietary information, it is also hard to evaluate how much of it will interfere with downstream analysis. Samples collected from blood circulation are consistently stored at -80 °C before analysis, mostly after depleting them of cells and platelets, but a validation for any storage condition is rarely disclosed.

As to the analysis of circulating EVs, it is typically focused on the (known) biomarkers of interest. For example, Nojima et al. 2016[126,288] isolated EVs from primary mice hepatocytes and Kupffer cells in vitro by differential UC and sucrose gradient. In the same studies they also described mice serum-derived EVs (even from cardiac puncture) being isolated by ExoQuick. They quantified their EVs by looking at the presence of CD81, a known exosomal marker.[289] The studies showcase how it is not always possible to directly transfer isolation strategies from an in vitro to an ex vivo setting. Characterization practices (DLS for size, CD81-antigen-ELISA for quantification) on the other hand could be applied unchanged in both instances. However, while CD81 is an established marker for exosomes, it is now considered insufficient on its own for positive determination of exosomes exclusively, and it should be accompanied by an additional marker (e.g., CD63, CD9, Alix).[62]

Other than markers for specific EV-subpopulations, researchers have endeavored to check for the presence of disease-associated molecules, as they can be found with ready-to-use panels developed for platforms such as the nCounter®. The latter is a patented variation on DNA microarray technologies that allows for the analysis of pre-selected sets of hundreds of protein, DNA and RNA targets.

Sohn et al. 2015[282] specifically analysed the expression levels of serum exosomal microRNAs (miR-18a, -21, -93, -106b, -221, -222 and -224, -101, -122 and -195) of patients suffering from different liver conditions including chronic hepatitis B, liver cirrhosis and hepatocellular carcinoma.

Lambrecht et al. 2017[137] evaluated the levels of miRNA-122, -150, -192, -21, -200b, and -92a by qRT-PCR from human plasma samples as well as from primary mice HSCs. In both instances, EV isolation was performed by TEI.

Interestingly, in some cases comparisons between in vitro and ex vivo models were made. Duan et al. 2019[123] compared findings from primary rat hepatocytes and those from human plasma. A wider comparison was performed by Hirsova et al. 2016:[124] Huh7 cells and primary mice hepatocytes both served as in vitro models in addition to their research with ex vivo human samples. In their research with cholangiocytes, Li X. et al. 2018[290] looked at EVs isolated from primary mice cells in vitro, but took it a step further ex vivo, evaluating both murine and human sera-derived EVs. Their methods included differential centrifugation (with a UC step) for EV-isolation, DLS and TEM for size analysis and assessment of mRNA H19 levels. Cho et al. 2017[291] isolated EVs from a variety of samples as well: human cell lines (HepG2, He3B), rat primary hepatocytes, human sera, rat sera. Interestingly, while differential centrifugation worked in vitro, they noted how extra steps were required ex vivo to reduce contamination with plasma proteins (e.g., albumin). EV isolation from plasma samples was thus optimized by comparing three alternative methods: density gradient UC (30% Optiprep), ExoQuick, and an optimized ExoQuick protocol, which included 3 washing steps. Deregibus et al. 2016[159] were perhaps even more interesting from a methodological transferability perspective, since they compared the performance of a custom charge-based precipitation method to differential UC, using samples derived from human liver stem-like cells (HLSCs), human serum and human saliva.

As reviewed elsewhere,[292,293] there are significant challenges (small yields, co-purification of contaminants, etc.) in finding the most efficient protocols for the isolation and sufficient characterization of EVs. We have also made a contribution reporting on the many different strategies adopted for the isolation and characterization of liver-derived EVs specifically,[294] concluding that they are as varied as the research groups tackling the challenge. While presenting the main advantages and disadvantages for each approach, we highlighted some of the key aspects that emerged, which should be taken into consideration before delving into this research field.

First, the handling of fetal bovine serum (FBS). Cell culture approaches have become indispensable to simplify EV research before diving into significantly more complex ex vivo samples, but most cell lines require FBS for optimal growth. Depriving them of it might easily result in additional stress that will affect results to an unpredictable extent. Alternatives to FBS have already been proposed, such as chemically defined media, or human platelet lysate, and these may replace FBS-supplemented cell culture models.[295–298] Cells can be successively deprived of FBS to limit the impact of outright elimination of it, but more frequently than that, research groups opt to deplete their FBS of EVs by UC prior to use, or they directly use commercially available ExoFreeFBS. The experimental validation for either of these steps is rarely reported, but it would be an important addition given the questionable efficacy of some the most common methods.[299] Even under serum-replacement conditions, miRNA contaminants have reportedly been found.[300] Whenever serums starvation (i.e., culturing without serum) is feasible, it would be the preferred option.

An important second aspect is cell viability. Looking at the EVs collected in vitro, the cell number and viability at EV-harvest are seldom mentioned. Depending on the study, 90-99% vital cells is what was deemed appropriate when documented at all. As even a few dead cells can contribute to the presence of apoptotic bodies that can influence the EV-population, it is important to report the number of viable cells in each study.[62]

Third on our lists was the reporting of EV yield. EV yield directly impacts the characterization possibilities because it determines whether there is enough material to perform analyses such as cryo-TEM imaging. It also speaks to the efficiency of the isolation methods., revealing how well does a specific technique perform, especially when compared to alternatives. An absolute yield would also allow to evaluate upstream applicability, i.e., whether mass production would be a feasible option or not (e.g., for the use of liver-derived EVs as drug delivery systems). Because of all of these considerations, the importance of disclosing and being able to compare this data is easy to see. Yet when looking at the quantification of EV-recovery, we found the information either omitted/lacking or hard to extrapolate and ultimately to compare between studies. The particle number per million cells measure would be a convenient option to express the yield and to compare its efficiency across studies. Quantification by mass of EV-associated proteins would also be a viable alternative, if other co-isolated proteins can be excluded, preferably by number of cells as well.

A fourth aspect that emerged is the choice of an appropriate method for storing EVs. EV storage is a particularly relevant subject when EV isolation and characterization are not performed on the same day, which is often the case given how much time most of the described protocols require. Storage insights were not always provided, and their validation even less frequently. It has already been reported that storage modality can affect the EVs, which is why we think it is important to share this information.[301–303] Trehalose, mannitol and polyethylene glycol had been evaluated as possible cryoprotectants in the aforementioned studies, although not in the context of liver-derived EVs as of yet. With the exception of dimethyl sulfoxide,[149–158] the use of cryoprotectants for storage below -20 °C is rarely considered.

Fifth, we found that there were significant differences in the application of differential (ultra-) centrifugation (dUC) methods. This isolation technique has become the gold standard in EV research for the very good reason that it works. It is cited in well over half the articles referenced in this thesis. A recent study into salivary EVs offered a comparison of dUC with polymeric precipitation methods, showing how the former performs much better than the latter.[159] However, the vast literary landscape of protocols that include dUC are far from standardized. Even when analyzing EVs originating from the same cell types, different groups tend to have different approaches. Sometimes unexplained differences arise within the same group, which makes comparison all the more challenging. The number of centrifugation steps vary, and the relative centrifugal forces and centrifugal times applied at each step are rarely consistent. When there is sufficient purity validation and subsequent sample characterization, this methodological diversity might not be an insurmountable issue, but it is worth keeping it in mind when comparing results, and also when choosing which protocol to follow.

A final issue was the suboptimal method description and reporting in some cases. There is a general lack of rigorous standardization of methods in EV research, that was addressed with a position paper first published in 2014, then expanded upon in 2018 ("Minimal information for studies of extracellular vesicles", MISEV).[62] EV-TRACK is a platform aiming at method transparency.[304] Methods descriptions could be shared on EV-TRACK when the information would otherwise be left out of a publication. Implementing this would improve reproducibility and, more nuancedly, it would allow to compare method efficiencies across studies. Experimental validation of some practices is not always shared, which may be a problem when the methods used have been reported to have weaknesses, such as depletion of FBS-EVs, the success of which has been called into question.[299,300] The growing community working on EVs is becoming more aware of the need for standardization in this young field of research,[305] and the MISEV guidelines remain undoubtedly the reference text in these regards.[62]

This is particularly relevant in the context of method transferability and translational applicability. Working with EVs is inherently complicated even in single cell cultures, but many researchers have endeavored to escalate the challenge to co-cultures systems, to animal models (rodents), and to human patients. The comparisons have not always been complete, but the efforts put into positively tracing EVs and their associated biomolecules back to a specific cell type in increasingly more complex settings are a first important step to better understand and more easily diagnose liver diseases.

1.4. Aim of the thesis

We set out to characterize phenotypical changes of HSCs upon phospholipid-based treatment, and to determine biochemical variations in the EVs they consequently release. By correlating phenotypical changes within HSCs with the EVs they produce, we ultimately seek to lay the foundation for the development of a non-invasive diagnostic tool for liver diseases based on EV-analysis. The increasing prevalence of fibrosis, and the associated risks for asymptomatic patients, calls for novel and highly sensitive diagnostic methods.[2]

We have previously shown how PPC-based liposomes can effectively deactivate LX-2 cells human HSCs in vitro.[46] **Chapter 2** expands our LX-2 protocols to include EVs. We establish rigorous methodological practices for the isolation and characterization of EVs originating from LX-2 cells upon different control treatments, creating the necessary foundation for a deeper investigation into the biological role played by these EVs in our in vitro system.

Building upon the previous chapter, in **Chapter 3** we evaluate the direct effect exerted by EVs isolated from previously treated HSCs onto naïve cells. Insights into the biological activity thus displayed by these EVs is followed up with an investigation by extensive proteomic profiling. The collected data is mined to ultimately generate a cell status-discriminating panel of 44 proteins.

The final experimental chapter (**Chapter 4**) of the present work covers the development of additional antifibrotic lipid vesicles formulated with and without potentially new antifibrotic drugs (i.e., obeticholic acid

and elafibranor)[35,36] to validate their use in our LX-2 model for HSC activation. It additionally delves into the successful establishment of a convenient fluorescence nanoparticle tracking analysis (f-NTA) method for the non-destructive verification of the presence of exosomal markers CD81 and CD9, as well as for the detection of physiologically relevant proteins. Using our proteomic data, we rationally selected the secreted protein acidic and cysteine rich (SPARC) for the purpose, a decision supported by previous reports of its possible role in fibrogenic processes.[306–308]

Our optimized f-NTA method is finally used to quantitatively assess the performance of anti-fibrotic PPCs, while also providing novel insights into their mode of action. Here, for the first time, we can correlate the cellular response to PPC-treatment to the relative presence of SPARC on the generated EVs.

Chapter 2.
Development of Rigorous Methodological Practices for LX-2 Cells' Extracellular Vesicles

"*The cost of perfection is infinite.*"
CGP Grey's dad

Parts of this chapter are published:
Zivko, C., Fuhrmann G., Luciani, P., Liver-derived extracellular vesicles: A cell by cell overview to isolation and characterization practices. Biochimica et Biophysica Acta (BBA) - General Subjects (2020), 129559
Parts of this chapter are ready to be submitted for publication.

2.1. Introduction

The LX-1 and LX-2 human hepatic stellates cells (HSCs) are cell lines established to preserve the in vivo phenotype of human HSCs, and effectively allow research into relevant pathways of hepatic fibrosis.[309] LX-2 cells specifically have been selected to grow in serum starved conditions, i.e., without any FBS, thus obviating one of the most substantial obstacles in EV research, since serum contains contaminating EVs (see **Chapter 1**).[310] Even when working with EVs originating exclusively from a single cell line, the inherit complexity of EVs is an important hurdle in our understanding of them.[311] EVs comprise highly heterogenous populations of biological entities which require careful method development in terms of isolation and characterization strategies.

For the in vitro isolation of HSC-derived EVs specifically, the LX-2 human hepatic stellate cell line is a popular choice (**Table 1-1**). However, the validation of many published practices is not always shared. Isolation strategies included the use of the ExoQuick[131] precipitation kit, but without further purification steps afterwards, which would be recommended when opting for polymeric precipitation strategies.[62,312] Alternatively, differential centrifugation, including UC, was performed.[19,132,133] Cells were either serum starved for 48-72 h[19,132,133] or cultured with 10% (v/v) of commercially available Exo-free FBS (i.e., FBS depleted of EVs prior to sale).[131] In these particular cases, information about cell number and viability at the time of EV-collection and the total yield were missing, making it hard to judge the efficiency of their method. The specific isolation protocols were also found to be inconsistent, because of (over)reliance on referencing in method descriptions, with citations to publications such as Thery et al. 2006,[313] a broad overview of different protocols for the isolation of EVs. While the projects described in these articles were not focusing on the EVs isolated from HSCs, more descriptive protocols would better facilitate reproducibility.

As for the specifics of HSC-EVs characterization, Brandon-Warner et al. 2016[19] investigated total RNA, which was isolated using the SeraMiR™ exosome RNA purification kit, then quantified and analysed it to compare differences in the expression levels of individual miRNAs in cells and exosomes. Charrier et al. 2014 characterized their isolated EVs based on protocols from Thery et al. 2011 and Chen et al. 2014.[19,132,314] Working witch mice HSCs and LX-2, they performed western blots to check for the exosomal marker CD9, transmission electron microscopy to confirm morphology, size analysis by dynamic light scattering and zeta potential measurements. They also analysed exosomal and cellular RNAs for the presence of miR-21, one of the most commonly upregulated miRNAs in tumors,[315] which was determined by real time polymerase chain reaction (RT-PCR).

What emerged is that HSC-EVs have been analysed by a highly diverse array of means imperfectly reported. While research with HSC-derived EVs has been steadily gaining traction, a rigorous parallelization of isolation and characterization practices is missing. For our purposes of ultimately investigating the relationship between PPC-based antifibrotic treatments and their impact on EVs, we intend to lay a systematic foundation. Its detailed development is presented in this chapter.

2.2. Experimental Section

Experiments were performed with three biologically independent replicates unless stated otherwise.

2.2.1. Materials

The LX-2 immortalized human hepatic stellate cell line, Dulbecco's Modified Eagle Medium (DMEM) (4.5 g/L glucose, with or without phenol red, no glutamine, no sodium pyruvate), penicillin/streptomycin mixture (penicillin: 10'000 U/mL, streptomycin: 10'000 µg/mL), L-glutamine (200 mM), EmbryoMax® fetal bovine serum (FBS), Accutase®, and TGF-β1 (TGF) were purchased from MilliporeSigma (Burlington, United States). DMEM (4.5 g/L glucose, with phenol red, with sodium pyruvate, no glutamine) was also bought from Carl Roth (Karlsruhe, Germany). Dimethyl sulfoxide (DMSO), sterile syringe filters (polyethersulfone, PES, and cellulose acetate, CA, 200 nm) and sterile phosphate buffer saline (PBS, pH 7.4) were purchased from Carl Roth (Karlsruhe, Germany). Tissue culture plates and flasks were bought from Greiner Bio One International GmbH (Monroe, United States) or from Sarstedt (Nümbrecht, Germany). Sepharose CL-2B was from GE-Healthcare (Chicago, United States). Pierce™ BCA Protein Assay Kit, Gibco® PBS tablets and PageRuler™ Plus Prestained Protein Ladder (10 to 250 kDa), methanol (MeOH), chloroform ($CHCl_3$), isopropanol (IPA), acetic acid, glycerol and Pierce™ Silver Stain Kit were from Thermo Fisher Scientific (Waltham, United States). Acrylamide/Bis Solution, 37.5:1 (30% w/v), 2.6% C Tris-(hydroxymethyl)-aminomethane (TRIS), Tris-Glycine/SDS sample buffer (2x), Tris-Glycine/SDS Electrophoresis Buffer (10x), 2-Mercaptoethanol, Coomassie® Brilliant Blue G 250, Ammonium Persulfate (APS), N,N,N',N'-Tetramethyl-ethylenediamine (TEMED), sodium dodecyl sulfate (SDS) Solution (20% w/v) were all purchased from Serva Organics (Heidelberg, Germany).

2.2.2. Cell Culture

LX-2 cells (passage numbers 7-16) were grown in high glucose (4500 mg/L) DMEM supplemented with 200 mM L-Glutamine, 10'000 units/L of penicillin and streptomycin, and 2% (v/v) of sterile filtered (200 nm, CA membrane) FBS. For EV isolation, they were seeded in cell culture flasks of various sizes, with different cell densities, for variable amounts of times until reaching 80-90% confluency, at which point they would undergo treatments (**Table A2-1**). Cells were then washed with PBS and treated for 24 h with different solutions prepared in serum free cell culture media (DMEM): either ROL/PA (10/300 µM) or TGF (10 ng/mL).

2.2.3. EV isolation and purification

LX-2 cells were treated in serum free conditions for 24 h and the conditioned cell culture medium (CCM) from T175 flasks per treatment (2 x 25 mL, unless stated otherwise, see **Table A2-1**) was collected (CCMa, which includes treatment solutions). Cells were then washed with PBS and, regardless of previous treatment, they were all supplied with fresh serum free medium (DMEM). After 24 h, the CCM was collected again (CCMb) and cells were split to determine their number and viability. Alternatively, they were split and counted after CCMa harvest.

CCMs were centrifuged (300 x g, 5 min, 4 °C), the supernatant was moved into a new tube and centrifuged again (10'000 x g, 20 min, 4 °C). The pelleted cell debris was discarded and the supernatant was ultracentrifuged (100'000 x g, 90 min, 4 °C). A modified (new) differential ultracentrifugation (UC) method consisted of centrifuging the CCMs as follows: 300 x g for 3 min at 4 °C, after which the supernatant was moved into a new tube and centrifuged at 9'000 x g, for 30 min (4 °C); the pelleted cell debris was discarded and the supernatant was ultracentrifuged (120'000 x g, 2 h 30 min, 4 °C). Unless explicitly stated otherwise, the differential UC method used was the latter (newer) one. Moreover, PBS was always freshly filtered (CA, 200 nm) and degassed by sonication for 30 min prior to use. After discarding the supernatant, the EV-containing pellet was re-suspended in ~0.5 mL PBS and purified by size exclusion chromatography (SEC, Sepharose CL-2B), collecting 1 mL fractions. A schematic overview is offered in **Figure 2-1**.

The collected SEC fractions were analyzed for protein content by means of bicinchoninic acid (BCA) assay. Particle yield and size distribution profiles were determined by nanoparticle tracking analysis (NTA) either with NanoSight LM10 (software: NTA v3.2, Malvern, Malvern, United Kingdom) equipped with a 532 nm laser, or with a ZetaView (software version 8.05.05 SP2, ParticleMetrix, Inning am Ammersee, Germany) equipped with a 488 nm laser, zetapotential and temperature control units. Measurements were performed at 25 °C, a camera sensitivity of 80, and 100 1/ms shutter value. Particles were traced for at least 15 consecutive frames, videos were taken at 3 positions for 30-60 s with the Nanosight, and at 11 positions with the ZetaView. Samples had to have ≥ 200 traced particles, ideally 1'000. Zeta potential was measured with Zetasizer Nano ZS (Malvern, Malvern, United Kingdom) or with the ZetaView.

Results from the single SEC fractions were consolidated to obtain an average yield and an average particle size, as well as a combined size distribution profile for EVs originating from the differently treated LX-2. Unless otherwise stated, the presented results refer to EVs isolated from CCMb. Side by side comparisons with CCMa-EVs at many different stages are provided in the Appendix (**Chapter 2 supplementary information**). Every sample was freshly purified and analyzed on the day it was collected, except for those used for electron microscopy imaging, which had been previously stored at -80 °C, and those undergoing storage validation testing (see **Chapter 2.2.5**).

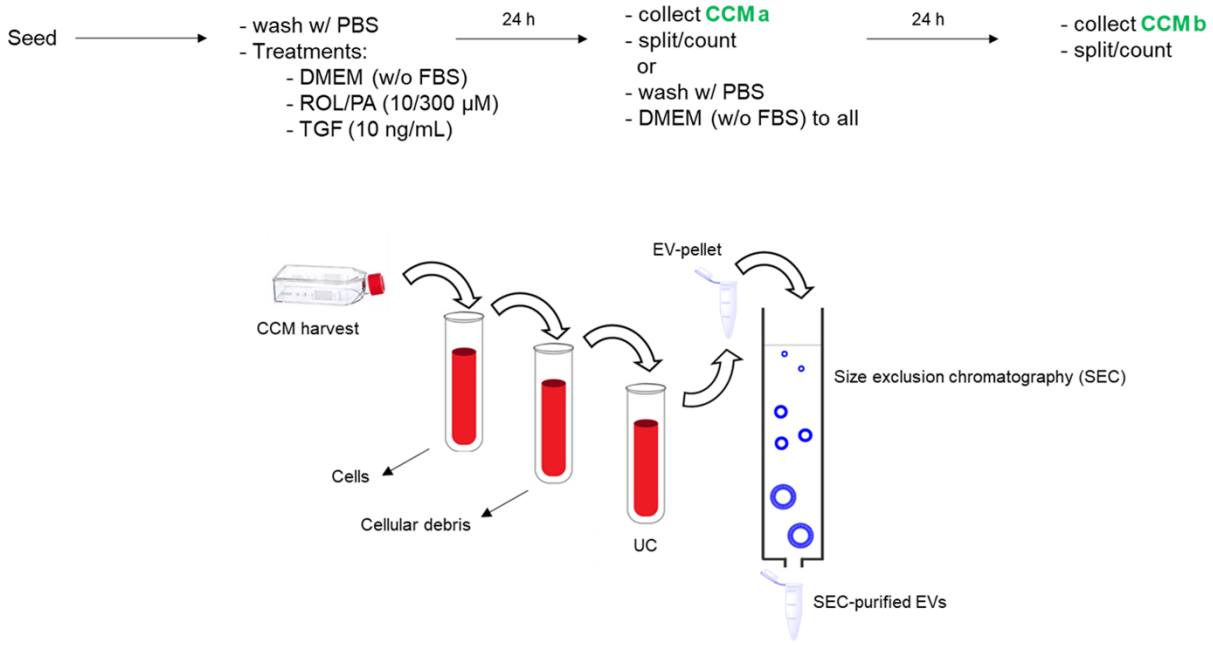

Figure 2-1: Schematic overview of the EV isolation and purification protocols.

2.2.4. Electron micrscopy

For scanning electron microscopy (SEM), 10 µL re-suspended EV samples were left to dry overnight on silica wafers; they were then sputter-coated with a thin layer of gold for imaging under high vacuum with an accelerating voltage of 5 kV using a Zeiss EVO (Zeiss EVO MA15 LaB6, Oberkochen, Germany) instrument. SEM was performed with the help of Dr. Chiara De Rossi (Helmholtz Institute for Pharmaceutical Research, Saarbrücken).

For cryogenic transmission electron microscopy (cryo-TEM), samples were prepared as previously described.[316] Briefly, 5 µL of EV sample were transferred to a copper grid covered by holey carbon film (R1/2, 300 mesh, Quantifoil Micro Tools, Großlöbichau, Germany) and excess liquid was blotted between two strips of filter paper. Samples were plunged into liquid ethane (180 °C) in a cryobox and they were rapidly moved with a Gatan 626 cryo-transfer holder into the pre-cooled cryo-electron microscope (Philips CM 120, Munich, Germany) operated at 120 kV. The Images were acquired with a 2k CMOS Camera. Cryo-TEM imaging was performed by Dr. Jana Tamm (Friedrich Schiller University, Jena).

2.2.5. EV storage

EV storage was tested for the short and mid-term. For the former, EV-containing pellets were be purified by SEC directly on the day of EV-collection or only upon 24 h storage at -80 °C. SEC fractions were then analyzed right after SEC or after 24 h storage at 4 °C. For mid-term storage, SEC-purified EVs were

stored under different conditions: -80 °C, -25 °C, 4 °C, 37 ° and at room temperature after being freeze-dried with 1% trehalose (w/v).[302] At different time points and for up to 21 d, yield and size were measured.

2.2.6. EV proteins separation by electrophoresis

Samples of EV-containing pellets or purified EVs were supplemented with sample buffer (finally diluted to 1:5, see **Table A2-3** for the exact composition), added 1/20 (v/v) 2-mercaptoethanol and denatured at 95 °C for 5 min. SDS-polyacrylamide gel electrophoresis (PAGE) was performed on polyacrylamide gels (0.75 or 1 mm thick). The gels were freshly cast or kept 1-3 days at 4 °C before use. The stacking gel was 4% acrylamide, the resolving gel 12%; alternatively, the stacking gel was omitted and the samples were run on 12% or 7% resolving gels alone. The electrophoretic separation was performed using a Mini-PROTEAN® (BioRad, Hercules, United States) or an ominiPAGE® system (Cleaver Scientific, Rugby, United Kingdom). A prestained protein ladder (10 to 250 kDA) was used to estimate protein size.[317]

Gel staining with Coomassie blue was performed as previously reported.[318] Briefly, gels were fixed with 25% IPA and 10% acetic acid solution in milliQ-H_2O (by volume) at RT for 10-15 min. The fixing solution was then removed and the gels were covered with rapid Coomassie blue staining solution (0.006% w/v Coomassie brilliant blue G-250 in a 10% v/v solution of acetic acid in milliQ-H_2O) for 2 h. The gels were subsequently destained with 10% acetic acid (v/v) in milliQ-H_2O for at least 2 h, until the background was clear.

Alternatively, gels were stained using the Pierce silver staining kit according to manufacturer's instructions. Briefly, gels were washed twice with milliQ-H_2O for 5 min and then twice with fixing solution (30% EtOH and 10% acetic acid in milliQ-H_2O, by volume) for 15 min. After fixation, gels were washed twice with 10% EtOH in milliQ-H_2O (v/v) (5 min), then twice in milliQ-H_2O (5 min). Gels were subsequently sensitized with the provided Sensitizer Solution (freshly diluted 1:500 with milliQ-H_2O) for 1 min, and washed twice for 1 min with milliQ-H_2O. They were then stained for 30 min with the provided Stain Solution after the kit's Enhancer solutions has been freshly added to it (Enhancer:Stain final ratio 1:50). Gels were washed two times for 20 s with milliQ-H_2O. They were then developed with Developer Solution (supplied with the kit) which was freshly enhanced (Enhancer:Developer final ratio 1:50). After 2-3 minutes, protein bands appeared and the gels were rapidly transferred to a 5% (v/v) acetic acid in milliQ-H_2O stopping solution for 10 min.

Gels could be stored in 7% acetic acid (v/v, in milliQ-H_2O) at 4 °C if needed.

2.2.7. EV lipids extraction and detection

Bligh and Dyer extraction of lipids was performed as previously described.[319] Briefly, EV-containing pellets in PBS were transferred into glass centrifugation tubes. Ice-cold $CHCl_3$:MeOH solution (1:2 ratio) was added and mixed (1:2:0.8 final ratio of $CHCL_3$:MeOH:PBS) and left to incubate for 5 min. More PBS

and $CHCl_3$ were added ($CHCl_3$:MeOH:PBS final ratio was 1:1:0.9). The mixture was centrifuged (1000 x g, 2 min, RT). The resulting lipid-containing lower phase ($CHCl_3$:MeOH:PBS in a ratio of 86:14:1, by volume) was carefully recovered with a Pasteur pipette, avoiding the contaminant material from the upper phase and the denatured proteins at the interface. After adding 1 mL $CHCl_3$ to the recovered lipid phase, the centrifugation and lipid-containing lower phase retrieval steps were repeated. Finally, the samples were concentrated under N_2, the lipid pellets were resuspended in MeOH.

Lipid analysis of EVs was performed using an Ultimate 3000 HPLC system (Thermo Fisher Scientific, Reinach, Switzerland), equipped with a charged aerosol detector (CAD, Corona Veo RS). The column was a MN Nucleosil (C18, 3.0 x 125 mm, 5 µm, Macherey Nagel, Düren, Germany), used at 30 °C, and ran with a recently published method.[320] Briefly, the mobile phase consisted of ACN with 0.2% (v/v) TFA (solvent A), MeOH with 0.2% (v/v) TFA (solvent B) and ultrapure H_2O with 0.2% (v/v) TFA (solvent C). The method started with a linear gradient of the mobile phase, from a ratio of 35:50:15 of solvents A:B:C, and it changed to 5:95 of solvents A:B by 20 min. It was kept isocratic for 1.5 min, and brought back to the initial A:B:C ratio of 35:50:15 by 23 min, and left constant for 3 min for equilibration. The analysis was done with Chromeleon 7.2 software.

2.3. Results and Discussion

2.3.1. EV isolation

To optimize EV-yield different approaches were tested. First, the amount of isolated EVs increased steadily with the number of cells from which they were harvested (**Figure 2-2a**), while no observable change in average size (**Figure 2-2b**) nor size distribution profiles (**Figure 2-3**) followed. At the same time, testing for short-term stability, there was also no change to detect (**Figure 2-2** and **Figure 2-3**).

The second step in yield improvement was checking different harvesting time points (**Figure 2-4**). While EV-recovery increased up to 24 h, waiting 72 h did not triple EV yield. It did however lead to a decrease of cell viability below 90%. Taking into consideration that we did not want to create an artificial increase in the relative presence of apoptotic bodies in our EV-samples, we decided to keep 24 h as the CCM harvesting time point.

Third, we adapted our differential centrifugation and UC protocol: the new methods doubled our EV-yield recovery starting from the same number of cells generating them (**Figure 2-4b**). Combining the information thus far, our best EV-yield was obtained with the new UC protocol, and starting from the highest tested cell count, which is obtained using 5-layers tissue culture flasks. These flasks give the highest ratio of cells/volume, but based on their dimensions they would limit throughput and parallelization considerably. Anticipating the different conditions from which we ultimately want to isolate EVs, we compromised and unless stated otherwise, our reported results come from isolating and combining the EVs from 2x T175 flasks.

The efficiency of our UC step was evaluated for EVs originating from differently treated LX-2 cells and proved to be consistently above 70-80% (**Figure 2-4c**).

Having optimized yields of EVs, we were finally able to find them under EM (**Figure 2-5**), confirming their spherical morphology by SEM and cryo-TEM. Moreover, the imaged EVs were found to be in the size range we were measuring them by NTA.

A summary of the average cell count and viability at the time of EV harvest is provided in **Table 2-1**, along with mean EV-yield, size and zetapotential values.

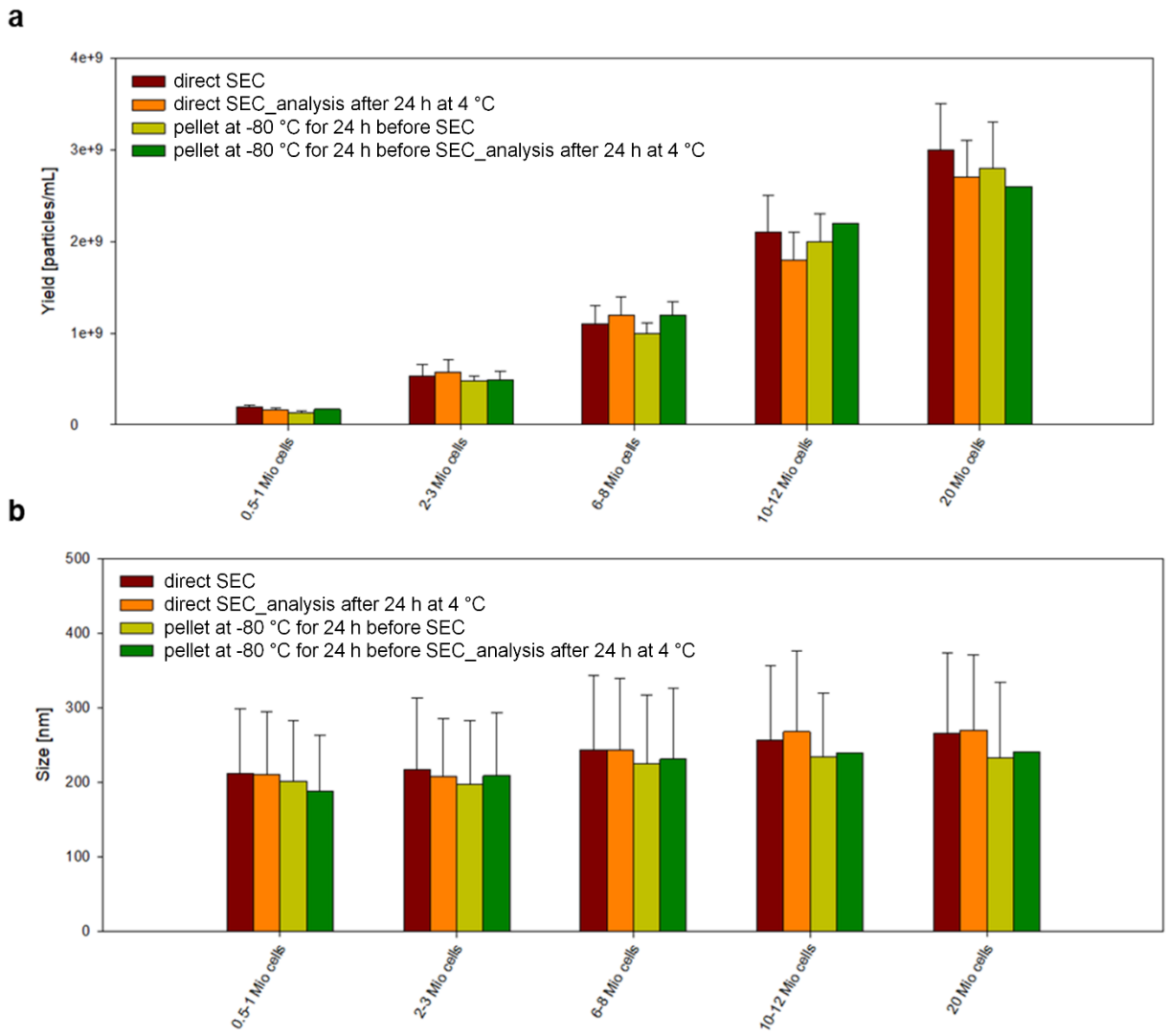

Figure 2-2: Average yields (**a**) and sizes (**b**) for EVs purified and analyzed at different times, after the short-term storage of EV-containing pellets and/or SEC-purified EVs (mean ± SD, n = 1-3, software: NTA v3.2).

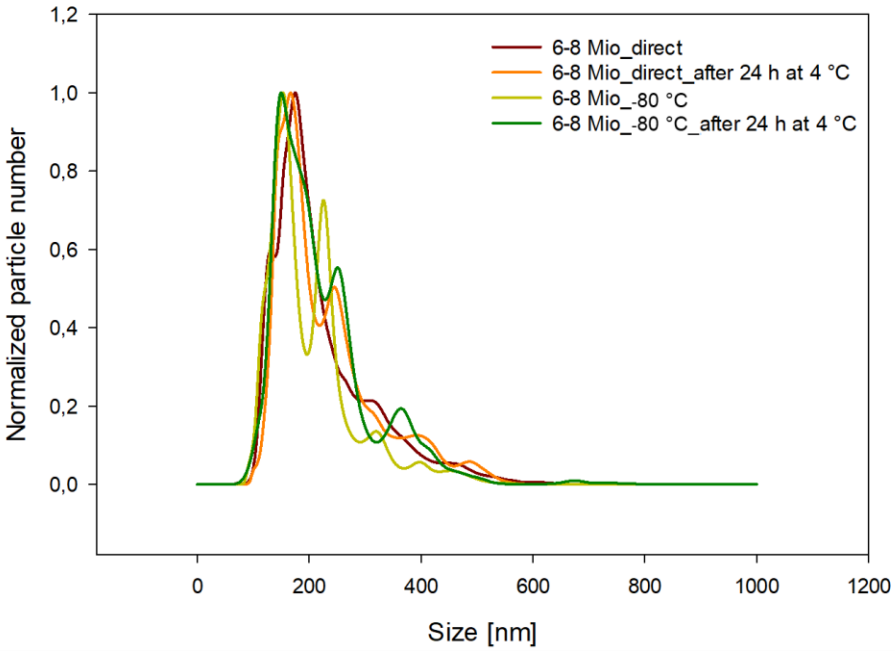

Figure 2-3: Representative size distribution profiles for EVs purified and analyzed at different times, after the short-term storage of EV-containing pellets and/or SEC-purified EVs (software: NTA v3.2).

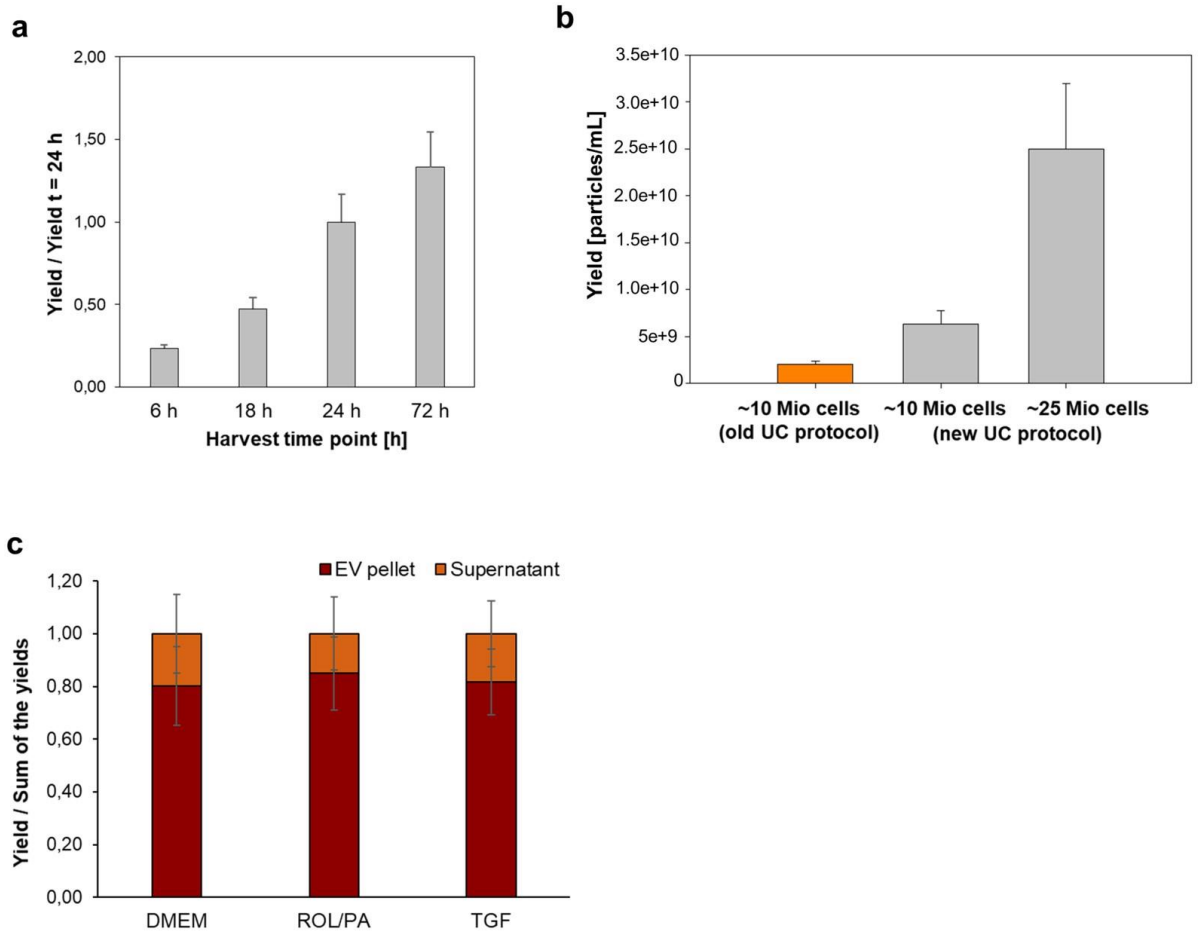

Figure 2-4: EV yield at different harvesting time points (**a**), and upon changing the UC protocol (**b**). Comparison between the pelleted particles' yield and the particles' yield in the supernatant after UC (**c**) (mean ± SD, n = 2-3, software: NTA v3.2).

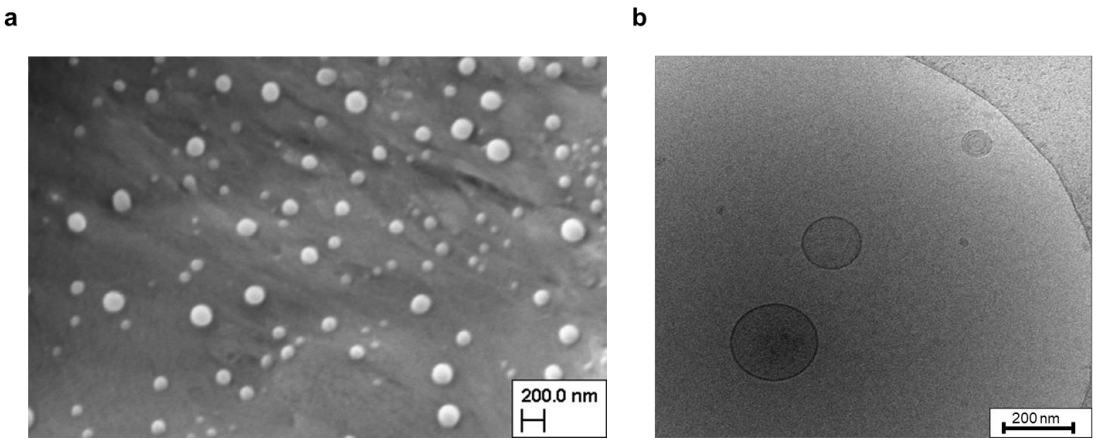

Figure 2-5: SEM (**a**) and cryo-TEM (**b**) images of EVs isolated from untreated cells.

Table 2-1: Average yield, size and zeta potential values of the EVs isolated from differently treated cells. Cell count and viability at the time of CCM harvest is shown as well (mean ± SD, n = 3, software: ZetaView 8.05.05 SP2).

	Cell count (cell viability%)	**EV yield [particle number]**	**EV Size [nm]**	**EV Zeta Potential [mV]**
DMEM	$10.9 \pm 1.1 \times 10^6$ (97.2 ± 3.1)	$8.43 \pm 2.4 \times 10^9$	178 ± 87	-39.9 ± 2.2
ROL/PA	$9.3 \pm 1.2 \times 10^6$ (96.5 ± 2.5)	$9.91 \pm 3.9 \times 10^9$	185 ± 93	-34.1 ± 2.5
TGF	$11.7 \pm 1.4 \times 10^6$ (96.2 ± 3.1)	$9.07 \pm 3.5 \times 10^9$	182 ± 93	-36.6 ± 2.7

2.3.2. EV mid-term storage

Storage at -80 °C proved to be the best option as seen in the graphs showing the EV-yield over time (**Figure 2-6**), with at least 60% of the yield being consistently preserved even after 21 days. Looking at the full size distribution profiles from day 1, 8 and 21 gives additional insights. The lyophilized sample more prominently displays a new peak around 100 nm compared to other storing conditions. It is also the only condition resulting in new peaks (possibly aggregates) in the micrometer range (**Figure 2-7**). Storage at -80 °C and 4 °C performed better in preserving the original size profile (the one from 0 d). Additional results for the mid-term storage stability of EVs that are not displayed here can be found in **Figure A2-1** and **Figure A2-2**.

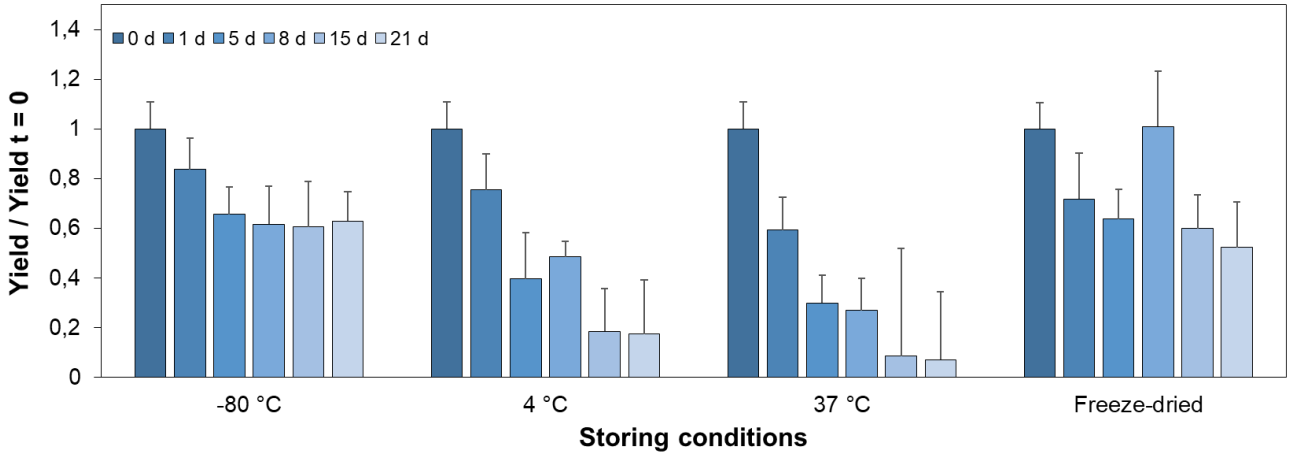

Figure 2-6: EV yield upon mid-term storage under different conditions for up to 21 d (mean ± SD, n = 3-5, software: NTA v3.2).

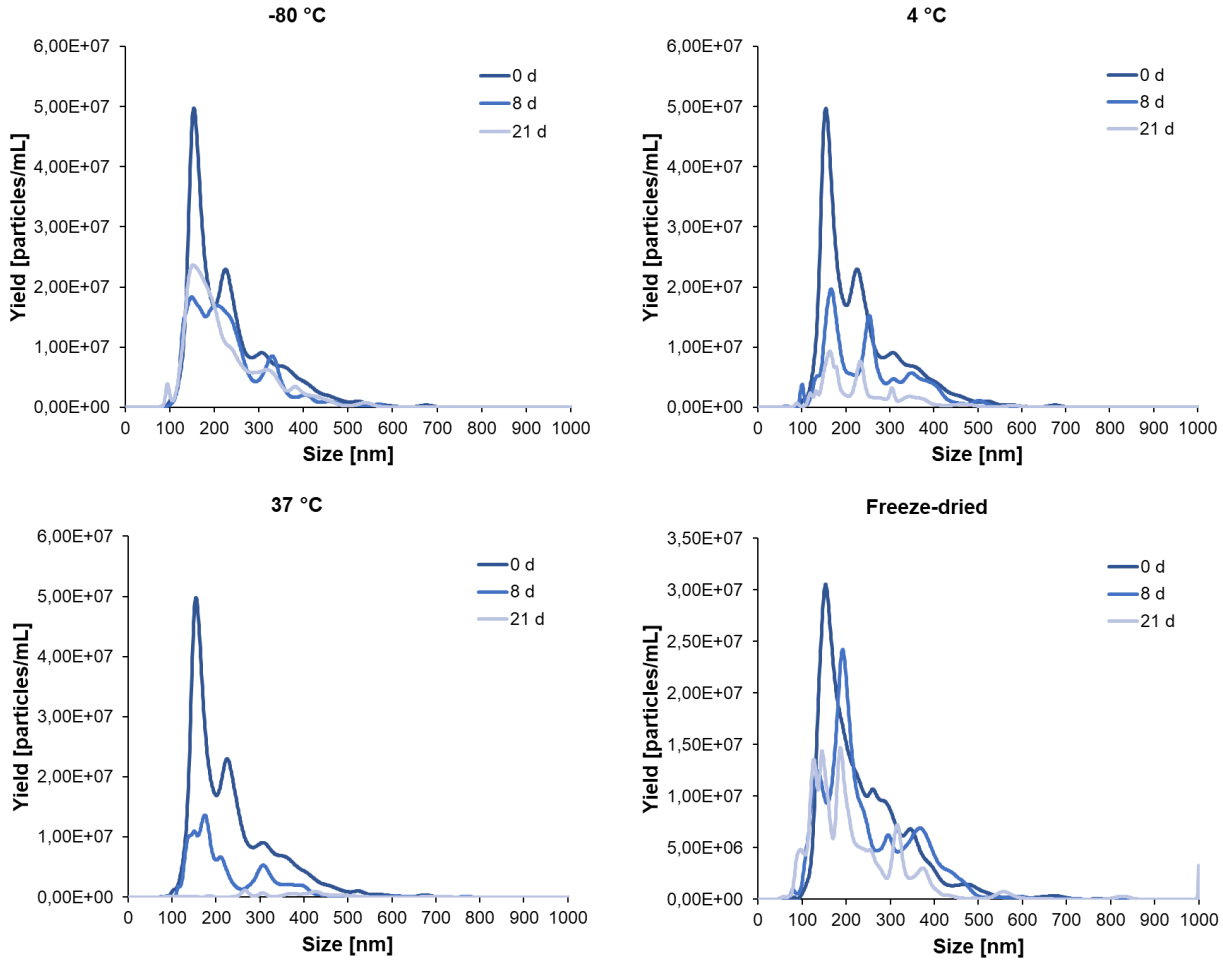

Figure 2-7: EV size distribution profile during mid-term storage under different conditions (combined from n = 3-5, software: NTA v3.2).

2.3.3. EV purification

SEC purification showed a clear resolution between EV-containing fractions and protein aggregates that might have been co-purified during UC, as determined by BCA assay (**Figure 2-8**). Protein content associated with EVs was only detectable in the SEC-fractions with the highest EV-yields, and it was at the lower detection limit of the assay (2-5 µg/mL). These findings were consistent throughout, regardless of the treatment undergone by cells prior to EV-harvest. The consolidated size distribution profiles of the isolated EVs consistently showed overlapping and polydisperse populations (**Figure 2-9d**), regardless of cell treatment. Quantile subtraction of the distribution curve obtained from untreated cells showed that quiescent-like LX-2 produce larger EVs (> 100 nm) more prominently than TGF-treated cells (**Figure 2-9e**).

When purified with a longer SEC-column (40 mL as opposed to 25 mL), EVs could be found in fractions eluting from 14 to 21 mL, with a decreasing size average owing mostly to the steady decrease of the peak size within the single SEC-fractions (**Figure 2-10**). However, the EV populations found in all fractions still overlap, and distinct subpopulations could not be retrieved based on SEC. Since they result in less sample dilution, shorter SEC columns are preferred for EV-purification in our protocols, as long as a sufficient resolution with co-purified contaminants can be ensured.

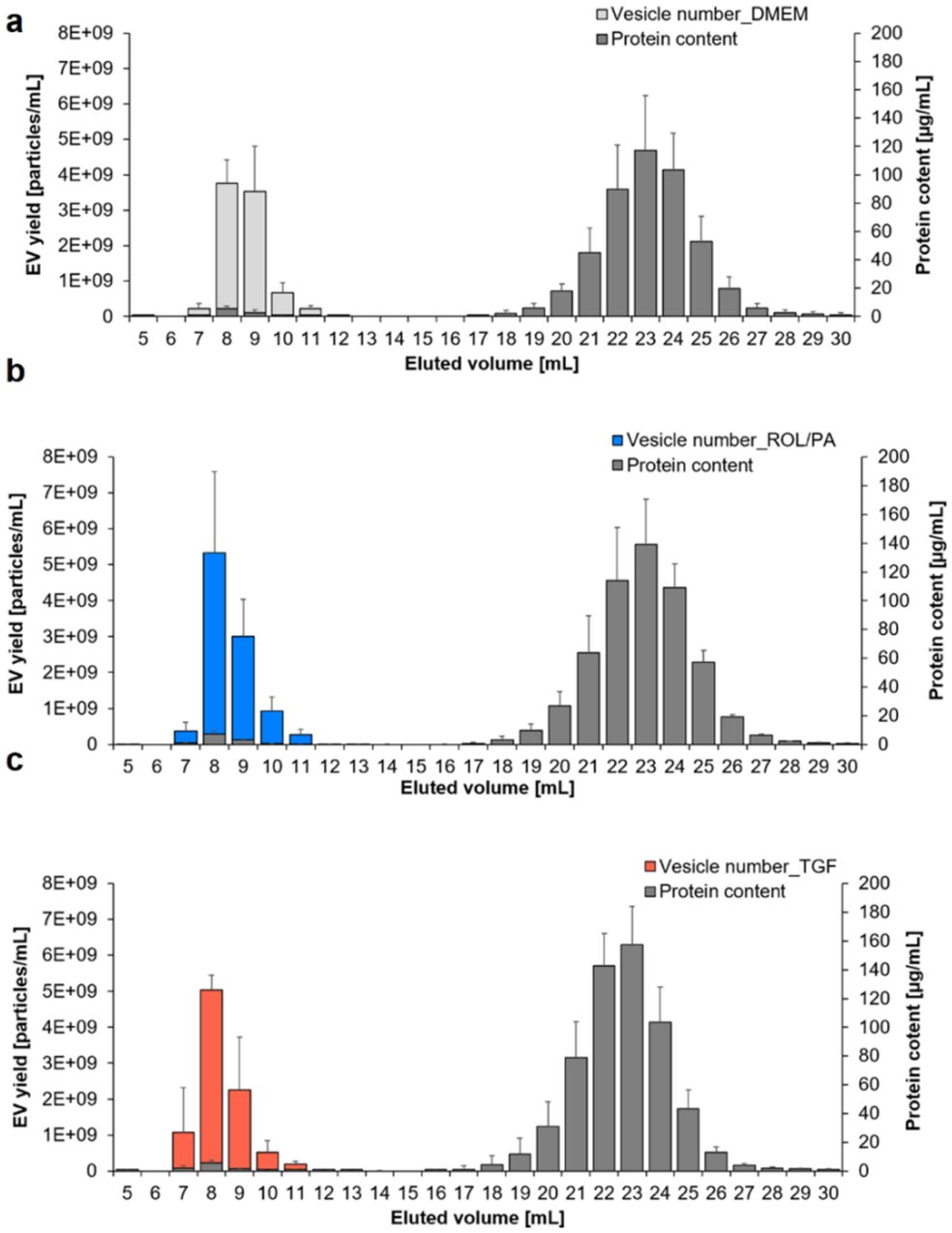

Figure 2-8: Protein content and vesicle number in the collected SEC fractions obtained during the purification of EVs from untreated (**a**), quiescent-like (**b**) and perpetuated (**c**) LX-2 cells (mean ± SD, n = 3, software: ZetaView 8.05.05 SP2).

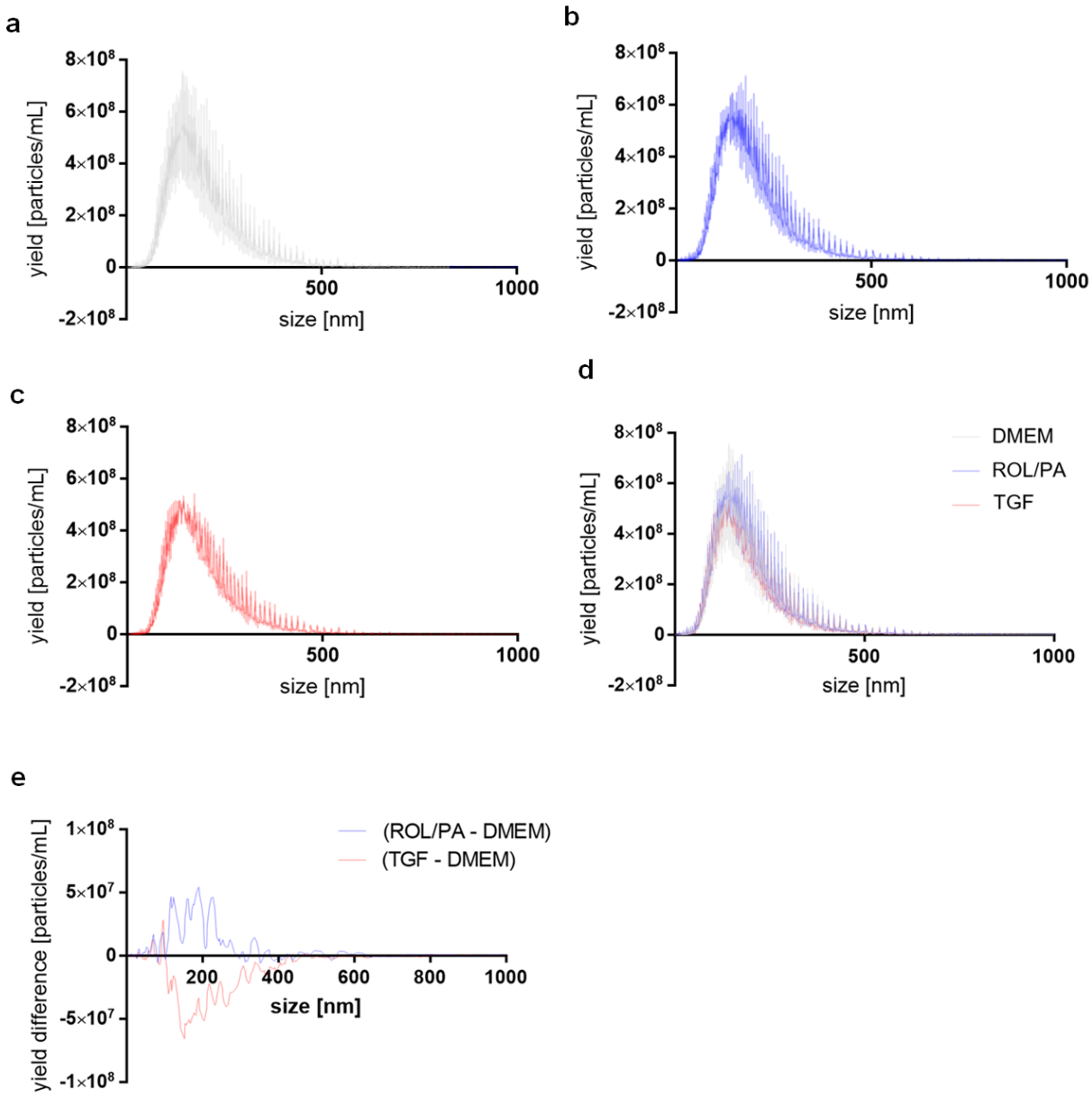

Figure 2-9: Size distribution profiles of EVs isolated from DMEM (**a**), ROL/PA (**b**) and TGF (**c**) treated cells seen separately and combined (**d**) (mean ± SD, n = 3, software: ZetaView 8.05.05 SP2) and quantile subtraction of the yields (**e**).

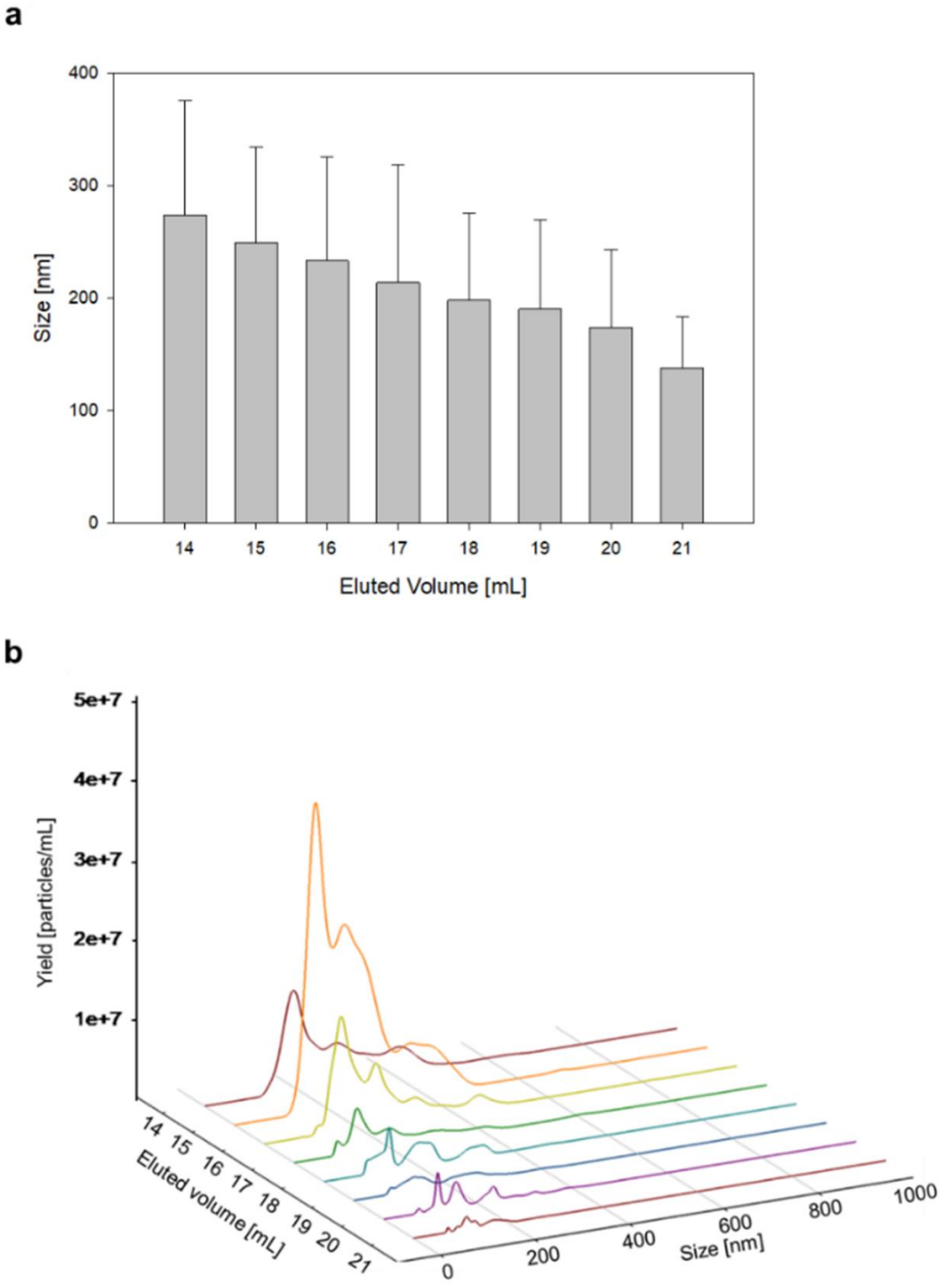

Figure 2-10: Average size (**a**) and representative full distribution profiles of EVs found in different SEC fractions (**b**) (software: NTA v3.2). Size distribution profiles within the single SEC-fractions, each normalized to its own peak size, are shown in .

2.3.4. EV proteins separation by SDS-PAGE

Complex EV-associated protein profiles could be detected by SDS-PAGE upon silver staining (**Figure 2-11**). There are many distinct proteins in each sample type but they overlap considerably across treatment groups. Qualitative observations were made possible by careful optimization of the protocols, which is detailed in the supporting information (starting from **Figure A2-8**). Around 70 kDa (highlighted in **Figure 2-11a**), it looks like DMEM and TGF have a more prominent band compared to samples originating from ROL/PA-treated cells, while ROL/PA also has the band right below it being more intensely stained than the corresponding bands in TGF and DMEM samples. For lower molecular weights there was no real staining, so we tried a different acrylamide% for the gels with the goal of focusing on and resolving bigger molecular weight proteins better (**Figure 2-11b**). What emerged in this setting, was a band around 130 kDa present in TGF-EVs but not in ROL/PA and DMEM. The subtlety in the sparse differences that could be found across rich and complex protein profiles shows the limits of what can be accomplished with SDS-PAGE analysis of EV samples. Shotgun proteomics, combining high performance liquid chromatography and mass spectroscopy (LC/MS), would be the ideal next step in the analysis EV-proteins.

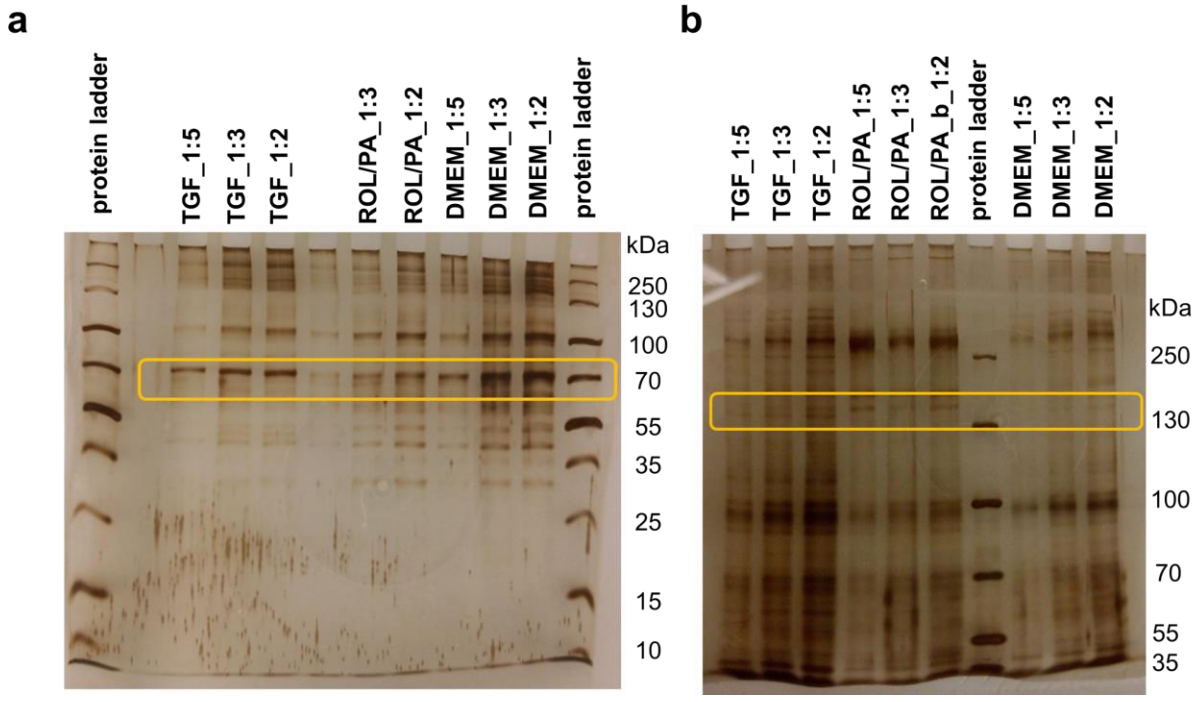

Figure 2-11: Representative silver stained SDS-gels with 12% (**a**) or 7% Acrylamide (**b**), separating EV-associated proteins from DMEM, ROL/PA and TGF treated cells. Samples are different dilutions of EV-containing pellets.

.

2.3.5. EV lipids extraction and detection

We explored the potential application of a CAD detector for profiling EVs based on their lipids following the development of a powerful method for phospholipid analysis in our research group.[320] EV-lipids could be extracted from EVs, but the protocol needs optimization before the lipid profiles from EVs originating from differently treated LX-2 can be effectively compared to each other (**Figure 2-12**). The peaks emerging in the chromatograms are very few and below limits of detection and quantification. However, the peak with a retention time of 13 min is accurately shared across all three control samples, and the peak eluting after 7.5 min is precisely shared between DMEM and ROL/PA-EV samples. While not probative, these findings are persuasive enough to suggest that, with a decidedly higher mass of EV-lipids, a profiling based on this method would indeed be possible. With the lipid material that we are able to obtain at present, mass spectrometry would be the only viable analytical method, and it will be tackled in the future.

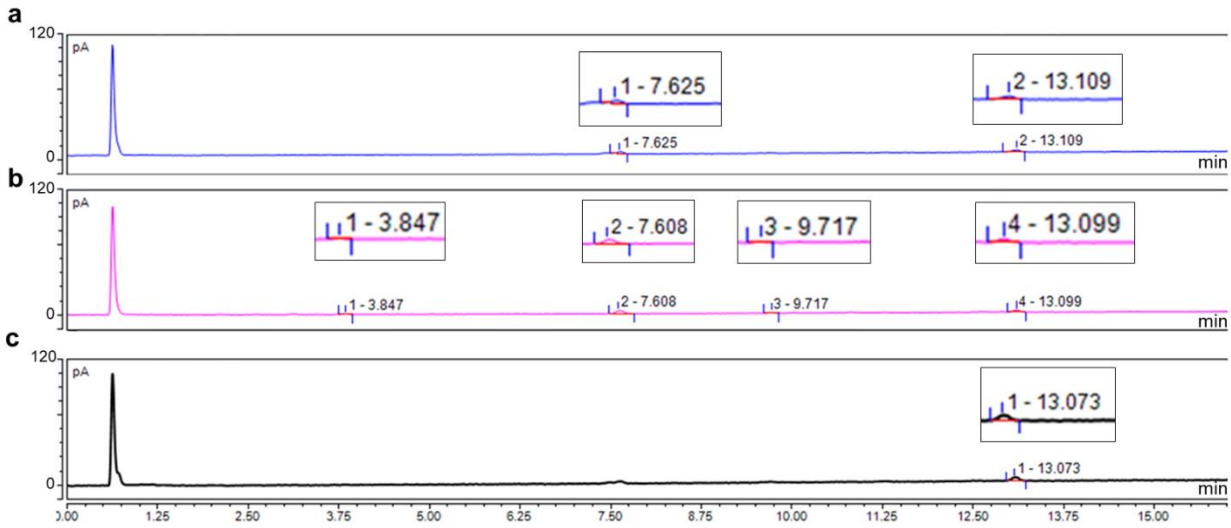

Figure 2-12: Representative HPLC chromatograms for lipids extracted from DMEM (**a**), ROL/PA (**b**) and TGF (**c**) treated cells. Zoomed insert show the peaks detected by software analysis (Chromeleon 7.2).

2.4. Conclusions

We reported on highly reproducible isolation and purification methods for EVs released by LX-2 HSCs. The systematic improvement of EV-recovery followed by careful purification has enabled us to consistently look into EVs produced by LX-2 cells upon different control treatments: DMEM (untreated), ROL/PA (positive control, for a quiescent-like status) and TGF (negative control for perpetuated LX-2). We thus effectively expanded our previously optimized in vitro model[46] to include the analysis of EVs generated by LX-2 cells upon different treatments.

The heterogeneity of EV samples has hindered the research into distinctive subpopulations due to their overlapping sizes, densities, zeta potential values and biochemical compositions.[321,322] We were nonetheless able to observe subtle size shifts within these polydisperse samples of EVs originating from differently treated cells by NTA. Lipids were hard to extract and detect from our EV samples. At present, we are unable to say whether or not sufficient differences in the profile of EV-lipids could emerge from more sensitive techniques, such as MS. Further analyses and substantial optimization are required. However, we successfully laid the foundation for deeper investigations into EV-proteins. SDS-PAGE methods were optimized to eventually show rich protein profiles. While considerably overlapping across treatment groups, subtle differences did nonetheless emerge. With LC/MS-based methods, we believe that, in spite of all similarities, a proteomic-based discrimination between EVs from differently treated LX-2 cells is not only possible, but also well worth exploring (see **Chapter 3**).

Chapter 3.
Biological Effect of LX-2 cells' Extracellular Vesicles and Insights thereinto from Proteomic Data Mining

"Your reward will be the widening of the horizon as you climb."
Cecilia Payne-Gaposchkin

Parts of this chapter are ready to be submitted for publication.

3.1. Introduction

EVs' multifaceted roles in inter- and intracellular communication is one of the reasons for the prolific research devoted to turning them into novel therapeutic delivery systems.[323–326] Engineering efforts toward effective EV loading with different types of drugs,[327–329] surface modifications to improve biodistribution properties,[66,330–333] to increase target specificity[334,335] or to overcome biological barriers are all being explored.[329,336] However, scientific attention has also been paid to EVs' intrinsic potential to cause physiologically favorable outcomes.[337] In the context of liver fibrosis specifically, serum EVs isolated from healthy volunteers have been tested on HSCs and hepatocytes, and were shown to attenuate fibrogenesis and inflammatory response as observed by collagen and interleukins expression levels.[97,338–340]

Having established our own methods for the sufficient isolation of EVs from differently treated HSCs (see **Chapter 2**), we decided to test them on naïve LX-2, with the aim of studying the biological effect that EVs can exert in our in vitro model.

We have previously used LX-2 cells to study the performance of different PPC-based formulations with highly purified soybean extracts.[46] Among those, S80, SMg (S80 complexed with $MgCl_2$) and SCa (S80 complexed with $CaCl_2$) stood out in their ability to deactivate perpetuated LX-2, which had been exposed to pro-fibrotic tissue growth factor β1 (TGF). The abundant presence of cytoplasmic lipid droplets, combined with the absence of collagen and α-SMA upon treatments with S80, SMg, or SCa suggested a reversion of HSCs transdifferentiation that was qualitatively similar to positive control treatments with a mixture of retinol (ROL) and palmitic acid (PA),[341,342] but measurably superior to it in terms of lipid droplets formation especially. When co-formulated with the hepatoprotectant silymarin,[343] S80 liposomes displayed an enhanced, synergistic effect in LX-2 deactivation, which was absent in negative controls using the pure phospholipid 1,2-dioleoyl-*sn*-glycero-3-phosphocholine (DOPC).

We have also established that EVs from differently treated LX-2 have extremely rich protein profiles with subtle differences among different controls (**Chapter 2**). We hypothesized that a detailed proteomic profiling will reveal sufficient discriminatory information between treatment groups, possibly shedding some light into the direct impact of PPC-therapeutics on the nature of the resulting EVs.

3.2. Experimental Section

Experiments were performed with three biologically independent replicates unless stated otherwise.

3.2.1. Materials

In addition to the materials listed in **Chapter 2**, soybean phospholipids with ≥75% PC (S80) as well as 1,2-dioleoyl-*sn*-glycero-3-phosphocholine (DOPC) were generously provided by Lipoid GmbH (Ludwigshafen, Germany). Polycarbonate membranes (200 nm) for liposome extrusion were bought from Whatman® Nucleopore™ (Maidstone, United Kingdom). Roti®-Histofix 4% (acid free, pH 7.4% w/v phosphate-buffered formaldehyde solution), formaldehyde (37% w/v in H_2O), chloroform ($CHCl_3$), ethanol (EtOH), trifluoroacetic acid (TFA), methanol (MeOH), acetonitrile (ACN), acetic acid, and (4-(2-hydroxyethyl)-1-piperazineethanesulfonic acid) (HEPES buffer), phosphate buffer saline (PBS, pH 7.4), sterile syringe filters (polyethersulfone, PES, and cellulose acetate, CA, 200 nm) and dimethyl sulfoxide (DMSO) were purchased from Carl Roth (Karlsruhe, Germany). Some organic solvents (ACN, MeOH) were also from Thermo Fisher Scientific (Waltham, United States). Sepharose CL-2B was bought from GE-Healthcare (Chicago, United States). Gibco™ PBS tablets, polyvinylidene difluoride (PVDF) transfer membranes (0.2 µm), sodium dodecyl sulphate (SDS) and dithiothreitol (DTT) were from Thermo Fisher Scientific (Waltham, United States).

3.2.2. Formulation of PPC-based liposomes

Liposomal formulations with S80 or DOPC were prepared by thin the film hydration method as previously described.[46] Briefly, S80 or DOPC were dissolved with $CHCl_3$, the organic solvent was removed with a nitrogen stream, and left under vacuum overnight. The resulting lipid film was hydrated with 10 mM HEPES buffer pH 7.4. The liposomes were then extruded 10 times through a 200 nm polycarbonate membrane at room temperature with a Lipex® extruder (Evonik, Essen, Germany). For liposomal formulations loaded with Ela or OA, the appropriate amount of drug was added to the lipid film. Lipids (final concentration 50 mM) and drugs (up to 150 µM) concentrations were quantified chromatographically as previously reported.[46,320] Briefly, samples were diluted with MeoH 1:49 (v/v) to destroy lipid vesicles prior to injection in an Ultimate 3000 HPLC system (Thermo Fisher Scientific, Reinach, Switzerland), equipped with a charged aerosol detector (CAD, Corona Veo RS). The column was a MN Nucleosil (C18, 3.0 x 125 mm, 5 µm, Macherey Nagel, Düren, Germany), used at 30 °C. Samples were run with a flow rate of 0.5 mL/min. For the mobile phase, solvent A was ACN:H_2O 90:10 (v/v) with 0.05% TFA (v/v), and solvent B was MeOH with 0.05% TFA (v/v). The method was isocratic (Solvent A:Solvent B, 60:40) for 25 min, followed by a linear gradient of solvent B over 15 min (from 40 to 100%). The analysis was done with Chromeleon 7.2

software. The hydrodynamic diameter and the size distribution (polydispersity index, PDI) of the liposomes were measured with a Litesizer 500 (Anton Paar).

3.2.3. Analysis of lipid droplet content

Cells were cultured as previously described (**Chapter 2**). For experiments, 0.5 x 10^5 cells/well were seeded in 12-well microtiter plates and cultured for 24 h. Cells were then washed with PBS and treated for 24 h with different solutions prepared in serum free cell culture media (DMEM): either ROL/PA (10/300 µM), TGF (10 ng/mL), liposomal formulations (5 mM final lipid concentration) of S80 or DOPC, HEPES buffer (10% v/v in DMEM). Final treatment solutions in DMEM were filtered (CA, 200 nm) before use (see **Figure A3-1**).

After cell treatment, LX-2 in 12-well plates were washed with PBS, fixed with Roti-Histofix and stained with a 0.5% (w/v) ORO solution in propylene glycol. Nuclei were counterstained with DAPI. Fluorescence and phase contrast images acquisition was performed using a Nikon Ti-U inverted microscope. The quantification of the ORO-stained, fluorescent binary area was normalized to the cell count as determined by DAPI-stained nuclei within the image after thresholding (**Figure A3-2** and **Figure A3-3**). For every condition, a total of at least 27 images were acquired: 3 images/well, from 3 separate wells, repeated with 3 biologically independent replicates (performed on separate days from different cellular splits).

3.2.4. Treatment of naïve LX-2 with EVs from differently treated LX-2

EVs were collected as previously optimized (see **Chapter 2**). Briefly, EVs were harvested 24 h after cells had undergone DMEM, ROL/PA (10/300 µM), TGF (10 ng/mL), HEPES (10% v/v), S80 (5 mM) and DOPC (5mM) treatments (CCMa-EVs). Cells were then washed with PBS and given fresh serum-free DMEM, regardless of previous treatment, and EVs were isolated again 24 h later (CCMb-EVs, see **Figure 2-1**). EV-containing pellets obtained after differential centrifugation and UC were re-suspended in fresh, serum-free DMEM, and they were then used to treat LX-2 cells seeded in 12-well plates the day before for 24 h (50’000 cells/well). Controls for all direct treatments were performed as well. The presence of cytosolic lipid droplets was determined by ORO/DAPI staining as described (see **Chapter 3.2.3**).

3.2.5. Asymmetrical Flow Field Flow Fractionation (AF4)

EV pellets from ultracentrifugation were resuspended in approximately 550 µL of DMEM. Volumes of 100 µL were injected from a pump and autosampler (Agilent Technologies Germany, Waldbronn, Germany), sample tray cooled to 8 °C, with an Eclipse Dualtec (Wyatt Technologies Europe, Dernbach, Germany) equipped with a Mobility electrical AF4 (Wyatt), a UV absorbance detector (Agilent), and a multi-

angle light scattering (MALS) detector Dawn Heleos (Wyatt) for particle detection and size measurement. The Mobility channel was prepared with a narrow spacer (250 µm) and contained a 30 kDa molecular weight cut-off regenerated cellulose membrane, which was equilibrated with six injections of cell culture supernatant with 10 mM phosphate buffer pH 7.4 as mobile phase and a detector flow rate of 1 mL/min. After an equilibration of 1 min in focus mode with 1.5 mL cross-flow, the sample was injected in focus mode for 5 min, then eluted for 20 min at 0.2 mL cross-flow followed by a linear decrease over 5 min to 0.03 mL/min cross-flow and held for 10 min. This was followed by a wash out phase at 0 mL/min cross-flow and an elution inject step. Different amperages ranging from +2 to -6 mA were applied during the elution with cross-flow phase in consecutive runs. For preparative fractionation the same hardware and membrane were used with a narrow spacer (350 µm) and the focus inject time was increased to 8 min to accommodate and focus the injection volume of 500 µL in the channel. Samples were collected at 1 mL per fraction with an automated fraction collector (Agilent), which was set to the respective sample peaks. Collection times for peak 1 and 2 were previously optimized (see **Figure A3-4**) and determined as follows: 14.5-18.5 min and 33.5-38.5 min for DMEM, TGF, and DOPC, 21.5-25.5 min and 34.5-42.5 min for ROLPA, 15.5-19.5 min and 34.5-42.5 min for HEPES, and 13.5-19.5 min and 30.5-37.5 min for EVs originating from S80-treated LX-2. These experiments were performed by Dr. Kathrin Fuhrmann (Helmholtz Institute for Pharmaceutical Research, Saarbrücken).

3.2.6. EV proteomics

SEC-purified EVs, as well AF4-fractioned samples, were transferred to a pre-conditioned polyvinylidene fluoride (PVDF) membrane. First, the PVDF membrane was cut into uniform discs, and the pieces were wetted with methanol (MeOH) for 5 min. After removal of the MeOH, a solution of 0.05% sodium dodecyl sulfate (SDS)/5% MeOH/0.05% Dithiothreitol (DTT) was added for 5 min. Membrane pieces were placed into the bottom of the collection tubes right before EV collection with a little PBS to keep them wet. After the purification step (either by SEC or AF4), the PVDF membranes and EV-containing samples were centrifuged (3'000 x g, 1 h, RT), and the supernatant discarded. PVDF membrane pieces were dried under N_2 flow for 15 min and stored at 4 °C. Comparative, shotgun proteomics was performed after reductive alkylation and trypsin digestion of the samples by the Proteomics Mass Spectrometry Core Facility (PMSCF) at the Department of Biomedical Research (DBMR) of the University of Bern.[344,345] Peptides were analyzed by liquid chromatography tandem mass spectrometry (nano-LC-MS/MS) and spectra were searched by MaxQuant/Andromeda.[346–348] The data was carefully mined to generate lists of interest.

For selected (explicitly stated) instances of analysis, protein-level imputation was allowed when there were at least two detections in at least one treatment group. For details, see **Figure A3-6** and **Figure A3-7**.

3.3. Results and Discussion

3.3.1. EV biological effect

We previously confirmed[46] that the combination of ROL/PA can deactivate LX-2 cells, and we reported how liposomes containing polyunsaturated phosphatidylcholines (PPCs) perform even better, as seen by the formation of cytoplasmic lipid droplets, which are indicative of the cells being in a quiescent-like status. ORO staining was thus performed to reveal the presence of lipid droplets upon different treatments. Confirming our previous results, cells treated with S80 displayed considerably more lipid droplets than with any of the other treatments (**Figure 3-1**). Using EV-pellets from CCMa (**Figure 3-2**) resulted in trends mirroring those observed by direct treatment. This was true also when following CCMa-EV treatment with CCMb-EVs (**Figure 3-3**). While not as dramatic as the response to direct treatment, residual PPCs from CCMa cannot be excluded as a contributing factor. It is for this reason that the more striking results come from CCMb-EVs, either with cells that were serum starved (sst, i.e., DMEM-treated) the day before (**Figure 3-4**), or naïve cells directly challenged with EVs from the CCMb of differently treated cells (**Figure 3-5**). Fluorescence microscopy images were quantitatively analyzed and used to evaluate cellular response (**Figure 3-6**). Cells that were treated with EV-containing pellets originating from the CCMb of TGF or S80-treated cells had a response that was strikingly similar to cells that were treated with TGF or S80 directly, albeit to a minor extent. When looking at the effects of CCMb-TGF on naive cells, the microscopy images show that, remarkably, they arrange themselves along a structured network, much like TGF-treated cells. Since the EVs were not purified in any of these cases, contamination with cellular factors co-purified during UC cannot be excluded. On the other hand, lipid droplets could still be found in cells treated using CCMb-S80 only, even though these cells were never in direct contact with the liposomal formulation, and even though any possible residual S80 from the supernatant of the treated LX-2 was washed away after the collection of CCMa. The newly stored lipid material must have been recycled through EVs released by the originally treated LX-2.

Taken together, these results strongly suggest that EVs from either quiescent-like or perpetuated LX-2 cells might be sufficient to induce a correlated phenotypical status change in otherwise untreated cells.

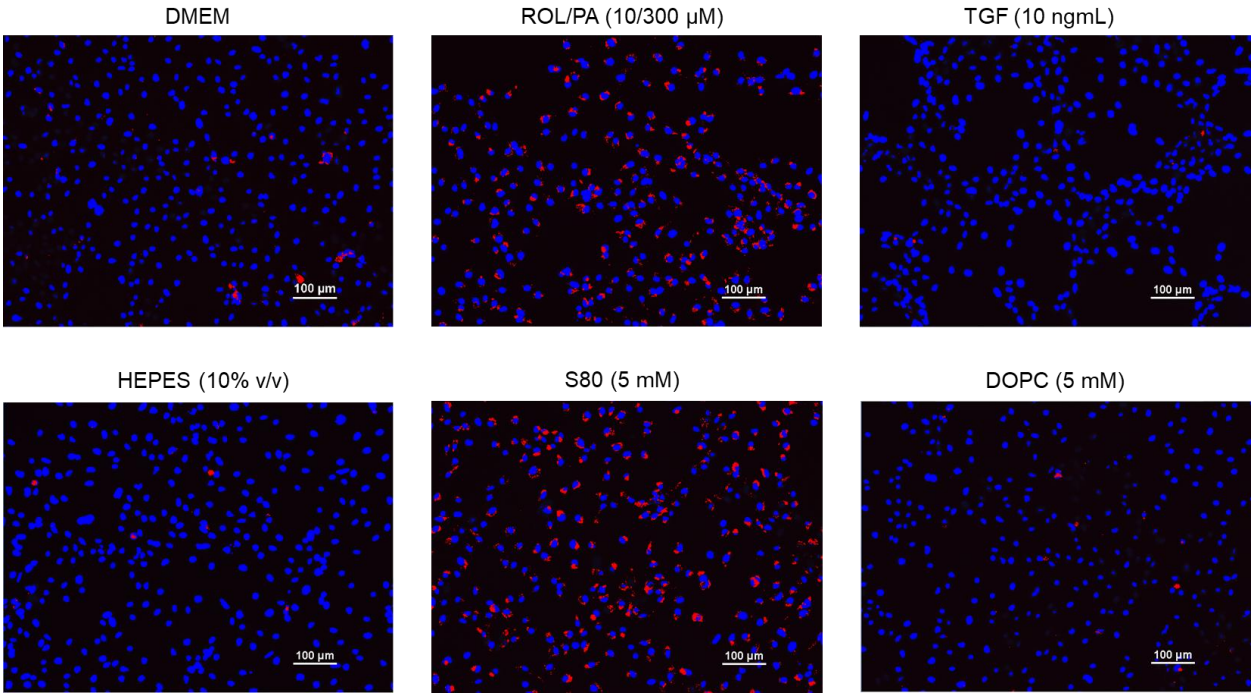

Figure 3-1: Representative images of ORO staining in fluorescence (seen as red areas; nuclei stained with blue DAPI) of differently treated LX-2 cells after thresholding.

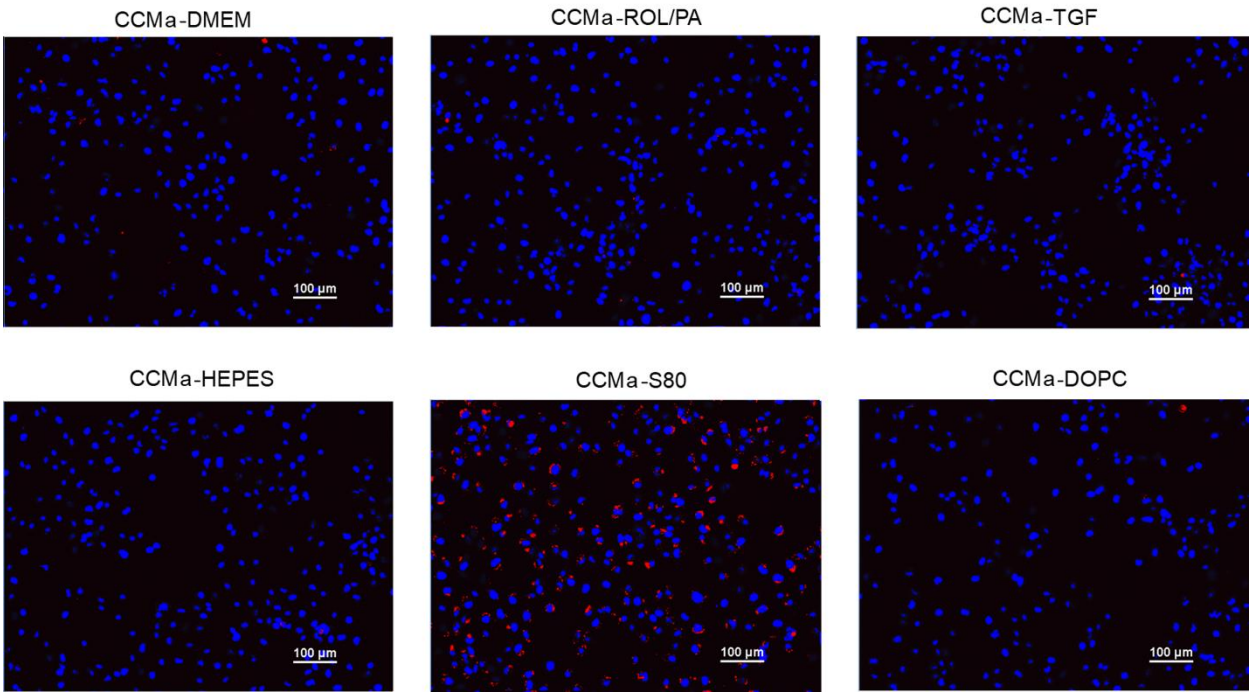

Figure 3-2: Representative images of ORO staining in fluorescence (seen as red areas; nuclei stained with blue DAPI) of differently treated cells after thresholding. LX-2 cells were treated with CCMa-EVs from previously treated HSCs.

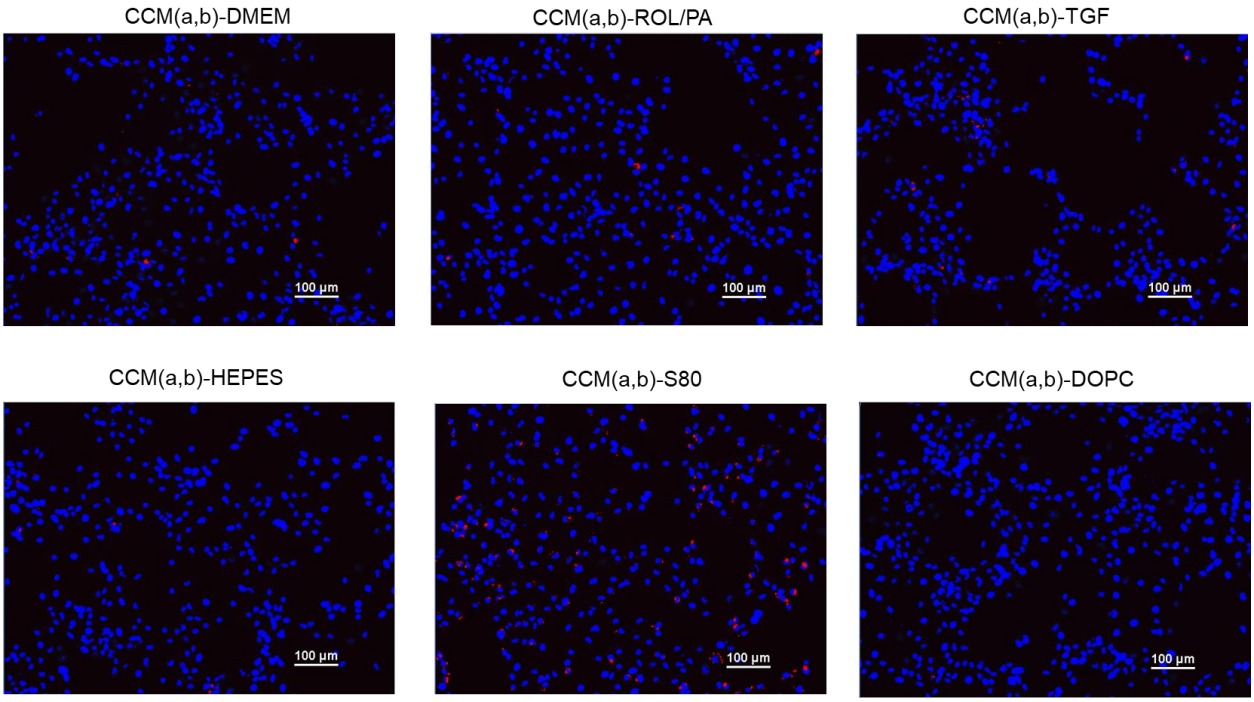

Figure 3-3: Representative images of ORO staining in fluorescence (seen as red areas; nuclei stained with blue DAPI) of differently treated cells after thresholding. LX-2 cells were treated with CCMa-EVs from previously treated HSCs for 24 h, washed with PBS then treated for 24 h with CCMb-EVs from previously treated LX-2.

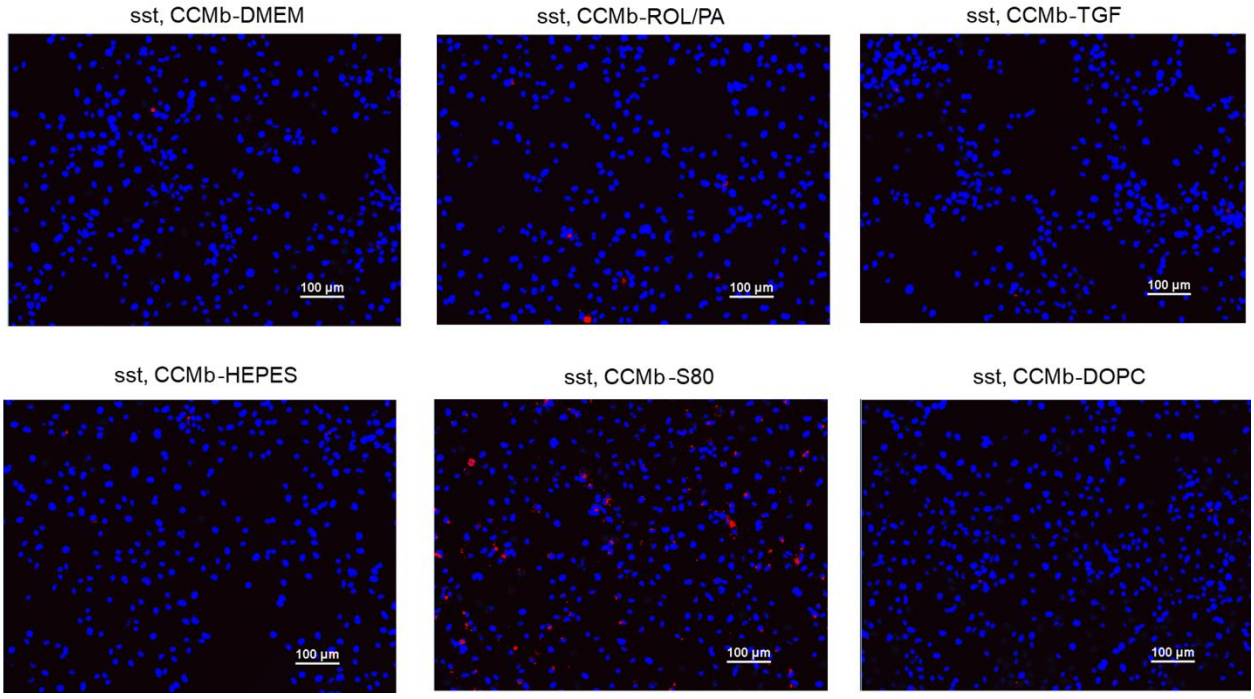

Figure 3-4: Representative images of ORO staining in fluorescence (seen as red areas; nuclei stained with blue DAPI) of differently treated cells after thresholding. LX-2 cells were treated with serum-free DMEM for 24 h (serum starved, sst), washed with PBS then treated for 24 h with CCMb-EVs from previously treated LX-2.

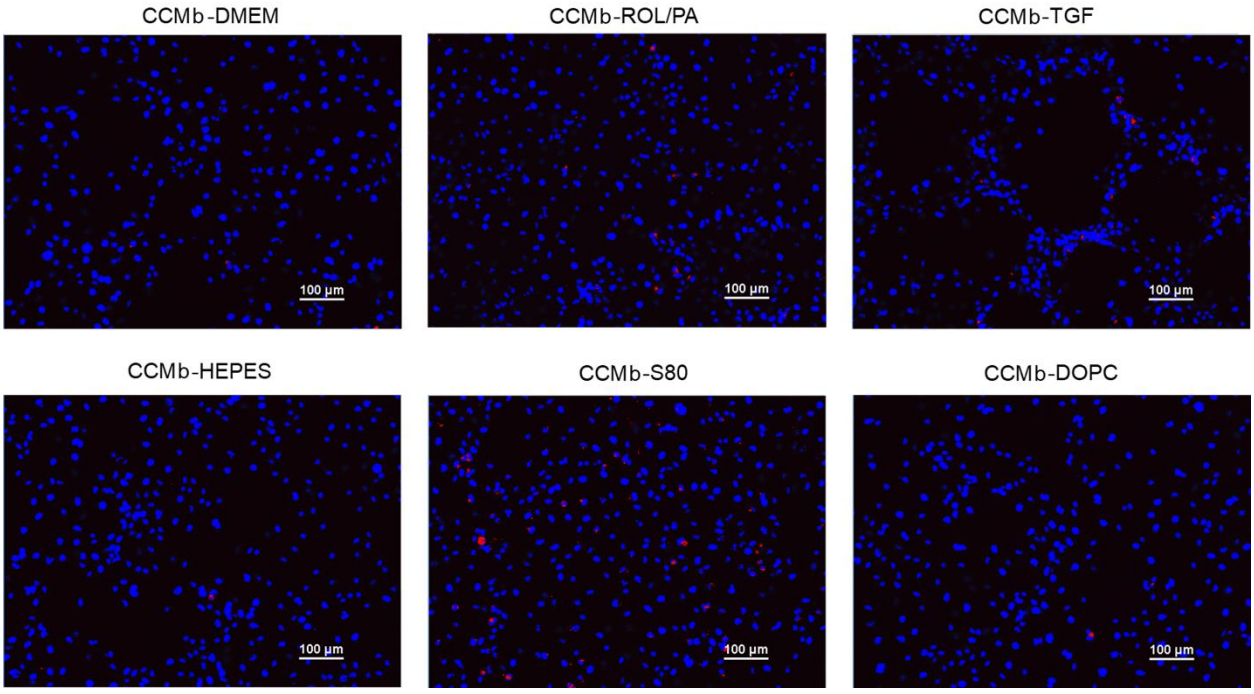

Figure 3-5: Representative images of ORO staining in fluorescence (seen as red areas; nuclei stained with blue DAPI) of differently treated cells after thresholding. LX-2 cells were treated with CCMb-EVs from previously treated HSCs.

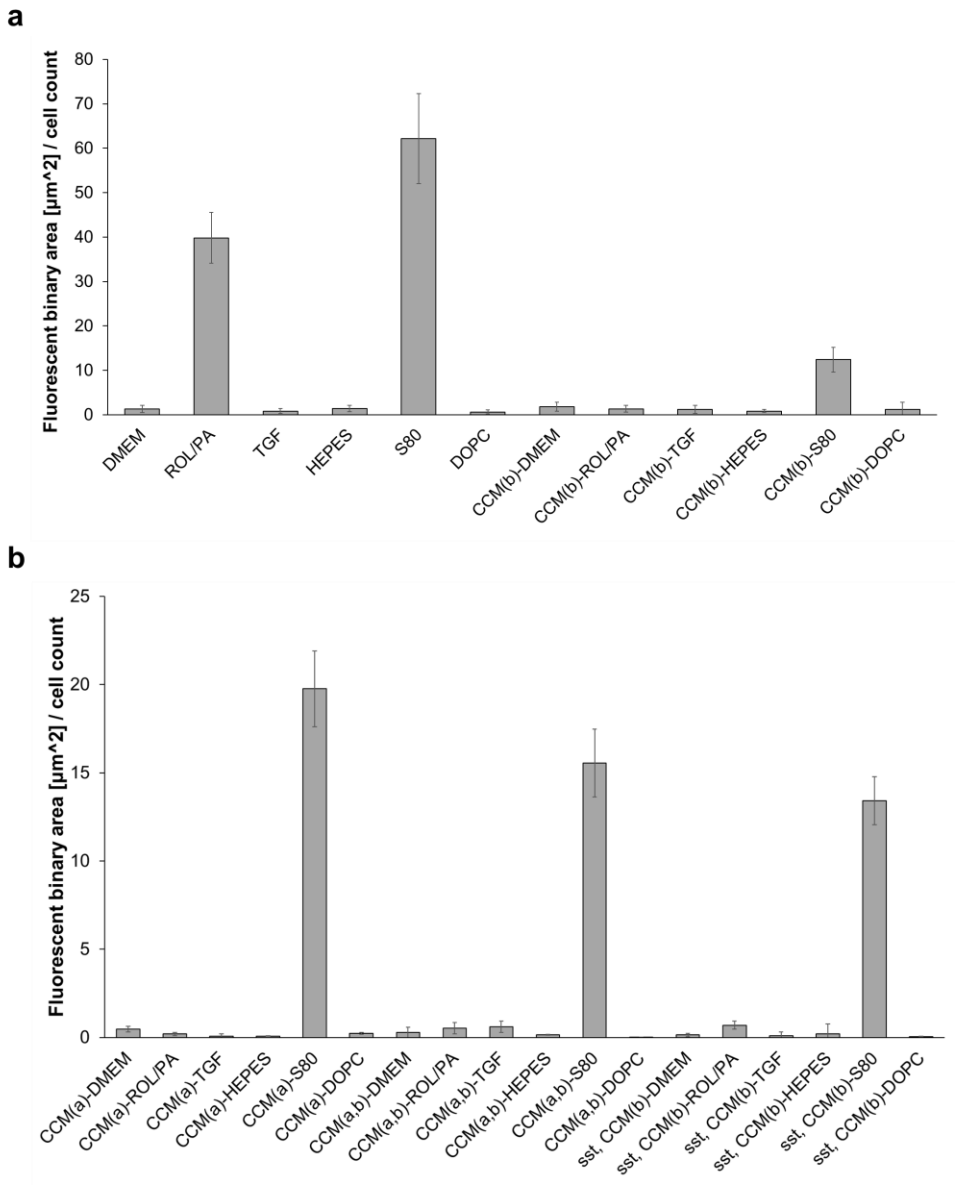

Figure 3-6: Quantitative analysis of stained lipid droplets, whereby the fluorescent area (correlating to a quiescent-like status) was normalized to cell count. Results from direct treatment are compared with CCMb-EVs (**a**). Results from all other control conditions are also shown (**b**) (mean ± SD, n = 3).

3.3.2. EV proteomics for SEC-purified EVs

To further investigate the analytical differences emerged in **Chapter 2,** as well as the biological effects exerted by CCM-EV-pellets onto fresh cells observed by fluorescence microscopy, we developed methods for the isolation and analysis of EV-associated proteins. Distinctive protein profiles could already be seen by SDS-PAGE (**Figure 2-11**), so mass spectrometry analysis was first carried out on EV-containing

pellets from untreated LX-2, and those findings were compared to DMEM-EVs purified by SEC, using the peak fraction eluting from 7 to 8 mL (see **Figure 2-8**).

The samples were prepared for proteomic analysis in a way that would minimize their manipulation (e.g., without labeling or addition of standards) since our main goal was the development of methods that would allow protein discovery while limiting the risk of contamination and the risk of insufficient protein recovery. Label-free quantification, even without the spiking of the samples with protein standards is possible to some extent by different approaches.[349] Shotgun proteomic findings comparing the two settings by three different types of analysis resulted in the successful and consistent quantification of over 2'000 proteins (**Figure 3-7a**), with a considerable overlap between EV-pellets and SEC-purified EVs. These observations were similar for all quantification approaches, i.e., with iBAQ (intensity-based, absolute quantification, useful in some context but rarely used), iTop3 (based on the detected intensity of the top three peptides) and LFQ (label-free quantification) (**Figure 3-7b**).[349–352] The latter two methods are frequently used on their own, but when both quantification methods are adopted, comparing the results from LFQ and iTop3 can be used to confirm findings from one with the findings from the other. Volcano plots (scatter-plots showing significance on the y-axis versus fold-change on the x-axis) comparing SEC-fractions and EV-pellet proteins by LFQ and iTop3 offer a more detailed representation of compared datasets (**Figure 3-7c**). A significance curve was calculated based on a minimal log2 fold change of 1 and a maximum adjusted p-value of 0.05, and is shown as a red line: everything below that curve is not considered to be significantly different between SEC-purified EVs and EV-pellet samples. There are however differences between samples, and data points are marked in red when there is agreement between LFQ and iTop3 evaluations, which would give them even more credence. Looking at the grouping of replicates by principal component analysis (PCA), we could show that SEC-purified samples are more reproducibly similar to each other than proteomic profiles of EV-pellets, resulting in much clearer grouping (**Figure 3-7d**). This does not come as a surprise given the additional purification step, but it is now supported by more validated data.

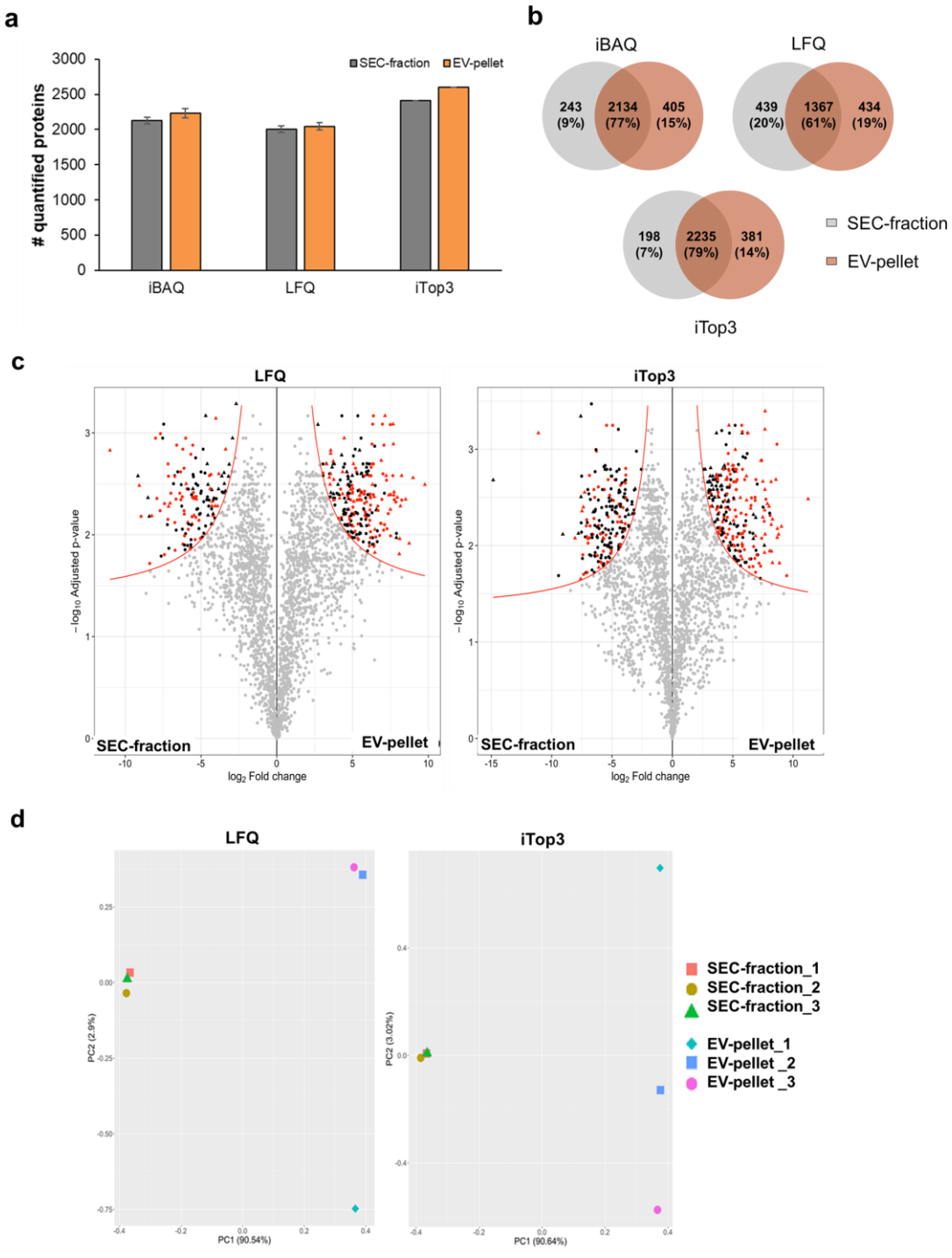

Figure 3-7: Summary of the number of quantified proteins using iBAQ, LFQ and iTOP3 from differently obtained DMEM-EV samples (**a**), and Venn diagrams summarizing the differences and overlap between SEC-EVs and EV-pellet proteins (**b**). Volcano plots (**c**) offer a closer look into the comparisons of proteomic profiling results obtained from EVs from SEC-fractions and EV-pellets; data points in grey are those without significant differences between samples; data points are marked in red when there is agreement between LFQ and iTop3 in defining them as significantly different between sample type. Principal component analysis (**d**) shows similarity degrees between biologically independent triplicates undergoing the same sample preparation in LFQ and iTOP3 analyses.

Having established that SEC-purified EV samples include thousands of proteins which we can reliably identify, we opted for this setting when expending shotgun proteomic analysis to EVs originating from six different treatment groups: DMEM, ROL/PA (10/300 µM), TGF (10 ng/mL), HEPES (10% v/v), S80 (5 mM), DOPC (5 mM). This has led to the identification of 3'881 unique proteins.

A first examination of the SEC-purified EVs by PCA shows the degree of systematic variation in the proteomic profiles among biologically independent samples: EVs originating from similarly treated cells are more similar to each other than to the EVs from any of the other treatment setups (**Figure 3-8a**). Hierarchal clustering of the same samples further demonstrated the similarities within treatment groups (**Figure 3-8b**), as the unsupervised script correctly grouped protein profiles accordingly. Clustering of the proteins on the other axis of the heat map shows two more things. First, there are fundamental similarities across all HSC-EVs, with many protein families shared across samples, especially in the upper third of the heat map. Second, even with all these similarities, the rest of the heat map is characterized by differences in the intensity levels, and also by patterns of missing protein hits (white areas).

While it is interesting to compare which proteins were detected in some treatment groups but not in others, given the size of the dataset we decided to proceed in a very restrictive manner. For our second exploratory step, we generated lists of proteins from all the single protein hits that would allow more immediate comparisons. However, we considered only proteins which were identified in all three single replicates of a treatment group. Additionally, we only looked into proteins that could be reliably quantified both by label free quantification (LFQ) and by the sum of the three most intense peptide intensities (iTop3) by MaxQuant, referring to them as persistent proteins from here on in. This reduced our initial dataset of 3'881 to 3'388 unique protein hits. Out of those, 1'931 proteins could be found and quantified in all replicates from all six different treatments (**Figure 3-8c**). This data was mined to confirm the presence of exosomal markers such as CD81 and CD9 tetraspanins in all samples, as well as the absence of known contaminant such as calnexin.[62]

For every treatment group, there were proteins which were consistently found in addition to the 1'931 proteins that were shared among all. A few of them were also exclusive, i.e., not strictly detected in any of the other groups (**Figure 3-8c**). The thus generated lists of treatment group-specific persistent proteins were all cross-referenced against each other. A summary of the number of proteins found upon every direct comparison is found in **Figure 3-8d**. Volcano plots for every comparison (by LFQ analysis) are found in **Figure A3-5**.

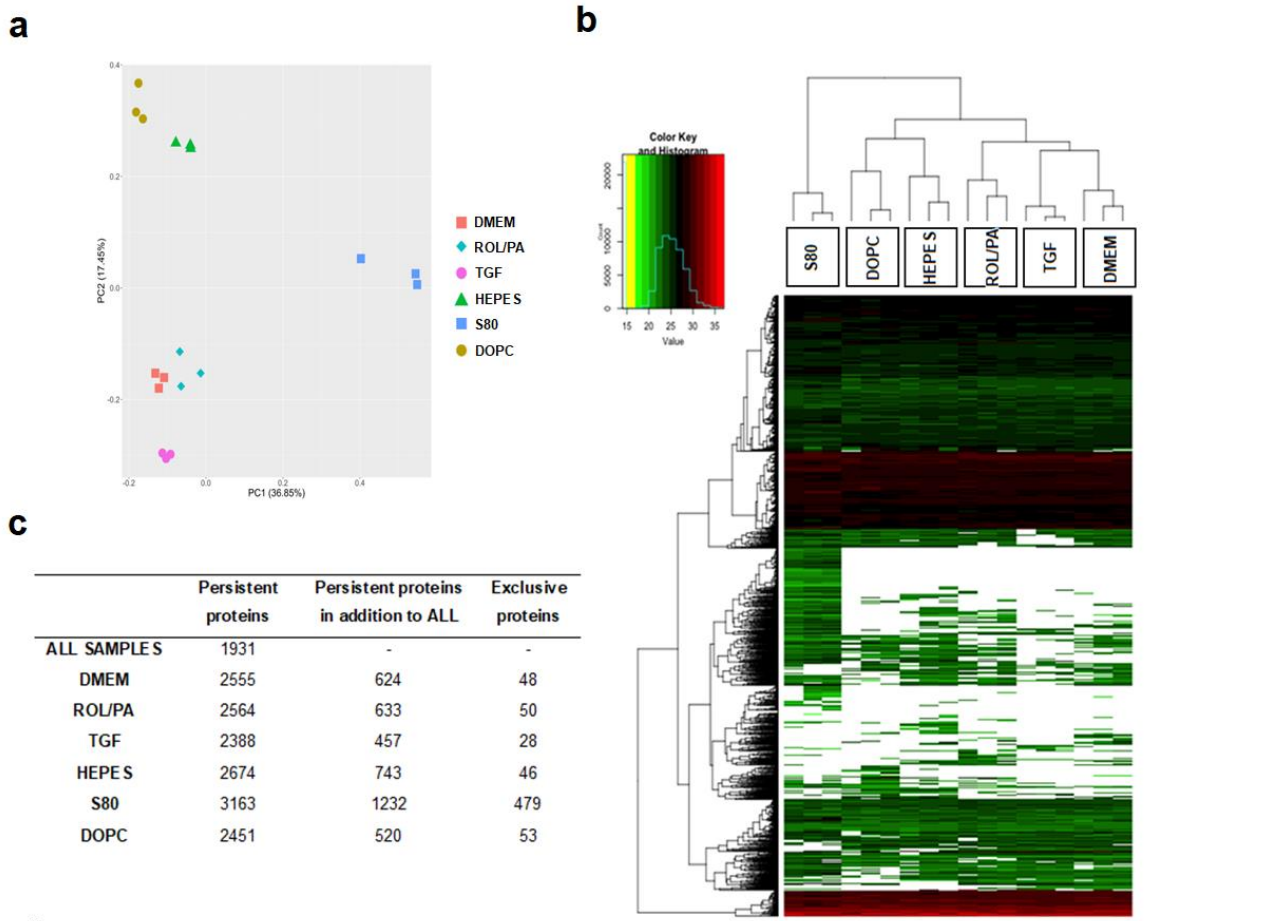

c

	Persistent proteins	Persistent proteins in addition to ALL	Exclusive proteins
ALL SAMPLES	1931	-	-
DMEM	2555	624	48
ROL/PA	2564	633	50
TGF	2388	457	28
HEPES	2674	743	46
S80	3163	1232	479
DOPC	2451	520	53

d

[shared proteins (exclusively shared)]	DMEM	ROL/PA	TGF	HEPES	S80	DOPC
DMEM	-	383 (13)	313 (15)	394 (11)	395 (22)	282 (10)
ROL/PA		-	297 (10)	388 (16)	416 (35)	250 (2)
TGF			-	266 (3)	269 (17)	171 (3)
HEPES				-	514 (82)	357 (31)
S80					-	320 (16)
DOPC						-

e

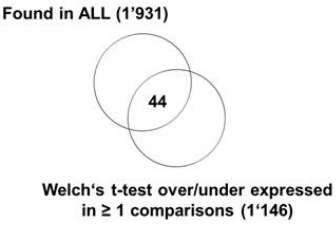

Figure 3-8: Main proteomic findings from SEC purified EVs originating from differently treated LX-2. Principal component analysis (**a**) and hierarchal clustering (**b**) showing similarity degrees between biologically independent samples undergoing the same treatments, and differences between treatment groups. A summary of the number of persistent proteins found in each treatment group is provided (**c**). The number of persistent proteins shared across treatment groups, excluding the 1'931 shared by all is also shown (**d**). A Venn diagram depicts the cross-referencing of the list of proteins persistently found in all samples and the list of those which were significantly over or under-expressed in at least one treatment comparison (**e**).

Next, results from Welch's t-test were used to look for significant differences of protein recovery levels by comparing profiles from every condition to every one of the others. This created a new list of 1'146 proteins that were either over or under expressed in at least one of the single comparisons. Cross-referencing this list with the 1'931 persistent proteins that were shared among all treatment groups yielded

a panel of 44 proteins (**Figure 3-8e**). For ease of comparison, a simple, normalized recovery score was developed by adding the LFQ values of every protein for each treatment condition and normalizing it to the sum of all of them, so that the panel could be visually inspected as a heat map (**Figure 3-9**). It can now be readily seen that TGF-EVs (negative control, indicative of perpetuated LX-2 cells) are more akin to DMEM-EVs than they are to ROL/PA-EVs (positive control, indicative of a quiescent-like status). What is even more remarkable, is that profibrotic EVs from TGF-treated cells are the dramatic, polar opposite to S80-EVs, in this rationally designed panel. This is not the case for EVs from DOPC-treated cells (negative PPC control to S80), nor for the EVs from the HEPES buffer control. The observed effect is not a result of mere phospholipid treatment, it stems from the combined benefit of specific bioactive, antifibrotic lipids present in S80. We have thus created a screening tool powerful enough to not only distinguish between our three basic controls (DMEM, ROL/PA and TGF), but also holding the potential to semi-quantitatively evaluate the performance of additional treatments if further developed.

The Gene Ontology (GO) system to classify sets of genes allows to compare sets of genes according to functional properties, which have been pre-defined and made available through a huge variety of bioinformatics tools.[353–358] One such bioinformatics tool, designed to facilitate the high-throughput analysis and classification of proteins and respective genes, is the PANTHER (Protein ANalysis THrough Evolutionary Relationships) platform.[359,360] An exploratory GO analysis on the 44-proteins panel from **Figure 3-10** was performed using PANTHER. With 8 hits, the most represented protein class is that of nucleic acid metabolism proteins (**Figure 3-10**, **Protein class**) and the majority of the proteins are intracellular as well as anatomical components (**Figure 3-10**, **Cellular components**). From a molecular perspective (**Figure 3-10**, **Molecular function**), a few of the proteins are involved in binding and catalytic activities. Within this panel, proteins were mostly found to be generally involved in cellular and metabolic processes (**Figure 3-10**, **Biological Process**). There were no protein groups clearly associated to any specific pathway when taken together (**Figure 3-10**, **Pathway**), only sparse hits.

DMEM	ROL/PA	TGF	DOPC	HEPES	S80	
0.131041	0.143962	0.097731	0.049667	0.219253	0.358346	EXOC5
0.23759	0.184593	0.177327	0.194043	0.103549	0.102899	CCS
0.082487	0.119659	0.121999	0.070899	0.068961	0.535995	SNUT1
0.046227	0.047696	0.048711	0.032097	0.05194	0.773329	TGFI1
0.132741	0.102134	0.099212	0.176996	0.155226	0.333691	IF4E2
0.053309	0.082517	0.098608	0.042519	0.033504	0.689543	PSIP1
0.146318	0.105381	0.127021	0.079414	0.130328	0.411537	ASML
0.125187	0.104815	0.067602	0.094452	0.132509	0.475436	DYR
0.149243	0.118704	0.487867	0.101843	0.033909	0.108434	CO1A1
0.265088	0.242945	0.218848	0.178426	0.082204	0.012489	FIBA
0.15099	0.135041	0.46714	0.065352	0.051406	0.13007	TSP1
0.055054	0.087459	0.063442	0.045598	0.038399	0.710047	TOP1
0.146998	0.106521	0.649987	0.047058	0.040746	0.00869	CSPG2
0.114099	0.141511	0.067861	0.159889	0.19972	0.316921	NQO1
0.117776	0.11104	0.061021	0.19661	0.188027	0.325526	RFA2
0.054038	0.087652	0.116629	0.061325	0.074734	0.605621	FBRL
0.213238	0.182828	0.103304	0.240878	0.149222	0.11053	ENPP1
0.04168	0.149059	0.039669	0.057754	0.121367	0.590471	MRE11
0.080863	0.127724	0.047015	0.035018	0.092004	0.617377	HNRH2
0.134111	0.161602	0.183152	0.116089	0.186171	0.218876	SRPK2
0.126516	0.11533	0.092473	0.089154	0.087846	0.488681	CDK17
0.067079	0.10073	0.050706	0.027333	0.1696	0.584553	MYO9B
0.354338	0.158485	0.211064	0.117706	0.07429	0.084116	ITSN1
0.101897	0.091388	0.057368	0.032657	0.18909	0.5276	TBCE
0.111775	0.152392	0.181405	0.107127	0.120196	0.327104	SRSF7
0.089273	0.109141	0.032178	0.087862	0.151277	0.530269	RHG29
0.096081	0.189733	0.03494	0.048668	0.165154	0.465423	EFL1
0.187691	0.270953	0.354989	0.098817	0.064021	0.023529	MUC19
0.081366	0.094164	0.085096	0.068951	0.083833	0.586589	ANKH1
0.132783	0.163698	0.038042	0.121133	0.158974	0.38537	EH1L1
0.116219	0.115527	0.062519	0.08052	0.055472	0.569742	SFRP1
0.130536	0.140481	0.080074	0.173069	0.177018	0.298822	CPSF7
0.062216	0.068583	0.066066	0.079212	0.130432	0.593492	FA98A
0.035262	0.086115	0.060899	0.043234	0.056064	0.718427	PRP31
0.190427	0.246698	0.18235	0.101399	0.190035	0.089091	VMP1
0.078538	0.085823	0.071195	0.072456	0.081349	0.610638	QKI
0.178892	0.241125	0.089596	0.071678	0.132973	0.285736	UACA
0.135858	0.118225	0.077794	0.257036	0.197343	0.213743	PNPO
0.143909	0.190258	0.081586	0.1846	0.203068	0.196579	ARP10
0.146503	0.190384	0.174792	0.07894	0.126025	0.283356	OGFR
0.106136	0.123526	0.12567	0.059337	0.139446	0.445885	ABCF2

Figure 3-9: Treatment-discriminating proteomic panel. Expression levels for each protein were scored by normalizing to the sum of LFQ intensities to generate a heat map.

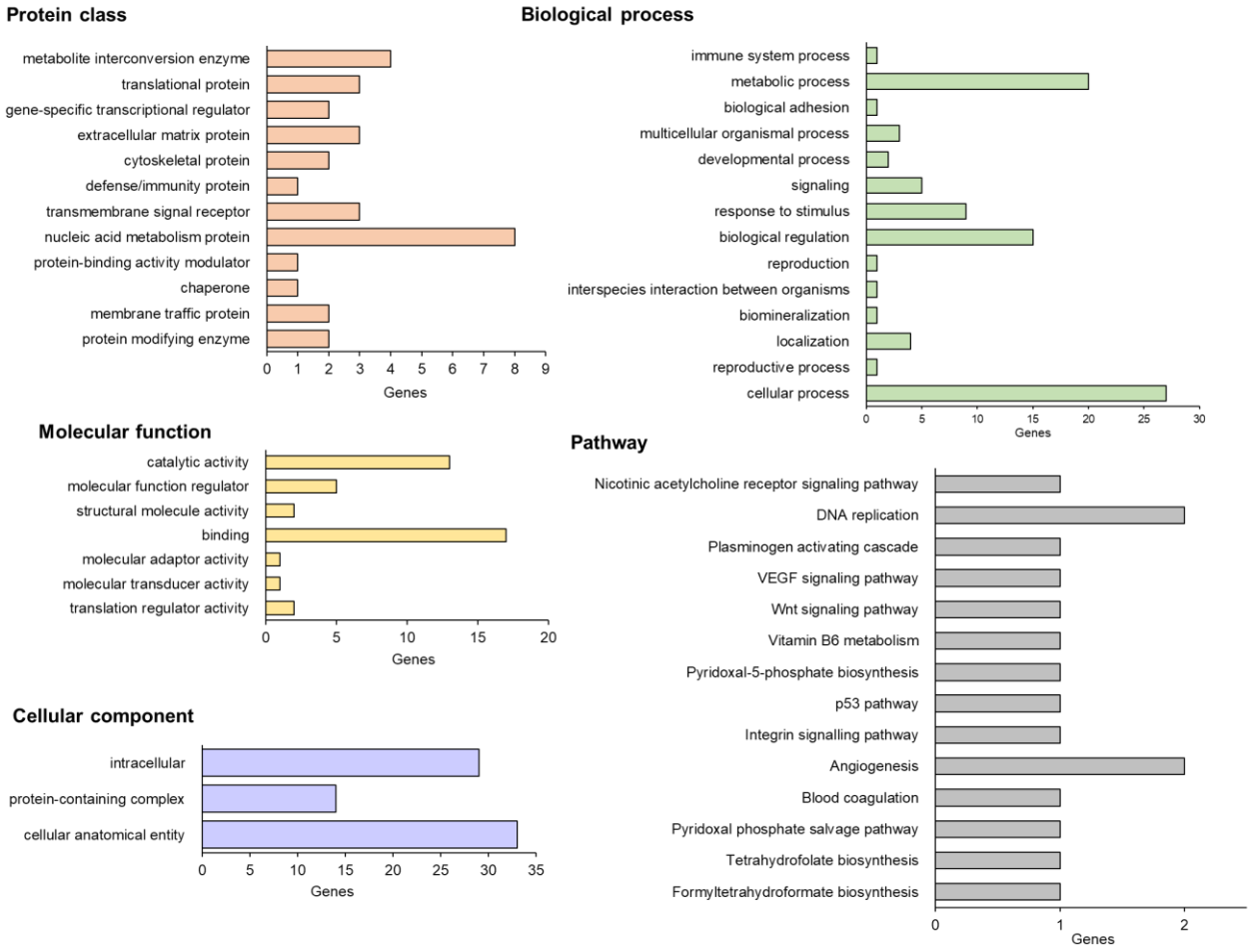

Figure 3-10: Classification of the 44 proteins comprising the treatment-discriminating panel using the PANTHER platform.

3.3.3. EV proteomics for AF4-purified samples

AF4 is a powerful technique increasingly adopted for the purification of nano-sized particles, polymers, protein complexes, viruses, and even EVs.[66,361–365] During AF4, particles are separated by two flows, namely a forward laminar flow and a crossflow perpendicular to it.[366] During AF4 purification of our EV samples, two main peaks emerged, and we collected both the early and late eluting peak (peak 1 and peak 2, respectively) (**Figure A3-4**). Similar to the proteomic analysis performed for the SEC-purified EVs, AF4-purified samples were examined with the purpose of finding lists of treatment-discriminating proteins. We investigated peak 1 and peak 2 separately, as well as combined, leading to the identification of a total of 1'807 distinct proteins.

Compared to the SEC-purified EV protein profiles, AF4-purified EVs produced shorter lists. The explanation can be twofold. First, the SEC EV-containing peak was just one, and sharper than either of the collected AF4-peaks. This directly affects the precision with which the EV-associated proteins can be

isolated, especially when considering that some could be found in both or either one of the AF4-peaks. Secondly, AF4-fractions are more diluted and limited in terms of recovered EVs, and thus in the recovered EV-associated proteins.

PCA revealed that looking at peak 2 resulted in better grouping of treatments compared to peak 1, confirming that this particular fraction holds the more distinctive EV-subset from the perspective of original cellular treatment (**Figure 3-11a**,**b**,**c**). Combined analysis of AF4 peaks showed nonetheless a substantial number of proteins that can be found across both bands, resulting in mixed hierarchal clustering even when looking at peak 2 alone, and even after imputation (**Figure 3-11d**, for visual examples of how imputation worked see **Figure A3-6** and **Figure A3-7**).

As with SEC-purified EVs, lists of treatment-correlating, persistent proteins were generated for AF4-purifed EVs, both by looking at the peaks separately and by looking at the peaks combined (**Figure 3-11e**,**f**). This allowed for a first comparison of purification methods, summarized with Venn diagrams (**Figure 3-12**). The vast majority of the proteins found by AF4 purification were also detected in SEC-samples. AF4-peak 2 had more original hits compared to AF4-peak 1, and indeed proteins isolated from AF4-peak 2 have a greater overlap with SEC-findings.

Purification by AF4 led to the confirmation of many of the proteomic findings from SEC-purified EVs, split across two distinctive subpopulations of EVs, which would warrant further exploration in the future.

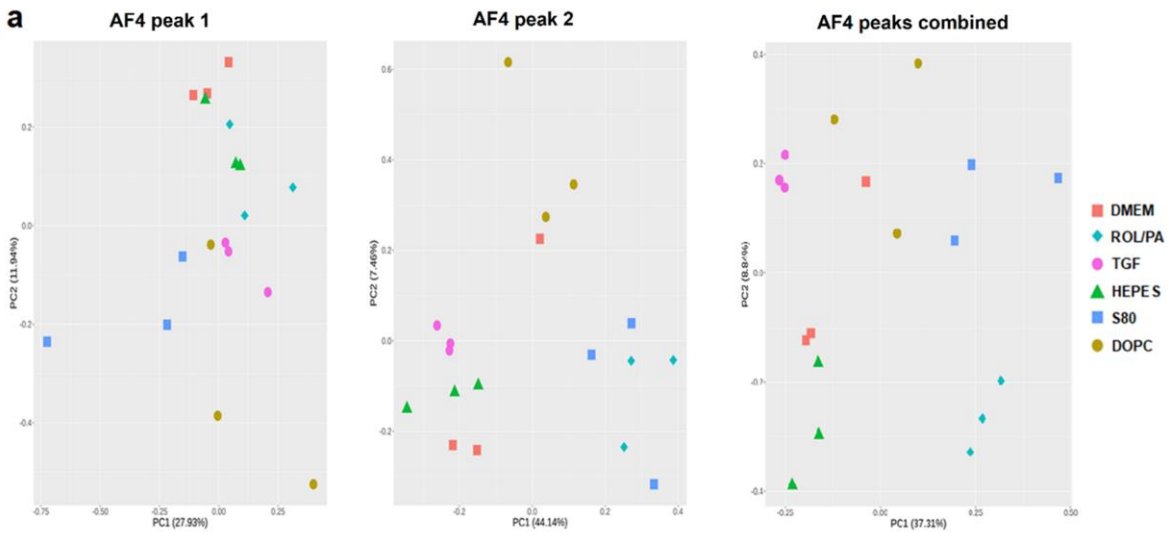

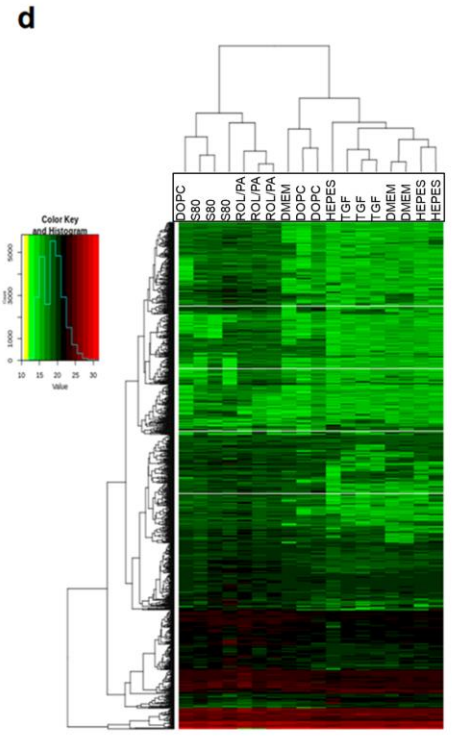

e

	Persistent proteins AF4 peak 1 (group exclusives)	Persistent proteins AF4 peak 2 (group exclusives)	Persistent proteins AF4 peaks combined (group exclusives)
ALL	69	348	407
DMEM	472 (60)	551 (5)	689 (14)
ROL/PA	254 (2)	1043 (283)	1078 (177)
TGF	363 (16)	531 (4)	638 (6)
HEPES	378 (16)	504 (2)	639 (3)
S80	395 (34)	858 (33)	946 (70)
DOPC	97 (3)	495 (3)	525 (3)

f

shared proteins (shared exclusively)	DMEM	ROL/PA	TGF	HEPES	S80	DOPC
DMEM	_	232 (14)	154 (3)	164 (2)	215 (15)	59 (0)
ROL/PA		_	198 (4)	211 (4)	429 (143)	107 (4)
TGF			_	139 (1)	186 (5)	40 (1)
HEPES				_	189 (3)	52 (0)
S80					_	98 (2)
DOPC						_

Figure 3-11: Main proteomic findings from AF4 purified EVs originating from differently treated LX-2. Principal component analyses for samples originating from AF4 peak 1 (**a**), peak 2 (**b**) and for the two peaks combined (**c**). The hierarchal clustering after imputation for biologically independent AF4-peak 2 samples is also shown (**d**). The tables (**e**, **f**) offer a summary of the number of persistent proteins found in each treatment group (**e**), and a summary list of the number of persistent proteins shared across treatment groups (**f**).

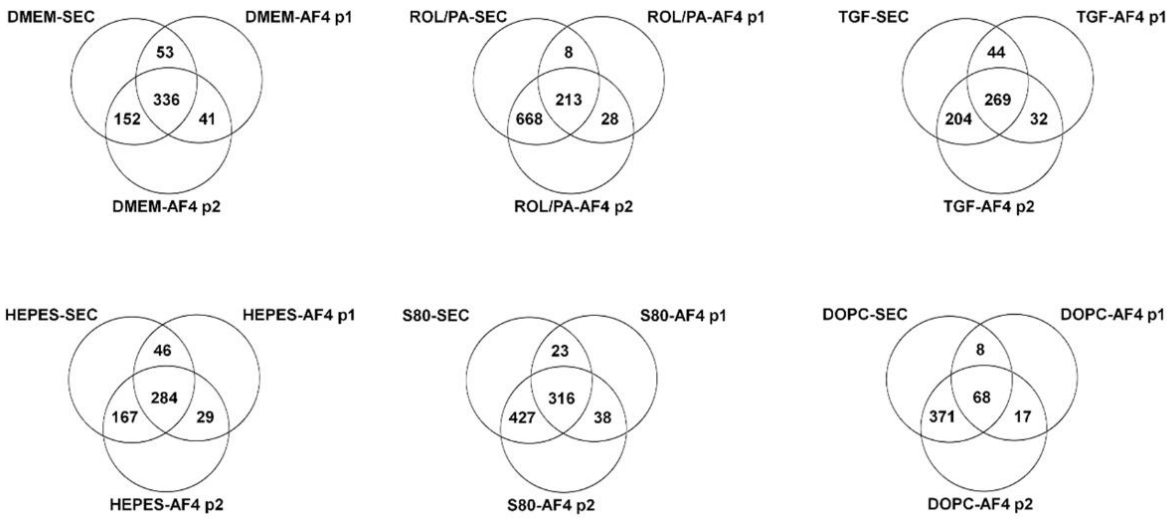

Figure 3-12: Venn diagram comparisons of SEC and AF4 purified samples: for every treatment group, the number of proteins found in the SEC fraction are compared to those found in AF4-peak1 (AF4 p1) and AF4-peak2 (AF4 p2).

3.4. Conclusions

EVs from treated LX-2 cells were sufficient to elicit phenotypic changes in naïve HSCs, strongly correlating to direct treatments, from which we can surmise that the biochemical composition of EVs includes molecules playing an active role in fibrotic processes. On the one hand, this means that EVs might provide unambiguous information associated to the physiological state of the cells from which they originated. On the other hand, it might also provide insights into explaining the biological effect HSCs exert onto neighboring cells.

Looking for what those insights might be, and following up our basic EV characterization protocols, we successfully developed methods to perform shotgun proteomics profiling of SEC and AF4-purified EVs. While there were many similarities across samples, the complex datasets were mined to generate a screening panel of 44 proteins that can be used to effectively distinguish between our three basic controls (DMEM, ROL/PA and TGF). At the same time, this panel holds the potential to semi-quantitatively evaluate the performance of additional treatments if further developed. The effect of S80 treatment on the proteomic profile of HSC-EVs was particularly striking when contrasted to the profile of EVs originating from TGF-treated cells.

The generated datasets can also be used to rationally select specific candidate markers for a direct and quantitative evaluation of treatment effect based on EV-analysis (see **Chapter 4**).

Chapter 4.
Detection of EV-associated proteins for the quantitative evaluation of PPC-based antifibrotic treatments

“Ever tried. Ever failed.
Nevermind.
Try Again. Fail again. Fail better.”
Samuel Beckett

Parts of this chapter are ready to be submitted for publication.

4.1. Introduction

While we have previously contributed to the research into the effect of essential phospholipids (EPLs) in liver fibrosis, we have also concluded that more studies into the mechanism of action of EPLs and candidate antifibrotic drugs are needed.[46] Elafibranor (Ela) and obeticholic acid (OA) have recently been undergoing clinical trials for approval as antifibrotics for patients with non-alcoholic fatty liver disease (NAFLD) and non-alcoholic steatohepatitis (NASH).[35,36,367–373] Numerous studies into their potential benefits in relieving hepatic fibrogenesis have explored both drugs alone and in combination.[374,375] Ela is a peroxisome proliferator-activated receptor (PPAR)-α and PPAR-δ dual agonist. PPAR agonists are a class of drugs used for the treatment of metabolic syndrome symptoms (i.e., lowering triglycerides and blood sugar).[376] Ela has shown high potency in PPARα/δ agonism, with half maximal effective concentrations (EC_{50}) of 45 nM and 175 nM, respectively.[377] OA, on the other hand, is a semi-synthetic analogue of bile acid, a potent agonist (EC_{50} = 99 nM) of the farnesoid X nuclear receptor (FXR) and the first such drug used in human clinical studies.[378,379]

Here, we aim to investigate the possibility of formulating Ela and OA in PPC-liposomes and test their possible effects on HSCs using our optimized LX-2 in vitro model.

The first challenge to that end is finding an appropriate concentration of Ela and OA to test for potential beneficial effects. In our previous study we screened S80 and the hepatoprotectant silymarin concentrations by looking at the progressive increase of cytoplasmic lipid droplets.[46] This approach, however, can only work for Ela and OA if they have a synergistic effect directly related to the eventual accumulation of lipids in HSCs' cytoplasm, as was the case for silymarin. Looking for an alternative quantitative analysis, we try here to develop a reactive oxygen species (ROS) detection strategy to add to our in vitro model, since ROS-measurements are widely applied in the research of inflammatory processes.[380,381]

Based on our results from **Chapter 2** and **Chapter 3**, we successfully expanded our LX-2 protocols to include the analysis of EVs, so we decided to investigate the potential use of rationally selected candidate protein markers for a quantitative evaluation of treatment effect that relies on direct EV analysis.

The detection of specific proteins on EVs is an integral part of the field. Typically, western blots is the go-to technique to show the presence of known exosomal markers in EV samples, including CD9, CD81, CD63, and Alix.[382–388] Alternatively, strategies relying on flow cytometry (FACS) are employed. Using FACS when working with EVs can be challenging, given that the instruments were designed for the analysis of single cells, which are considerably larger in size.[389] A workaround for this particular issue is the coupling of EVs to large beads, and subsequently analyzing the presence of the markers of interest on the beads covered in EVs. Nano-flow cytometers have recently entered the market for the specific analysis of nanoparticles in a way that is analogous to how classical FACS instruments work with full cells.[239,390–392] Research groups have been trying to measure fluorescently labeled EVs directly by fluorescence nanoparticle tracking analysis (f-NTA), demonstrating the feasibility of its application.[386,393,394] These reports

used unspecific dyes or immunolabeling for specific proteins, often opting for quantum dots (QD) conjugated antibodies to overcome photostability problems associated with many conventional fluorophores.[386] The latter approach, however, can be vitiated if effective protocols to purify QD-labelled EVs from free QD are not effectively validated.

In **Chapter 3** we detailed the mining of the full proteomic profiles of our EV samples, whereby we could also confirm the presence of exosomal markers. We also rationally developed a panel of treatment-discriminating set of proteins (**Figure 3-9**). While such a panel of 44 proteins is considerably smaller than a full proteomic dataset, we postulated that there might be a selection of proteins to more simply tell apart quiescent-like LX-2 cells and their perpetuated counterparts (TGF-treated) by looking at the EVs they produced. There were 78 proteins persistently found in ROL/PA and S80 groups that were absent in the persistent protein profile of EVs originating from TGF-treated cells. Conversely, there were 4 proteins in the TGF group that were not consistently found in ROL/PA and S80 (**Figure 4-1**). The UniProt database[395] was consulted to look for candidate protein markers within these two subsets that were either tissue specific, membrane bound and/or secreted, reducing the first (ROL/PA and S80) subset down to 22 and keeping the second (TGF) subset to 4. Tissue specificity would be desirable for the translational applicability of our protocols, opening up the possibility of analyzing more complex ex vivo samples of EVs, while possibly being able to trace the EVs back to their origin.[396] We hypothesized that proteins that have been reported to be membrane bound and/or secreted are less likely to be in the inner core of EVs. If so, they could be detected on the surface of EVs without destroying them, thus allowing for their analysis by f-NTA.

The secreted protein acidic and cysteine rich (SPARC) was thus selected as a proof-of-concept protein.[307,308,397,398] SPARC was among the 4 proteins consistently found in TGF samples, but not in ROL/PA and S80 (**Figure 4-1**). In **Chapter 3** we demonstrated that, while not necessarily an integrated part of EV-membranes, SPARC was associated strongly enough to EVs to be co-purified after SEC and AF4. SPARC is also reportedly secreted or found in the extracellular region, in or around the basement membrane, indicating that when found in EV samples, it is more likely to be associated with their membrane than with their aqueous inner compartment. This combined information made it a reasonable candidate for non-destructive detection on EVs by NTA. Importantly, SPARC can be highly expressed in tissues undergoing wound repair or morphogenesis, making it an excellent candidate for the reporting on the physiological state of the cells that released the EVs with which SPARC could be found.[307,399,400] In the present chapter we explore the establishing of an effective f-NTA method for the evaluation of PPC as well as single drug treatments performances.

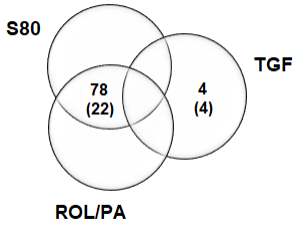

Figure 4-1: Venn diagram depicting the number of identified proteins persistently found in S80 and ROL/PA groups as opposed to TGF and vice versa; numbers in parenthesis indicate proteins within those subsets which were either tissue specific, membrane-bound and/or secreted.

4.2. Experimental Section

Experiments were performed with three biologically independent replicates unless stated otherwise.

4.2.1. Materials

In addition to the materials listed in **Chapter 2** and **Chapter 3**, Cell Counting Kit-8 (CCK-8) and PKH67 Green Fluorescent Cell Linker Mini Kit for General Cell Membrane Labeling were purchased from MilliporeSigma (Burlington, United States). CellROX™ Green Flow Cytometry Assay Kit, Aldehyde/Sulfate Latex Beads (4% w/v, 4 µm), Glycine, bovine serum albumin (BSA, 30% w/v solution), Goat anti-Human IgG (H+L) Cross-Adsorbed Secondary Antibody (Alexa Fluor®488 conjugated and unconjugated) were from Thermo Fisher Scientific (Waltham, United States). Anti-Human CD81 Antibody (IgG2B, Alexa Fluor488-conjugated and unconjugated, Clone #454720), anti-Human CD9 (Alexa Fluor488-conjugated and unconjugated, IgG2b, Clone #209306), anti-human SPARC and GPC1 (polyclonal IgG, unconjugated), anti-human IDE (Mouse IgG1, AlexaFluor®488 conjugated, Clone #334501), Lightning-Link® antibody labelling kit (AlexFluor488) were purchased from Biotechne (Minneapolis, United States). Tissue culture plates and flasks were bought from Greiner Bio One International GmbH (Monroe, United States) or from Sarstedt (Nümbrecht, Germany). Obeticholic acid (OA) and Elafibranor (Ela) were purchased from MedChem Express (Monmouth Junction, United States). Flow cytometry (FACS) tubes and BD-buffer were from BD Bioscience (Franklin Lakes, United States).

4.2.2. Formulation of drug-loaded PPC-based liposomes

Liposomal formulations with S80 or DOPC were prepared by thin the film hydration method as previously described (**Chapter 3.2.2**). For liposomal formulations loaded with Ela or OA, the appropriate amount of drug (from 100 mM stock solutions in MeOH) was added to the lipid film. Lipids (final concentration 50 mM) and drugs (up to 150 µM) concentrations were quantified chromatographically as previously reported.[46,320] The hydrodynamic diameter and the size distribution (polydispersity index, PDI) of the liposomes were measured with a Litesizer 500 (Anton Paar, Graz, Austria), and their stability at 4 °C was tested for up to 28 d.

4.2.3. CCK-8 assay

The CCK-8 assay was used following the manufacturer's instruction, with cells seeded in 96-wells plates (10^4 cells/well). Briefly, cells were washed twice with PBS after treatment with different amounts of Ela and OA (0.025-75 µM); controls for the highest DMSO concentrations (0.088% and 0.075% v/v in DMEM, for Ela and OA respectively) were performed as well. A volume of 90 µL DMEM and a volume of

10 µL of CCK-8 were added to each well. LX-2 were incubated for further 2 h at 37 °C, 5% CO_2. Afterwards, the absorbance was measured at 450 nm using an Infinite 200®Pro (F Plex) Tecan plate reader (Männedorf, Switzerland) at 37 °C.

4.2.4. Analysis of lipid droplet content upon treatment with drug-loaded PPC-based formulations

ORO/DAPI staining was performed in 12-wells plates as described (**Chapter 3.2.3**), but with an initial seeding density of 1 x 10^5 cells/well (as previously reported).[46] Two concentrations of Ela and OA could be tested (either alone or with S80 and DOPC). The first was a final concentration of 150 nM on the cells (around both drugs' EC_{50} values) and a final concentration of 50 µM (the lowest quantifiable by HPLC). Since the liposomes were not prepared under sterile conditions, all treatment solutions in DMEM were sterile filtered (CA, 200 nm, see **Figure A3-1**).

4.2.5. ROS detection by flow cytometry

After 24 h of treatment with DMEM, ROL/PA (10/300 µM) or TGF (10 ng/mL), cells were washed and detached, divided into 1.5 mL centrifugation tubes (5 x 10^5 cells/mL), and kept in a thermoshaker (Eppendorf, Hamburg, Germany) at 37 °C. Using DMEM-treated cells, a positive control (DMEM_ctrl+) for oxidative stress was achieved by the addition of tetr-butyl hydroperoxide (TBHP) to a final concentration of 100 µM for 60 min. A negative control (DMEM_ctrl-) was obtained by incubating DMEM-treated cells with 5 mM N-acetyl cysteine (NAC, an antioxidant) for 60 min, followed by treatment with TBHP (100 µM, 60 min). All samples were then incubated with CellRox Green staining reagent (λ_{ex} = 508 nm, λ_{em} = 527 nm, final concentration 5 µM) for 30 min. Cells were washed three times with PBS and re-suspend in BD-buffer. A volume of 0.5 mL cell dispersion in BD-buffer was filtered through a 70 µm mesh into a FACS tube and 1 µL of SYTOX™ red (λ_{ex} = 640 nm, λ_{em} = 658 nm, final concentration 0.02 µM) was added to report on dead cells. After 15 min, samples were run through a FACS LSR Fortessa™ flow cytometer (BD Bioscience, Franklin Lakes, United States). For every sample, a minimum of 20'000 events were recorded. The data was acquired with the BD FACS Diva 8.0.1 software, and subsequently analyzed with FlowJo V10.0. The gating strategy is detailed in the supporting information (**Figure A4-4**).

As an alternative to the 24 h treatments with DMEM, ROL/PA and TGF, the three controls were performed for 2 h prior to cell detachment, with the aim of evaluating the immediate cellular response. Unstained controls were produced for every sample.

4.2.6. PKH67 staining

SEC-purified EVs were incubated with 1.5 - 24 µM of PKH67 for 5 - 120 min at 24 °C under gentle shaking. NTA-measurements were performed in scatter mode as previously described (see **Chapter 2.2.3**), but the sensitivity was changed to 90 for measurements in fluorescence mode (f-NTA).

4.2.7. Detection of exosomal marker CD9 by flow cytometry

The analysis of EVs by flow cytometry (FACS) was performed as previously reported.[317] Briefly, EVs were coupled to 4 µm aldehyde/sulfate latex beads. EV-containing SEC-fractions (1 mL each, see **Chapter 2.2.3**) were divided into 0.5 mL aliquots. Freshly filtered (CA, 200 nm) BSA 1% w/v in PBS was also prepared as a negative control. All samples were then incubated for 15 min at RT with 10 µL of latex beads. PBS was added up to 1 mL and all samples were incubated for 1 h at RT with gentle shaking. The reaction was stopped with 0.5 mL of 200 mM glycine, incubated for 30 min at RT. Beads coupled to EVs (or BSA) were centrifuged (2'000 x g, 3 min, RT), the supernatant was removed and the pelleted beads were re-suspended with BSA 1% w/v in PBS. This washing step was repeated two more times. Samples were stained with fluorescently labeled antibodies for CD9 (6 ng/mL) or with the fluorescently labeled isotype control (IC) in ice and in the dark for 30 min. Finally, samples were washed twice with BSA 1% in PBS and analyzed on a BD LRS Fortessa (BD Biosciences) using BD FACSDiva 8.0.

4.2.8. Antibody labelling

Antibodies against human CD81 and SPARC were conjugated with AlexaFluor488 (AF488) using the Lighting-Link (LL) antibody labelling kit as per manufacturer's instructions and under sterile conditions. Briefly, the LL-modifier solution was added to the unconjugated antibody in sterile PBS (1 µL for every 10 µL of antibody). This was then used to re-suspend the lyophilized mixture with AF488, and left incubating for 15 min at RT. LL-quencher was then added to the antibody-AF488 mixture (1 µL for every 10 µL of antibody). The LL-kit was also used to prepare an isotype control with the IgG chain.

4.2.9. Detection of EV-associated proteins with f-NTA

Incubation with AlexaFluor488 conjugated antibodies for exosomal marker CD81 (AF488-CD81) was performed directly into SEC-purified samples for different times (every 10 min up to 120 min, every hour for up to 6 h and then overnight), at different temperatures (in ice, at 24 and 37 °C), with different concentrations (0.05 - 1 ng/mL). Only data with successful f-NTA detection can be shown.

Incubation with AF488-CD81, LL-AF488-CD81, AF488-CD9, LL-AF488-SPARC, were performed in the re-suspended EV-containing pellets obtained after UC, prior to SEC. The protocol optimization was

done with AF488-CD81. The tested conditions included different incubation temperatures (24 and 37°C), for variable amounts of time (for 3 or 5 h), using 2 - 8 ng/mL of antibody conjugates.

Measurements were performed in scatter mode as previously described (see **Chapter 2.2.3**), but the sensitivity was changed to 90 for measurements in fluorescence mode. For every protocol yielding a measurable result, incubation with isotype controls (either bought already conjugated, or LL-conjugated) were also performed.

For antibody incubations with EV-pellets originating from differently treated LX-2 cells, the regimens were as follows: DMEM, ROL/PA (10/300 µM), TGF (10 ng/mL), HEPES buffer (10% v/v), Ela (150 nM), OA (150 nM), S80 (5 mM), S80+Ela (5 mM+150 nM), S80+OA (5 mM+150 nM) DOPC (5 mM), DOPC+Ela (5 mM+150 nM) and DOPC+OA (5 mM+150 nM). The labeled EVs were then purified and collected after SEC.

4.3. Results and Discussion

4.3.1. Formulation of drug-loaded liposomes and cell toxicity assay

OA and Ela were stable to freeze-thaw (FT) cycles (**Figure A4-2**) and a calibration curve for their quantification with a CAD detector could be produced. When calculated using the standard deviations of the lowest concentration,[401] the lower detection and quantification limits (LOD, LOQ) for OA were 16 and 52 µM, respectively, 13 and 42 µM for Ela. Alternatively, basing the calculation on the signal-to-noise ratio, LOD for both drugs was 3-5 µM and LOQ 15 µM. Choosing 50 µM as our lowest quantifiable, final drug concentration, we evaluated drug encapsulation efficiency (EE%) to be ≥83% (**Figure 4-2**). However, even the lowest quantifiable concentration is considerably higher than the drugs' EC_{50} values of 100-175 nM. Without more sensitive detection methods (i.e., LC/MS), we have to work with the assumption that 100-times lower concentrations of these hydrophobic drugs were loaded at least as efficiently. The average size of the produced lipid vesicles was around 150 nm and monodisperse, as evidenced by the measured PDI values (**Figure 4-3**). They were stable for up to 28 d at 4 °C.

CCK-8 results showed no visible effect on cell metabolic activity in the tested concentration range. (**Figure 4-4**). With these results it is not possible to determine an optimal treatment concentration to elicit a quiescence-like response in LX-2 cells with the drugs alone. For further experiments on cells, we chose to test a final concentration of drugs of 150 nM (around both drugs' EC50 values) and 50 µM (the lowest quantifiable by HPLC).

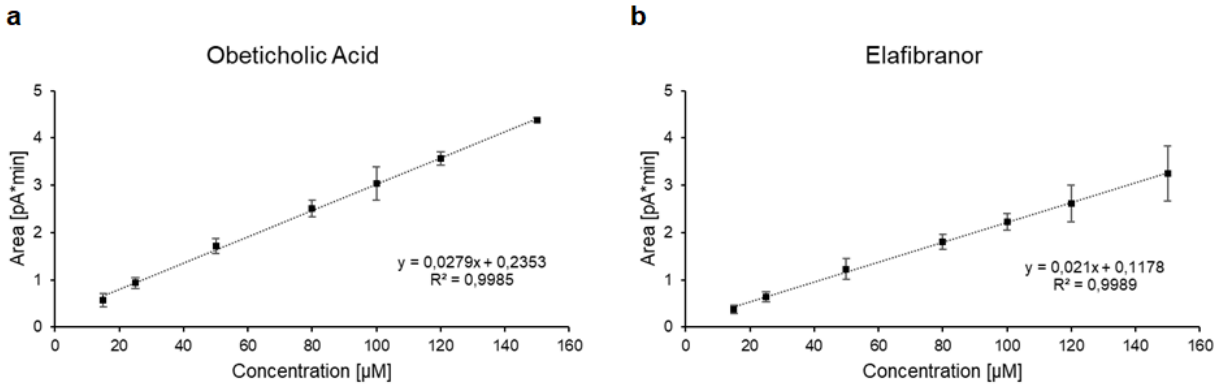

Figure 4-2: Calibration curves for OA (**a**) and Ela (**b**) by HPLC (mean ± SD, n = 3).

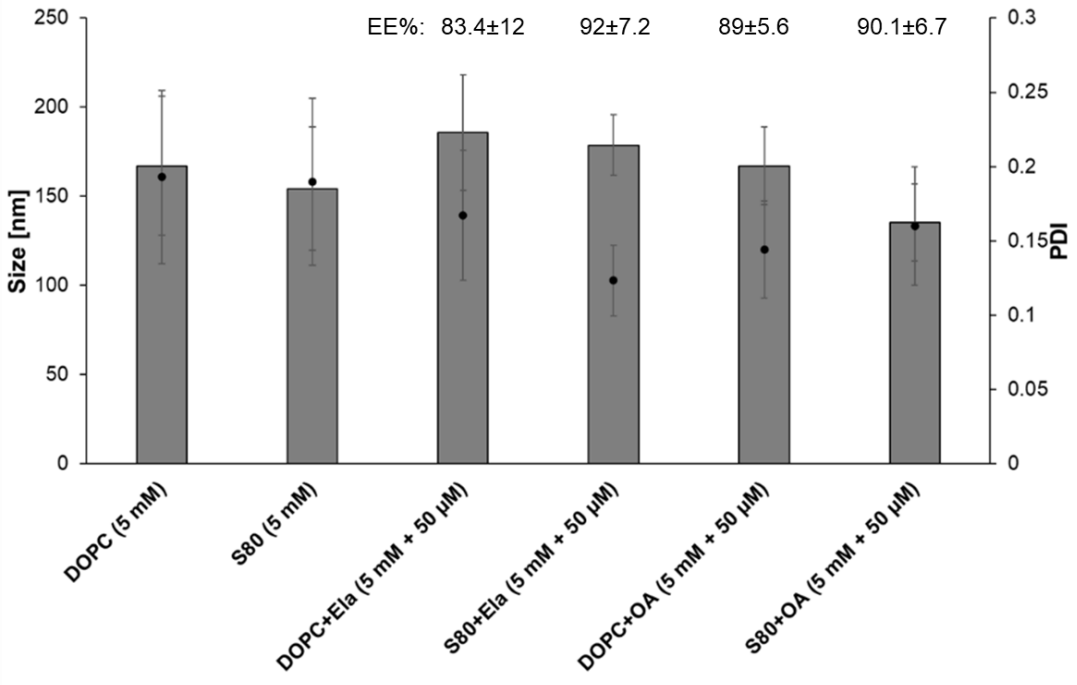

Figure 4-3: Average size, PDI and EE% for the different liposomal formulations (mean ± SD, n = 3-6).

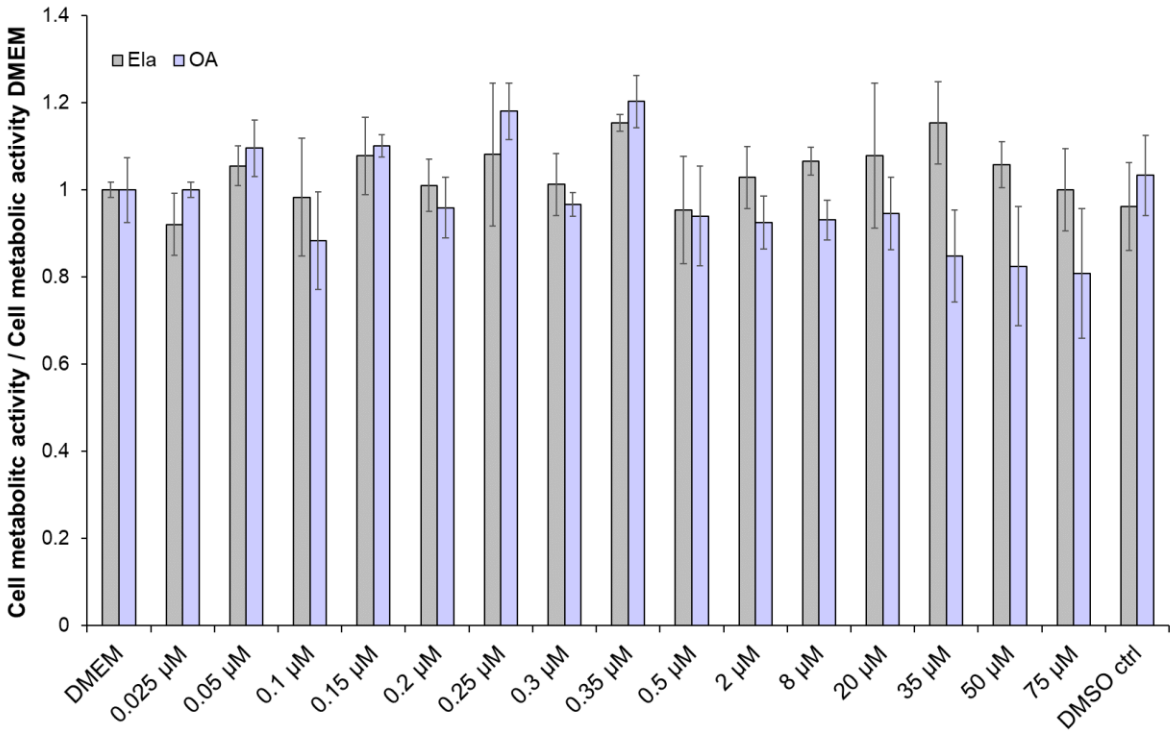

Figure 4-4: Normalized cell metabolic activity measured with CCK-8 assay after 24 h treatment (mean ± SD, n = 3-6).

4.3.2. Analysis of lipid droplet content

In our published study,[46] we reported that the combination of retinol and palmitic acid (ROL/PA) stimulates the formation of lipid droplets by an upregulation of the adipose differentiation-related protein, indicating LX-2 cell quiescence. We also showed that the PPC-containing liposomes are able to deactivate LX-2 to a non-fibrogenic status.

The control treatments validated in the current project are shown (**Figure 4-5**): native LX-2 (treated either with DMEM or HEPES 10%); quiescent-like HSCs (treated with ROL/PA); perpetuated HSCs (treated with TGF); liposome-treated LX-2 (S80 liposomes: positive control, antifibrogenic; DOPC: negative control, expected to be as DMEM or HEPES 10%). These images were then quantitatively analyzed and used as baseline to evaluate the antifibrogenic effect of the new candidate hepatoprotectors OA and Ela. PPC-based formulations were used either on the day they were produced or up to 3 d after being kept at 4 °C.

As expected, activated cells treated with ROL/PA and S80 display significantly more lipid droplets (**Figure 4-5**). PPC formulations that were loaded with OA and Ela showed a remarkable increase in the amount of lipid droplets, while none with DOPC. However, we could not detect a synergistic effect between S80 and either drug in terms of lipid droplets formation when using 150 nM. When using 50 µM of drugs, there were not many areas in the plate with enough cells for analysis, though (very) sparse spots could sometimes be found, and two examples are shown (**Figure 4-6**). Combined with the CCK-8 results, this suggest that 50 µM are indeed toxic to LX-2 cells, and the lowering of metabolic activity due to cell death must have been offset by an increase of it within the remaining HSCs. The presence of PPCs could rescue the LX-2 to some extent. Judging by the apparent number of cells from these images, S80 performs materially better than DOPC, but there were still fewer cells than could be found in any of the treatments summarized in **Figure 4-5**. We would suggest that there are indeed too many cells for a precise count, as nuclei start to overlap. This is especially noticeable in TGF-treated cells. Future applications of the ORO/DAPI staining protocol should start with a lower cell seeding density (50’000 cells/well instead of 100’000, as done in **Chapter 3**).

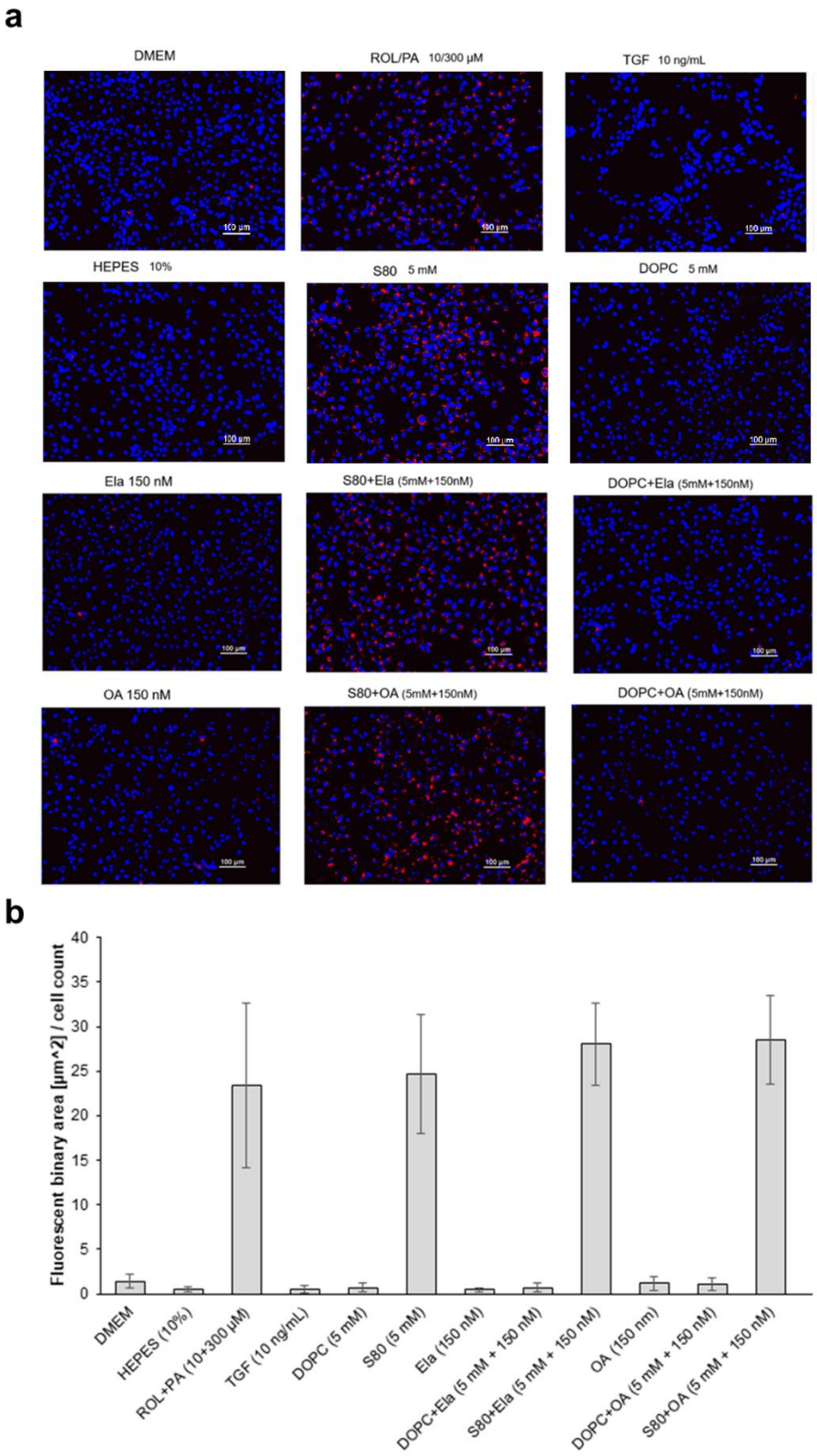

Figure 4-5: Representative images of ORO staining in fluorescence (seen as red spots; nuclei stained with blue DAPI) of differently treated cells after thresholding (**a**). Quantitative analysis of stained lipid droplets, whereby the fluorescent area (correlating to a quiescent-like status) was normalized to cell count (**b**) (mean ± SD, n = 3).

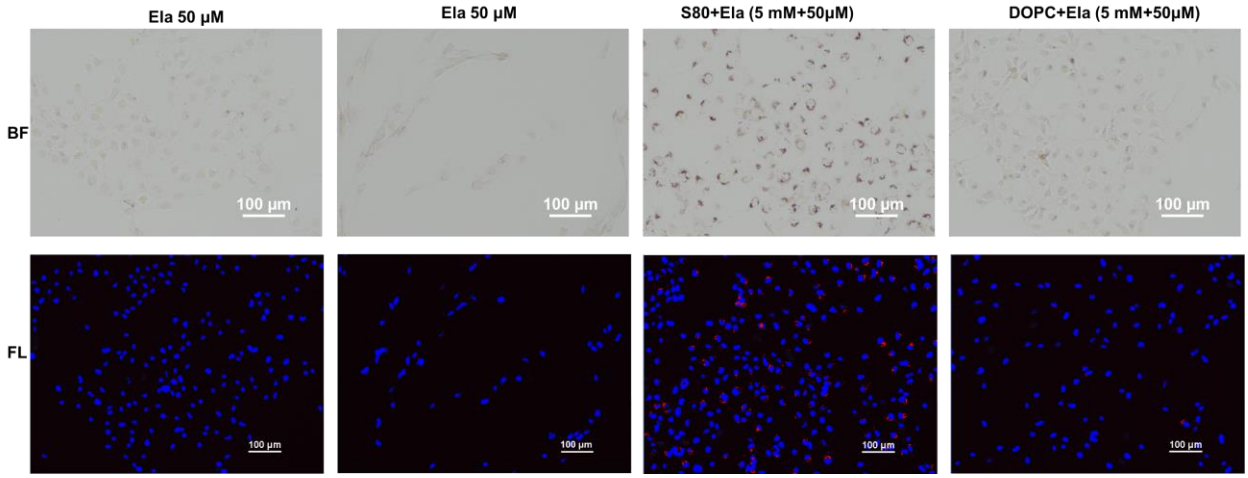

Figure 4-6: Representative brightfield (BF) and fluorescence (FL) images of spots within the 12-wells plates with surviving cells upon treatment with 50 µM of drugs, either alone or in combination with PPCs**.**

4.3.3. ROS detection by flow cytometry

In an attempt to develop effective screening methods for drug candidates in our in vitro model, we explored the quantitative detection of ROS, as their production is associated to inflammatory processes. The detection of ROS with CellRox Green proved possible (**Figure 4-7**). Positive controls with TBHP show a distinctive increase in ROS presence compared to untreated and ROL/PA-treated cells. Perpetuated (TGF-treated) LX-2 were also not generating significantly different ROS levels, although after 24 h they seem to be slightly increasing. NAC in the negative control did not protect the cells from TBHP. Mean fluorescence intensities are quite low even in the TBHP controls: either the LX-2 cell line is not generating many extracellular ROS in general, or the protocol needs to be systematically optimized before it can be applied for in vitro testing. This could be achieved in different ways in the future, e.g., by changing TBHP, NAC and CellROX Green reagent concentrations, or by adding a permeabilization and/or fixation step.

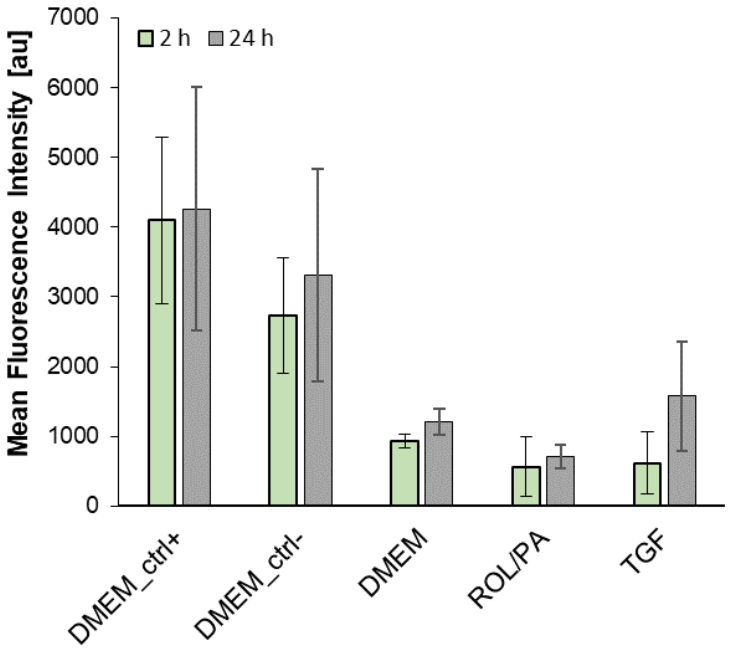

Figure 4-7: Mean fluorescence intensity (indicative of ROS) upon different control treatments for 2 and 24 h (mean ± SD, n = 3)**.**

4.3.4. EV staining with PKH67

In order to develop immunolabeling methods for the non-destructive analysis of physiologically relevant EV-associated proteins by f-NTA, we first assessed the feasibility of detecting fluorescently labeled EVs in general. PKH dyes are used in a wide variety of instances for the non-specific labelling of cellular and vesicular membranes.[402–404] SEC-purified EVs from untreated LX-2 cells were successfully labelled with the PKH67 membrane dye.[405] Testing different concentrations over time, we could determine that the labeling plateaued after 15 min (**Figure 4-8a**). We settled on 20 min incubation time when we systematically increased dye concentration, showing that almost all of the detected particles were indeed membranous, and that an almost linear dose-dependency could be reliably measured (R^2 = 0.909, **Figure 4-8b**). The use of PKH dyes has been recently called into question, particularly because of their hydrophobicity, lead to the formation of dye aggregates that can be detected by NTA, significantly affecting the size distribution profile.[406,407] However, given the freshly prepared PKH67 concentrations that we used in our samples (with relatively few EVs, see **Table 2-1**), we did not encounter new subpopulations of nanoparticles in our measurements compared to unstained samples (for representative size distribution profiles of PKH67 labeled particles see **Figure A4-6**).

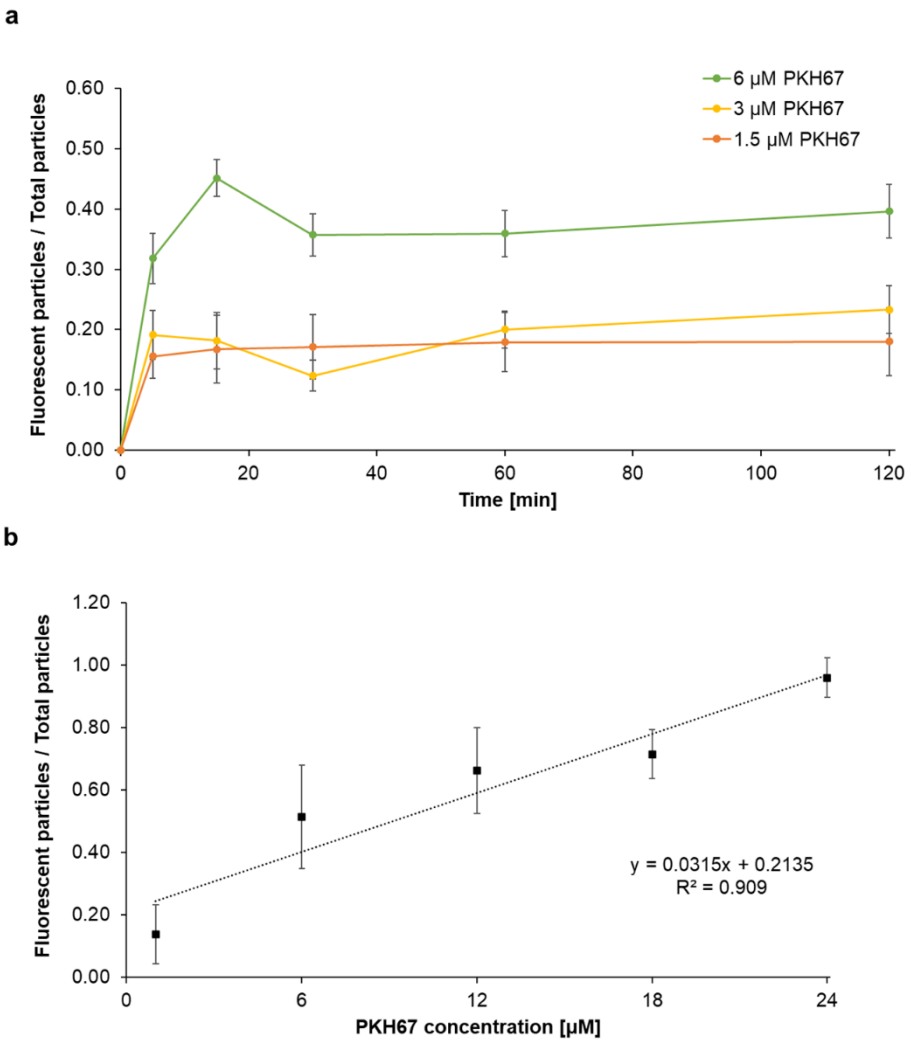

Figure 4-8: SEC-purified EVs from untreated LX-2 stained with unspecific membrane dye PKH67 for different incubation times (**a**) and by systematically increasing dye concentration (**b**) (mean ± SD, n = 3, software: ZetaView 8.05.05 SP2).

4.3.5. Detection of exosomal markers CD81 and CD9

The next steps involved labelling EVs with an AlexaFluor488-conjugated secondary antibody. We chose to start with CD81, since we found it to be present in all EV samples in our proteomic analyses. Being a tetraspanin, it was also likely to be available for binding without destroying the EVs, and previous reports have shown that it could be detected by f-NTA.[386,408]

A first approach was to incubate AF488-CD81 directly in the SEC-purified EV samples originating from DMEM-treated LX-2 cells, at different dilutions of AF488-CD81, for various amounts of time and at different temperatures (**Figure 4-9**). Higher concentrations increased the number of detected particles in fluorescence mode, but not in a dose-dependent manner. Incubation at 37 °C was not significantly better

than incubation at room temperature, although fluorescent particles were detectable starting from an earlier time point. Incubation time had the consistently higher influence: the range between 4 and 6 h was the optimal one for our samples.

The challenge for this setup was that without a purification step for excess AF488-CD81 prior to measurement, the background intensity always negatively impacted the software's ability to detect particles, regardless of final dye dilution. It might be worth pointing out that our relatively low EV-yields resulted in limited final dilutions of the SEC fractions before NTA measurements (1:50 or 1:100). More concentrated EV samples could potentially be labeled after SEC with fewer issues than what we had to overcome.

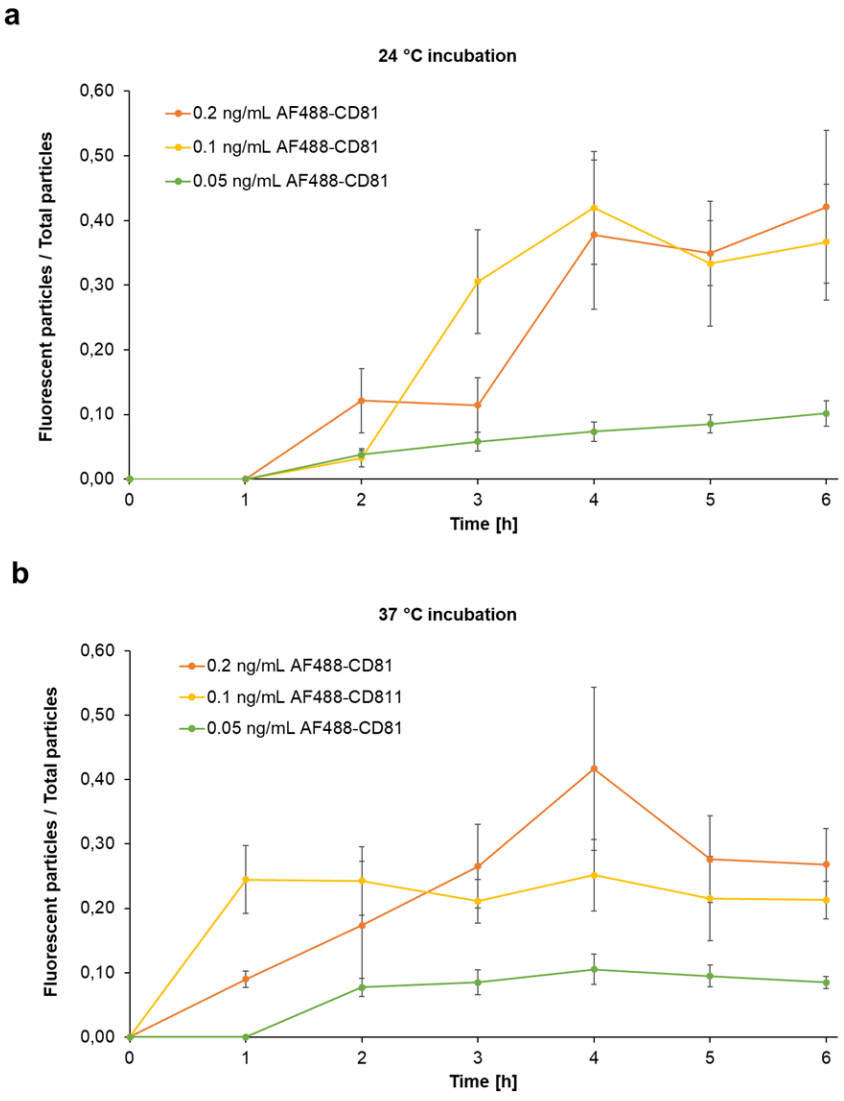

Figure 4-9: SEC-purified EVs from untreated cells incubation with varying amounts of AF488-CD81 and for different times at 24 °C (**a**) and at 37 °C (**b**) (mean ± SD, n = 3, software: ZetaView 8.05.05 SP2).

To obviate these limitations, we decided to incubate AF488-CD81 with the EV-pellet resuspended after UC, right before the SEC purification we perform regardless (**Figure 4-10a**). While the total AF488-CD81 labeled particles were seemingly fewer than before, the reliability and precision of the measurement were inarguably superior. The biggest drawback for this incubation strategy is the limited number of EV-pellets that can be obtained in one day for any HSC treatment condition; additionally, it slows down the already time-limiting SEC step. However, the benefit of measuring purified samples outweighs all other considerations. There was no significant difference between 3 and 5 h incubation times, other than the smaller standard deviations for the latter instance, which is why we chose it for further experiments.

Since 8 ng/mL resulted in higher labelling, that concentration was used when we looked at CD81 and CD9 labeling both separately and combined (**Figure 4-10b**). While we can neither confirm nor exclude co-localization of the two markers on a single EV, the combined results suggest that there is some incomplete overlap. This means that double or even triple staining with exosomal markers might be a viable strategy to cover 100% of the particles detected in scatter mode for a sample of pure exomes.

As a final step, we compared the performance of our newly developed f-NTA methods to the analysis of EV-markers by FACS (where we had used 6 ng/mL of AF488-CD9) (**Figure 4-10c**). Both methods detected CD9 positive events in all of the samples, regardless of the treatment undergone by the cells prior to EV harvest. This meant that we had now validated the presence of exosomal markers in our EV populations by three different means (proteomics, FACS, f-NTA). FACS analysis resulted in higher percentages of fluorescently labelled events compared to f-NTA, but also with considerably higher standard deviations. Our f-NTA methods on the other hand performed more reliably, especially considering that there were no false positives, i.e., no particles could be detected in samples incubated with isotype controls (IC).

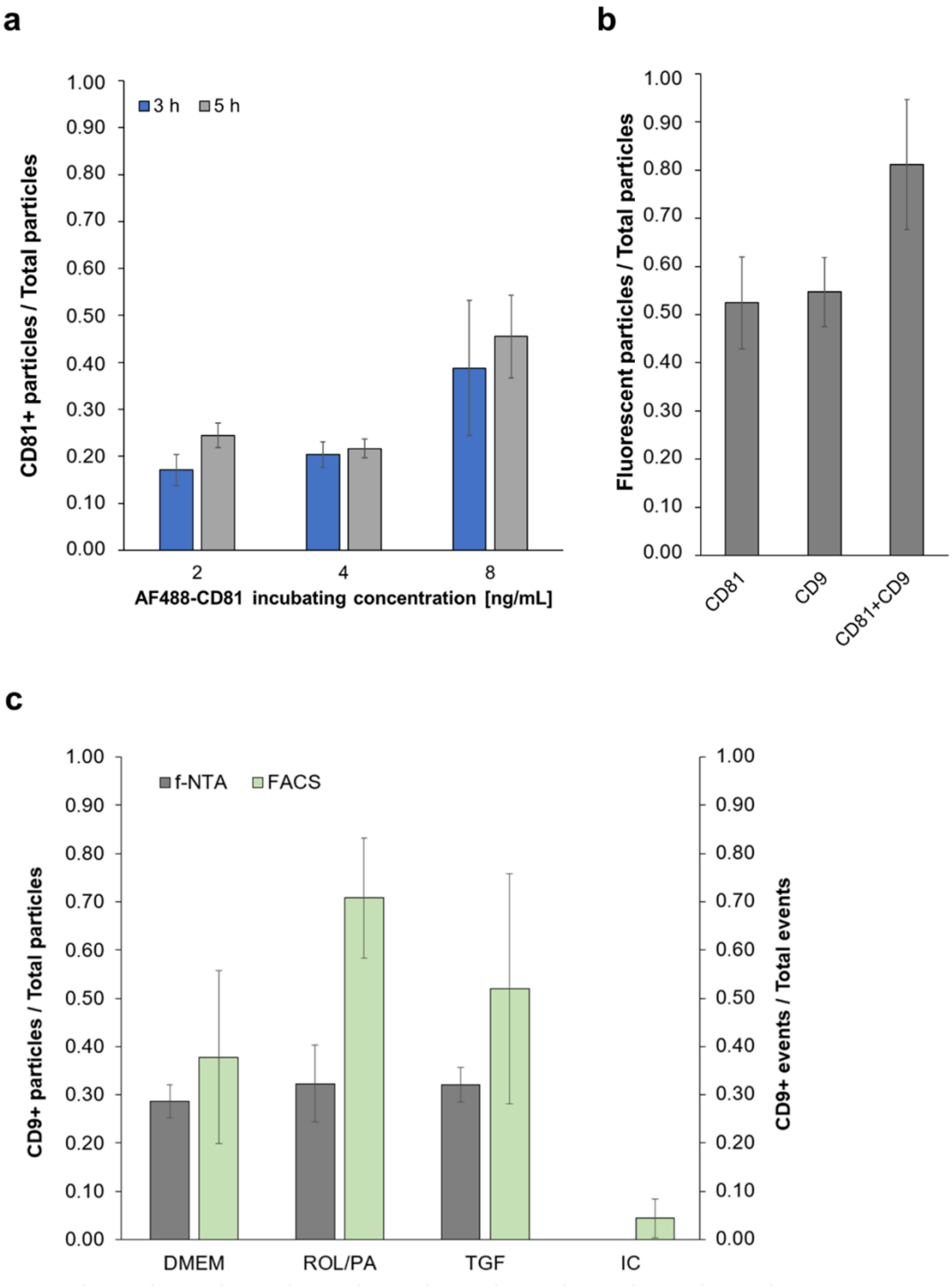

Figure 4-10: EV-containing pellets of untreated cells incubated with AF488-CD81 prior to SEC and detected after purification (**a**). The optimized conditions were then applied for the detection of CD81 and CD9, separately and combined (**b**). For CD9, a direct comparison with FACS is provided, using EVs from differently treated LX-2 (**c**) (mean ± SD, n = 3, software: ZetaView 8.05.05 SP2).

4.3.6. Detection of SPARC on EVs

Our optimized immunolabeling methods for the detection of proteins on single EVs by f-NTA could be transferred to check for the presence of SPARC on EVs isolated from differently treated LX-2 cells. Remarkably, f-NTA measurements were consistent with proteomic findings, and the presence of SPARC on EVs was reproducibly different for different treatment groups, with HEPES and TGF samples having the highest amounts, and S80 especially having hardly any (**Figure 4-11**). We thus found that S80 greatly reduces the relative presence of SPARC-positive EVs, either because it acts to actively suppress it, or because its mechanism of actions results in its lowered expression. SPARC presence in EV-samples from DOPC-treated cells was also decidedly lower than for HEPES and TGF in our f-NTA measurements. Additionally, Ela and OA treatments caused a striking increase in the relative amounts of SPARC-positive EVs, which was countered by DOPC to some extent, and even better by S80. These results are in agreement with our observations from **4.3.2**, where PPCs were seemingly able to rescue LX-2 cells from toxic concentrations of either drug. It is now also evident that even 150 nM concentrations of Ela and OA elicit a significant response from the HSCs, measurable by analytical evaluation of their EVs.

We do not know by which mechanism is SPARC being incorporated onto EVs. The higher presence in some of our samples but not in others could be directly linked to an increased expression of the protein. It could also be due to an improved affinity to EV-surface, either because of treatment-induced changes in EV-composition or because of treatment-induced differences in the extracellular chemical environment, which might lead to a worsening of SPARC's affinity to the extracellular matrix for example.

Nevertheless, these results prove that f-NTA could be used for a quantitatively meaningful detection of physiologically relevant EV-associated proteins, by incorporating the incubation of secondary antibodies into rigorously established EV isolation and purification steps, ultimately providing a convenient alternative to more time-consuming and hands-on heavy western blot and flow cytometry protocols.

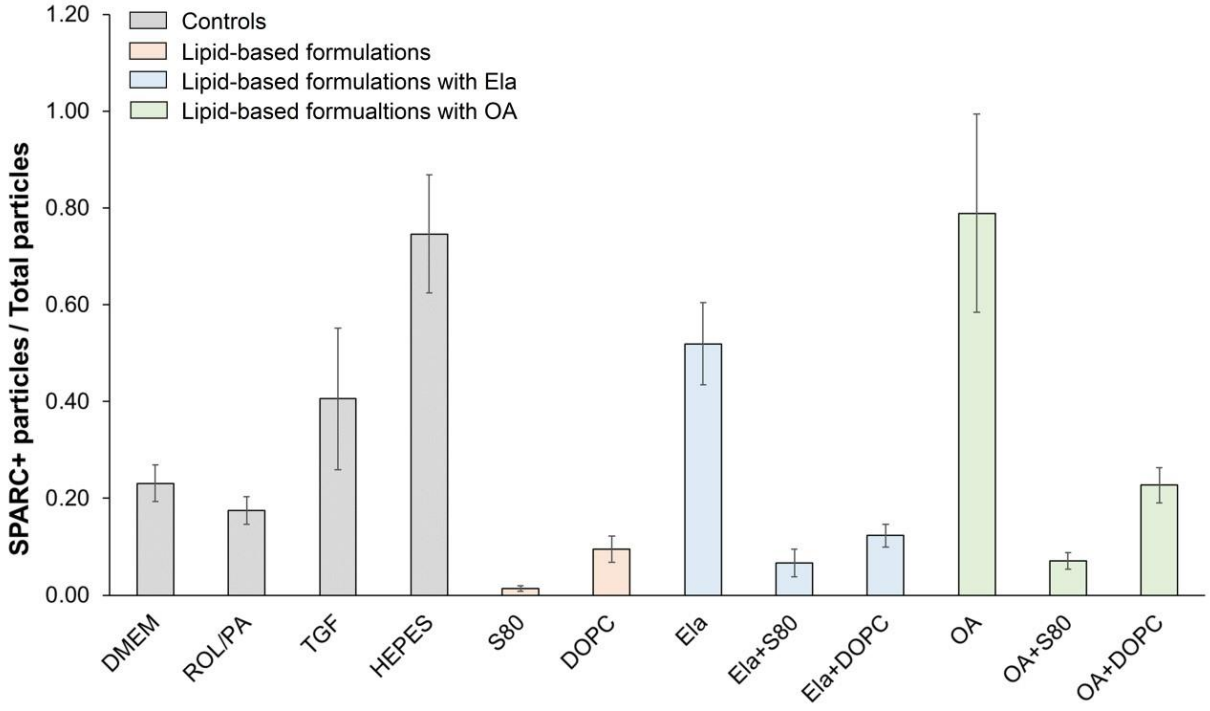

Figure 4-11: Detection of SPARC on EVs isolated from differently treated LX-2 cells (mean ± SD, n = 3, software: ZetaView 8.05.05 SP2).

4.4. Conclusions

After establishing the compatibility of Ela and OA with our liposome-production methods we showed that lipid-vesicles could successfully be loaded with Ela and OA. A reliable quantification can be achieved with concentrations greater than 50 µM. Given that Ela has a λ_{abs} = 358 nm, it was also possible to create a precise calibration curve (in the same concentration range) using a plate reader (**Figure A4-3**). Lipid vesicles were all monodisperse, around 150 nm in size, and stable at 4 °C for 21 d.

The effect of the drugs on the LX-2 cells could not be effectively screened to find a range of pharmaceutically effective concentrations, nor to unequivocally determine the toxic point of no return by CCK-8 assay. The drugs' effect alone and in combination with PPC-liposomes was explored by ORO/DAPI-staining of cytoplasmic lipid droplets and cell nuclei. While there was little toxicity shown with CCK-8 up to 75 µM concentrations, ORO/DAPI staining showed that higher drug concentrations (above 50 µM) are indeed detrimental to cells. Remarkably though, S80 in particular seems to be able to rescue them.

The beneficial effect of drugs such as OA and Ela will have to be determined by different means of screening. Cellular ROS was explored as an option but the protocols would require substantial improvements before being applicable. However, there is also a possibility that there is no beneficial effect to detect from Ela and OA in our in vitro model. While most of previous research was optimistic about the antifibrotic potential of Ela and OA,[35,36,367–373,409] most recent results show that both drugs have failed to meet expectations of significant improvement over placebo treatments in clinical trials.[374,410,411] While confirming previously obtained safety data, the use of Ela did not meet the primary endpoint of NASH resolution without worsening the fibrosis in 1'070 patients in the intended-to-treat (ITT) population. The use of Ela resulted in positive outcomes in 19.2% of patients receiving it, which was not significantly better than the 14.7% for placebo-treated patients. Genfit has accordingly decided to refocus Ela approval for primary biliary cholangitis alone for now, while revisiting their previous experimental findings. For OA, Intercept Pharmaceuticals was recently denied accelerated approval for the treatment of NASH-related hepatic fibrosis. The Food and Drug Agency (FDA) stated that, with the data at hand, predicted benefits of OA remain uncertain, and they do not sufficiently outweigh potential risks to support accelerated approval.

Having developed an optimized protocol for the detection of EV-associated proteins using fluorescently labeled secondary antibodies, we were ready to apply it to proteins selected from the proteomic analysis on HSC-EVs from **Chapter 3**. SPARC was rationally selected as a proof-of-concept protein to successfully explore the feasibility of using f-NTA as a non-destructive tool for the aforementioned discriminatory exercise, considering SPARC's pathophysiological roles. By thus looking into the relative presence of SPARC-positive EVs, we found that S80 greatly reduces it, either because S80 acts to actively suppress it, or because S80's mechanism of action results in SPARC's lowered expression.

NTA systems with more than one laser and fluorescence channel would allow for the almost simultaneous analysis of multiple EV-associated, physiologically relevant proteins, provided they are

labelled with non-interfering dyes. Our results pave the way for more precise ex vivo analyses: markers related to diseased and healthy states, as well as proteins that are tissue specific or preferentially expressed by specific cells could all be conceivably checked within one EV sample if appropriately selected. Our optimized f-NTA method could already be used to quantitatively assess the performance of drugs and anti-fibrotic PPCs, while also providing novel insights into their mode of action, most notably that of S80. Here, for the first time, we could measurably correlate the cellular response to PPC-treatment to the relative presence of SPARC on the generated EVs.

Chapter 5.
Final Remarks and Future Perspectives

“I was born not knowing
and have had only a little time to change that here and there.”
Richard Feynman

Parts of this chapter are ready to be submitted for publication.

Liver fibrosis is a major global health concern: its evolution into liver cirrhosis is followed by the death of over a million of people every year worldwide. The progressive deposition of collagen rich extracellular matrix often develops into cirrhosis, which predisposes patients to hepatocellular carcinoma (HCC) too. At present, at least a third of patients with NASH-induced cirrhosis die as a result of liver associated issues within 10 years of their onset.[412,413]

The pivotal role of HSCs (the main collagen-producing cells) in liver fibrosis makes them interesting from both a therapeutic and a diagnostic perspective. While there is currently no pharmacological treatment specifically approved for liver fibrosis, the use of EPLs (enriched in PPCs) as supportive therapy has a long history of being applied, even though many questions about their mechanism of action remain open. We have previously reported on the beneficial effect of S80 in particular in deactivating perpetuated HSCs.[46]

With the present work we aimed at further investigating the effect of PPC-based formulation in the context of our optimized in vitro model for liver fibrosis. We shifted the perspective to the impact lipid-based antifibrotic formulations have on the production and characteristics of EVs specifically.

In **Chapter 2** we established thorough, systematically optimized methods for isolating and characterizing EVs released by LX-2 cells under different phenotypical states. This essential work laid the foundation required for more in-depth analysis of the biological role played by HSC-EVs in our model. The heterogeneity of EV samples represents a standing obstacle in the research into distinctive subpopulations, since physical and biochemical properties overlap considerably. We were nevertheless successful in uncovering subtle yet measurable differences in size across samples of EVs originating from differently treated cells by NTA, suggestive of differences in EV-subpopulations within. While distinct EV subpopulations could not be separated, the optimization of protein separation methods by SDS-PAGE gel electrophoresis revealed rich and highly complex profiles that warranted further exploration.

Building upon the findings from the previous chapter, in **Chapter 3** we were able to harvest HSC-EVs and look into the effects EVs isolated from differently treated cells exert onto naïve LX-2. The role of EVs proved to be sufficient to cause phenotypical changes in cells that have not been exposed to treatment solutions directly, mirroring the effects of direct treatment. This means that EVs from HSCs can impact neighboring cells during liver fibrosis. It also means that there must be distinctive features in the biochemical properties of EVs to cause such diverse effects. Their composition holds information that can be unambiguously correlated to the status of the cells that had released them in the first place.

To explore that biochemical information, we followed up the findings from our baseline characterization of EVs and performed shotgun proteomics analysis on EVs originating from differently treated LX-2 cells. The methods we developed for the purpose allowed us to meaningfully profile EVs collected upon diverse cellular treatments as well as EV populations purified by different means, namely SEC and AF4. Many similarities emerged, but distinctions were possible too. A panel of 44 proteins was generated to semi-quantitively discriminate between treatments. Differences between our negative (TGF) and positive (ROL/PA) controls were clear, but differences between TGF and S80 were astounding.

In **Chapter 4**, PPC-based liposomes were formulated alone and with novel drugs Ela and OA. After establishing their successful development, we failed to show beneficial effects of either drug with the methods at hand. At the same time though, we could show that high concentrations were toxic, and yet S80 was able to counter detrimental effects.

Furthermore, we used the comparisons between proteomic profiles of EVs produced by differently treated cells to rationally select single candidate markers. The selection included considerations into the structural properties of the proteins, favoring those that were likely to be found on EV-surface rather than its inner core, thus allowing for their non-destructive detection by f-NTA. The first step in the development of the necessary protocols included the detection of material fluorescently labelled with the PKH67 nonspecific membrane dye. This resulted in the confirmation that our SEC-purified samples detected by NTA were indeed all membranous in nature. The second step involved the successful detection of known exosomal markers, i.e., tetraspanins CD81 and CD9, by f-NTA, and comparing the performance to previously established FACS methods. The final step allowed for the non-destructive detection of the relative presence of SPARC-positive EVs isolated from LX-2 cells that have undergone different treatments.

We could thus prove that S80 greatly reduces relative SPARC-positive EVs' abundance, whereas TGF-treatment does the opposite. We could apply this protocol to evaluate the effect of Ela and OA on their own. Where we had been previously unable to document a meaningful impact on HSCs using nanomolar concentrations of the drugs, we can now see a dramatic response based on a striking increase in SPARC on their EVs. This was especially remarkable when formulating Ela or OA within PPC-based liposomes, since the effect of drug and PPCs alone were each countered by the other to different extents. Confirming observations we first made during fluorescence microscopy experiments, we can now measurably show that S80 can effectively reverse a physiological response elicited by Ela or OA, even if such a response was not perceptible at lower drug concentrations. Moreover, these findings rooted in the analysis of EVs might help shed some light into the non-significant benefits of Ela and OA treatment in patients with NASH in clinical trials. While the potent PPARα/δ and FXR agonism of Ela and OA respectively could be beneficial on their own, they could be opposed by other effects these drugs elicit in HSCs, as measured by relative SPARC presence on their EVs. The mechanisms that lead to SPARC incorporation on EVs shed by LX-2 cells are not known, but for the first time we have clues into EPLs' beneficial impact on fibrotic liver based on EVs.

There are many ways to follow up all of this work. The groundwork from **Chapter 2** begs for further methods of characterization: lipidomic analysis was initiated and not yet successful, but the inspection of RNA or glycosylation patterns has not even been attempted. The investigation into the biological role of EVs started in **Chapter 3**, while plentiful, is far from being exhausted. For one, it would be important to see for how long after treatment do HSCs preserve the phenotypical changes acquired. Importantly, we do not know for how long would their EVs be effective in causing those same phenotypical changes onto naïve cells, and how do the protein profiles of the latter's EVs look like. Although beyond the scope of this

particular study, our proteomic data can be further examined by detailed gene set enrichment analysis (e.g., network and pathway analyses) for all the generated protein lists. We summarized in our tables more than 120 distinctive lists of proteins, all interesting in their own right. Deep learning approaches could be used to sort through different EV-proteomic data to find the minimum, specific signature profile for HSCs, similarly to what had been recently done for the identification of EVs originating from cancer cells.[414]

It would be interesting to optimize methods for the detection of ROS in our in vitro model, as initiated in **Chapter 4**, and possibly expending it to co-culture systems with hepatocytes. Our optimized f-NTA method could be applied to EVs from LX-2 upon even more treatments, effectively screening drug candidates targeting fibrogenesis. While SPARC proved to be an excellent marker for negative impact in our model, having a working candidate protein to report on positive phenotypes would be all the more meaningful, especially with a side-by-side comparison. We have tried selecting proteins from the quiescent-like status list (**Figure 4-1**) which could be detected non-destructively, namely GPC1 and IKKB, but we were unable to detect effective immunolabeling with either one of them by f-NTA. However, there are at least almost 20 more interesting candidates to test. The method could be expended to include multiple EV-associated, clinically relevant proteins, even within the same sample provided they are labelled with non-interfering dyes. While co-localization of single proteins onto single EVs would not be directly measurable by NTA, their collective presence within the same EV samples is already technologically possible to verify.

Our results pave the way for more precise ex vivo analyses: markers related to diseased and healthy states, as well as proteins that are tissue specific or preferentially expressed by specific cells could all be conceivably checked within one EV sample if appropriately selected. Assessing the translational applicability of our protocols for the evaluation of EVs from primary cells, or blood from healthy volunteers or patients would be the most important perspective validation to accomplish.

References

1. Trefts, E., Gannon, M. & Wasserman, D. H. The liver. *Current Biology* **27**, R1147–R1151 (2017).
2. Asrani, S. K., Devarbhavi, H., Eaton, J. & Kamath, P. S. Burden of liver diseases in the world. *Journal of Hepatology* **70**, 151–171 (2019).
3. Pimpin, L. *et al.* Burden of liver disease in Europe: Epidemiology and analysis of risk factors to identify prevention policies. *Journal of Hepatology* **69**, 718–735 (2018).
4. Ndugga, N. *et al.* Disparities between research attention and burden in liver diseases: Implications on uneven advances in pharmacological therapies in Europe and the USA. *BMJ Open* **7**, (2017).
5. Bataller, R. & Brenner, D. A. Liver fibrosis. *Journal of Clinical Investigation* (2005). doi:10.1172/JCI24282
6. Marcellin, P. & Kutala, B. K. Liver diseases: A major, neglected global public health problem requiring urgent actions and large-scale screening. *Liver International* **38**, 2–6 (2018).
7. Hagström, H. *et al.* Fibrosis stage but not NASH predicts mortality and time to development of severe liver disease in biopsy-proven NAFLD. *J. Hepatol.* **67**, 1265–1273 (2017).
8. Poole, L. G., Dolin, C. E. & Arteel, G. E. Organ-Organ Crosstalk and Alcoholic Liver Disease. *Biomolecules* **7**, (2017).
9. Samji, N. S., Verma, R. & Satapathy, S. K. Magnitude of NonAlcoholic Fatty Liver Disease: Western Perspective. *J. Clin. Exp. Hepatol.* (2019). doi:10.1016/J.JCEH.2019.05.001
10. Lemoinne, S., Cadoret, A., El Mourabit, H., Thabut, D. & Housset, C. Origins and functions of liver myofibroblasts. *Biochim. Biophys. Acta - Mol. Basis Dis.* **1832**, 948–954 (2013).
11. Castilla, A., Prieto, J. & Fausto, N. Transforming Growth Factors β1 and α in Chronic Liver Disease. *N. Engl. J. Med.* **324**, 933–940 (1991).
12. Tsuchida, T. & Friedman, S. L. Mechanisms of hepatic stellate cell activation. *Nature Reviews Gastroenterology and Hepatology* **14**, 397–411 (2017).
13. Senoo, H., Mezaki, Y. & Fujiwara, M. The stellate cell system (vitamin A-storing cell system). *Anatomical Science International* **92**, 387–455 (2017).
14. Puche, J. E., Saiman, Y. & Friedman, S. L. Hepatic stellate cells and liver fibrosis. *Compr. Physiol.* (2013). doi:10.1002/cphy.c120035
15. Friedman, S. L. Mechanisms of Hepatic Fibrogenesis. *Gastroenterology* (2008). doi:10.1053/j.gastro.2008.03.003
16. Ju, C. & Tacke, F. Hepatic macrophages in homeostasis and liver diseases: From pathogenesis to novel therapeutic strategies. *Cellular and Molecular Immunology* (2016). doi:10.1038/cmi.2015.104
17. Nguyen-Lefebvre, A. T. & Horuzsko, A. Kupffer Cell Metabolism and Function. *J. Enzymol. Metab.* **1**, (2015).

18. Dixon, L. J., Barnes, M., Tang, H., Pritchard, M. T. & Nagy, L. E. Kupffer cells in the liver. *Compr. Physiol.* (2013). doi:10.1002/cphy.c120026
19. Chen, L. *et al.* Epigenetic regulation of connective tissue growth factor by MicroRNA-214 delivery in exosomes from mouse or human hepatic stellate cells. *Hepatology* **59**, 1118–29 (2014).
20. Baranova, A., Lal, P., Birerdinc, A. & Younossi, Z. M. Non-Invasive markers for hepatic fibrosis. *BMC Gastroenterology* **11**, 91 (2011).
21. Chang, T. T. *et al.* Long-term entecavir therapy results in the reversal of fibrosis/cirrhosis and continued histological improvement in patients with chronic hepatitis B. *Hepatology* **52**, 886–893 (2010).
22. Yin, C., Evason, K. J., Asahina, K. & Stainier, D. Y. R. Hepatic stellate cells in liver development, regeneration, and cancer. *Journal of Clinical Investigation* **123**, 1902–1910 (2013).
23. Bataller, R. & Brenner, D. A. Hepatic stellate cells as a target for the treatment of liver fibrosis. *Seminars in Liver Disease* **21**, 437–451 (2001).
24. Parola, M. & Pinzani, M. Liver fibrosis: Pathophysiology, pathogenetic targets and clinical issues. *Molecular Aspects of Medicine* **65**, 37–55 (2019).
25. Mescher, L. A. *Junqueira's Basic Histology. Text and Atlas 14th edition*. *Junqueira's Basic Histology: Text and Atlas* (2016).
26. Altamirano-Barrera, A., Barranco-Fragoso, B. & Méndez-Sánchez, N. Management strategies for liver fibrosis. *Ann. Hepatol.* **16**, 48–56 (2017).
27. Paul, S. & Davis, A. M. Diagnosis and Management of Nonalcoholic Fatty Liver Disease. *JAMA* **320**, 2474 (2018).
28. Montano-Loza, A. J., Thandassery, R. B. & Czaja, A. J. Targeting Hepatic Fibrosis in Autoimmune Hepatitis. *Digestive Diseases and Sciences* **61**, 3118–3139 (2016).
29. Czaja, A. J. & Carpenter, H. A. Decreased fibrosis during corticosteroid therapy of autoimmune hepatitis. in *Journal of Hepatology* **40**, 646–652 (Elsevier, 2004).
30. Bowlus, C. L., Kenney, J. T., Rice, G. & Navarro, R. Primary biliary cholangitis: Medical and specialty pharmacy management update. *J. Manag. Care Spec. Pharm.* (2016). doi:10.18553/jmcp.2016.22.10-a-s.s3
31. Lefebvre, E. *et al.* Antifibrotic effects of the dual CCR2/CCR5 antagonist cenicriviroc in animal models of liver and kidney fibrosis. *PLoS One* (2016). doi:10.1371/journal.pone.0158156
32. Pedrosa, M. *et al.* A randomized, double-blind, multicenter, phase 2b study to evaluate the safety and efficacy of a combination of tropifexor and cenicriviroc in patients with nonalcoholic steatohepatitis and liver fibrosis: Study design of the TANDEM trial. *Contemp. Clin. Trials* **88**, (2020).
33. Anstee, Q. M. *et al.* Cenicriviroc for the treatment of liver fibrosis in adults with nonalcoholic steatohepatitis: AURORA Phase 3 study design. *Contemp. Clin. Trials* **89**, (2020).
34. Tully, D. C. *et al.* Discovery of Tropifexor (LJN452), a Highly Potent Non-bile Acid FXR Agonist for

the Treatment of Cholestatic Liver Diseases and Nonalcoholic Steatohepatitis (NASH). *J. Med. Chem.* **60**, 9960–9973 (2017).

35. Neuschwander-Tetri, B. A. *et al.* Farnesoid X nuclear receptor ligand obeticholic acid for non-cirrhotic, non-alcoholic steatohepatitis (FLINT): A multicentre, randomised, placebo-controlled trial. *Lancet* (2015). doi:10.1016/S0140-6736(14)61933-4
36. Ratziu, V. *et al.* Elafibranor, an Agonist of the Peroxisome Proliferator-Activated Receptor-α and -δ, Induces Resolution of Nonalcoholic Steatohepatitis Without Fibrosis Worsening. *Gastroenterology* (2016). doi:10.1053/j.gastro.2016.01.038
37. Gundermann, K. J., Kuenker, A., Kuntz, E. & Drożdzik, M. Activity of essential phospholipids (EPL) from soybean in liver diseases. *Pharmacological Reports* **63**, 643–659 (2011).
38. Dajani, A. I. M. *et al.* Essential phospholipids as a supportive adjunct in the management of patients with NAFLD. *Arab J. Gastroenterol.* **16**, 99–104 (2015).
39. Poniachik, J., Baraona, E., Zhao, J. & Lieber, C. S. Dilinoleoylphosphatidylcholine decreases hepatic stellate cell activation. *J. Lab. Clin. Med.* **133**, 342–348 (1999).
40. Gundermann, K. J., Gundermann, S., Drozdzik, M. & Mohan Prasad, V. G. Essential phospholipids in fatty liver: A scientific update. *Clinical and Experimental Gastroenterology* **9**, 105–117 (2016).
41. Varganova, D. L., Pavlov, C. S., Casazza, G., Nikolova, D. & Gluud, C. Essential phospholipids for people with non-alcoholic fatty liver disease (Protocol). *Cochrane Database Syst. Rev.* **2019**, (2019).
42. Aleynik, S. I., Leo, M. A., Ma, X., Aleynik, M. K. & Lieber, C. S. Polyenylphosphatidylcholine prevents carbon tetrachloride-induced lipid peroxidation while it attenuates liver fibrosis. *J. Hepatol.* **27**, 554–561 (1997).
43. Aleynik, S. I., Leo, M. A., Aleynik, M. K. & Lieber, C. S. Polyenylphosphatidylcholine protects against alcohol but not iron- induced oxidative stress in the liver. *Alcohol. Clin. Exp. Res.* (2000). doi:10.1097/00000374-200002000-00010
44. Aleynik, S. I. & Lieber, C. S. Polyenylphosphatidylcholine corrects the alcohol-induced hepatic oxidative stress by restorings s-adenosylmethionine. *Alcohol Alcohol.* (2003). doi:10.1093/alcalc/agg066
45. Ikeda, R. *et al.* Reactive oxygen species and NADPH oxidase 4 induced by transforming growth factor β1 are the therapeutic targets of polyenylphosphatidylcholine in the suppression of human hepatic stellate cell activation. *Inflamm. Res.* **60**, 597–604 (2011).
46. Valentino, G., Zivko, C., Weber, F., Brülisauer, L. & Luciani, P. Synergy of Phospholipid—Drug Formulations Significantly Deactivates Profibrogenic Human Hepatic Stellate Cells. *Pharmaceutics* **11**, 676 (2019).
47. Pellicoro, A., Ramachandran, P., Iredale, J. P. & Fallowfield, J. A. Liver fibrosis and repair: Immune regulation of wound healing in a solid organ. *Nature Reviews Immunology* **14**, 181–194

(2014).

48. Cheng, J. Y.-K. & Wong, G. L.-H. Advances in the diagnosis and treatment of liver fibrosis. *Hepatoma Res.* **3**, 156 (2017).
49. Tana, M. M. & Muir, A. J. Diagnosing Liver Fibrosis and Cirrhosis: Serum, Imaging, or Tissue? *Clin. Gastroenterol. Hepatol.* **16**, 16–18 (2018).
50. Suzuki, K., Yoneda, M., Imajo, K. & al., et. Transient elastography for monitoring the fibrosis of non-alcoholic fatty liver disease for 4 years. *Hepatol Res* **43**, 979–983 (2013).
51. Friedrich-Rust, M., Ong, M. F., Martens, S. & al., et. Performance of transient elastography for the staging of liver fibrosis: a meta-analysis. *Gastroenterology* **134**, 960–974 (2008).
52. Tovo, C. V. *et al.* Transient hepatic elastography has the best performance to evaluate liver fibrosis in non-alcoholic fatty liver disease (NAFLD). *Ann. Hepatol.* **18**, 445–449 (2019).
53. Liu, J. *et al.* Comparison of Two-Dimensional Shear Wave Elastography with Nine Serum Fibrosis Indices to Assess Liver Fibrosis in Patients with Chronic Hepatitis B: A Prospective Cohort Study. *Ultraschall der Medizin - Eur. J. Ultrasound* **40**, 237–246 (2019).
54. Jamialahmadi, T. *et al.* Measurement of Liver Stiffness with 2D-Shear Wave Elastography (2D-SWE) in Bariatric Surgery Candidates Reveals Acceptable Diagnostic Yield Compared to Liver Biopsy. *Obes. Surg.* 1–8 (2019). doi:10.1007/s11695-019-03889-2
55. Kang, H.-J. *et al.* Addition of Reliability Measurement Index to Point Shear Wave Elastography: Prospective Validation via Diagnostic Performance and Reproducibility. *Ultrasound Med. Biol.* (2019). doi:10.1016/j.ultrasmedbio.2019.03.007
56. Zhan;, S. X. R. N., Ren, X., Ni, Z. & Zhan, W. A Noninvasive Method—shear-wave Elastography Compared With Transient Elastography in Evaluation of Liver Fibrosis in Patients With Chronic Hepatitis B. *Ultrasound Q.* **35**, 147–152 (2019).
57. Nightingale, K. Acoustic Radiation Force Impulse (ARFI) Imaging: A Review. *Curr. Med. Imaging Rev.* (2011). doi:10.2174/157340511798038657
58. D'Onofrio, M. *et al.* Acoustic radiation force impulse of the liver. *World Journal of Gastroenterology* (2013). doi:10.3748/wjg.v19.i30.4841
59. Friedrich-Rust, M. *et al.* Performance of Acoustic Radiation Force Impulse imaging for the staging of liver fibrosis: A pooled meta-analysis. *J. Viral Hepat.* (2012). doi:10.1111/j.1365-2893.2011.01537.x
60. Wai, C. T. *et al.* A simple noninvasive index can predict both significant fibrosis and cirrhosis in patients with chronic hepatitis C. *Hepatology* **38**, 518–526 (2003).
61. Witwer, K. W. & Théry, C. Extracellular vesicles or exosomes? On primacy, precision, and popularity influencing a choice of nomenclature. *Journal of Extracellular Vesicles* **8**, (2019).
62. Théry, C. *et al.* Minimal information for studies of extracellular vesicles 2018 (MISEV2018): a position statement of the International Society for Extracellular Vesicles and update of the MISEV2014 guidelines. *J. Extracell. vesicles* **7**, 1535750 (2018).

63. Van Niel, G., D'Angelo, G. & Raposo, G. Shedding light on the cell biology of extracellular vesicles. *Nature Reviews Molecular Cell Biology* **19**, 213–228 (2018).
64. Stahl, P. D. & Raposo, G. Extracellular Vesicles: Exosomes and Microvesicles, Integrators of Homeostasis. *Physiology* **34**, 169–177 (2019).
65. Stahl, P. D. & Raposo, G. Exosomes and extracellular vesicles: The path forward. *Essays in Biochemistry* (2018). doi:10.1042/EBC20170088
66. Zhang, H. *et al.* Identification of distinct nanoparticles and subsets of extracellular vesicles by asymmetric flow field-flow fractionation. *Nat. Cell Biol.* **20**, 332–343 (2018).
67. Pinheiro, A. *et al.* Extracellular vesicles: intelligent delivery strategies for therapeutic applications. *Journal of Controlled Release* **289**, 56–69 (2018).
68. Takahashi, Y. & Takakura, Y. Development of exosome-based DDS targeting gastrointestinal cancer. *Drug Deliv. Syst.* **33**, 372–376 (2018).
69. Zhang, Y., Liu, Y., Liu, H. & Tang, W. H. Exosomes: Biogenesis, biologic function and clinical potential. *Cell and Bioscience* **9**, 2–18 (2019).
70. Zhao, Z. *et al.* Extracellular vesicles as cancer liquid biopsies: From discovery, validation, to clinical application. *Lab on a Chip* **19**, 1114–1140 (2019).
71. Urban, S. K., Mocan, T., Sänger, H., Lukacs-Kornek, V. & Kornek, M. Extracellular Vesicles in Liver Diseases: Diagnostic, Prognostic, and Therapeutic Application. *Semin. Liver Dis.* **39**, 70–77 (2019).
72. Barile, L. & Vassalli, G. Exosomes: Therapy delivery tools and biomarkers of diseases. *Pharmacol. Ther.* **174**, 63–78 (2017).
73. Kawamura, Y., Yamamoto, Y., Sato, T. A. & Ochiya, T. Extracellular vesicles as trans-genomic agents: Emerging roles in disease and evolution. *Cancer Science* **108**, 824–830 (2017).
74. Ono, R. *et al.* Exosome-mediated horizontal gene transfer occurs in double-strand break repair during genome editing. *Commun. Biol.* **2**, (2019).
75. Woith, E., Fuhrmann, G. & Melzig, M. F. Extracellular vesicles—connecting kingdoms. *International Journal of Molecular Sciences* **20**, (2019).
76. Povero, D. *et al.* Circulating extracellular vesicles with specific proteome and liver microRNAs are potential biomarkers for liver injury in experimental fatty liver disease. *PLoS One* **9**, (2014).
77. Urban, S., Mocan, T., Sänger, H., Lukacs-Kornek, V. & Kornek, M. Extracellular Vesicles in Liver Diseases: Diagnostic, Prognostic, and Therapeutic Application. *Semin. Liver Dis.* **39**, 070–077 (2019).
78. Sung, S., Kim, J. & Jung, Y. Liver-derived exosomes and their implications in liver pathobiology. *International Journal of Molecular Sciences* **19**, (2018).
79. Sato, K. *et al.* Intercellular communication between hepatic cells in liver diseases. *Int. J. Mol. Sci.* **20**, (2019).
80. Deng, F., Magee, N. & Zhang, Y. Decoding the role of extracellular vesicles in liver diseases. *Liver*

Research **1**, 147–155 (2017).

81. Sung, S., Kim, J. & Jung, Y. Liver-Derived Exosomes and Their Implications in Liver Pathobiology. *Int. J. Mol. Sci.* **19**, (2018).
82. Qiu, Y. *et al.* Blood-based novel biomarkers for nonalcoholic steatohepatitis. *Biomark. Med.* **12**, 501–515 (2018).
83. Falcon-Perez, J. M. & Royo, F. Circulating RNA: looking at the liver through a frosted glass. *Biomarkers* **20**, 339–354 (2015).
84. Masyuk, A. I., Masyuk, T. V. & LaRusso, N. F. Exosomes in the pathogenesis, diagnostics and therapeutics of liver diseases. *J. Hepatol.* **59**, 621–625 (2013).
85. Mann, J., Reeves, H. L. & Feldstein, A. E. Liquid biopsy for liver diseases. *Gut* **67**, 2204–2212 (2018).
86. Sato, K. *et al.* Intercellular Communication between Hepatic Cells in Liver Diseases. *Int. J. Mol. Sci.* **20**, 2180 (2019).
87. Lemoinne, S. *et al.* The emerging roles of microvesicles in liver diseases. *Nat. Rev. Gastroenterol. Hepatol.* **11**, 350–361 (2014).
88. Berardocco, M. *et al.* RNA-seq reveals distinctive RNA profiles of small extracellular vesicles from different human liver cancer cell lines. *Oncotarget* **8**, 82920–82939 (2017).
89. Kogure, T., Lin, W.-L., Yan, I. K., Braconi, C. & Patel, T. Intercellular nanovesicle-mediated microRNA transfer: A mechanism of environmental modulation of hepatocellular cancer cell growth. *Hepatology* **54**, 1237–1248 (2011).
90. Kogure, T., Yan, I. K., Lin, W.-L. & Patel, T. Extracellular Vesicle-Mediated Transfer of a Novel Long Noncoding RNA TUC339: A Mechanism of Intercellular Signaling in Human Hepatocellular Cancer. *Genes Cancer* **4**, 261–72 (2013).
91. Xiao, W.-H. *et al.* Effect of 5-aza-2'-deoxycytidine on immune-associated proteins in exosomes from hepatoma. *World J. Gastroenterol.* **16**, 2371–7 (2010).
92. Xiao, W. *et al.* Effects of the epigenetic drug MS-275 on the release and function of exosome-related immune molecules in hepatocellular carcinoma cells. *Eur. J. Med. Res.* **18**, 61 (2013).
93. Cho, Y.-E. *et al.* Increased liver-specific proteins in circulating extracellular vesicles as potential biomarkers for drug- and alcohol-induced liver injury. *PLoS One* **12**, e0172463 (2017).
94. Rao, Q. *et al.* Tumor-derived exosomes elicit tumor suppression in murine hepatocellular carcinoma models and humans *in vitro*. *Hepatology* **64**, 456–472 (2016).
95. Wei, J. *et al.* Vps4A functions as a tumor suppressor by regulating the secretion and uptake of exosomal microRNAs in human hepatoma cells. *Hepatology* **61**, 1284–1294 (2015).
96. Zhang, J. *et al.* Motile hepatocellular carcinoma cells preferentially secret sugar metabolism regulatory proteins via exosomes. *Proteomics* **17**, 1700103 (2017).
97. Eguchi, A. *et al.* Extracellular vesicles released by hepatocytes from gastric infusion model of alcoholic liver disease contain a MicroRNA barcode that can be detected in blood. *Hepatology* **65**,

475–490 (2017).

98. Fang, J. *et al.* Hepatoma cell-secreted exosomal microRNA-103 increases vascular permeability and promotes metastasis by targeting junction proteins. *Hepatology* **68**, 1459–1475 (2018).
99. Fang, T. *et al.* Tumor-derived exosomal miR-1247-3p induces cancer-associated fibroblast activation to foster lung metastasis of liver cancer. *Nat. Commun.* **9**, 191 (2018).
100. Huang, A. *et al.* Exosomal transfer of vasorin expressed in hepatocellular carcinoma cells promotes migration of human umbilical vein endothelial cells. *Int. J. Biol. Sci.* **11**, 961–9 (2015).
101. Lv, L.-H. *et al.* Anticancer drugs cause release of exosomes with heat shock proteins from human hepatocellular carcinoma cells that elicit effective natural killer cell antitumor responses in vitro. *J. Biol. Chem.* **287**, 15874–85 (2012).
102. Povero, D. *et al.* Lipid-induced toxicity stimulates hepatocytes to release angiogenic microparticles that require Vanin-1 for uptake by endothelial cells. *Sci. Signal.* **6**, ra88 (2013).
103. Povero, D. *et al.* Lipid-Induced Hepatocyte-Derived Extracellular Vesicles Regulate Hepatic Stellate Cells via MicroRNA Targeting Peroxisome Proliferator-Activated Receptor-γ. *Cmgh* **1**, 646-663.e4 (2015).
104. Raji, G. R. *et al.* Horizontal transfer of miR-106a/b from cisplatin resistant hepatocarcinoma cells can alter the sensitivity of cervical cancer cells to cisplatin. *Cell. Signal.* **38**, 146–158 (2017).
105. Tomiyama, T. *et al.* The modulation of co-stimulatory molecules by circulating exosomes in primary biliary cirrhosis. *Cell. Mol. Immunol.* **14**, 276 (2017).
106. Thacker, S. E., Nautiyal, M., Otieno, M. A., Watkins, P. B. & Mosedale, M. Optimized Methods to Explore the Mechanistic and Biomarker Potential of Hepatocyte-Derived Exosomes in Drug-Induced Liver Injury. *Toxicol. Sci.* **163**, 92–100 (2018).
107. Verma, V. K. *et al.* Alcohol stimulates macrophage activation through caspase-dependent hepatocyte derived release of CD40L containing extracellular vesicles. *J. Hepatol.* **64**, 651–660 (2016).
108. Xu, Y. *et al.* miR-200a targets Gelsolin: A novel mechanism regulating secretion of microvesicles in hepatocellular carcinoma cells. *Oncol. Rep.* **37**, 2711–2719 (2017).
109. Cannito, S. *et al.* Microvesicles released from fat-laden cells promote activation of hepatocellular NLRP3 inflammasome: A pro-inflammatory link between lipotoxicity and non-alcoholic steatohepatitis. *PLoS One* **12**, e0172575 (2017).
110. Cao, Y. *et al.* A catalytic molecule machine-driven biosensing method for amplified electrochemical detection of exosomes. *Biosens. Bioelectron.* **141**, 111397 (2019).
111. Cheng, L. *et al.* Exosomes from Melatonin Treated Hepatocellularcarcinoma Cells Alter the Immunosupression Status through STAT3 Pathway in Macrophages. *Int. J. Biol. Sci.* **13**, 723–734 (2017).
112. Takahashi, K., Yan, I. K., Kogure, T., Haga, H. & Patel, T. Extracellular vesicle-mediated transfer of long non-coding RNA ROR modulates chemosensitivity in human hepatocellular cancer. *FEBS*

Open Bio **4**, 458–67 (2014).

113. Zhou, Y. *et al.* Hepatocellular carcinoma-derived exosomal miRNA-21 contributes to tumor progression by converting hepatocyte stellate cells to cancer-associated fibroblasts. *J. Exp. Clin. Cancer Res.* **37**, 324 (2018).
114. Liu, H. *et al.* Tumor-derived exosomes promote tumor self-seeding in hepatocellular carcinoma by transferring miRNA-25-5p to enhance cell motility. *Oncogene* **37**, 4964–4978 (2018).
115. Cobb, D. A., Kim, O.-K., Golden-Mason, L., Rosen, H. R. & Hahn, Y. S. Hepatocyte-derived exosomes promote T follicular regulatory cell expansion during hepatitis C virus infection. *Hepatology* **67**, 71–85 (2018).
116. Devhare, P. B. & Ray, R. B. Extracellular vesicles: Novel mediator for cell to cell communications in liver pathogenesis. *Mol. Aspects Med.* **60**, 115–122 (2018).
117. He, M. *et al.* Hepatocellular carcinoma-derived exosomes promote motility of immortalized hepatocyte through transfer of oncogenic proteins and RNAs. *Carcinogenesis* **36**, 1008–1018 (2015).
118. Conigliaro, A. *et al.* CD90+ liver cancer cells modulate endothelial cell phenotype through the release of exosomes containing H19 lncRNA. *Mol. Cancer* **14**, 155 (2015).
119. Kapoor, N. R. *et al.* The HBx gene of hepatitis B virus can influence hepatic microenvironment via exosomes by transferring its mRNA and protein. *Virus Res.* **240**, 166–174 (2017).
120. Fang, J. H. *et al.* Hepatoma cell-secreted exosomal microRNA-103 increases vascular permeability and promotes metastasis by targeting junction proteins. *Hepatology* **68**, 1459–1475 (2018).
121. Wu, J.-Y. *et al.* Exosome-Mimetic Nanovesicles from Hepatocytes promote hepatocyte proliferation in vitro and liver regeneration in vivo. *Sci. Rep.* **8**, 2471 (2018).
122. Rodríguez-Suárez, E. *et al.* Quantitative proteomic analysis of hepatocyte-secreted extracellular vesicles reveals candidate markers for liver toxicity. *J. Proteomics* **103**, 227–40 (2014).
123. Duan, L. *et al.* Role of extracellular vesicles in release of protein adducts after acetaminophen-induced liver injury in mice and humans. *Toxicol. Lett.* **301**, 125–132 (2019).
124. Hirsova, P., Ibrahim, S. H., Gores, G. J. & Malhi, H. Lipotoxic lethal and sublethal stress signaling in hepatocytes: relevance to NASH pathogenesis. *J. Lipid Res.* **57**, 1758–1770 (2016).
125. Ibrahim, S. H. *et al.* Lipid-Induced Signaling Causes Release of Inflammatory Extracellular Vesicles From Hepatocytes. *Gastroenterology* **150**, 956–967 (2016).
126. Nojima, H. *et al.* Chemokine Receptors, CXCR1 and CXCR2, Differentially Regulate Exosome Release in Hepatocytes. *PLoS One* **11**, e0161443 (2016).
127. Nojima, H. *et al.* Hepatocyte exosomes mediate liver repair and regeneration via sphingosine-1-phosphate. *J. Hepatol.* **64**, 60–68 (2016).
128. Li, L.-M., Liu, H., Liu, X.-H., Hu, H.-B. & Liu, S.-M. Clinical significance of exosomal miRNAs and proteins in three human cancers with high mortality in China. *Oncol. Lett.* **17**, 11–22 (2019).

129. Ma, B. *et al.* Murine bone marrow stromal cells pulsed with homologous tumor-derived exosomes inhibit proliferation of liver cancer cells. *Clin. Transl. Oncol.* **14**, 764–773 (2012).
130. Kakazu, E., Mauer, A. S., Yin, M. & Malhi, H. Hepatocytes release ceramide-enriched pro-inflammatory extracellular vesicles in an IRE1α-dependent manner. *J. Lipid Res.* **57**, 233 (2016).
131. Brandon-Warner, E. *et al.* Processing of miR17-92 Cluster in Hepatic Stellate Cells Promotes Hepatic Fibrogenesis During Alcohol-Induced Injury. *Alcohol. Clin. Exp. Res.* **40**, 1430–1442 (2016).
132. Charrier, A. *et al.* Exosomes mediate intercellular transfer of pro-fibrogenic connective tissue growth factor (CCN2) between hepatic stellate cells, the principal fibrotic cells in the liver. *Surg. (United States)* **156**, 548–555 (2014).
133. Wang, X. *et al.* Extracellular mRNA detected by molecular beacons in tethered lipoplex nanoparticles for diagnosis of human hepatocellular carcinoma. *PLoS One* **13**, e0198552 (2018).
134. Witek, R. P. *et al.* Liver Cell–Derived Microparticles Activate Hedgehog Signaling and Alter Gene Expression in Hepatic Endothelial Cells. *Gastroenterology* **136**, 320-330.e2 (2009).
135. Chen, L., Chen, R., Velazquez, V. M. & Brigstock, D. R. Fibrogenic Signaling Is Suppressed in Hepatic Stellate Cells through Targeting of Connective Tissue Growth Factor (CCN2) by Cellular or Exosomal MicroRNA-199a-5p. *Am. J. Pathol.* **186**, 2921–2933 (2016).
136. Chen, L. & Brigstock, D. R. Integrins and heparan sulfate proteoglycans on hepatic stellate cells (HSC) are novel receptors for HSC-derived exosomes. *FEBS Lett.* **590**, 4263–4274 (2016).
137. Lambrecht, J. *et al.* Circulating ECV-Associated miRNAs as Potential Clinical Biomarkers in Early Stage HBV and HCV Induced Liver Fibrosis. *Front. Pharmacol.* **8**, 56 (2017).
138. Povero, D. *et al.* Circulating extracellular vesicles with specific proteome and liver microRNAs are potential biomarkers for liver injury in experimental fatty liver disease. *PLoS One* **9**, e113651 (2014).
139. Chen, L., Chen, R., Kemper, S., Charrier, A. & Brigstock, D. R. Suppression of fibrogenic signaling in hepatic stellate cells by Twist1-dependent microRNA-214 expression: Role of exosomes in horizontal transfer of Twist1. *Am. J. Physiol. Gastrointest. Liver Physiol.* **309**, G491-9 (2015).
140. Arbelaiz, A. *et al.* Serum extracellular vesicles contain protein biomarkers for primary sclerosing cholangitis and cholangiocarcinoma. *Hepatology* **66**, 1125–1143 (2017).
141. Sato, K. *et al.* The role of the secretin/secretin receptor axis in inflammatory cholangiocyte communication via extracellular vesicles. *Sci. Rep.* **7**, 11183 (2017).
142. Li, X. *et al.* Cholangiocyte-derived exosomal long noncoding RNA H19 promotes cholestatic liver injury in mouse and humans. *Hepatology* **68**, 599–615 (2018).
143. Giugliano, S. *et al.* Hepatitis C virus infection induces autocrine interferon signaling by human liver endothelial cells and release of exosomes, which inhibits viral replication. *Gastroenterology* **148**, 392-402.e13 (2015).
144. Li, J. *et al.* Exosomes mediate the cell-to-cell transmission of IFN-α-induced antiviral activity. *Nat.*

Immunol. **14**, 793–803 (2013).

145. Wang, R. *et al.* Exosome Adherence and Internalization by Hepatic Stellate Cells Triggers Sphingosine 1-Phosphate-dependent Migration. *J. Biol. Chem.* **290**, 30684–96 (2015).
146. Aucher, A., Rudnicka, D. & Davis, D. M. MicroRNAs Transfer from Human Macrophages to Hepato-Carcinoma Cells and Inhibit Proliferation. *J. Immunol.* **191**, 6250–60 (2013).
147. Saha, B., Momen-Heravi, F., Kodys, K. & Szabo, G. MicroRNA Cargo of Extracellular Vesicles from Alcohol-exposed Monocytes Signals Naive Monocytes to Differentiate into M2 Macrophages. *J. Biol. Chem.* **291**, 149–59 (2016).
148. Zhou, Y. *et al.* Toll-like receptor 3-activated macrophages confer anti-HCV activity to hepatocytes through exosomes. *FASEB J.* **30**, 4132–4140 (2016).
149. Fonsato, V. *et al.* Human Liver Stem Cell-Derived Microvesicles Inhibit Hepatoma Growth in SCID Mice by Delivering Antitumor MicroRNAs. *Stem Cells* **30**, 1985 (2012).
150. Fonsato, V. *et al.* Human liver stem cell-derived extracellular vesicles enhance cancer stem cell sensitivity to tyrosine kinase inhibitors through Akt/mTOR/PTEN combined modulation. *Oncotarget* **9**, 36151–36165 (2018).
151. Herrera, M. B. *et al.* Human liver stem cell-derived microvesicles accelerate hepatic regeneration in hepatectomized rats. *J. Cell. Mol. Med.* **14**, 1605–18 (2010).
152. Herrera Sanchez, M. B. *et al.* Human liver stem cells and derived extracellular vesicles improve recovery in a murine model of acute kidney injury. *Stem Cell Res. Ther.* **5**, 124 (2014).
153. Herrera Sanchez, M. B. *et al.* Extracellular vesicles from human liver stem cells restore argininosuccinate synthase deficiency. *Stem Cell Res. Ther.* **8**, 176 (2017).
154. Kholia, S. *et al.* Human Liver Stem Cell-Derived Extracellular Vesicles Prevent Aristolochic Acid-Induced Kidney Fibrosis. *Front. Immunol.* **9**, (2018).
155. Lopatina, T. *et al.* Extracellular vesicles from human liver stem cells inhibit tumor angiogenesis. *Int. J. Cancer* **144**, 322–333 (2019).
156. Romagnoli;, F. R. D. S. N.-T. D. R. C. G. M. G. R. M. P. S. C. *et al.* Extracellular Vesicles from Human Liver Stem Cells Reduce Injury in an Ex Vivo Normothermic Hypoxic Rat Liver Perfusion Model. *Transplantation* **102**, e205–e210 (2018).
157. Grange, C. *et al.* Stem cell-derived extracellular vesicles inhibit and revert fibrosis progression in a mouse model of diabetic nephropathy. *Sci. Rep.* **9**, 4468 (2019).
158. Gualerzi, A. *et al.* Raman spectroscopy as a quick tool to assess purity of extracellular vesicle preparations and predict their functionality. *J. Extracell. Vesicles* **8**, 1568780 (2019).
159. Deregibus, M. C. *et al.* Charge-based precipitation of extracellular vesicles. *Int. J. Mol. Med.* **38**, 1359–1366 (2016).
160. Ichinohe, N. *et al.* Transplantation of Thy1 $^{+}$ Cells Accelerates Liver Regeneration by Enhancing the Growth of Small Hepatocyte-Like Progenitor Cells via IL17RB Signaling. *Stem Cells* **35**, 920–931 (2017).

161. Abbate, V. *et al.* HepPar1-Positive Circulating Microparticles Are Increased in Subjects with Hepatocellular Carcinoma and Predict Early Recurrence after Liver Resection. *Int. J. Mol. Sci.* **18**, (2017).
162. Arbelaiz, A. *et al.* Serum extracellular vesicles contain protein biomarkers for primary sclerosing cholangitis and cholangiocarcinoma. *Hepatology* **66**, 1125–1143 (2017).
163. Eldh, M. *et al.* MicroRNA in exosomes isolated directly from the liver circulation in patients with metastatic uveal melanoma. *BMC Cancer* **14**, 962 (2014).
164. Fang, T. *et al.* Tumor-derived exosomal miR-1247-3p induces cancer-associated fibroblast activation to foster lung metastasis of liver cancer. *Nat. Commun.* **9**, 191 (2018).
165. Fornari, F. *et al.* Circulating microRNAs, miR-939, miR-595, miR-519d and miR-494, Identify Cirrhotic Patients with HCC. *PLoS One* **10**, e0141448 (2015).
166. Fu, Q. *et al.* Primary tumor-derived exosomes facilitate metastasis by regulating adhesion of circulating tumor cells via SMAD3 in liver cancer. *Oncogene* **37**, 6105–6118 (2018).
167. Holman, N. S., Mosedale, M., Wolf, K. K., LeCluyse, E. L. & Watkins, P. B. Subtoxic alterations in hepatocyte-derived exosomes: An early step in drug-induced liver injury? *Toxicol. Sci.* **151**, 365–375 (2016).
168. Jiao, C., Jiao, X., Zhu, A., Ge, J. & Xu, X. Exosomal miR-34s panel as potential novel diagnostic and prognostic biomarker in patients with hepatoblastoma. *J. Pediatr. Surg.* **52**, 618–624 (2017).
169. Jiao, X. *et al.* Serum and exosomal miR-122 and miR-199a as a biomarker to predict therapeutic efficacy of hepatitis C patients. *J. Med. Virol.* **89**, 1597–1605 (2017).
170. Kornek, M. *et al.* Circulating Microparticles as Disease-Specific Biomarkers of Severity of Inflammation in Patients With Hepatitis C or Nonalcoholic Steatohepatitis. *Gastroenterology* **143**, 448–458 (2012).
171. Kornek, M., Popov, Y., Libermann, T. A., Afdhal, N. H. & Schuppan, D. Human T cell microparticles circulate in blood of hepatitis patients and induce fibrolytic activation of hepatic stellate cells. *Hepatology* **53**, 230–242 (2011).
172. Kostallari, E. *et al.* Hepatic stellate cell-derived platelet-derived growth factor receptor-alpha-enriched extracellular vesicles promote liver fibrosis in mice through SHP2. *Hepatology* **68**, 333–348 (2018).
173. Banz, Y. *et al.* Endothelial- and Platelet-Derived Microparticles Are Generated During Liver Resection in Humans. *J. Investig. Surg.* **29**, 20–31 (2016).
174. Lambrecht, J. *et al.* Circulating ECV-Associated miRNAs as Potential Clinical Biomarkers in Early Stage HBV and HCV Induced Liver Fibrosis. *Front. Pharmacol.* **8**, 56 (2017).
175. Li, B. *et al.* LncRNA FAL1 promotes cell proliferation and migration by acting as a CeRNA of miR-1236 in hepatocellular carcinoma cells. *Life Sci.* **197**, 122–129 (2018).
176. Li, J. *et al.* Exosomes mediate the cell-to-cell transmission of IFN-$α$-induced antiviral activity. *Nat. Immunol.* **14**, 793–803 (2013).

177. Li, X. *et al.* Cholangiocyte-derived exosomal long noncoding RNA H19 promotes cholestatic liver injury in mouse and humans. *Hepatology* **68**, 599–615 (2018).
178. LI, Y. I. *et al.* Assessment of endogenous reference gene suitability for serum exosomal microRNA expression analysis in liver carcinoma resection studies. *Mol. Med. Rep.* **12**, 4683–4691 (2015).
179. Li, Y. *et al.* Identification of Endogenous Controls for Analyzing Serum Exosomal miRNA in Patients with Hepatitis B or Hepatocellular Carcinoma. *Dis. Markers* **2015**, 1–12 (2015).
180. Li, Y. *et al.* Identification of endogenous controls for analyzing serum exosomal miRNA in patients with hepatitis B or hepatocellular carcinoma. *Dis. Markers* **2015**, 893594 (2015).
181. Liu, W., Chen, S. & Liu, B. Diagnostic and prognostic values of serum exosomal microRNA-21 in children with hepatoblastoma: a Chinese population-based study. *Pediatr. Surg. Int.* **32**, 1059–1065 (2016).
182. Lu, L. *et al.* Abnormal miRNAs Targeting Chromosome Open Reading Frame Genes were Enriched in Microvesicles Derived from the Circulation of HCC. *Biochem. Genet.* **54**, 120–133 (2016).
183. Mastoridis, S. *et al.* Multiparametric Analysis of Circulating Exosomes and Other Small Extracellular Vesicles by Advanced Imaging Flow Cytometry. *Front. Immunol.* **9**, 1583 (2018).
184. Brandon-Warner, E. *et al.* Processing of miR17-92 Cluster in Hepatic Stellate Cells Promotes Hepatic Fibrogenesis During Alcohol-Induced Injury. *Alcohol. Clin. Exp. Res.* **40**, 1430–1442 (2016).
185. Matsuura, K. *et al.* Circulating let-7 levels in plasma and extracellular vesicles correlate with hepatic fibrosis progression in chronic hepatitis C. *Hepatology* **64**, 732–745 (2016).
186. Momen-Heravi, F. *et al.* Increased number of circulating exosomes and their microRNA cargos are potential novel biomarkers in alcoholic hepatitis. *J. Transl. Med.* **13**, 1–13 (2015).
187. Murray, D. D. *et al.* Circulating miR-122 and miR-200a as biomarkers for fatal liver disease in ART-treated, HIV-1-infected individuals. *Sci. Rep.* **7**, 10934 (2017).
188. Payancé, A. *et al.* Hepatocyte microvesicle levels improve prediction of mortality in patients with cirrhosis. *Hepatology* **68**, 1508–1518 (2018).
189. Pu, C. *et al.* Extracellular Vesicle-Associated mir-21 and mir-144 Are Markedly Elevated in Serum of Patients With Hepatocellular Carcinoma. *Front. Physiol.* **9**, 930 (2018).
190. Rautou, P. *et al.* Abnormal Plasma Microparticles Impair Vasoconstrictor Responses in Patients With Cirrhosis. *Gastroenterology* **143**, 166--176.e6 (2012).
191. Rautou, P.-E., Vion, A.-C., Luyendyk, J. P. & Mackman, N. Circulating microparticle tissue factor activity is increased in patients with cirrhosis. *Hepatology* **60**, 1793–1795 (2014).
192. Rega-Kaun, G. *et al.* Changes of Circulating Extracellular Vesicles from the Liver after Roux-en-Y Bariatric Surgery. *Int. J. Mol. Sci.* **20**, 2153 (2019).
193. Saha, B., Momen-Heravi, F., Kodys, K. & Szabo, G. MicroRNA Cargo of Extracellular Vesicles from Alcohol-exposed Monocytes Signals Naive Monocytes to Differentiate into M2 Macrophages.

J. Biol. Chem. **291**, 149–159 (2016).

194. Santangelo, L. *et al.* Hepatitis C virus direct-acting antivirals therapy impacts on extracellular vesicles microRNAs content and on their immunomodulating properties. *Liver Int.* **38**, 1741–1750 (2018).
195. Brodsky, S. V *et al.* Dynamics of circulating microparticles in liver transplant patients. *J. Gastrointestin. Liver Dis.* **17**, 261–268 (2008).
196. Shi, M. *et al.* Decreased levels of serum exosomal miR-638 predict poor prognosis in hepatocellular carcinoma. *J. Cell. Biochem.* **119**, 4711–4716 (2018).
197. Sohn, W. *et al.* Serum exosomal microRNAs as novel biomarkers for hepatocellular carcinoma. *Exp. Mol. Med.* **47**, e184 (2015).
198. Stravitz, R. T. *et al.* Role of procoagulant microparticles in mediating complications and outcome of acute liver injury/acute liver failure. *Hepatology* **58**, 304–313 (2013).
199. Sugimachi, K. *et al.* Identification of a bona fide microRNA biomarker in serum exosomes that predicts hepatocellular carcinoma recurrence after liver transplantation. *Br. J. Cancer* **112**, 532–538 (2015).
200. Sukriti, S. *et al.* Extracellular vesicles from hepatitis B patients serve as reservoir of hepatitis B virus DNA. *J. Viral Hepat.* **26**, 211–214 (2019).
201. Taleb, R. S. Z. *et al.* Quantitative proteome analysis of plasma microparticles for the characterization of HCV-induced hepatic cirrhosis and hepatocellular carcinoma. *PROTEOMICS - Clin. Appl.* **11**, 1700014 (2017).
202. Tomiyama, T. *et al.* The modulation of co-stimulatory molecules by circulating exosomes in primary biliary cirrhosis. *Cell. Mol. Immunol.* **14**, 276 (2017).
203. Wang, H. *et al.* Expression of serum exosomal microRNA-21 in human hepatocellular carcinoma. *Biomed Res. Int.* **2014**, 864894 (2014).
204. Wang, W., Li, H., Zhou, Y. & Jie, S. Peripheral blood microvesicles are potential biomarkers for hepatocellular carcinoma. *Cancer Biomarkers* **13**, 351–357 (2013).
205. Wang, X. *et al.* Extracellular mRNA detected by molecular beacons in tethered lipoplex nanoparticles for diagnosis of human hepatocellular carcinoma. *PLoS One* **13**, e0198552 (2018).
206. Chen, L. *et al.* Therapeutic effects of serum extracellular vesicles in liver fibrosis. *J. Extracell. vesicles* **7**, 1461505 (2018).
207. Welker, M.-W. *et al.* Soluble Serum CD81 Is Elevated in Patients with Chronic Hepatitis C and Correlates with Alanine Aminotransferase Serum Activity. *PLoS One* **7**, e30796 (2012).
208. Welsh, J. A., Scorletti, E., Clough, G. F., Englyst, N. A. & Byrne, C. D. Leukocyte extracellular vesicle concentration is inversely associated with liver fibrosis severity in NAFLD. *J. Leukoc. Biol.* **104**, 631–639 (2018).
209. Xu, H., Dong, X., Chen, Y. & Wang, X. Serum exosomal hnRNPH1 mRNA as a novel marker for hepatocellular carcinoma. *Clin. Chem. Lab. Med.* **56**, 479–484 (2018).

210. Xu, H., Liao, C., Zuo, P., Liu, Z. & Ye, B.-C. Magnetic-Based Microfluidic Device for On-Chip Isolation and Detection of Tumor-Derived Exosomes. *Anal. Chem.* **90**, 13451–13458 (2018).
211. Xue, X., Wang, X., Zhao, Y., Hu, R. & Qin, L. Exosomal miR-93 promotes proliferation and invasion in hepatocellular carcinoma by directly inhibiting TIMP2/TP53INP1/CDKN1A. *Biochem. Biophys. Res. Commun.* **502**, 515–521 (2018).
212. Yang, Y. *et al.* Exosomes mediate hepatitis B virus (HBV) transmission and NK-cell dysfunction. *Cell. Mol. Immunol.* **14**, 465–475 (2017).
213. Yu, L.-X. *et al.* Exosomal microRNAs as potential biomarkers for cancer cell migration and prognosis in hepatocellular carcinoma patient-derived cell models. *Oncol. Rep.* **41**, 257–269 (2019).
214. Zhang, H. *et al.* Exosome circRNA secreted from adipocytes promotes the growth of hepatocellular carcinoma by targeting deubiquitination-related USP7. *Oncogene* **38**, 2844–2859 (2019).
215. Zhang, H. *et al.* Exosome-delivered EGFR regulates liver microenvironment to promote gastric cancer liver metastasis. *Nat. Commun.* **8**, 15016 (2017).
216. Li, L. *et al.* Human bile contains microRNA-laden extracellular vesicles that can be used for cholangiocarcinoma diagnosis. *Hepatology* **60**, 896–907 (2014).
217. Cho, Y. *et al.* Increased ethanol-inducible cytochrome P450-2E1 and cytochrome P450 isoforms in exosomes of alcohol-exposed rodents and patients with alcoholism through oxidative and endoplasmic reticulum stress. *Hepatol. Commun.* **1**, 675 (2017).
218. Deregibus, M. C. *et al.* Charge-based precipitation of extracellular vesicles. *Int. J. Mol. Med.* **38**, 1359–1366 (2016).
219. Duan, L. *et al.* Role of extracellular vesicles in release of protein adducts after acetaminophen-induced liver injury in mice and humans. *Toxicol. Lett.* **301**, 125–132 (2019).
220. Eguchi, A. *et al.* Circulating Extracellular Vesicles and Their miR 'Barcode' Differentiate Alcohol Drinkers With Liver Injury and Those Without Liver Injury in Severe Trauma Patients. *Front. Med.* **6**, 30 (2019).
221. Eldh, M. *et al.* MicroRNA in exosomes isolated directly from the liver circulation in patients with metastatic uveal melanoma. *BMC Cancer* **14**, 962 (2014).
222. Li, L. *et al.* Human bile contains MicroRNA-laden extracellular vesicles that can be used for cholangiocarcinoma diagnosis. *Hepatology* **60**, 896–907 (2014).
223. Fu, Q. *et al.* Primary tumor-derived exosomes facilitate metastasis by regulating adhesion of circulating tumor cells via SMAD3 in liver cancer. *Oncogene* **37**, 6105–6118 (2018).
224. Alhomrani, M. *et al.* The Human Amnion Epithelial Cell Secretome Decreases Hepatic Fibrosis in Mice with Chronic Liver Fibrosis. *Front. Pharmacol.* **8**, (2017).
225. Bala, S. *et al.* Biodistribution and function of extracellular miRNA-155 in mice. *Sci. Rep.* **5**, 10721 (2015).

226. Bala, S. *et al.* Circulating microRNAs in exosomes indicate hepatocyte injury and inflammation in alcoholic, drug-induced and inflammatory liver diseases. *Hepatology* **56**, 1946 (2012).
227. Baron, M. *et al.* PPARα activation differently affects microparticle content in atherosclerotic lesions and liver of a mouse model of atherosclerosis and NASH. *Atherosclerosis* **218**, 69–76 (2011).
228. Cao, H. *et al.* In Vivo Real-Time Imaging of Extracellular Vesicles in Liver Regeneration via Aggregation-Induced Emission Luminogens. *ACS Nano* **13**, 3522–3533 (2019).
229. Cefaratti, C. & Romani, A. Modulation of Na+/Mg2+ exchanger stoichiometry ratio by Cl− ions in basolateral rat liver plasma membrane vesicles. *Mol. Cell. Biochem.* **351**, 133–142 (2011).
230. Cefaratti, C., Romani, A. & Scarpa, A. Characterization of two Mg^{2+} transporters in sealed plasma membrane vesicles from rat liver. *Am. J. Physiol. Physiol.* **275**, C995–C1008 (1998).
231. Chen, J. *et al.* MicroRNA-30a ameliorates hepatic fibrosis by inhibiting Beclin1-mediated autophagy. *J. Cell. Mol. Med.* **21**, 3679–3692 (2017).
232. Chen, L. *et al.* Therapeutic effects of serum extracellular vesicles in liver fibrosis. *J. Extracell. vesicles* **7**, 1461505 (2018).
233. Cho, Y. *et al.* Increased ethanol-inducible cytochrome P450-2E1 and cytochrome P450 isoforms in exosomes of alcohol-exposed rodents and patients with alcoholism through oxidative and endoplasmic reticulum stress. *Hepatol. Commun.* **1**, 675 (2017).
234. Cho, Y.-E. *et al.* Exogenous exosomes from mice with acetaminophen-induced liver injury promote toxicity in the recipient hepatocytes and mice. *Sci. Rep.* **8**, 16070 (2018).
235. Conde-Vancells, J. *et al.* Characterization and comprehensive proteome profiling of exosomes secreted by hepatocytes. *J. Proteome Res.* **7**, 5157–66 (2008).
236. de Assuncao, T. M. *et al.* Exosome Adherence and Internalization by Hepatic Stellate Cells Triggers Sphingosine 1-Phosphate-dependent Migration. *J. Biol. Chem.* **290**, 30684–30696 (2015).
237. Dolovcak, S., Waldrop, S. L., Xiao, F. & Kilic, G. Evidence for sustained ATP release from liver cells that is not mediated by vesicular exocytosis. *Purinergic Signal.* **7**, 435–446 (2011).
238. Epping, R. J. & Bygrave, F. L. A procedure for the rapid isolation from rat liver of plasma membrane vesicles exhibiting Ca2+-transport and Ca2+-ATPase activities. *Biochem. J.* **223**, 733–45 (1984).
239. Freeman, C. M. *et al.* Characterization of microparticles after hepatic ischemia-reperfusion injury. *PLoS One* **9**, e97945 (2014).
240. Holman, N. S., Mosedale, M., Wolf, K. K., LeCluyse, E. L. & Watkins, P. B. Subtoxic alterations in hepatocyte-derived exosomes: An early step in drug-induced liver injury? *Toxicol. Sci.* **151**, 365–375 (2016).
241. Ibrahim, S. H. *et al.* Mixed lineage kinase 3 mediates release of C-X-C motif ligand 10-bearing chemotactic extracellular vesicles from lipotoxic hepatocytes. *Hepatology* **63**, 731–44 (2016).
242. Kostallari, E. *et al.* Hepatic stellate cell-derived platelet-derived growth factor receptor-alpha-

enriched extracellular vesicles promote liver fibrosis in mice through SHP2. *Hepatology* **68**, 333–348 (2018).

243. Li, M. *et al.* Horizontal transfer of exosomal CXCR4 promotes murine hepatocarcinoma cell migration, invasion and lymphangiogenesis. *Gene* **676**, 101–109 (2018).
244. Liu, W. *et al.* Combination of exosomes and circulating microRNAs may serve as a promising tumor marker complementary to alpha-fetoprotein for early-stage hepatocellular carcinoma diagnosis in rats. *J. Cancer Res. Clin. Oncol.* **141**, 1767–1778 (2015).
245. McCommis, K. S. *et al.* Targeting the mitochondrial pyruvate carrier attenuates fibrosis in a mouse model of nonalcoholic steatohepatitis. *Hepatology* **65**, 1543–1556 (2017).
246. Momen-Heravi, F. *et al.* Increased number of circulating exosomes and their microRNA cargos are potential novel biomarkers in alcoholic hepatitis. *J. Transl. Med.* **13**, 1–13 (2015).
247. Motawi, T. K., Mohamed, M. R., Shahin, N. N., Ali, M. A. M. & Azzam, M. A. Time-course expression profile and diagnostic potential of a miRNA panel in exosomes and total serum in acute liver injury. *Int. J. Biochem. Cell Biol.* **100**, 11–21 (2018).
248. Palomo, L. *et al.* Abundance of Cytochromes in Hepatic Extracellular Vesicles Is Altered by Drugs Related With Drug-Induced Liver Injury. *Hepatol. Commun.* **2**, 1064–1079 (2018).
249. Pan, Q. *et al.* Hepatic cell-to-cell transmission of small silencing RNA can extend the therapeutic reach of RNA interference (RNAi). *Gut* **61**, 1330–1339 (2012).
250. Qu, Z. *et al.* Exosomes derived from HCC cells induce sorafenib resistance in hepatocellular carcinoma both in vivo and in vitro. *J. Exp. Clin. Cancer Res.* **35**, 159 (2016).
251. Royo, F., Cossío, U., Ruiz de Angulo, A., Llop, J. & Falcon-Perez, J. M. Modification of the glycosylation of extracellular vesicles alters their biodistribution in mice. *Nanoscale* **11**, 1531–1537 (2019).
252. Royo, F. *et al.* Differences in the metabolite composition and mechanical properties of extracellular vesicles secreted by hepatic cellular models. *J. Extracell. vesicles* **8**, 1575678 (2019).
253. Royo, F. *et al.* Hepatocyte-secreted extracellular vesicles modify blood metabolome and endothelial function by an arginase-dependent mechanism. *Sci. Rep.* **7**, 42798 (2017).
254. Royo, F. *et al.* Metabolically active extracellular vesicles released from hepatocytes under drug-induced liver-damaging conditions modify serum metabolome and might affect different pathophysiological processes. *Eur. J. Pharm. Sci.* **98**, 51–57 (2017).
255. Royo, F. *et al.* Transcriptome of extracellular vesicles released by hepatocytes. *PLoS One* **8**, e68693 (2013).
256. Saha, B. *et al.* Extracellular vesicles from mice with alcoholic liver disease carry a distinct protein cargo and induce macrophage activation through heat shock protein 90. *Hepatology* **67**, 1986–2000 (2018).
257. Schmelzle, M. *et al.* Increased plasma levels of microparticles expressing CD39 and CD133 in acute liver injury. *Transplantation* **95**, 63–9 (2013).

258. Seo, W. *et al.* Exosome-mediated activation of toll-like receptor 3 in stellate cells stimulates interleukin-17 production by γδ T cells in liver fibrosis. *Hepatology* **64**, 616–631 (2016).
259. Simon, L. *et al.* Injured hepatocyte-released microvesicles induce bone marrow-derived mononuclear cells differentiation. *Differentiation* **90**, 40–47 (2015).
260. Sips, H. J., Brown, D., Oonk, R. & Orci, L. Orientation of rat-liver plasma membrane vesicles. A biochemical and ultrastructural study. *Biochim. Biophys. Acta - Biomembr.* **692**, 447–454 (1982).
261. Szostak, N. *et al.* Sorting signal targeting mRNA into hepatic extracellular vesicles. *RNA Biol.* **11**, 836–44 (2014).
262. Teoh, N. C. *et al.* Microparticles mediate hepatic ischemia-reperfusion injury and are the targets of Diannexin (ASP8597). *PLoS One* **9**, e104376 (2014).
263. Yang, M.-Q. *et al.* Interferon regulatory factor 1-Rab27a regulated extracellular vesicles promote liver ischemia/reperfusion injury. *Hepatology* **67**, 1056–1070 (2018).
264. Zhang, J. *et al.* Propofol exerts anti-hepatocellular carcinoma by microvesicle-mediated transfer of miR-142-3p from macrophage to cancer cells. *J. Transl. Med.* **12**, 279 (2014).
265. Zhukov, A., Hellman, U. & Ingelman-Sundberg, M. Purification and characterization of hepsin from rat liver microsomes. *Biochim. Biophys. Acta - Protein Struct. Mol. Enzymol.* **1337**, 85–95 (1997).
266. Karaosmanoğlu, O., Banerjee, S. & Sivas, H. Identification of biomarkers associated with partial epithelial to mesenchymal transition in the secretome of slug over-expressing hepatocellular carcinoma cells. *Cell. Oncol.* **41**, 439–453 (2018).
267. Zhao, X. *et al.* Quantitative Proteomic Analysis of Exosome Protein Content Changes Induced by Hepatitis B Virus in Huh-7 Cells Using SILAC Labeling and LC–MS/MS. *J. Proteome Res.* **13**, 5391–5402 (2014).
268. Kapoor, N. R., Ahuja, R., Shukla, S. K. & Kumar, V. The HBx protein of hepatitis B virus confers resistance against nucleolar stress and anti-cancer drug-induced p53 expression. *FEBS Lett.* **587**, 1287–1292 (2013).
269. Wei, J. *et al.* Vps4A functions as a tumor suppressor by regulating the secretion and uptake of exosomal microRNAs in human hepatoma cells. *Hepatology* **61**, 1284–94 (2015).
270. Holman, N. S., Mosedale, M., Wolf, K. K., LeCluyse, E. L. & Watkins, P. B. Subtoxic Alterations in Hepatocyte-Derived Exosomes: An Early Step in Drug-Induced Liver Injury? *Toxicol. Sci.* **151**, 365–75 (2016).
271. Zhang, H. *et al.* Exosome-delivered EGFR regulates liver microenvironment to promote gastric cancer liver metastasis. *Nat. Commun.* **8**, 15016 (2017).
272. Xu, H., Dong, X., Chen, Y. & Wang, X. Serum exosomal hnRNPH1 mRNA as a novel marker for hepatocellular carcinoma. *Clin. Chem. Lab. Med.* **56**, 479–484 (2018).
273. Mosedale, M. *et al.* miR-122 Release in Exosomes Precedes Overt Tolvaptan-Induced Necrosis in a Primary Human Hepatocyte Micropatterned Coculture Model. *Toxicol. Sci.* **161**, 149–158 (2018).
274. Eguchi, A. *et al.* Extracellular vesicles released by hepatocytes from gastric infusion model of

alcoholic liver disease contain a MicroRNA barcode that can be detected in blood. *Hepatology* **65**, 475–490 (2017).

275. Hirsova, P. *et al.* Lipid-Induced Signaling Causes Release of Inflammatory Extracellular Vesicles From Hepatocytes. *Gastroenterology* **150**, 956–967 (2016).
276. Wang, H. *et al.* iTRAQ quantitatively proteomic analysis of the hippocampus in a rat model of accumulative microwave-induced cognitive impairment. *Environ. Sci. Pollut. Res.* (2019). doi:10.1007/s11356-019-04873-0
277. Devhare, P. B. *et al.* Exosome-Mediated Intercellular Communication between Hepatitis C Virus-Infected Hepatocytes and Hepatic Stellate Cells. *J. Virol.* **91**, (2017).
278. Ibrahim, S. H., Hirsova, P. & Gores, G. J. Non-alcoholic steatohepatitis pathogenesis: sublethal hepatocyte injury as a driver of liver inflammation. *Gut* **67**, 963–972 (2018).
279. Kogure, T. & Patel, T. Isolation of Extracellular Nanovesicle MicroRNA from Liver Cancer Cells in Culture. in 11–18 (Humana Press, Totowa, NJ, 2013). doi:10.1007/978-1-62703-453-1_2
280. Chen, Z. *et al.* Cytoskeleton-centric protein transportation by exosomes transforms tumor-favorable macrophages. *Oncotarget* **7**, 67387–67402 (2016).
281. Arbelaiz, A. *et al.* Serum and urine extracellular vesicles contain mRNA biomarkers for primary sclerosing cholangitis (PSC) and cholangiocarcinoma (CCA). *J. Hepatol.* **68**, S435 (2018).
282. Sohn, W. *et al.* Serum exosomal microRNAs as novel biomarkers for hepatocellular carcinoma. *Exp. Mol. Med.* **47**, e184 (2015).
283. Torres Crigna, A. *et al.* Inter-Laboratory Comparison of Extracellular Vesicle Isolation Based on Ultracentrifugation. *Transfus. Med. Hemotherapy* **48**, 48–59 (2021).
284. Holman, N. S., Mosedale, M., Wolf, K. K., LeCluyse, E. L. & Watkins, P. B. Subtoxic Alterations in Hepatocyte-Derived Exosomes: An Early Step in Drug-Induced Liver Injury? *Toxicol. Sci.* **151**, 365–375 (2016).
285. Brandon-Warner, E. *et al.* Processing of miR17-92 Cluster in Hepatic Stellate Cells Promotes Hepatic Fibrogenesis During Alcohol-Induced Injury. *Alcohol. Clin. Exp. Res.* **40**, 1430–1442 (2016).
286. Lewis, G. D. & Metcalf, T. G. Polyethylene glycol precipitation for recovery of pathogenic viruses, including hepatitis A virus and human rotavirus, from oyster, water, and sediment samples. *Appl. Environ. Microbiol.* **54**, 1983–1988 (1988).
287. Brennan, K. *et al.* A comparison of methods for the isolation and separation of extracellular vesicles from protein and lipid particles in human serum. *Sci. Rep.* **10**, 1–13 (2020).
288. Nojima, H. *et al.* Hepatocyte exosomes mediate liver repair and regeneration via sphingosine-1-phosphate. *J. Hepatol.* **64**, 60–8 (2016).
289. Tian, Y. *et al.* Quality and efficiency assessment of six extracellular vesicle isolation methods by nano-flow cytometry. *J. Extracell. Vesicles* **9**, (2020).
290. Liu, R. *et al.* Cholangiocyte-Derived Exosomal Long Noncoding RNA H19 Promotes Hepatic

Stellate Cell Activation and Cholestatic Liver Fibrosis. *Hepatology* hep.30662 (2019). doi:10.1002/hep.30662

291. Cho, Y. E. *et al.* Increased liver-specific proteins in circulating extracellular vesicles as potential biomarkers for drug- and alcohol-induced liver injury. *PLoS One* **12**, (2017).
292. Ramirez, M. I. *et al.* Technical challenges of working with extracellular vesicles. *Nanoscale* **10**, 881–906 (2018).
293. Wang, J., Chen, D. & Ho, E. A. Challenges in the development and establishment of exosome-based drug delivery systems. *J. Control. Release* (2020). doi:10.1016/j.jconrel.2020.10.020
294. Zivko, C., Fuhrmann, G. & Luciani, P. Liver-derived extracellular vesicles: A cell by cell overview to isolation and characterization practices. *Biochim. Biophys. Acta - Gen. Subj.* 129559 (2020). doi:10.1016/j.bbagen.2020.129559
295. Rauch, C. *et al.* Alternatives to the use of fetal bovine serum: Human platelet lysates as a serum substitute in cell culture media. *ALTEX* (2011). doi:10.14573/altex.2011.4.305
296. Jochems, C. E. A., Van der Valk, J. B. F., Stafleu, F. R. & Baumans, V. The use of fetal bovine serum: Ethical or scientific problem? *ATLA Altern. to Lab. Anim.* (2002). doi:10.1177/026119290203000208
297. Wei, Z., Batagov, A. O., Carter, D. R. F. & Krichevsky, A. M. Fetal Bovine Serum RNA Interferes with the Cell Culture derived Extracellular RNA. *Sci. Rep.* **6**, (2016).
298. van der Valk, J. *et al.* Fetal Bovine Serum (FBS): Past - Present - Future. *ALTEX* (2018). doi:10.14573/altex.1705101
299. Shelke, G. V., Lässer, C., Gho, Y. S. & Lötvall, J. Importance of exosome depletion protocols to eliminate functional and RNA-containing extracellular vesicles from fetal bovine serum. *J. Extracell. Vesicles* **3**, 24783 (2014).
300. Auber, M., Fröhlich, D., Drechsel, O., Karaulanov, E. & Krämer-Albers, E.-M. Serum-free media supplements carry miRNAs that co-purify with extracellular vesicles. *J. Extracell. vesicles* **8**, 1656042 (2019).
301. Frank, J. *et al.* Extracellular vesicles protect glucuronidase model enzymes during freeze-drying. *Sci. Rep.* **8**, 12377 (2018).
302. Richter, M., Fuhrmann, K. & Fuhrmann, G. Evaluation of the Storage Stability of Extracellular Vesicles. *J. Vis. Exp.* e59584 (2019). doi:10.3791/59584
303. Schulz, E., Karagianni, A., Koch, M. & Fuhrmann, G. Hot EVs – How temperature affects extracellular vesicles. *Eur. J. Pharm. Biopharm.* **146**, 55–63 (2020).
304. Van Deun, J. *et al.* EV-TRACK: transparent reporting and centralizing knowledge in extracellular vesicle research. *Nat. Methods* **14**, 228–232 (2017).
305. Russell, A. E. *et al.* Biological membranes in EV biogenesis, stability, uptake, and cargo transfer: an ISEV position paper arising from the ISEV membranes and EVs workshop. *J. Extracell. Vesicles* **8**, 1684862 (2019).

306. Bradshaw, A. D. & Sage, E. H. SPARC, a matricellular protein that functions in cellular differentiation and tissue response to injury. *Journal of Clinical Investigation* **107**, 1049–1054 (2001).
307. Barker, T. H. *et al.* SPARC regulates extracellular matrix organization through its modulation of integrin-linked kinase activity. *J. Biol. Chem.* **280**, 36483–36493 (2005).
308. Peixoto, E. *et al.* SPARC (secreted protein acidic and rich in cysteine) knockdown protects mice from acute liver injury by reducing vascular endothelial cell damage. *Gene Ther.* **22**, 9–19 (2015).
309. Xu, L. *et al.* Human hepatic stellate cell lines, LX-1 and LX-2: new tools for analysis of hepatic fibrosis. *Gut* **54**, 142–51 (2005).
310. Lehrich, B. M., Liang, Y. & Fiandaca, M. S. Foetal bovine serum influence on in vitro extracellular vesicle analyses. *J. Extracell. Vesicles* **10**, e12061 (2021).
311. Ramirez, M. I. *et al.* Technical challenges of working with extracellular vesicles. *Nanoscale* **10**, 881–906 (2018).
312. Macías, M. *et al.* Comparison of six commercial serum exosome isolation methods suitable for clinical laboratories. Effect in cytokine analysis. *Clin. Chem. Lab. Med.* **0**, (2019).
313. Théry, C., Amigorena, S., Raposo, G. & Clayton, A. Isolation and Characterization of Exosomes from Cell Culture Supernatants and Biological Fluids. *Curr. Protoc. Cell Biol.* **30**, 3.22.1-3.22.29 (2006).
314. Théry, C. Exosomes: Secreted vesicles and intercellular communications. *F1000 Biol. Rep.* **3**, 1–8 (2011).
315. Feng, Y. H. & Tsao, C. J. Emerging role of microRNA-21 in cancer (Review). *Biomedical Reports* **5**, 395–402 (2016).
316. Rahnfeld, L., Thamm, J., Steiniger, F., van Hoogevest, P. & Luciani, P. Study on the in situ aggregation of liposomes with negatively charged phospholipids for use as injectable depot formulation. *Colloids Surfaces B Biointerfaces* **168**, 10–17 (2018).
317. Hoppstädter, J. *et al.* Toll-Like Receptor 2 Release by Macrophages: An Anti-inflammatory Program Induced by Glucocorticoids and Lipopolysaccharide. *Front. Immunol.* **10**, 1634 (2019).
318. Zhu, L., Qu, X.-H., Sun, Y.-L., Qian, Y.-M. & Zhao, X.-H. Novel method for extracting exosomes of hepatocellular carcinoma cells. *World J. Gastroenterol.* **20**, 6651–7 (2014).
319. Murakami, M. *Bioactive lipid mediators: Current reviews and protocols*. *Bioactive Lipid Mediators: Current Reviews and Protocols* (Springer Japan, 2015). doi:10.1007/978-4-431-55669-5
320. Weber, F., Rahnfeld, L. & Luciani, P. Analytical profiling and stability evaluation of liposomal drug delivery systems: A rapid UHPLC-CAD-based approach for phospholipids in research and quality control. *Talanta* **220**, 121320 (2020).
321. Lötvall, J. *et al.* Minimal experimental requirements for definition of extracellular vesicles and their functions: a position statement from the International Society for Extracellular Vesicles. *J. Extracell. vesicles* **3**, 26913 (2014).

322. Van Deun, J. *et al.* The impact of disparate isolation methods for extracellular vesicles on downstream RNA profiling. *J. Extracell. Vesicles* **3**, 24858 (2014).
323. Goes, A. & Fuhrmann, G. Biogenic and Biomimetic Carriers as Versatile Transporters To Treat Infections. *ACS Infect. Dis.* **4**, 881–892 (2018).
324. Fais, S. *et al.* Evidence-Based Clinical Use of Nanoscale Extracellular Vesicles in Nanomedicine. *ACS Nano* **10**, 3886–3899 (2016).
325. de Jong, O. G. *et al.* Drug Delivery with Extracellular Vesicles: From Imagination to Innovation. *Acc. Chem. Res.* acs.accounts.9b00109 (2019). doi:10.1021/acs.accounts.9b00109
326. Vader, P., Mol, E. A., Pasterkamp, G. & Schiffelers, R. M. Extracellular vesicles for drug delivery. *Advanced Drug Delivery Reviews* **106**, 148–156 (2016).
327. Kim, M. S. *et al.* Development of exosome-encapsulated paclitaxel to overcome MDR in cancer cells. *Nanomedicine Nanotechnology, Biol. Med.* **12**, 655–664 (2016).
328. Kim, M. S. *et al.* Engineering macrophage-derived exosomes for targeted paclitaxel delivery to pulmonary metastases: in vitro and in vivo evaluations. *Nanomedicine Nanotechnology, Biol. Med.* **14**, 195–204 (2018).
329. Huyan, T. *et al.* Extracellular vesicles – advanced nanocarriers in cancer therapy: Progress and achievements. *International Journal of Nanomedicine* **15**, 6485–6502 (2020).
330. Takahashi, Y. *et al.* Visualization and in vivo tracking of the exosomes of murine melanoma B16-BL6 cells in mice after intravenous injection. *J. Biotechnol.* **165**, 77–84 (2013).
331. Lai, C. P. *et al.* Dynamic Biodistribution of Extracellular Vesicles In Vivo Using a Multimodal Imaging Reporter. *ACS Nano* **8**, 483 (2014).
332. Smyth, T. *et al.* Biodistribution and delivery efficiency of unmodified tumor-derived exosomes. *J. Control. Release* **199**, 145–155 (2015).
333. Faruqu, F. N. *et al.* Membrane Radiolabelling of Exosomes for Comparative Biodistribution Analysis in Immunocompetent and Immunodeficient Mice - A Novel and Universal Approach. *Theranostics* **9**, 1666–1682 (2019).
334. Di Rocco, G., Baldari, S. & Toietta, G. Towards Therapeutic Delivery of Extracellular Vesicles: Strategies for In Vivo Tracking and Biodistribution Analysis. *Stem Cells Int.* **2016**, 5029619 (2016).
335. Tamura, R., Uemoto, S. & Tabata, Y. Augmented liver targeting of exosomes by surface modification with cationized pullulan. *Acta Biomater.* **57**, 274–284 (2017).
336. Melling, G. E., Carollo, E., Conlon, R., Simpson, J. C. & Carter, D. R. F. The Challenges and Possibilities of Extracellular Vesicles as Therapeutic Vehicles. *European Journal of Pharmaceutics and Biopharmaceutics* **144**, 50–56 (2019).
337. Lener, T. *et al.* Applying extracellular vesicles based therapeutics in clinical trials - An ISEV position paper. *J. Extracell. Vesicles* **4**, (2015).
338. Zheng, L. *et al.* Exosomes Derived from Dendritic Cells Attenuate Liver Injury by Modulating the Balance of Treg and Th17 Cells After Ischemia Reperfusion. *Cell. Physiol. Biochem.* **46**, 740–756

(2018).

339. Nong, K. *et al.* Hepatoprotective effect of exosomes from human-induced pluripotent stem cell–derived mesenchymal stromal cells against hepatic ischemia-reperfusion injury in rats. *Cytotherapy* **18**, 1548–1559 (2016).
340. Liu, Y. *et al.* AMSC-derived exosomes alleviate lipopolysaccharide/d-galactosamine-induced acute liver failure by miR-17-mediated reduction of TXNIP/NLRP3 inflammasome activation in macrophages. *EBioMedicine* **36**, 140–150 (2018).
341. El Taghdouini, A., Najimi, M., Sancho-Bru, P., Sokal, E. & van Grunsven, L. A. In vitro reversion of activated primary human hepatic stellate cells. *Fibrogenes. Tissue Repair* **8**, (2015).
342. Duan, N. N., Liu, X. J. & Wu, J. Palmitic acid elicits hepatic stellate cell activation through inflammasomes and hedgehog signaling. *Life Sci.* **176**, 42–53 (2017).
343. Lieber, C. S. New concepts of the pathogenesis of alcoholic liver disease lead to novel treatments. *Current Gastroenterology Reports* **6**, 60–65 (2004).
344. Lydic, T. A. *et al.* Rapid and comprehensive 'shotgun' lipidome profiling of colorectal cancer cell derived exosomes. *Methods* **87**, 83–95 (2015).
345. Heller, M., Schlappritzi, E., Stalder, D., Nuoffer, J. M. & Haeberli, A. Compositional protein analysis of high density lipoproteins in hypercholesterolemia by shotgun LC-MS/MS and probabilistic peptide scoring. *Mol. Cell. Proteomics* **6**, 1059–1072 (2007).
346. Cox, J. *et al.* Andromeda: A peptide search engine integrated into the MaxQuant environment. *J. Proteome Res.* (2011). doi:10.1021/pr101065j
347. Tyanova, S., Temu, T. & Cox, J. The MaxQuant computational platform for mass spectrometry-based shotgun proteomics. *Nat. Protoc.* **11**, 2301–2319 (2016).
348. Braga-Lagache, S. *et al.* Robust label-free, quantitative profiling of circulating plasma microparticle (MP) associated proteins. *Mol. Cell. Proteomics* **15**, 3640–3652 (2016).
349. Al Shweiki, M. H. D. R. *et al.* Assessment of Label-Free Quantification in Discovery Proteomics and Impact of Technological Factors and Natural Variability of Protein Abundance. *J. Proteome Res.* **16**, 1410–1424 (2017).
350. Wang, M., You, J., Bemis, K. G., Tegeler, T. J. & Brown, D. P. G. Label-free mass spectrometry-based protein quantification technologies in proteomic analysis. *Briefings in Functional Genomics and Proteomics* (2008). doi:10.1093/bfgp/eln031
351. Griffin, N. M. *et al.* Label-free, normalized quantification of complex mass spectrometry data for proteomic analysis. *Nat. Biotechnol.* (2010). doi:10.1038/nbt.1592
352. Matzke, M. M. *et al.* A comparative analysis of computational approaches to relative protein quantification using peptide peak intensities in label-free LC-MS proteomics experiments. *Proteomics* (2013). doi:10.1002/pmic.201200269
353. Ashburner, M. *et al.* Gene ontology: Tool for the unification of biology. *Nature Genetics* (2000). doi:10.1038/75556

354. Carbon, S. *et al.* Expansion of the gene ontology knowledgebase and resources: The gene ontology consortium. *Nucleic Acids Res.* (2017). doi:10.1093/nar/gkw1108

355. Caccia, D., Dugo, M., Callari, M. & Bongarzone, I. Bioinformatics tools for secretome analysis. *Biochimica et Biophysica Acta - Proteins and Proteomics* (2013). doi:10.1016/j.bbapap.2013.01.039

356. Huang, D. W., Sherman, B. T. & Lempicki, R. A. Bioinformatics enrichment tools: Paths toward the comprehensive functional analysis of large gene lists. *Nucleic Acids Res.* (2009). doi:10.1093/nar/gkn923

357. Cock, P. J. A. *et al.* Biopython: Freely available Python tools for computational molecular biology and bioinformatics. *Bioinformatics* (2009). doi:10.1093/bioinformatics/btp163

358. Wu, X., Hasan, M. Al & Chen, J. Y. Pathway and network analysis in proteomics. *J. Theor. Biol.* (2014). doi:10.1016/j.jtbi.2014.05.031

359. Thomas, P. D. *et al.* PANTHER: A library of protein families and subfamilies indexed by function. *Genome Res.* **13**, 2129–2141 (2003).

360. Mi, H. *et al.* Protocol Update for large-scale genome and gene function analysis with the PANTHER classification system (v.14.0). *Nat. Protoc.* **14**, 703–721 (2019).

361. Wu, B. *et al.* Separation and characterization of extracellular vesicles from human plasma by asymmetrical flow field-flow fractionation. *Anal. Chim. Acta* **1127**, 234–245 (2020).

362. Sitar, S. *et al.* Size Characterization and Quantification of Exosomes by Asymmetrical-Flow Field-Flow Fractionation. *Anal. Chem.* **87**, 9225–9233 (2015).

363. Fraunhofer, W., Winter, G. & Coester, C. Asymmetrical Flow Field-Flow Fractionation and Multiangle Light Scattering for Analysis of Gelatin Nanoparticle Drug Carrier Systems. *Anal. Chem.* (2004). doi:10.1021/ac0353031

364. Bria, C. R. M. & Williams, S. K. R. Impact of asymmetrical flow field-flow fractionation on protein aggregates stability. *J. Chromatogr. A* (2016). doi:10.1016/j.chroma.2016.08.037

365. Citkowicz, A. *et al.* Characterization of virus-like particle assembly for DNA delivery using asymmetrical flow field-flow fractionation and light scattering. *Anal. Biochem.* (2008). doi:10.1016/j.ab.2008.02.011

366. Hawe, A., Romeijn, S., Filipe, V. & Jiskoot, W. Asymmetrical flow field-flow fractionation method for the analysis of submicron protein aggregates. *J. Pharm. Sci.* (2012). doi:10.1002/jps.23298

367. Sumida, Y. & Yoneda, M. Current and future pharmacological therapies for NAFLD/NASH. *Journal of Gastroenterology* **53**, 362–376 (2018).

368. Ratziu, V. Novel Pharmacotherapy Options for NASH. *Digestive Diseases and Sciences* (2016). doi:10.1007/s10620-016-4128-z

369. Townsend, S. A. & Newsome, P. N. Non-alcoholic fatty liver disease in 2016. *British Medical Bulletin* (2016). doi:10.1093/bmb/ldw031

370. Perazzo, H. & Dufour, J. F. The therapeutic landscape of non-alcoholic steatohepatitis. *Liver*

International (2017). doi:10.1111/liv.13270

371. Gore, E. *et al.* Investigating fibrosis and inflammation in an ex vivo NASH murine model. *Am. J. Physiol. - Gastrointest. Liver Physiol.* (2020). doi:10.1152/AJPGI.00209.2019
372. Westerouen Van Meeteren, M. J., Drenth, J. P. H. & Tjwa, E. T. T. L. Elafibranor: a potential drug for the treatment of nonalcoholic steatohepatitis (NASH). *Expert Opin. Investig. Drugs* (2020). doi:10.1080/13543784.2020.1668375
373. Tølbøl, K. S. *et al.* Metabolic and hepatic effects of liraglutide, obeticholic acid and elafibranor in diet-induced obese mouse models of biopsy-confirmed nonalcoholic steatohepatitis. *World J. Gastroenterol.* (2018). doi:10.3748/wjg.v24.i2.179
374. Zhou, J. *et al.* Combined obeticholic acid and apoptosis inhibitor treatment alleviates liver fibrosis. *Acta Pharm. Sin. B* (2019). doi:10.1016/j.apsb.2018.11.004
375. Roth, J. D. *et al.* Combined obeticholic acid and elafibranor treatment promotes additive liver histological improvements in a diet-induced ob/ob mouse model of biopsy-confirmed NASH. *Sci. Rep.* **9**, 1–13 (2019).
376. Staels, B. & Fruchart, J. C. Therapeutic roles of peroxisome proliferator-activated receptor agonists. *Diabetes* **54**, 2460–2470 (2005).
377. Ratziu, V. *et al.* Elafibranor, an Agonist of the Peroxisome Proliferator-Activated Receptor-α and -δ, Induces Resolution of Nonalcoholic Steatohepatitis Without Fibrosis Worsening. *Gastroenterology* **150**, 1147-1159.e5 (2016).
378. Pellicciari, R. *et al.* 6α-ethyl-chenodeoxycholic acid (6-ECDCA), a potent and selective FXR agonist endowed with anticholestatic activity. *J. Med. Chem.* **45**, 3569–3572 (2002).
379. Fiorucci, S. *et al.* Protective effects of 6-ethyl chenodeoxycholic acid, a farnesoid x receptor ligand, in estrogen-induced cholestasis. *J. Pharmacol. Exp. Ther.* **313**, 604–612 (2005).
380. Andina, D. *et al.* Development of a Modular Ratiometric Fluorescent Probe for the Detection of Extracellular Superoxide. *Chem. - A Eur. J.* **23**, (2017).
381. Andina, D., Leroux, J. C. & Luciani, P. Ratiometric Fluorescent Probes for the Detection of Reactive Oxygen Species. *Chemistry - A European Journal* (2017). doi:10.1002/chem.201702458
382. Oliveira-Rodríguez, M. *et al.* Development of a rapid lateral flow immunoassay test for detection of exosomes previously enriched from cell culture medium and body fluids. *J. Extracell. Vesicles* **5**, 31803 (2016).
383. Pols, M. S. & Klumperman, J. Trafficking and function of the tetraspanin CD63. *Experimental Cell Research* (2009). doi:10.1016/j.yexcr.2008.09.020
384. Perez-Hernandez, D. *et al.* The intracellular interactome of tetraspanin-enriched microdomains reveals their function as sorting machineries toward exosomes. *J. Biol. Chem.* (2013). doi:10.1074/jbc.M112.445304
385. Bissig, C. & Gruenberg, J. ALIX and the multivesicular endosome: ALIX in Wonderland. *Trends in Cell Biology* (2014). doi:10.1016/j.tcb.2013.10.009

386. Thane, K. E., Davis, A. M. & Hoffman, A. M. Improved methods for fluorescent labeling and detection of single extracellular vesicles using nanoparticle tracking analysis. *Sci. Rep.* **9**, 1–13 (2019).

387. Momen-Heravi, F. *et al.* Increased number of circulating exosomes and their microRNA cargos are potential novel biomarkers in alcoholic hepatitis. *J. Transl. Med.* **13**, 261 (2015).

388. Hoshino, A. *et al.* Extracellular Vesicle and Particle Biomarkers Define Multiple Human Cancers. *Cell* **182**, 1044-1061.e18 (2020).

389. Welsh, J. A. *et al.* MIFlowCyt-EV: a framework for standardized reporting of extracellular vesicle flow cytometry experiments. *J. Extracell. Vesicles* **9**, 1713526 (2020).

390. Gardiner, C. *et al.* Techniques used for the isolation and characterization of extracellular vesicles: Results of a worldwide survey. *J. Extracell. Vesicles* **5**, 32945 (2016).

391. Schulz, E., Karagianni, A., Koch, M. & Fuhrmann, G. Hot EVs - How temperature affects extracellular vesicles. *Eur. J. Pharm. Biopharm.* **146**, 55–63 (2020).

392. Sáenz-Cuesta, M. *et al.* Methods for extracellular vesicles isolation in a hospital setting. *Front. Immunol.* **6**, 50 (2015).

393. Dragovic, R. A. *et al.* Sizing and phenotyping of cellular vesicles using Nanoparticle Tracking Analysis. *Nanomedicine Nanotechnology, Biol. Med.* **7**, 780–788 (2011).

394. Dragovic, R. A. *et al.* Isolation of syncytiotrophoblast microvesicles and exosomes and their characterisation by multicolour flow cytometry and fluorescence Nanoparticle Tracking Analysis. *Methods* **87**, 64–74 (2015).

395. Bateman, A. *et al.* UniProt: A hub for protein information. *Nucleic Acids Res.* **43**, D204–D212 (2015).

396. Larssen, P. *et al.* Tracing cellular origin of human exosomes using multiplex proximity extension assays. *Mol. Cell. Proteomics* **16**, 502–511 (2017).

397. Choi, J., Fuentes, C., Fransson, J., Wahlgren, M. & Nilsson, L. Separation and zeta-potential determination of proteins and their oligomers using electrical asymmetrical flow field-flow fractionation (EAF4). *J. Chromatogr. A* **1633**, 461625 (2020).

398. Atorrasagasti, C. *et al.* Lack of the Matricellular Protein SPARC (Secreted Protein, Acidic and Rich in Cysteine) Attenuates Liver Fibrogenesis in Mice. *PLoS One* **8**, e54962 (2013).

399. Trombetta-eSilva, J. The Function of SPARC as a Mediator of Fibrosis. *Open Rheumatol. J.* **6**, 146–155 (2012).

400. Camino, A. M. *et al.* Adenovirus-mediated inhibition of SPARC attenuates liver fibrosis in rats. *J. Gene Med.* **10**, 993–1004 (2008).

401. Currie, L. A. Detection and quantification limits: Origins and historical overview. *Anal. Chim. Acta* **391**, 127–134 (1999).

402. Riches, A., Campbell, E., Borger, E. & Powis, S. Regulation of exosome release from mammary epithelial and breast cancer cells-A new regulatory pathway. *Eur. J. Cancer* **50**, 1025–1034

(2014).

403. Shabbir, A., Cox, A., Rodriguez-Menocal, L., Salgado, M. & Van Badiavas, E. Mesenchymal Stem Cell Exosomes Induce Proliferation and Migration of Normal and Chronic Wound Fibroblasts, and Enhance Angiogenesis in Vitro. *Stem Cells Dev.* **24**, 1635–1647 (2015).
404. Morelli, A. E. *et al.* Endocytosis, intracellular sorting, and processing of exosomes by dendritic cells. *Blood* **104**, 3257–3266 (2004).
405. Takov, K., Yellon, D. M. & Davidson, S. M. Confounding factors in vesicle uptake studies using fluorescent lipophilic membrane dyes. *J. Extracell. Vesicles* **6**, 1388731 (2017).
406. Dehghani, M., Gulvin, S. M., Flax, J. & Gaborski, T. R. Systematic Evaluation of PKH Labelling on Extracellular Vesicle Size by Nanoparticle Tracking Analysis. *Sci. Rep.* **10**, 1–10 (2020).
407. Gangadaran, P., Hong, C. M. & Ahn, B. C. An update on in vivo imaging of extracellular vesicles as drug delivery vehicles. *Frontiers in Pharmacology* **9**, 169 (2018).
408. Dragovic, R. A. *et al.* Sizing and phenotyping of cellular vesicles using Nanoparticle Tracking Analysis. *Nanomedicine Nanotechnology, Biol. Med.* **7**, 780–788 (2011).
409. Verbeke, L. *et al.* FXR agonist obeticholic acid reduces hepatic inflammation and fibrosis in a rat model of toxic cirrhosis. *Sci. Rep.* **6**, 1–12 (2016).
410. Nevens, F. *et al.* A Placebo-Controlled Trial of Obeticholic Acid in Primary Biliary Cholangitis. *N. Engl. J. Med.* (2016). doi:10.1056/nejmoa1509840
411. Younossi, Z. M. *et al.* Obeticholic acid for the treatment of non-alcoholic steatohepatitis: interim analysis from a multicentre, randomised, placebo-controlled phase 3 trial. *Lancet* (2019). doi:10.1016/S0140-6736(19)33041-7
412. Vreman, R. A. *et al.* Health and economic benefits of reducing sugar intake in the USA, including effects via non-alcoholic fatty liver disease: A microsimulation model. *BMJ Open* **7**, e013543 (2017).
413. LaBrecque, D. R. *et al.* World Gastroenterology Organisation Global Guidelines. *J. Clin. Gastroenterol.* **48**, 467–473 (2014).
414. Yang, Y., Zhai, C., Zeng, Q., Khan, A. L. & Yu, H. Multifunctional Detection of Extracellular Vesicles with Surface Plasmon Resonance Microscopy. *Anal. Chem.* **92**, 4884–4890 (2020).

Appendix

“Sometimes science is a lot more art than science, Morty.
A lot of people don't get that.”
Rick Sanchez

Supplementary information per chapter

Chapter 2 supplementary information

Table A2-1: Summary of the culturing conditions prior to EV harvest.

Cell count at split [cell #]	Tissue culture flasks used	Seeding density [cells/flask]	Culturing time before treatment start [d]
0.5-1 Mio	1x T75	0.5 Mio	3
2-3 Mio	2x T75	0.5 Mio	5
6-8 Mio	1x T175	1 Mio	5
10-12 Mio	2x T175	1 Mio	5
20 Mio	3x T175	1 Mio	5
25 Mio	1x 5-layers flask	5 Mio	5

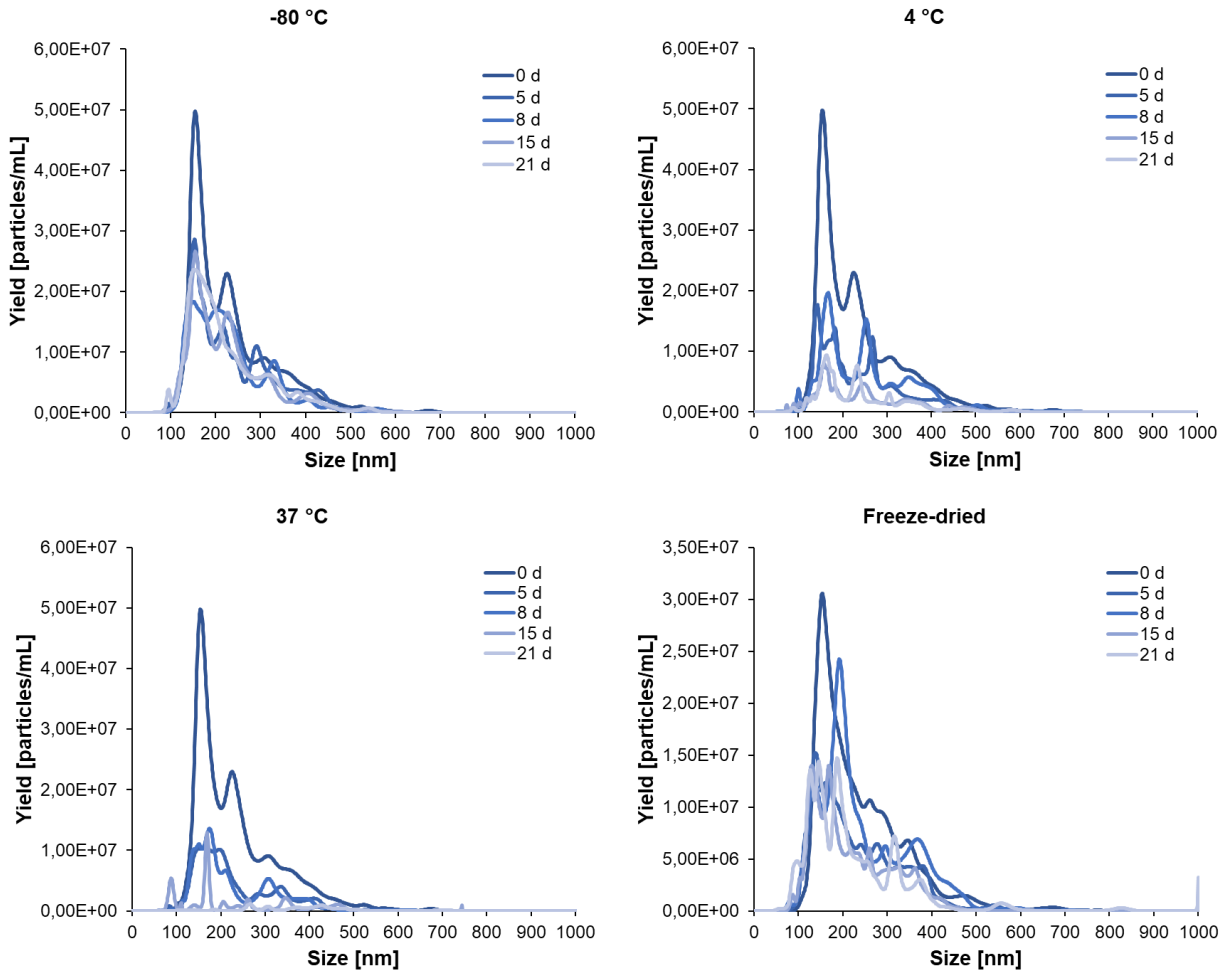

Figure A2-1: EV size distribution profiles upon mid-term storage under different conditions for up to 21 d (combined from n = 3-5, software: NTA v3.2). The experiment was performed with my then master students in from the University of Saarland (Saarbrücken), Rebecca Hämsch and Katharina Leinenbach.

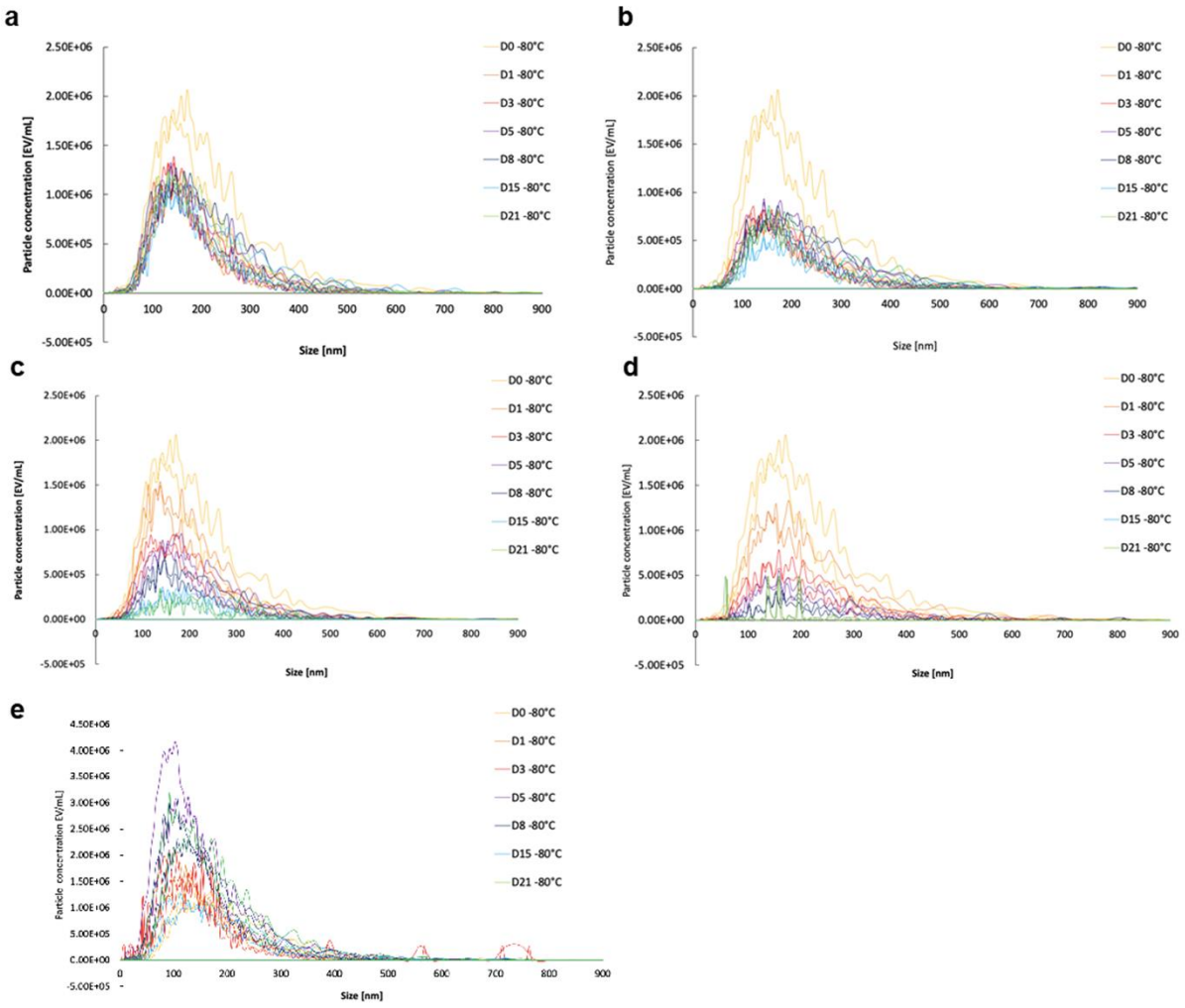

Figure A2-2: Representative size distribution profiles for EVs stored at -80 °C (**a**), -25 °C (**b**), 4 °C (**c**), 37 °C (**d**) and at room temperature after being freeze-dried with 1% (w/v) trehalose (**e**) (software: ZetaView 8.05.05 SP2). The experiment was performed with n = 3-4 with my then bachelor student from the University of Bern, Jana Leuenberger.

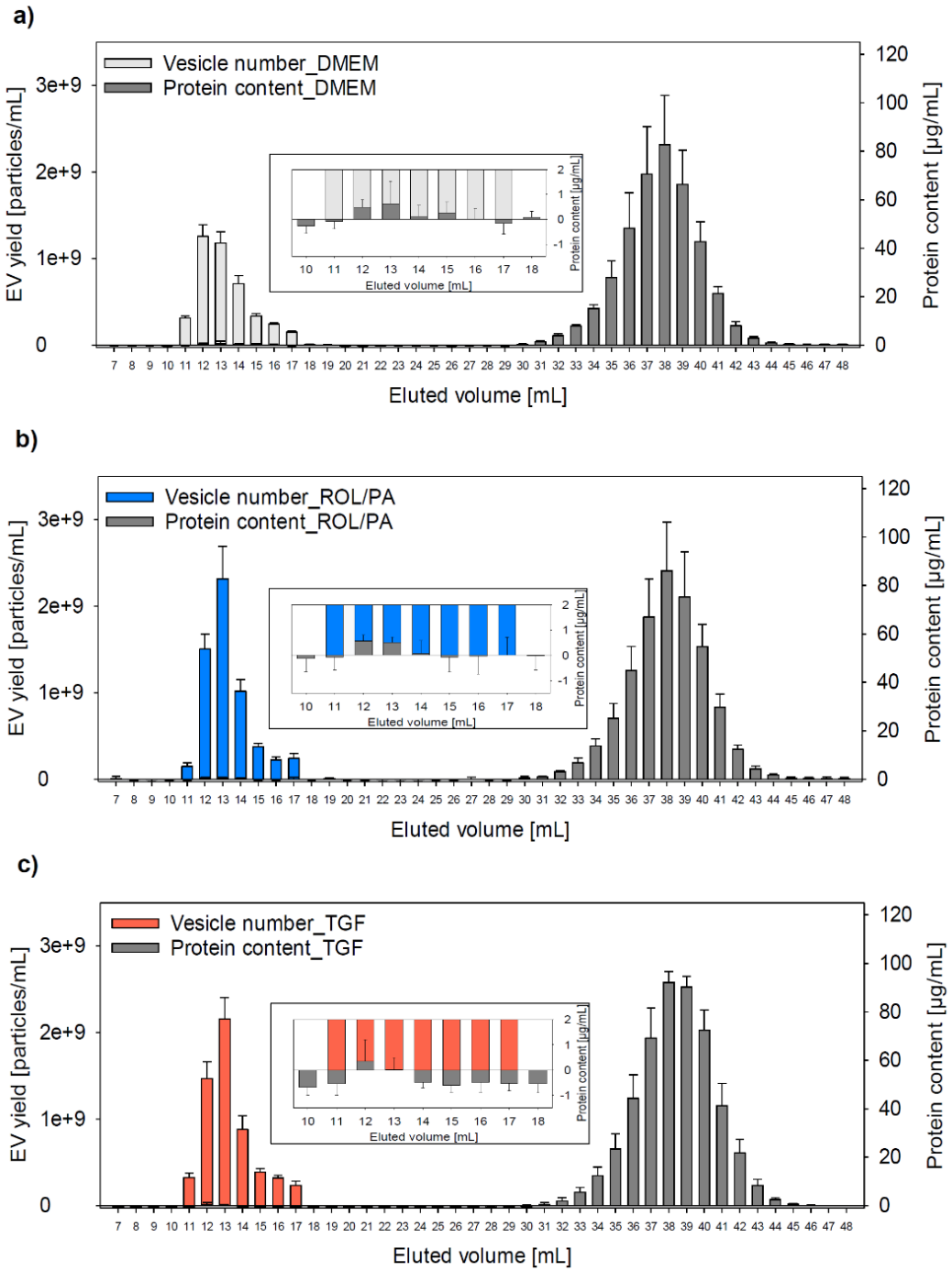

Figure A2-3: EV purification data obtained before using the new UC protocol, and a 30 mL SEC column. Protein content and vesicle number in the collected SEC fractions obtained from untreated (**a**), quiescent (**b**) and perpetuated (**c**) LX-2 (mean ± SD, n = 3, software: NTA v3.2). Zoomed portions of the graphs show the protein content in fractions 10 to 18 mL.

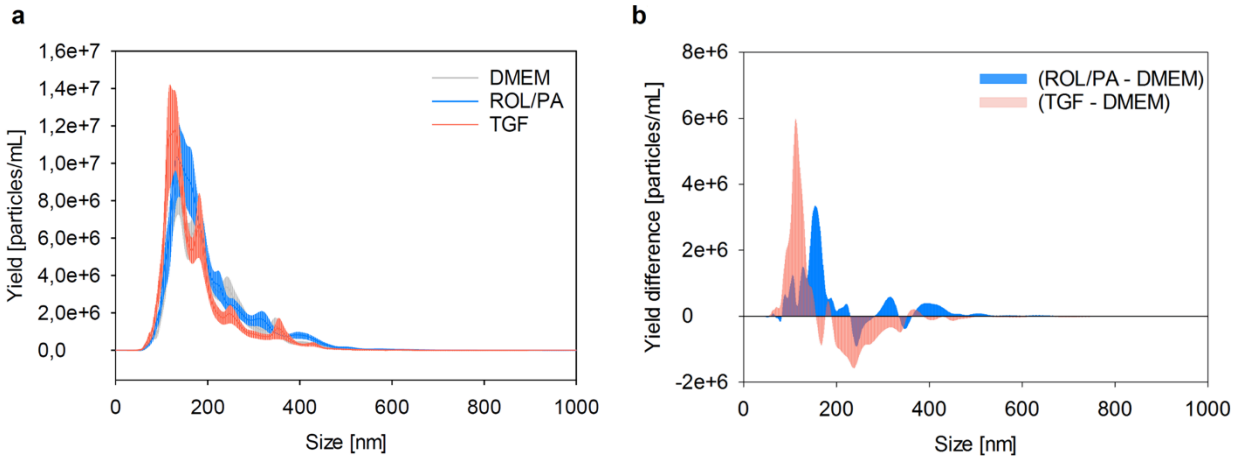

Figure A2-4: Consolidated size distribution profiles of EVs purified in (**a**) (mean ± SE, n = 4) and quantile differences in the isolated EV populations (**b**) (software: NTAv3.2).

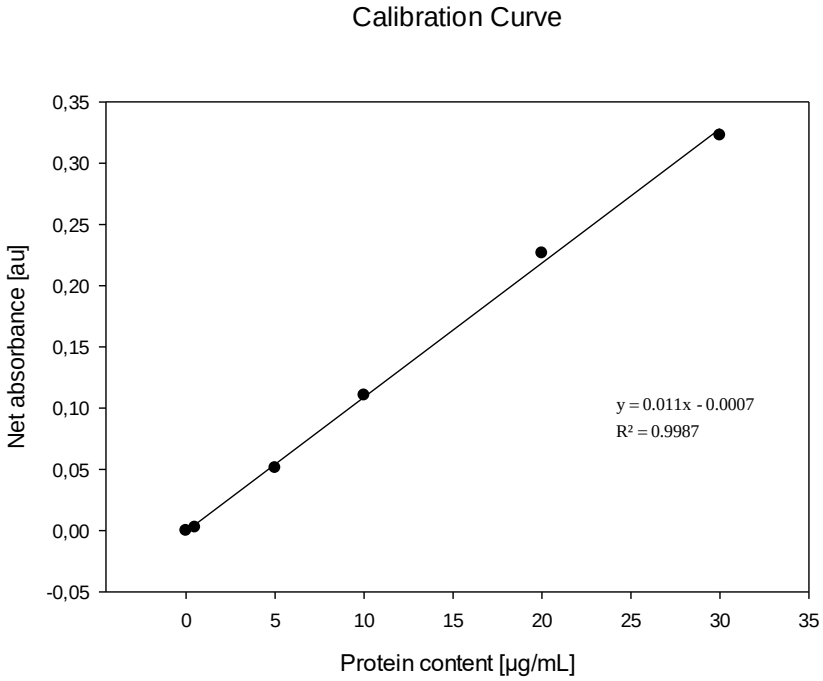

Figure A2-5: Representative calibration curve for BCA assay using BSA protein standards. Calibrations curves were prepared anew for every 96-wells microtiter plate.

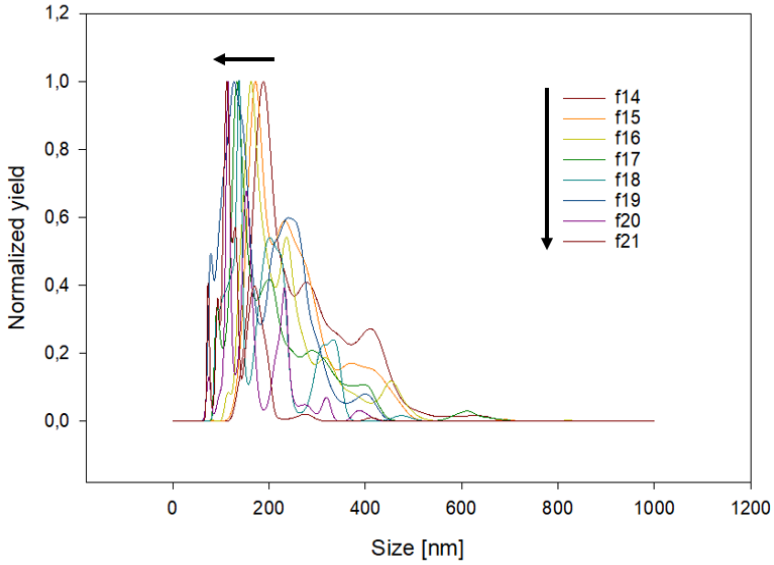

Figure A2-6: Representative size distribution profile of DMEM-EVs found in different SEC-fractions (eluting from 14 to 21 mL), each normalized to its highest peak (software: NTAv3.2).

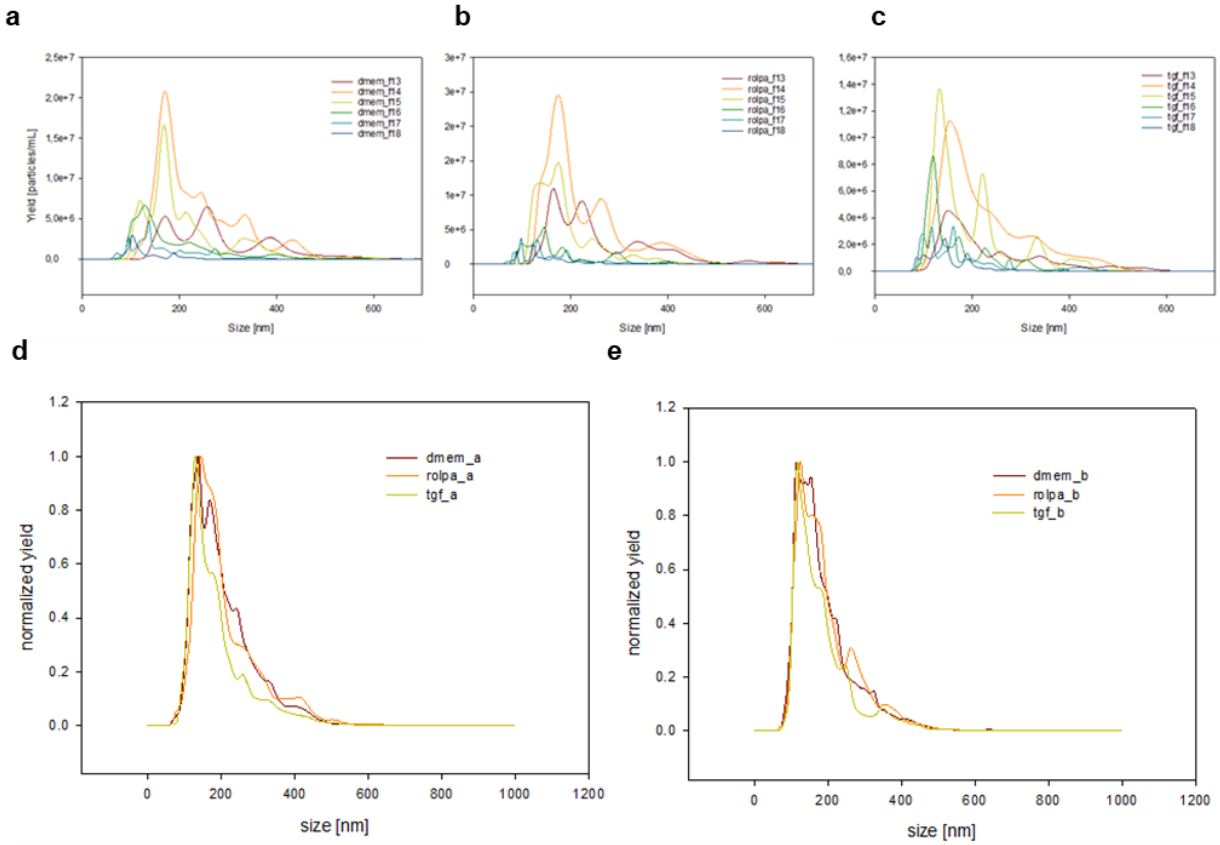

Figure A2-7: Representative size distribution profile of EVs found in different SEC-fractions with EVs originating from DMEM (**a**), ROL/PA (**b**) and TGF-treated cells (**c**), each normalized to its highest peak (software: NTAv3.2). Combined size distribution profiles from CCMa-EVs (**d**) and CCMb-EVs (**e**) show great overlap between treatments, as well as between CCM-types.

Table A2-2: Mean zetapotential values in different EV-containing SEC-fractions, harvested from differently treated LX-2 cells and from both CCMa and CCMb. The samples had been stored at -80 °C for a couple of days before measurement, and they were at the limit of detection for the ZetaSizer (mean ± SD, n = 3).

	f09 [mV]	f10 [mV]	f11 [mV]	f12 [mV]
DMEM_a	-13.01 ± 1.19	-13.68 ± 0.67	-14.67 ± 1.11	-15.30 ± 0.86
DMEM_b	-14.30 ± 1.23	-15.40 ± 0.42	-14.80 ± 0.81	-14.95 ± 0.75
ROL/PA_a	-14.78 ± 1.54	-13.87 ± 0.93	-13.38 ± 0.84	-13.80 ± 0.80
ROL/PA_b	-13.15 ± 0.83	-13.87 ± 0.73	-14.85 ± 1.05	-14.10 ± 1.03
TGF_a	-15.20 ± 1.05	-13.78 ± 1.41	-14.87 ± 0.65	-15.10 ± 1.42
TGF_b	-14.55 ± 2.06	-15.92 ± 1.13	-15.52 ± 1.68	-15.27 ± 1.53

Table A2-3: Composition of 5x sample buffer.

5x concentrated sample buffer for SDS-PAGE gel electrophoresis
1 mM Tris HCl (pH 6.8)
10% SDS (v/v)
30% Glycerol (v/v)
0.5 mg/mL bromophenol blue
milliQ-H_2O to desired volume

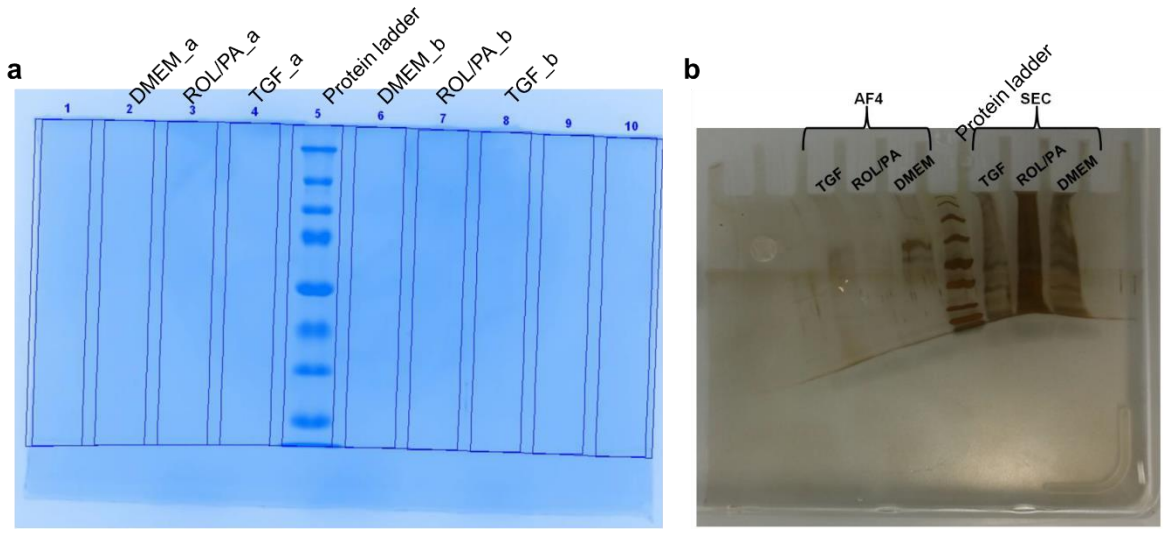

Figure A2-8: SEC-Purified EV samples originating from CCMa and CCMb after SDS-PAGE, Coumassie blue stained (**a**). SEC and AF4-purified samples, originating from CCMa-EV as well as CCMb-EV samples were combined and concentrated with VivaSpin® before SDS-PAGE electrophoresis, and stained with the Pierce™ silver staining kit (**b**). For AF4-purified samples, refer to **.** VivaSpin® concentration worked so well that SEC-samples were too concentrated in silver staining. This also shows how much lower AF4-purified samples are. The stacking gel was 4% acrylamide, the resolving gel 12%.

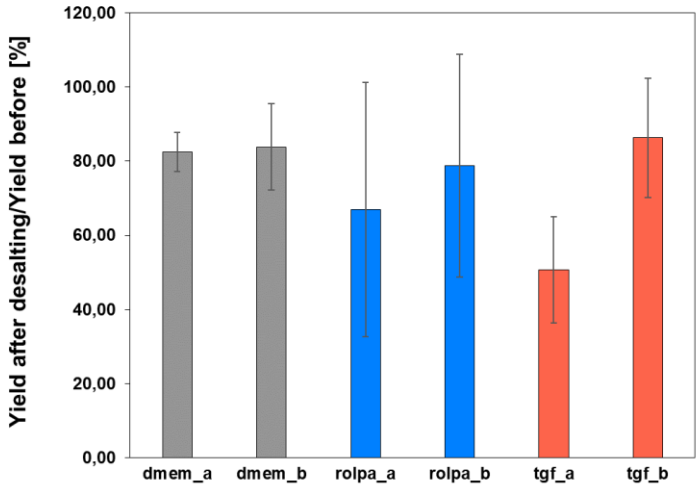

Figure A2-9: PD-midi trap columns were used to desalt SEC-purified EVs obtained from differently treated LX-2 cells (both CCMa-EVs and CCMb-EVs). Yield recovery was not perfect. (mean ± SD, n = 4, software: NTA v3.2). The ultimate goal was to freeze-dry and re-suspend the samples in a smaller volume for concentrating. After seeing that freeze-drying would need dedicated optimization (see **Chapter 2.3.2**) we dropped the idea. We considered concentrating our samples with Vivapore® (it lost us the whole sample) and Amicon® (see **Figure A4-5**).

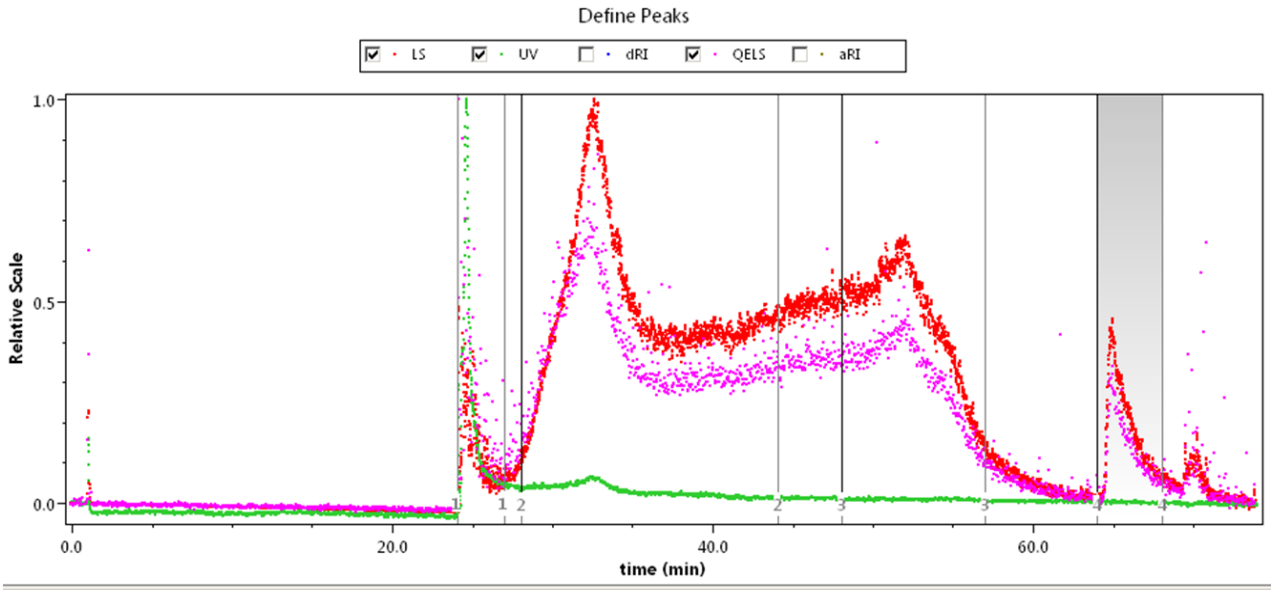

	1	2	3	4
Name	Peak 1	Peak 2	Peak 3	Peak 4
Start (min)	24.0000	28.0000	48.0000	64.0000
Stop (min)	27.0000	44.0000	57.0000	68.0000
dn/dc (mL/g)	0.1000	0.1000	0.1000	0.1000
UV Extinction Coefficient (mL/(mg cm))	1.0000	1.0000	1.0000	1.0000
Injected Mass (µg)	75.000	75.000	75.000	75.000
Concentration (mg/mL)	1.000	1.000	1.000	1.000
A2 (mol mL/g^2)	0.0000e+000	0.0000e+000	0.0000e+000	0.0000e+000

Figure A2-10: Representative AF4 fractogram of EVs isolated from DMEM-treated cells. These particular AF4 experiments were performed with the help of Dr. Kathrin Fuhrmann (Helmholtz Institute for Pharmaceutical Research, Saarbrücken). AF4-fractions used for SDS-PAGE experiments were obtained before EV-yields had substantially improved and also long before AF4-protocols were optimized by Dr. Kathrin Fuhrmann for further experiments (**Chapter 3**).

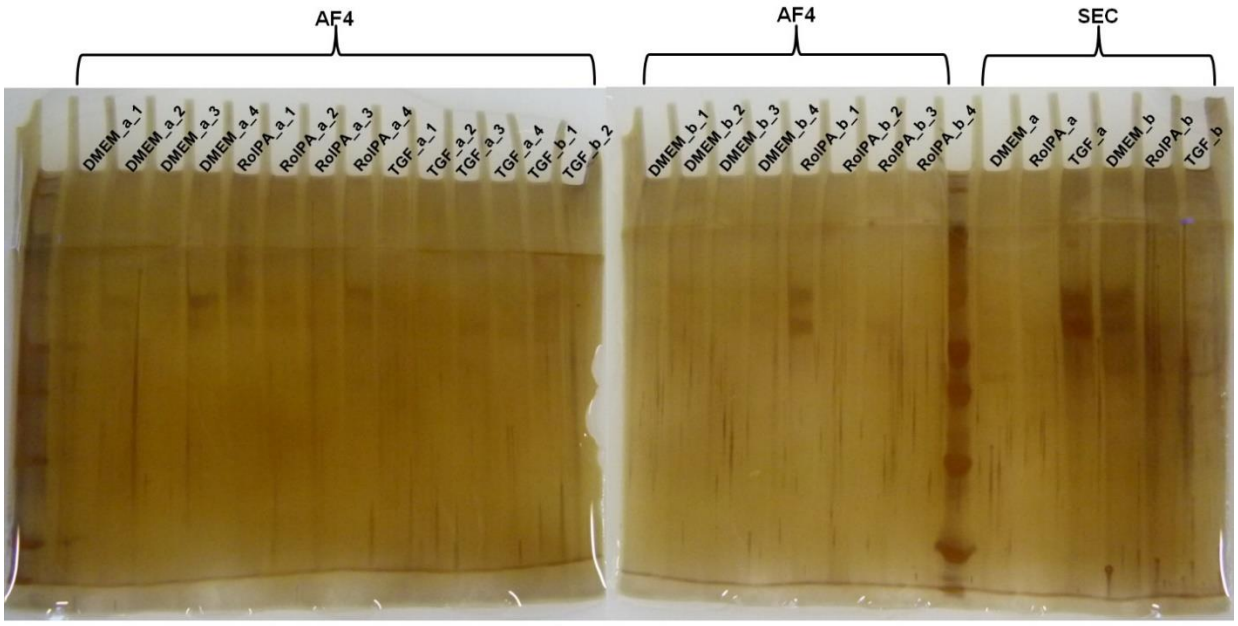

Figure A2-11: AF4-purified samples, originating from CCMa-EV as well as from CCMb-EV samples were combined and concentrated with VivaSpin® before SDS-PAGE electrophoresis, and stained with the Pierce silver staining kit. For AF4-purified samples, refer to **Figure A2-10**. VivaSpin concentration was not used for SEC-purified samples, which originated from CCMa-EV as well as from CCMb-EV samples. The stacking gel was 4% acrylamide, the resolving gel 12%.

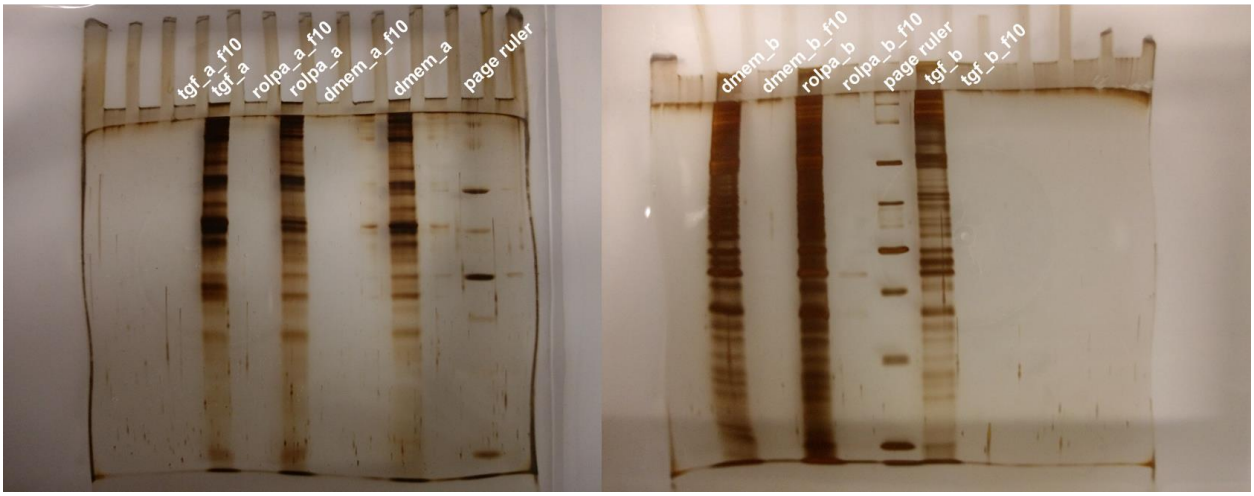

Figure A2-12: SDS-PAGE gel electrophoresis (silver staining) was performed using EV-pellets as well SEC-purified EVs. For SEC-purified-EVs, the fraction with the highest EV-yield was chosen (with the then used column, it was the fraction eluting between 9 and 10 mL, i.e., “f10”). Samples originated from differently treated cells and from both CCMa and CCMb. Staining development had to be stopped because of the intensity of the protein bands belonging to EV-pellet samples. The stacking gel was 4% acrylamide, the resolving gel 12%.

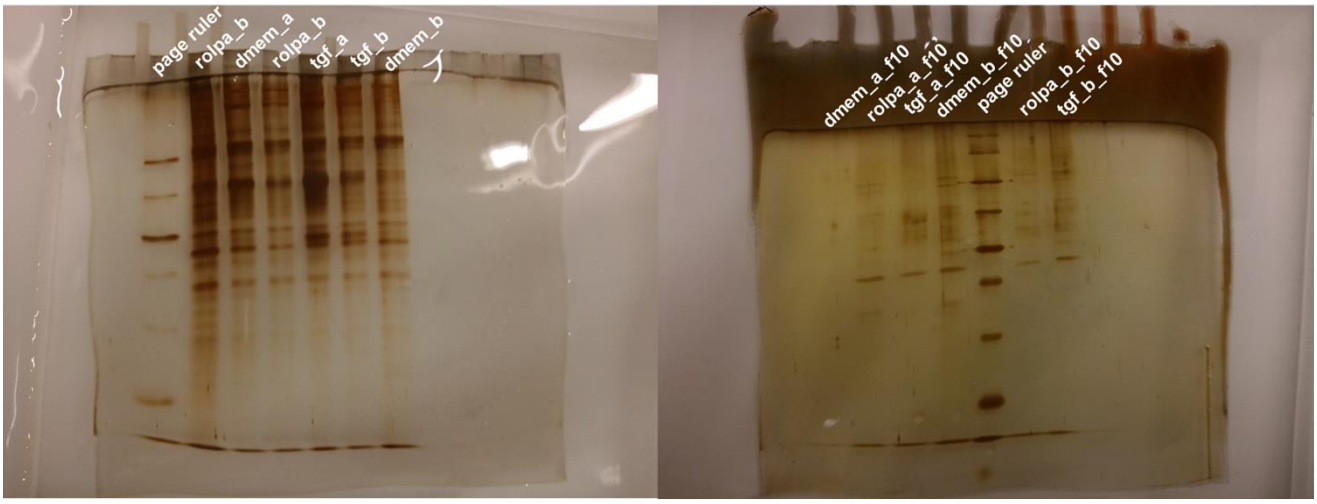

Figure A2-13: SDS-PAGE gel electrophoresis (silver staining) using the same samples as in **Figure A2-12**, but on separate gels to allow for different development times. While the bands from SEC-fractions are becoming more visible, it is quite evident that they are too diluted for effective SDS-PAGE. The stacking gel was 4% acrylamide, the resolving gel 12%.

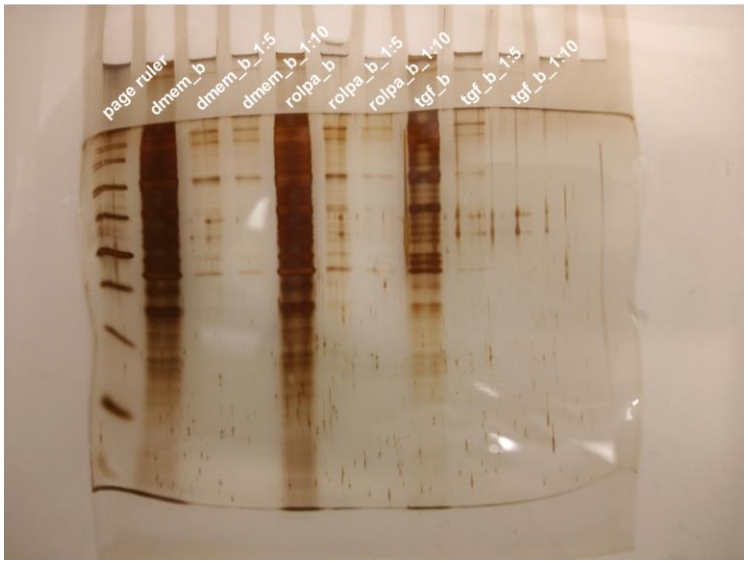

Figure A2-14: SDS-PAGE (silver staining) was performed using EV-pellets, at different dilutions. Samples originated from differently treated cells and from both CCMa and CCMb. The 1:5 and especially the 1:10 dilution were possibly too diluted and should not be run in the same gel as the undiluted pellets. The stacking gel was 4% acrylamide, the resolving gel 12%

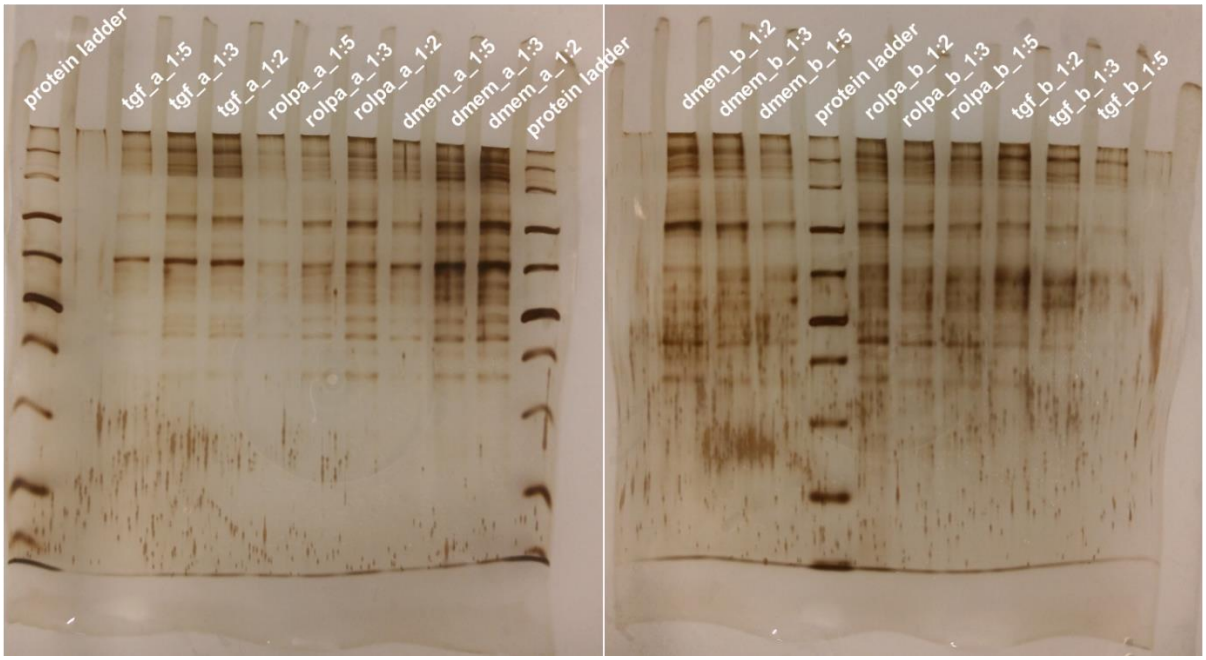

Figure A2-15: SDS-PAGE (silver staining) was performed using EV-pellets, at different dilutions. Samples originated from differently treated cells and from both CCMa and CCMb. Proteins are finally becoming much clearer to see. The stacking gel was omitted, the resolving gel was 12% acrylamide. It does not seem like there is a significant presence of lower molecular weight proteins in the samples, so we ran an analogous experiment but using a 7% acrylamide gel to be better resolve the higher molecular weight proteins (see **Figure A2-16**).

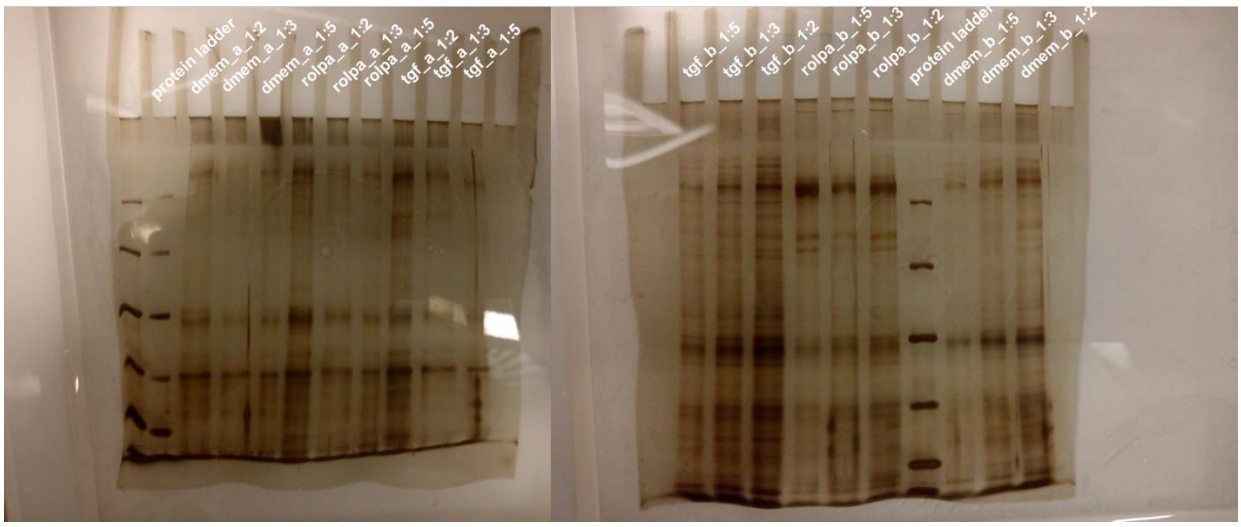

Figure A2-16: Analogous to **Figure A2-15**, but with a 7% acrylamide gel instead of 12%.

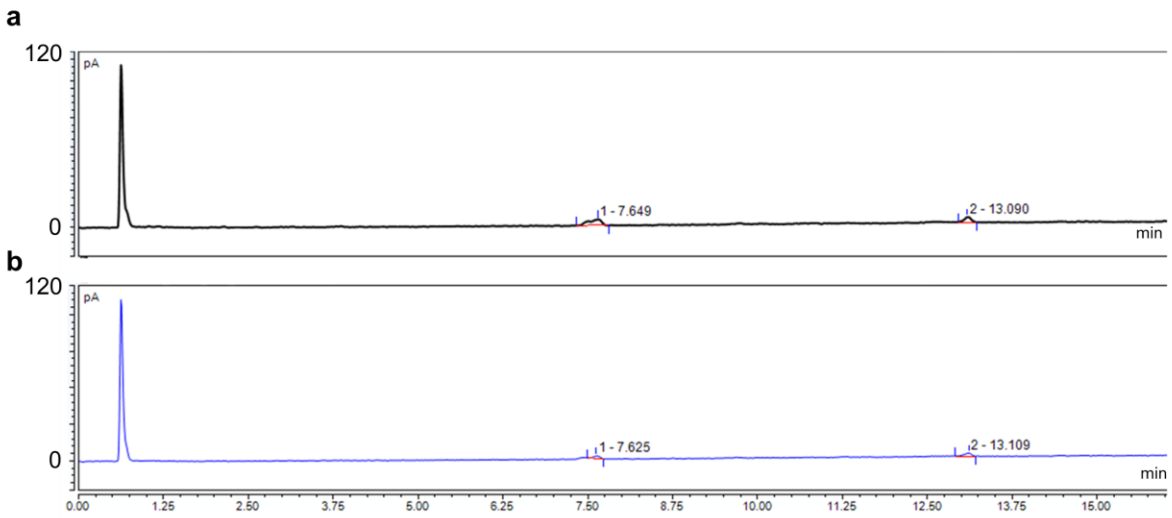

Figure A2-17: Representative HPLC chromatograms for lipids extracted from CCMa-EVs (a) and CCMb-EVs originating from DMEM-treated cells.

Chapter 3 supplementary information

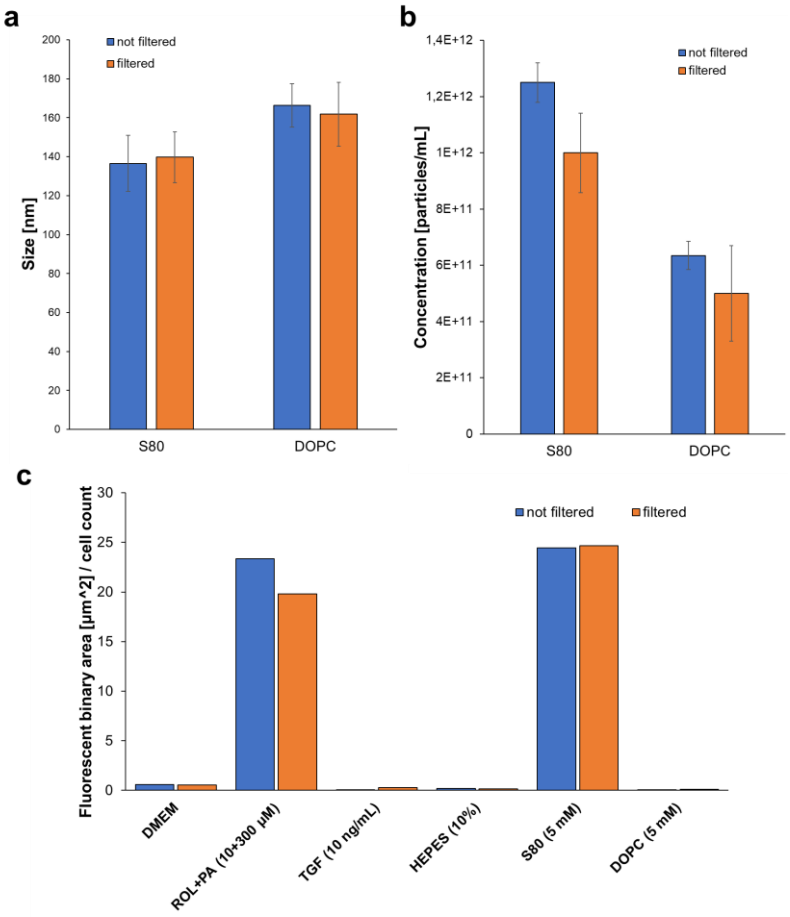

Figure A3-1: Average size (**a**) and yield (**b**) for PPC-samples in DMEM before and after sterile filtration. Lipid droplet analysis from a representative set of differently treated LX-2 cells, based on our previously published protocol using 100'000 cells/well (**c**).[46] The addition of the sterile filtration step did not affect liposome size or recovery, and neither the physiological response as seen by ORO/DAPI staining, so we performed it before every treatment.

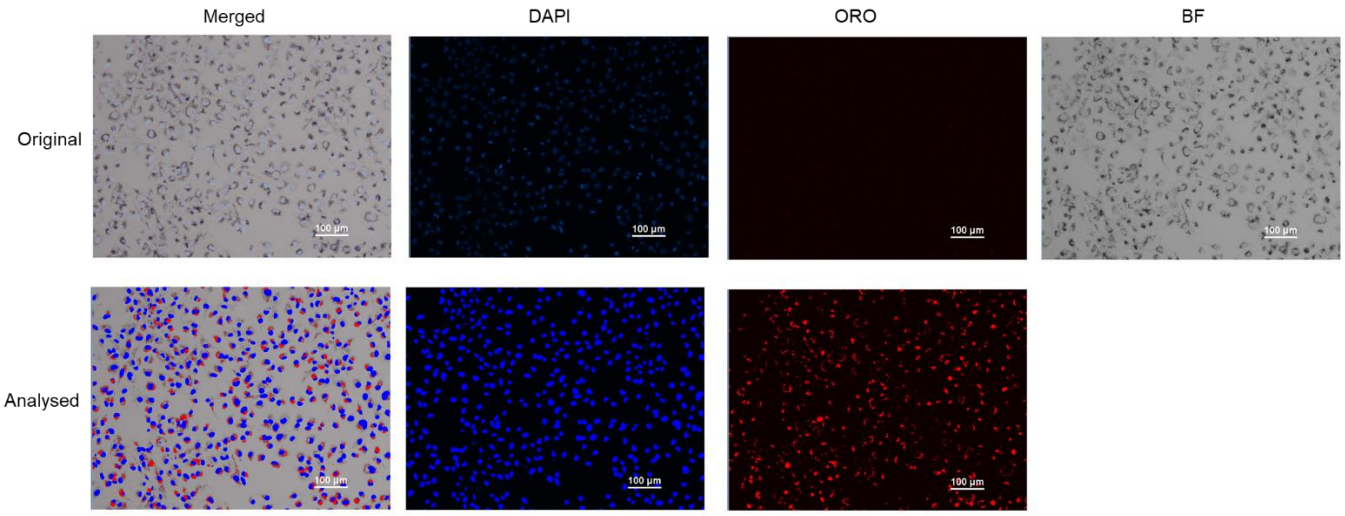

Figure A3-2: Representative microscopy image of ROL/PA-treated cells split into acquisition channels. The upper row shows the original pictures taken on the same spot, whereas the bottom row shows the same pictures after thresholding. It is readily seen (especially after merging), how the software is able to detect all single DAPI-stained nuclei, and almost all red areas corresponding to cytoplasmic lipid droplets (i.e, almost perfect detection of true positives). Pictures of LX-2 cells without lipid droplets, acquired with the same settings and analysed using the same thresholding are displayed in **Figure A3-3**, showing almost no red spots, i.e., only little detection of false positives.

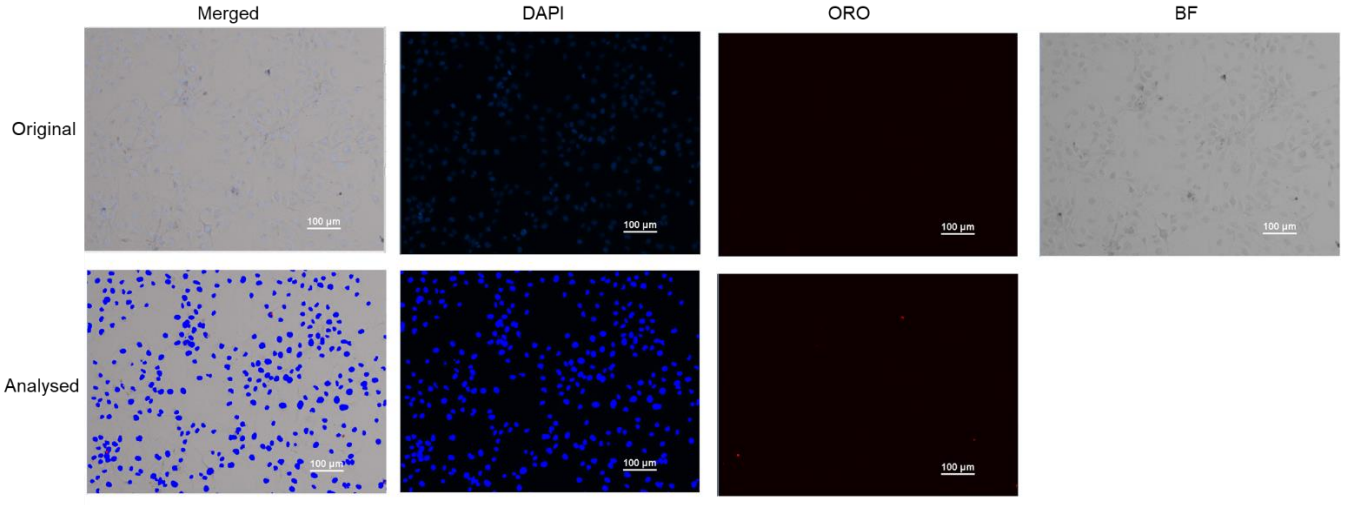

Figure A3-3: Representative microscopy image TGF-treated cells split into acquisition channels. The upper row shows the original pictures taken on the same spot, whereas the bottom row shows the same pictures after thresholding. It is readily seen (especially after merging), how the software is able to detect all single DAPI-stained nuclei, and almost no red areas corresponding to cytoplasmic lipid droplets (i.e., almost perfect avoidance of false positives). Pictures of LX-2 cells with lipid droplets, acquired with the same settings and analysed using the same thresholding are displayed in **Figure A3-2**, showing many red spots, i.e., almost perfect detection of true positives.

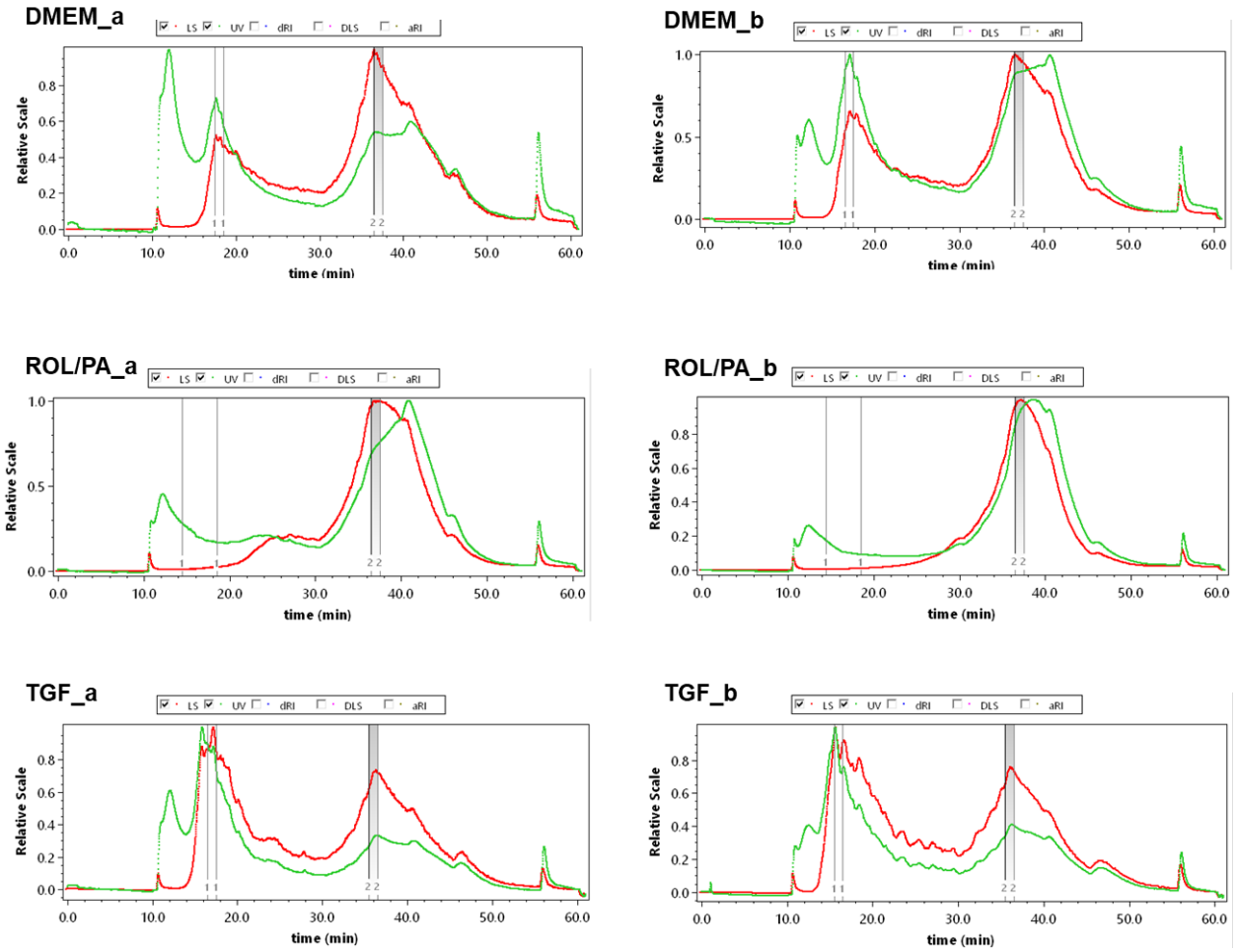

Figure A3-4: Representative AF4 fractograms of CCMa and CCMb-EVs isolated from differently treated cells. Fractograms also show the timepoints for the collection of AF4-peak 1 and AF4-peak 2 (see **Chapter 3.3.2**). AF4 experiments were performed by Dr. Kathrin Fuhrmann (Helmholtz Institute for Pharmaceutical Research, Saarbrücken).

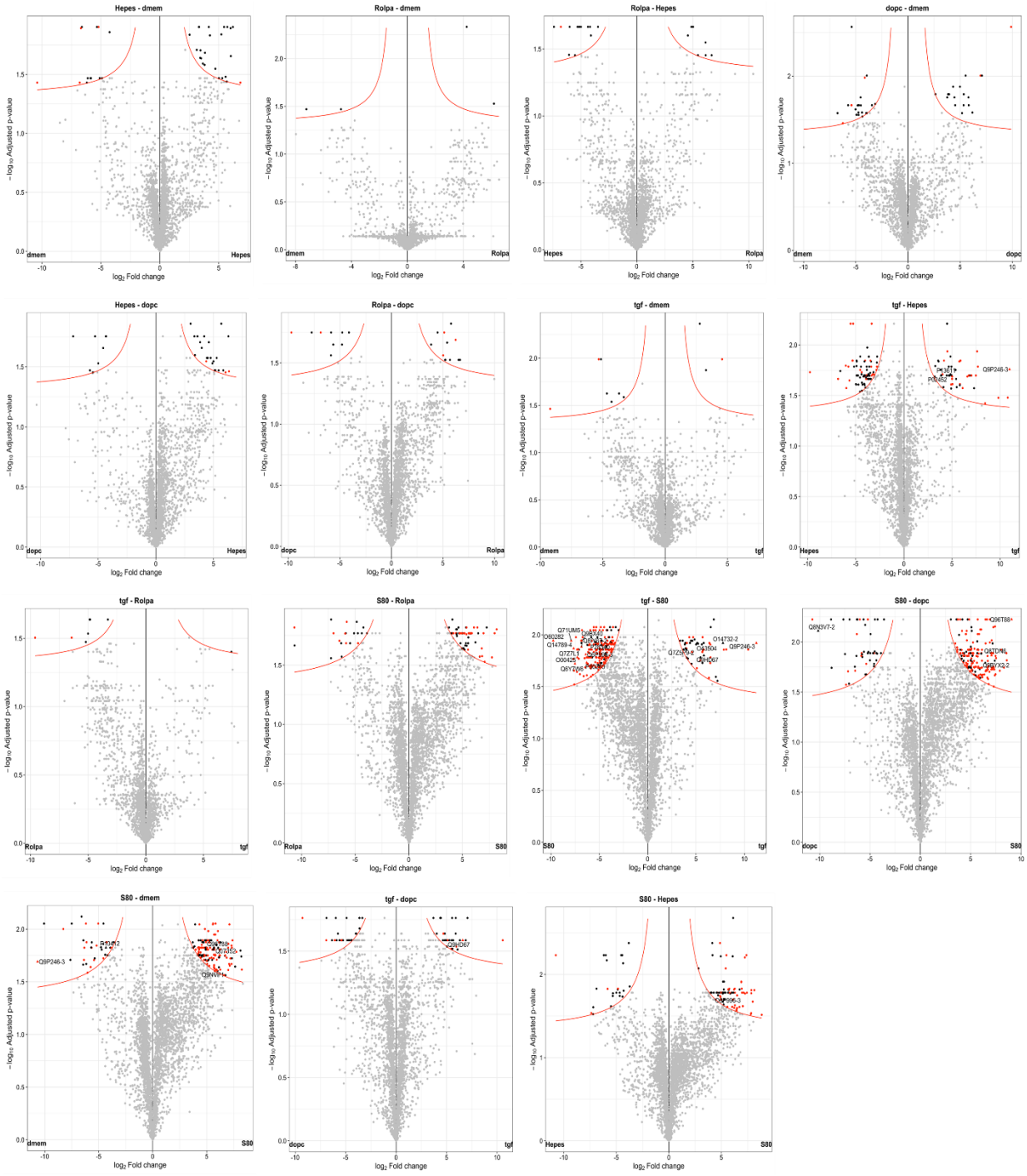

Figure A3-5: Volcano plots with direct comparisons of treatment groups based on EV-proteins from SEC-purified samples (using LFQ).

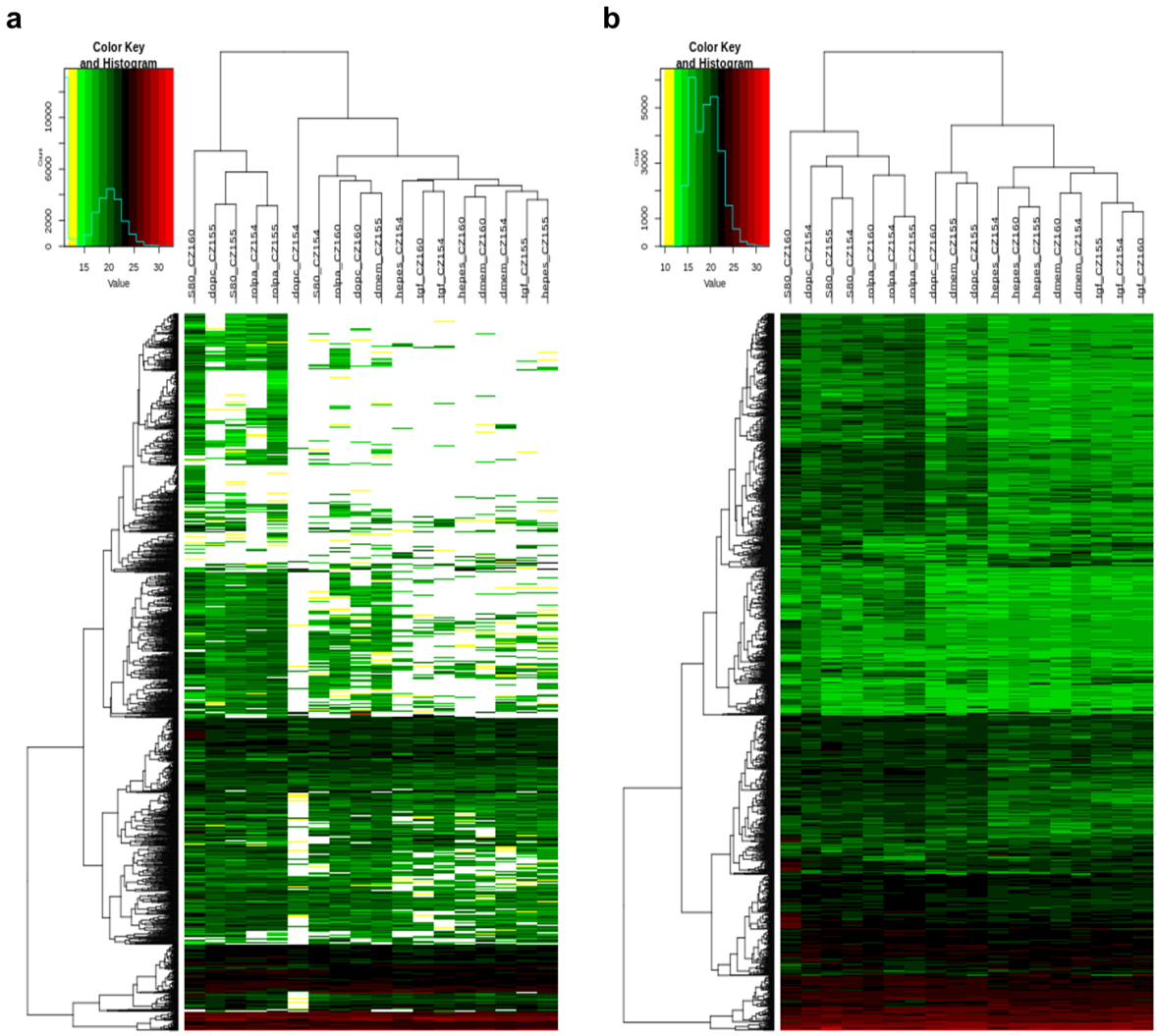

Figure A3-6: Hierarchical clustering with of iTop3 before (**a**) and after imputation (**b**) for the combined AF4-peaks. Per sample, imputation values were drawn from a gaussian distribution of width 0.3x sample standard deviation centered at the sample distribution mean minus 2.5x sample standard deviation. This is a left-censored method and is done if there is at most 1 non-zero values in the group for a protein. Any remaining missing values are imputed by the Maximum Likelihood Estimation (MLE) method.

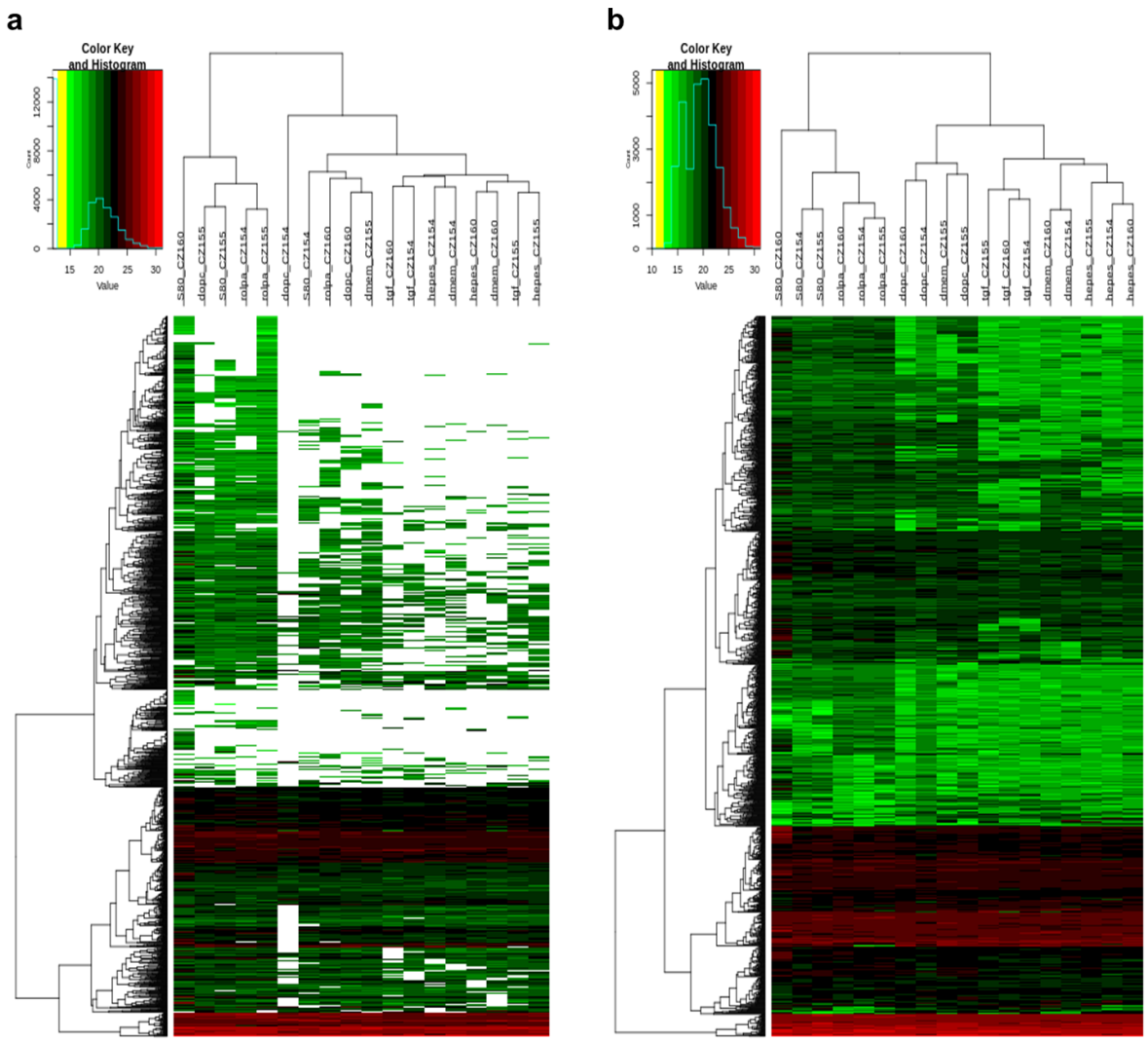

Figure A3-7: Hierarchical clustering with of LFQ before (**a**) and after imputation (**b**) for the combined AF4-peaks. Per sample, imputation values were drawn from a gaussian distribution of width 0.3x sample standard deviation centered at the sample distribution mean minus 2.5x sample standard deviation. This is a left-censored method and is done if there is at most 1 non-zero values in the group for a protein. Any remaining missing values are imputed by the Maximum Likelihood Estimation (MLE) method.

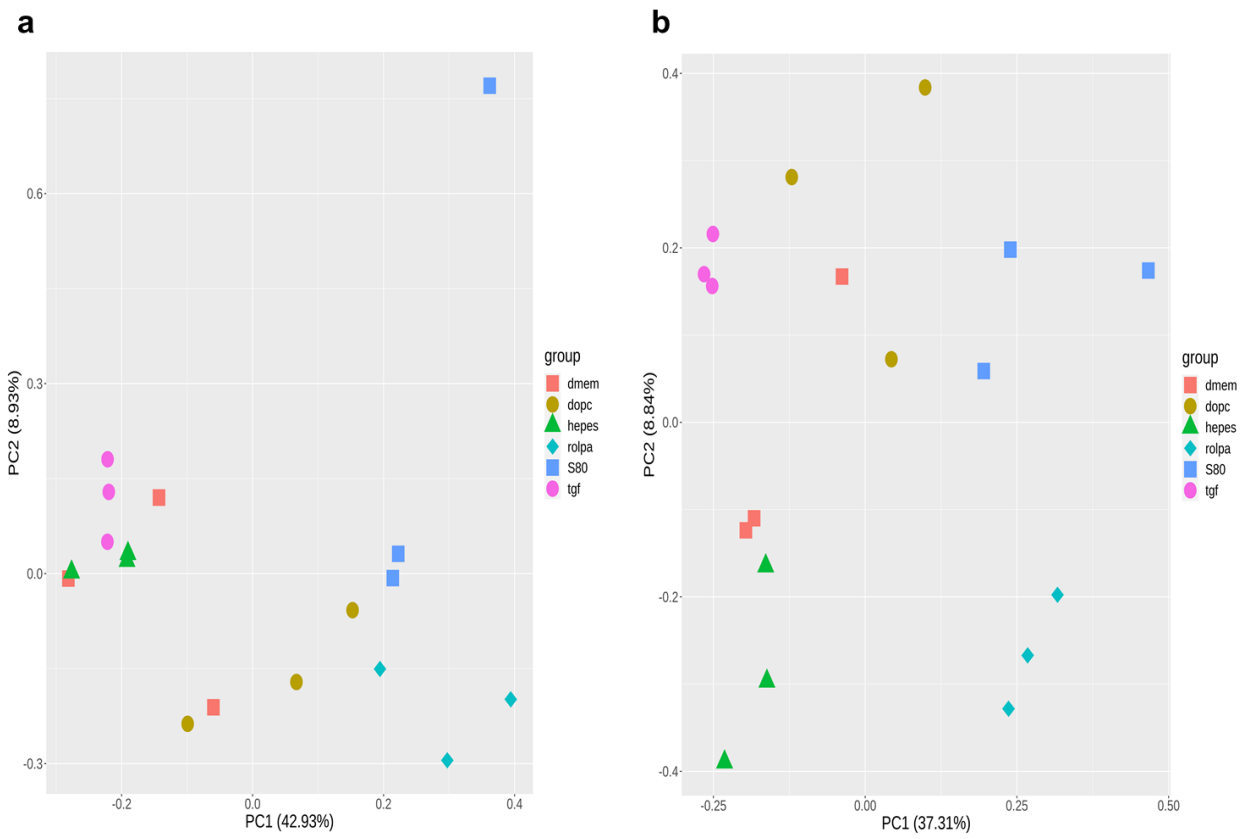

Figure A3-8: PCA analysis with iTop3 (**a**) and LFQ (**b**) for the combined AF4-peaks. While there was never perfect grouping, LFQ performed slightly better, which is why we chose it for the main text.

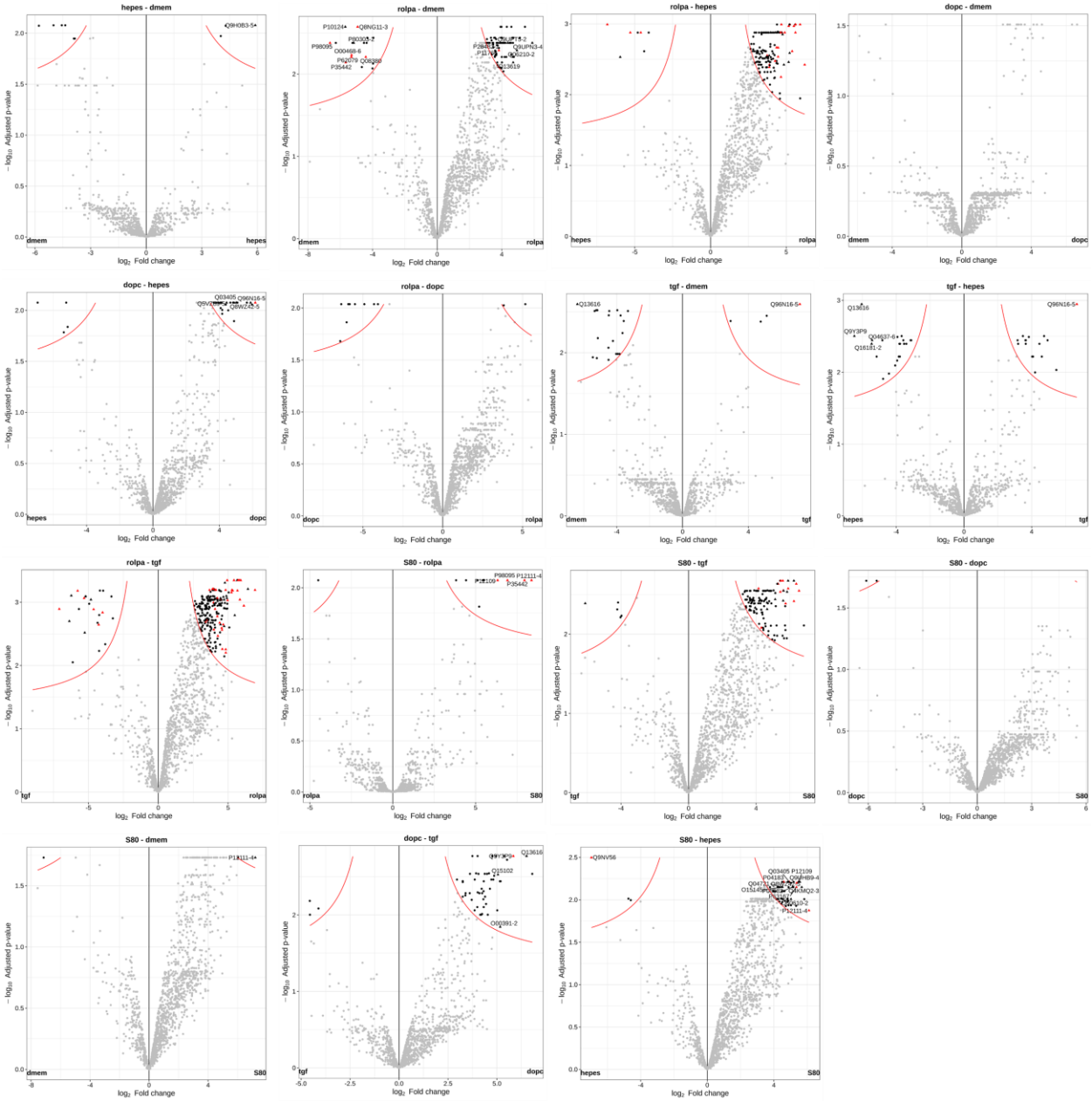

Figure A3-9: Volcano plots with direct comparisons of treatment groups based on EV-proteins from AF4-purified samples, peaks combined (LFQ).

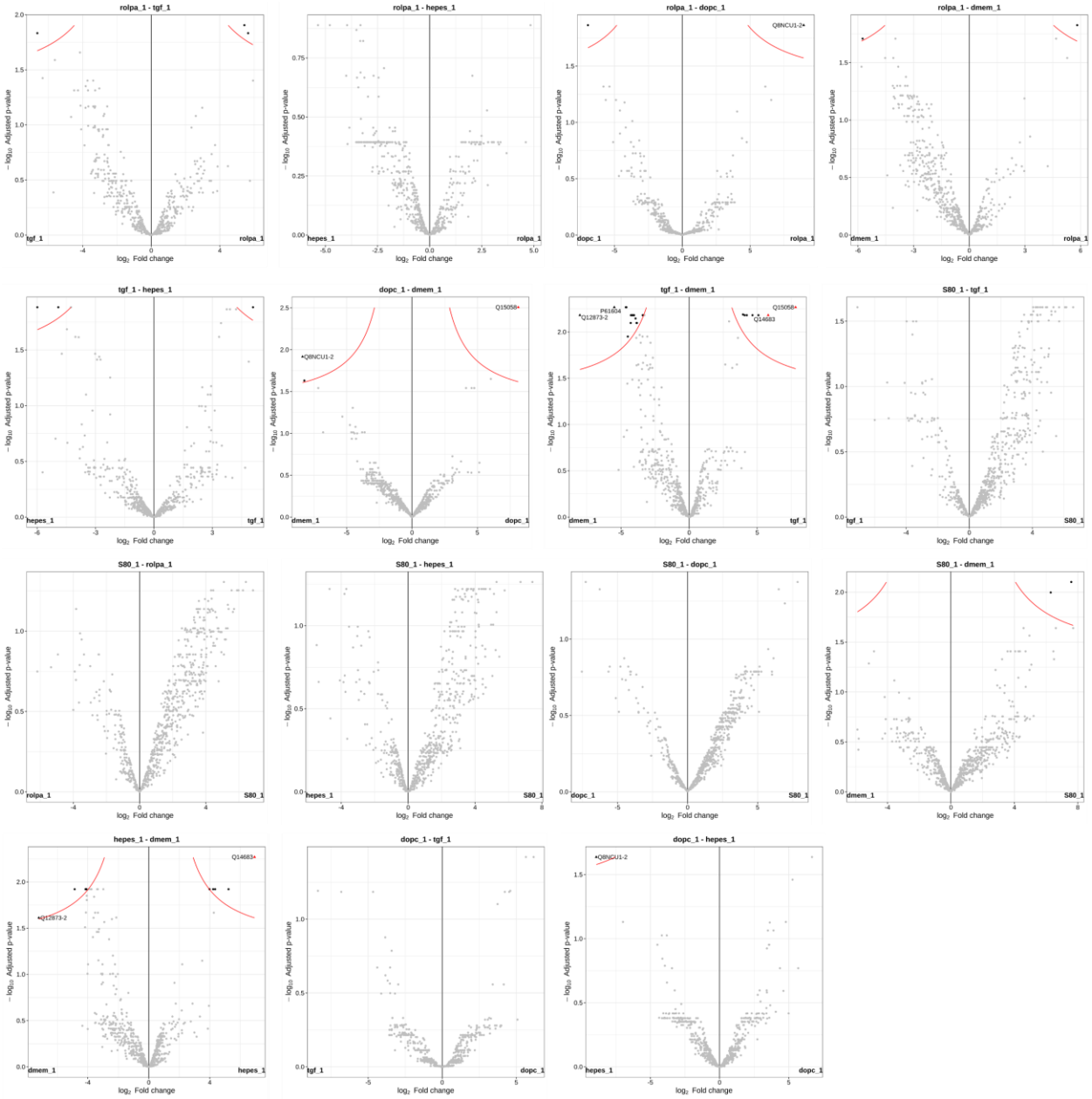

Figure A3-10: Volcano plots with direct comparisons of treatment groups based on EV-proteins from AF4-purified samples, peak 1 (LFQ).

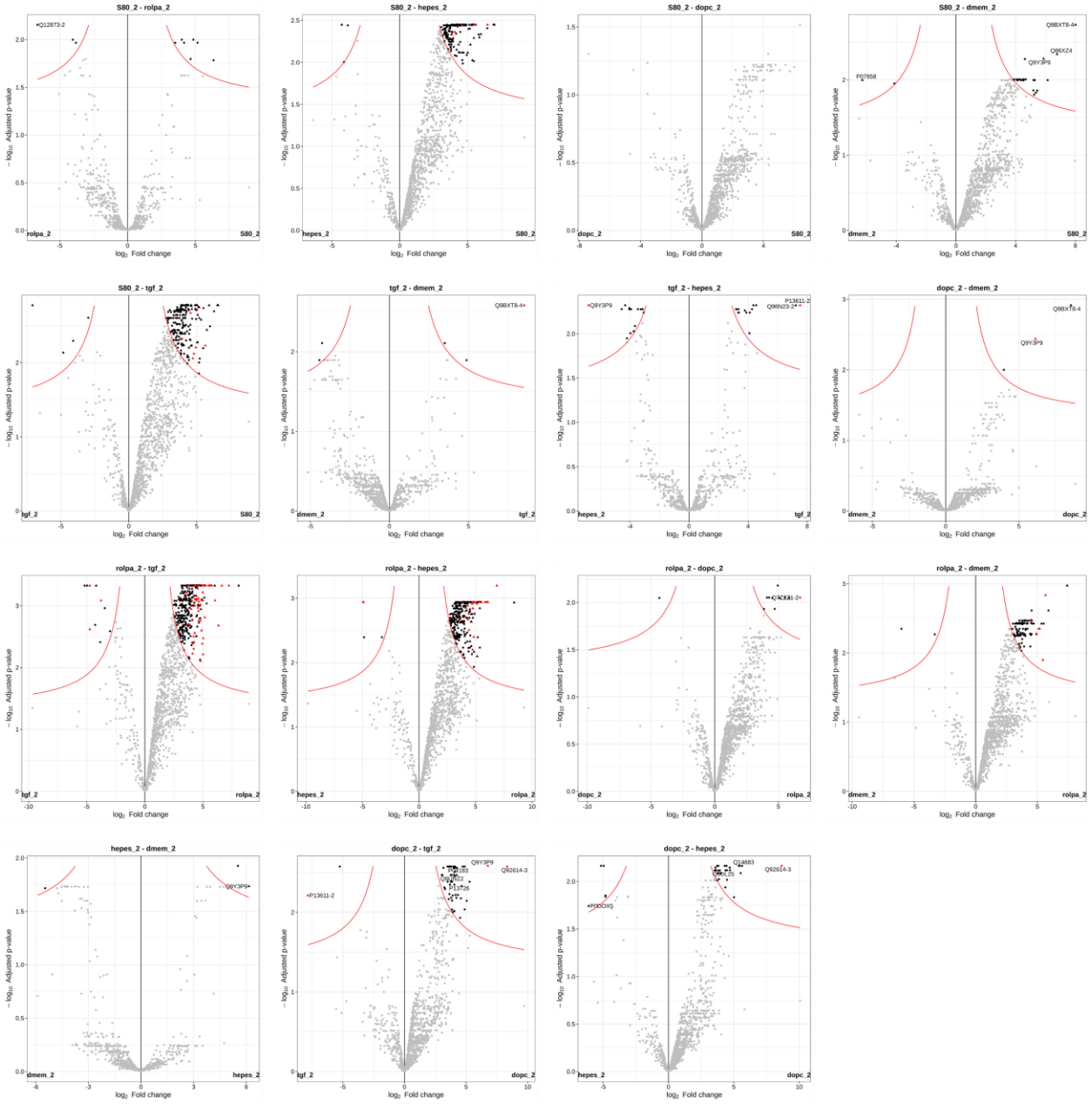

Figure A3-11: Volcano plots with direct comparisons of treatment groups based on EV-proteins from AF4-purified samples, peak 2 (LFQ).

Chapter 4 supplementary information

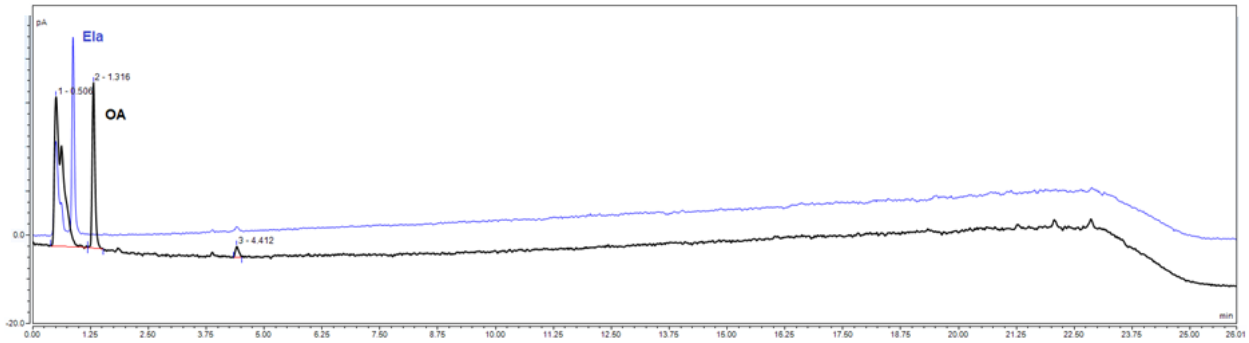

Figure A4-1: Representative chromatograms for Ela and OA with the same method as with as detected with the CAD. The ghost peaks along the baseline were present in blank samples too, as well as in HPLC runs of other users.

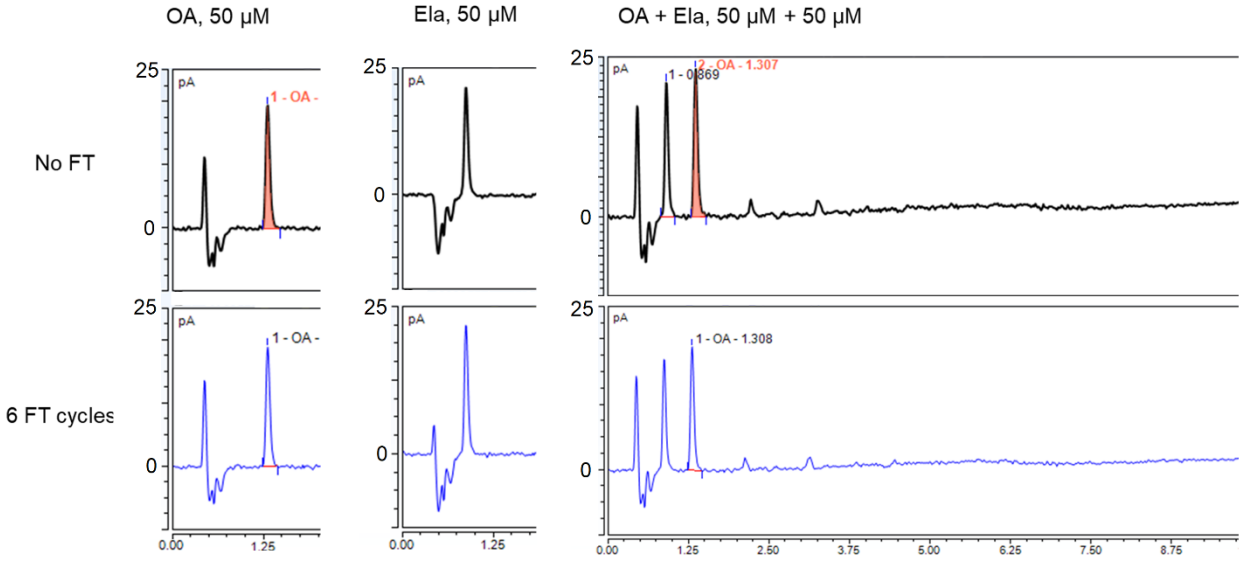

Figure A4-2: Representative chromatograms of Ela and OA before and after undergoing 6 freeze-thaw (FT) cycles, either separately or in the same sample.

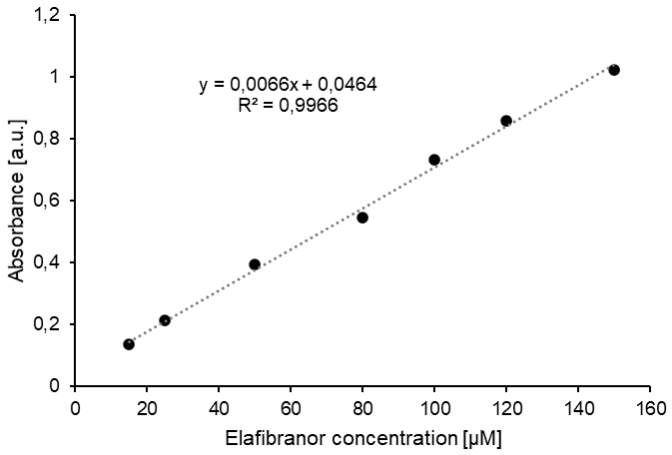

Figure A4-3: Calibration curve for Ela obtain with a plate reader (λ_{abs} = 358 nm) (mean ± SD, n = 3).

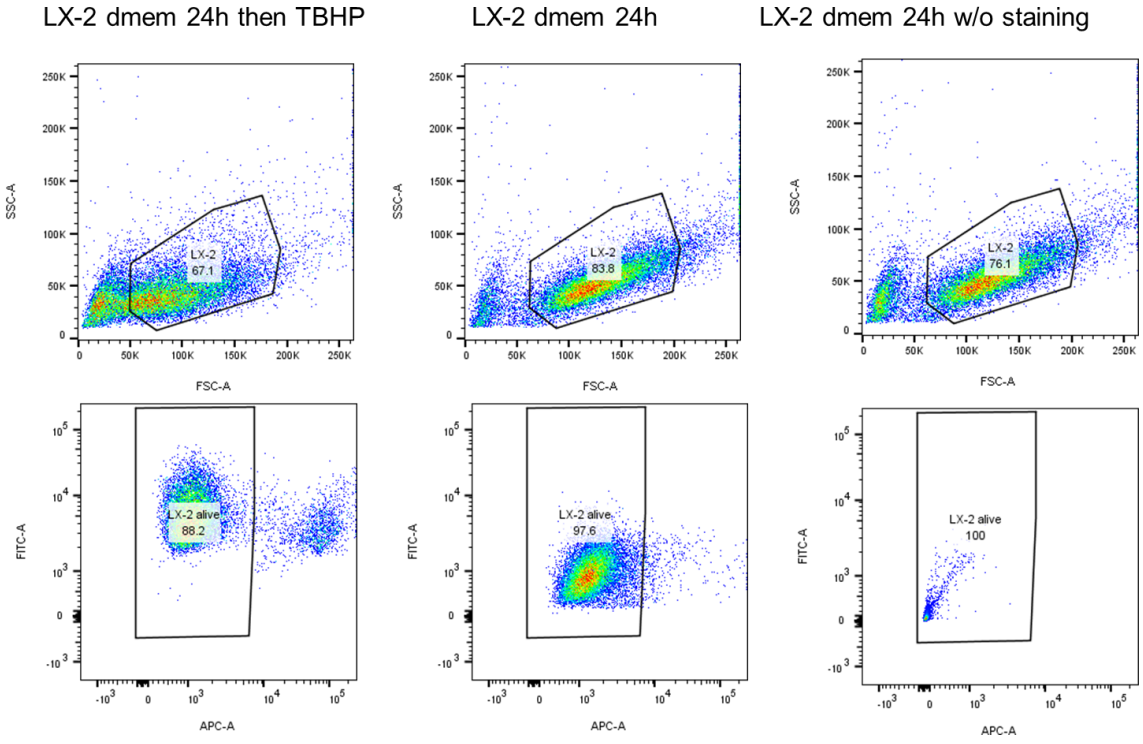

Figure A4-4: Gating strategy for **Chapter 4.2.5**, illustrated with the example of DMEM-treated cells. The upper row shows the gating around the population we believe to be LX-2 cells. The bottom row shows the gating around alive LX-2 cells (not stained by the dead cell dye SYTOX). Within the events associated with living LX-2, the Mean Fluorescence Intensity associated with the CellROX Green dye (indicative of ROS) was finally reported in **Figure 4-7**).

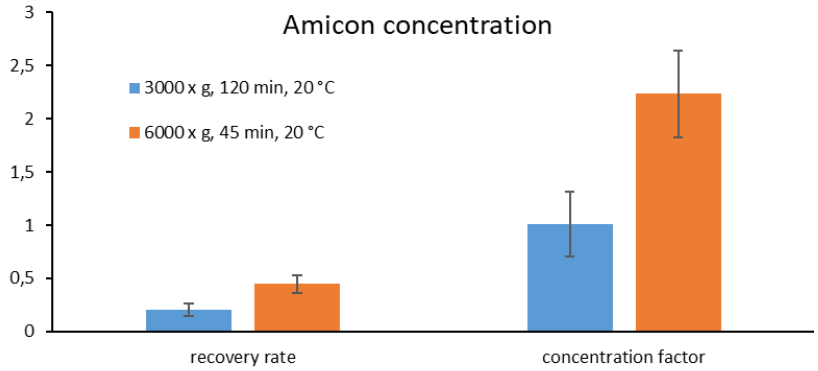

Figure A4-5: Best recovery rates and concentrating factors of SEC-purified EVs we achieved with Amicon® centrifugal units with 10'000 kDa membrane cutoff. Additional, unsuccessfully tested conditions included combinations of different relative centrifugal forces (3'000, 6'000, 14'0000 x g), for various amounts of times (45, 90, 120, 180 min) and both at 4 and 20 °C. In those cases, we either lost (almost) all of our EV-sample, or there was no change. Other membrane cutoffs might work out better (e.g., 100'000 kDa).

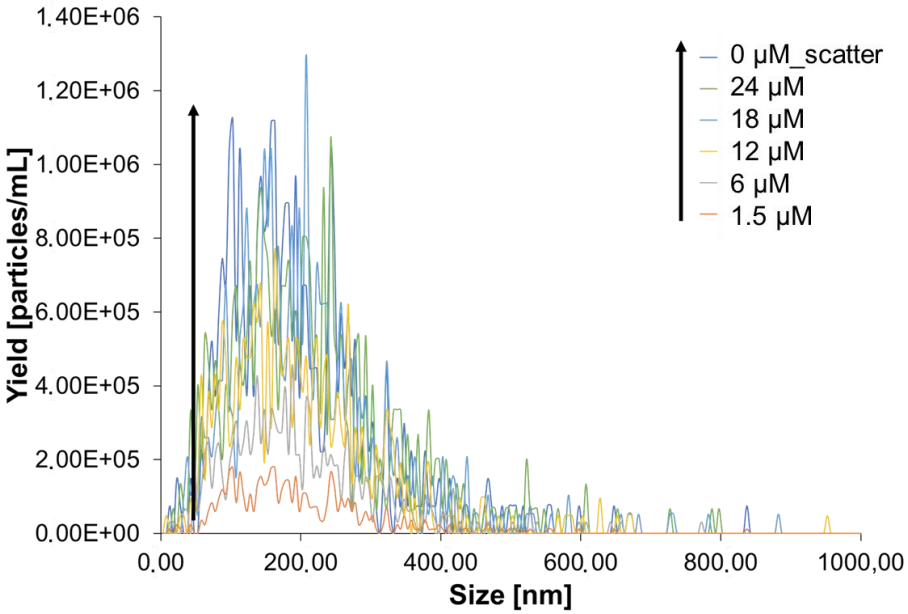

Figure A4-6: Representative size distribution profiles of particles measured in fluorescence mode upon addition of increasing amounts of PKH67.

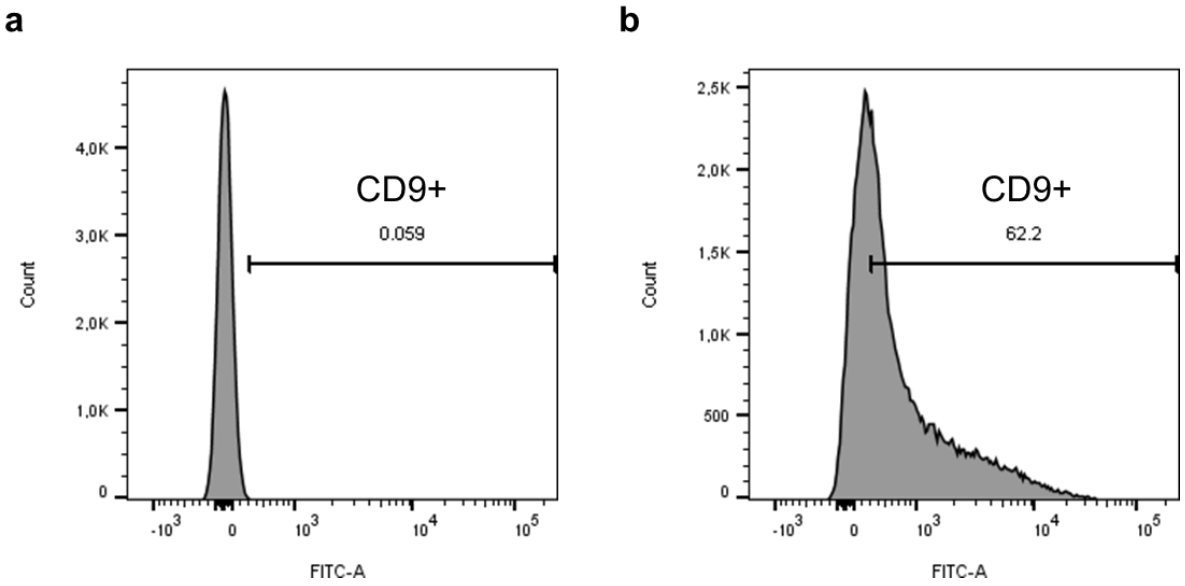

Figure A4-7: Representative histograms showing the count of CD9 positive beads in unstained (**a**) and stained (**b**) samples analysed by FACS in **Figure 4-10c**).

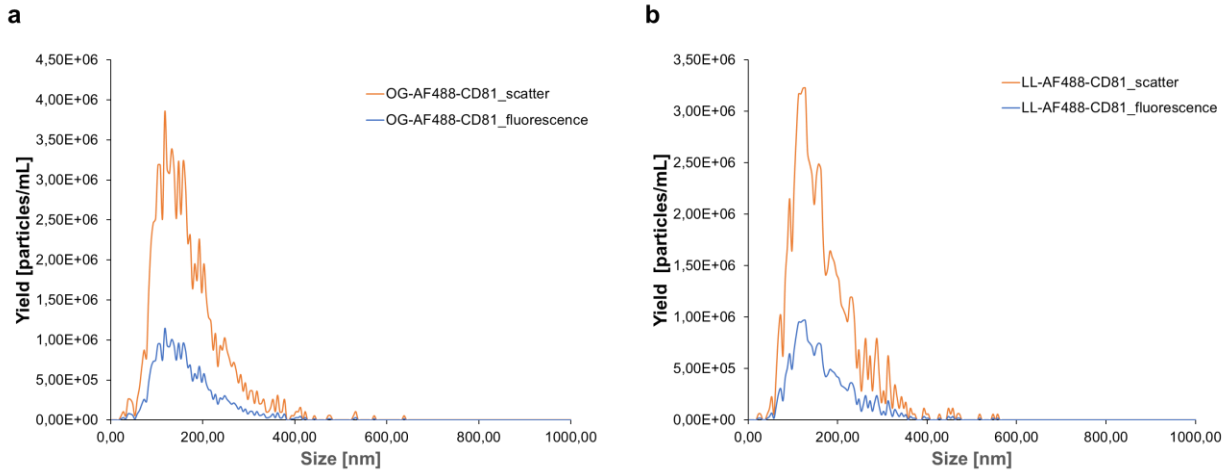

Figure A4-8: Representative size distribution profiles of particles measured in scatter and fluorescence mode upon addition of AF488-CD81, using the original (OG, purchased already AF488-conjugated) probe (**a**), or using the Lightning-Link® (LL) labelled probe we conjugated (**b**).

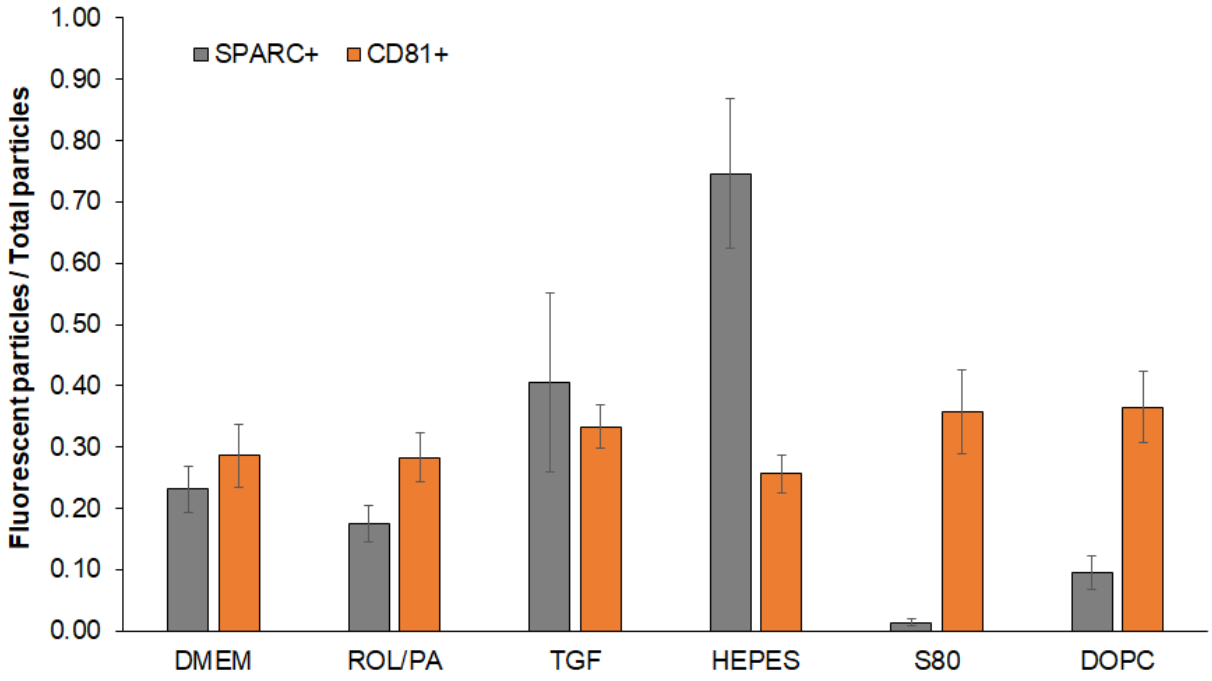

Figure A4-9: Detection of SPARC and CD81 on EVs originating from differently treated LX-2 cells. CD81 levels are consistent throughout whereas the relative presence of SPARC+ EVs varies considerably (this graph adds to **Figure 4-11**).

Abbreviations

AF4	Asymmetrical Flow Field Flow Fractionation
AF488	AlexaFluor®488
AF488-CD81	AlexaFluor®488 conjugated, anti human CD81 antibody
AF488-CD9	AlexaFluor®488 conjugated, anti human CD9 antibody
CCM	Conditioned cell culture medium
CCMa	CCM harvested 24 h after treatment (potentially including residual treatment)
CCMb	CCM harvested 24 h after CCMa collection and substitution with serum fresh free cell culture medium (DMEM)
CCMa-EVs	Extracellular vesicles derived from CCMa
CCMb-EVs	Extracellular vesicles derived from CCMb
CCM(a,b)-EVs	Treatment using CCMa-EVs first, followed by treatment with CCMb-EVs
DAPI	4′,6-diamidino-2-phenylindole
DOPC	1,2-dioleoyl-*sn*-glycero-3-phosphocholine
EAF4	Electric AF4
EPLs	Essential phospholipids
EVs	Extracellular vesicles
FACS	Flow cytometry
f-NTA	Fluorescence nanoparticle tracking analysis
HEPES	4-(2-hydroxyethyl)-1-piperazineethanesulfonic acid buffer
HSCs	Hepatic stellate cells
iBAQ	Intensity-based, absolute quantification of proteins
IC	Isotype control
iTop3	Protein quantification based on the three most intense peptides
LFQ	Label free quantification of proteins
LL-AF488-CD81	AF488-CD81, conjugated using the Lightning-Link kit
LL-AF488-GPC1	AF488-GPC1, conjugated using the Lightning-Link kit
LL-AF488-SPARC	AF488-SPARC, conjugated using the Lightning-Link kit
LL-IC	Isotype control, conjugated using the Lightning-Link kit
LC/MS	Liquid chromatography coupled to mass spectrometry
NAFLD	Non-alcoholic fatty liver disease
NASH	Non-alcoholic steatohepatitis
NTA	Nanoparticle tracking analysis
OG-AF488-CD81	Synonymous to AF488-CD81 (OG standing for “original”)
ORO	Oil Red O
PA	Palmitic acid

PC	Phosphatidylcholine
PPC	Polyenylphosphatidylcholines
ROL	Retinol
ROS	Reactive oxygen species
S80	Soybean phospholipid with >75% PC
SPARC	Secreted protein acidic and rich in cysteine
sst	Serum starvation (treatment with DMEM)
Treatment: DMEM	Serum free cell culture medium
Treatment: DOPC	DOPC 5 mM in DMEM, negative control to S80
Treatment: HEPES	HEPES 10% v/v in DMEM, negative control to S80
Treatment: ROL/PA	ROL/PA 10/300 μM in DMEM, positive control for quiescent-like status
Treatment: S80	S80 mM, inducing quiescent-like status
Treatment: TGF	TGF 10 ng/mL, inducing perpetuation of activated status
TGF	Tissue growth factor-β1
α-SMA	α-smooth muscle actin

Acknowledgments

Prof. Dr. Paola Luciani and I go back a little. Around the time I finished my Master's, I asked her if I could mention her as a reference in my CV, and she wrote a letter of support saying that she found me "a diligent and enthusiastic person who has an obvious passion for research." I never thought of myself like that before, but the moment I read it I realized that, all my life through, that's exactly who I've always wanted to be. I'm no expert, but I'm pretty sure that's the definition of inspiring. So what I'm grateful for is so much more than just this amazing opportunity. Paola, you believed I could and should do this when nobody else in my life did, including myself, and that's all it took to make everything else possible. Thank you so, so much.

Of course, the minute I started my PhD you sent me off for almost a year, 500 km away. We've had our share of bad luck during the project, but it pales in comparison to how lucky I was getting to work with Jun.-Prof. Dr. Gregor Fuhrmann. There are not many people I'm a fan of, and even fewer who I actively admire, and Gregor, you became one in the span of a fortnight. This doesn't sound like a lot, but it really is: you made it so very easy for me to do the very best science I could imagine, and even some that I couldn't before you opened my mind to it. Being a thesis advisor doesn't necessarily require being a mentor, so while a lot of PhD students don't even get one, I got two. How is that not obscenely lucky?

But it gets better, because of the exceptional teams of scientists I met along the way.

The Luciani research group from Jena, then expended in Bern, with Gina, Florian, Lisa, Aymar, Simone, Gregor, Marianna, Ivo: we've been through a lot together and you'll always hold a special place in my heart.

The Fuhrmann Lab (BION) group and the HIPSters in Saarbrücken: Kathrin, Max, Adriely, Thomas, Eilien, Hanzey, Robert, Sara, Remi, Olga, Chiara, Xabi, Alex, and so many more… that 100€ guitar everybody signed before I left is still my most valuable possession in the world.

I couldn't possibly tell you all how important you are, but I have to say at least this much: thank you Dr. Gina Valentino for sharing your resiliency and enthusiasm, not even in my wildest dreams I could have asked for a better co-worker and friend. Thank you, Dr. Kathrin Fuhrmann, for everything you've taught me, and especially for your undying optimism, showing me, time and again, how there's always a way. Thank you, Dr. Robert Richter, for giving me the invaluable gift of music. And thank you, Dr. Hanzey Yaser, for everything: I wish I was half the scientist you are, and even just a third of the person.

A special mention goes to my students Rebecca Hämsch and Katharina Leinenbach (University of Saarland, Saarbrücken), Sahra Stein and Maxi Zeise (Friedrich Schiller University, Jena), and Jana Leuenberger (University of Bern). I learned so much teaching you, and it's my sincerest hope you guys shared some of the joy I find in science.

My final thank you is to my friends (Hakim, Fede, Sim, Betti) and especially to my family back home and abroad, the group of Zivko cousins and my parents Bozo and Dina. For putting up with my constant absences, for cheering me along the way, and for always being a safe haven when I needed it. To my siblings Maria and Tome I don't really know what to say: you mean everything, you give everything meaning.

Declaration of consent

on the basis of Article 18 of the PromR Phil.-nat.19

Name/First Name: Zivko Cristina

Registration Number: 10-926-392

Study Program: Bachelor ☐ Master ☐ Dissertation ☑

Title of the Thesis: Lipid-based anti-fibrotic formulations and their impact on extracelluar vesicles

Supervisor: Prof. Dr. Paola Luciani

I declare herewith that this thesis is my own work and that I have not used any sources other than those stated. I have indicated the adoption of quotations as well as thoughts taken from other authors as such in the thesis. I am aware that the Senate pursuant to Article 36 paragraph 1 litera r of the University Act of September 5th, 19996 and Article 69 of the University Statute of June 7th, 2011 is authorized to revoke the doctoral degree awarded on the basis of this thesis.

For the purpose of evaluation and verification of compliance with the declaration of originality and the regulations governing plagiarism, I hereby grant the University of Bern the right to process my personal data and to perform the acts of use this requires, in particular, to reproduce the written thesis and to store it permanently in a database, and to use said database, or to make said database available, to enable comparison with theses submitted by others.

Place/Date

Bern, 16.02.2021

Signature